Flow Dynamics and Control of a High Expansion Ratio Backward-Facing Step Flow with Acoustic Excitation



Owen Sinclair
St Anne's College
University of Oxford

A thesis submitted for the degree of
Doctor of Philosophy

Michaelmas 2025

Supervised by Marko Bacic

Abstract

A backward-facing step (BFS) flow with expansion ratio 2 is investigated as a canonical example of a separated internal flow subject to acoustic actuation from the opposite-to-step side at practically relevant Reynolds numbers based on step height from 22000 to 38000. Opposite-side acoustic actuation may be a practical alternative to forcing near/at the separation line in duct flows where packaging or installation constraints limit access to the reattaching side.

A Helmholtz-resonator style acoustic actuator array is designed, leveraging actuator and test section resonances to maximize excitation amplitude. Reattachment length reduction of 24-28% compared to baseline is demonstrated, confirming that opposite-side acoustic actuation is of similar effectiveness to the more typical periodic forcing at the step edge, and more effective than previous examples of non-local ('external') acoustic excitation in the literature. Metrics for the spatial uniformity of the flow field relevant to heat exchanger performance are introduced, and the actuation is shown to improve flow uniformity downstream of the step substantially. Novel spanwise distributed actuation strategies are also investigated and demonstrated to have a reasonable effect on the secondary side-wall vortices, but limited influence on overall flow uniformity compared to spanwise uniform actuation.

The dynamics of the BFS flow are investigated by spectral analysis of hot-wire and wall pressure measurements. The main acoustic modes of the experimental rig are identified as the half-wave 'organ pipe' resonance of the channel (300 Hz), and the Helmholtz resonance of the combined plenum and test section (21 Hz). A combination of long duration hot-wire point measurements (59 points for 1000 s each) and high spatial resolution hot-wire traverses (9999 points for 10 s each) allow for an exceptionally detailed examination of the vortex dynamics in the BFS flow, from which the dominant modes commonly observed in literature (Kelvin–Helmholtz roll-up, step mode, shedding mode, flapping mode) are identified.

Scale resolving CFD simulations representative of the real flow are used for visualisation and further interrogation of the physics of coherent structures and vortex-acoustic lock-on. Each of the dominant modes/coherent structures identified from the experimental hot-wire spectra is extracted from the CFD data by dynamic mode decomposition (DMD), providing a clear picture of the spatial distributions of each mode and demonstrating their modification under acoustic excitation.

Acoustic forcing modifies vortex dynamics by the locking-on of coherent vortex modes to the excitation tone and its harmonics/sub-harmonics, enhancing vortex strength and consistency. An important distinction between the mechanism of control by opposite-side acoustic actuation (and 'external' acoustic excitation in general), and the local periodic excitation at the step edge more common in the literature is consolidated: unlike periodic excitation from the step edge, which has been widely reported to directly force vortex roll-up, 'external' acoustic excitation couples to the scale of vortex structure with natural frequency closest to the forcing tone. At $20\,\mathrm{m\,s^{-1}}$ inlet velocity, the actuation is demonstrated to couple to the intermediate scale of shear layer vortices between roll-up and the larger scale 'step mode' vortices, and roll-up is shown to lock on to the second and third harmonics of the actuation tone.

Experimental system identification is conducted for the amplitude modulated system across a range of operating conditions (inlet velocity and actuation amplitude), from which two closed-loop controllers are designed and implemented. First, a gain-scheduling PI controller is designed, with the aims of tracking reattachment length (using wall pressure as proxy) and disturbance rejection. However, high levels of noise and transport delay limit controller performance, giving bandwidth $\sim$2 Hz. Second, a novel interpolating LQG controller is designed to specifically target the periodic disturbance due to the Helmholtz resonance of the plenum-test section system, and successfully suppresses the velocity disturbance by around 1 dB, at the cost of slightly amplifying unsteadiness above and below the target frequency band. Robustness to plant non-linearities is achieved by running 16 individual LQG controllers in parallel, each designed at a different operating point, and interpolating the control action based on current conditions.

Contents

List of Figures **vii**

1 Introduction **1**

1.1 Motivation 1

1.2 Thesis Content 2

2 Background and Literature Review **4**

2.1 Introduction 4

2.2 Flow Control 4

2.2.1 Common Actuation Strategies 6

2.2.2 Flow Control Actuators 10

2.3 Backward-facing Step Flow 12

2.3.1 Dynamical Modes/Flow Structures 15

2.3.2 Vortex Break-up and Recovery Region 19

2.3.3 Influence of Inlet Conditions and Channel Geometry 20

2.4 Open-Loop Flow Control Examples 22

2.4.1 Backward-facing Step Flow Control 22

2.4.2 S-duct Flow Control 27

2.4.3 Non-BFS Acoustic Flow Control 28

2.5 Fundamentals of Closed-loop Control 29

2.5.1 Optimal Control: Linear Quadratic Regulator 33

2.5.2 Kalman Filter 35

2.5.3 Linear Quadratic Gaussian (LQG) 38

2.6 Reduced Order Modelling 38

2.6.1 Proper Orthogonal Decomposition . . . 39
2.6.2 Dynamic Mode Decomposition . . . 41
2.7 Closed-loop Control of Separated Flows . . . 45
2.7.1 Model-based Approaches . . . 45
2.7.2 Model-free Approaches . . . 48

3 Experimental and Numerical Setup 50
3.1 Experimental Setup . . . 50
3.1.1 Effect of measurement tube length . . . 55
3.1.2 Acoustic Actuator Design . . . 56
3.2 Characterisation of Acoustic Actuation . . . 60
3.3 Numerical Setup . . . 62
3.3.1 Mesh and Boundary Conditions . . . 63
3.3.2 Comparison of Laminar Simulation to URANS . . . 65
3.4 Validation of Numerical Simulations . . . 68
3.4.1 Mean and RMS Wall Pressure . . . 68
3.4.2 Mean and RMS Velocity Field . . . 69
3.4.3 Frequency Spectra . . . 71
3.4.4 Conclusion . . . 72

4 Effect of Actuation on Time-mean Flow 75
4.1 Introduction . . . 75
4.2 Wall Pressures and Reattachment Length Estimation . . . 76
4.2.1 Static response of flow with actuation frequency . . . 80
4.3 Velocity Field . . . 81
4.3.1 Effect of Actuation on Spatial Flow Uniformity . . . 93
4.4 Spanwise Non-uniform Actuation . . . 97
4.5 Conclusions . . . 102

5 Flow Dynamics 104
5.1 Introduction . . . 104
5.2 Baseline Wall Pressure Measurements . . . 105

5.2.1 Identification of Acoustic Resonances . . . 106
5.2.2 Identification of Flow Features . . . 113
5.3 Baseline Hot-Wire Velocity Measurements . . . 115
5.3.1 Identification of Coherent Modes . . . 115
5.3.2 Very Low Speed Flow . . . 123
5.4 Hot-wire Velocity Measurements under Acoustic Forcing . . . 125
5.4.1 Effect of Excitation Volume . . . 129
5.4.2 Effect of Inlet Speed . . . 130
5.5 Laminar CFD Analysis . . . 133
5.5.1 Roll-Up and First Merging . . . 133
5.5.2 'Step mode' Vortex . . . 135
5.5.3 Modal Decomposition . . . 136
5.6 Spanwise Frequency Content . . . 148
5.6.1 Baseline Flow . . . 148
5.6.2 Forced Flow . . . 152
5.7 Conclusion . . . 156

6 Closed-loop Control **158**

6.1 Introduction . . . 158
6.2 Model Identification of Backward-facing Step Dynamics . . . 159
6.2.1 Empirical Transfer Function Estimates . . . 159
6.2.2 Wall Pressure ETFEs . . . 160
6.2.3 Hot-Wire ETFEs . . . 165
6.2.4 Choice of Feedback Measurement . . . 167
6.2.5 High Order Plant Model fits . . . 168
6.2.6 Low Order State Space Model Fits . . . 168
6.2.7 Static Mapping . . . 171
6.3 PI Controller . . . 173
6.3.1 Gain Tuning . . . 176
6.3.2 Gain Scheduling . . . 179
6.3.3 Validation of Gain Scheduling . . . 180

6.3.4 Step Responses . . . 182
6.3.5 Inlet Velocity Disturbance Rejection . . . 184
6.3.6 Output Disturbance Rejection . . . 185
6.4 Interpolating LQG Controller . . . 188
6.4.1 Introduction . . . 188
6.4.2 Non-linear control by interpolation of control action . . . 188
6.4.3 Adjusting the LQT for static non-linearity . . . 190
6.4.4 LQG Tuning . . . 191
6.4.5 Experimental Closed-Loop Transfer Functions . . . 194
6.4.6 Step Response . . . 196
6.4.7 Inlet Velocity Disturbance Rejection . . . 197
6.4.8 Output Disturbance Rejection . . . 198
6.5 Conclusions and Discussion . . . 202

7 Summary and Conclusions **205**

7.1 Summary of Work . . . 205
7.2 Conclusions . . . 208
7.3 Recommendations for Future Work . . . 209

A Identified Transfer Function and State Space Models **212**

A.1 Transfer Function Model Fits . . . 212
A.2 State Space Model Fits . . . 214

List of Figures

1.1 Example of a heat management system for a hydrogen combustion turbofan engine featuring pre-cooling, inter-cooling, recuperation, and cooled turbine cooling air, taken from Patrao et al. [4] 2

2.1 Categorisation of Flow Control [11] 6
2.2 Illustration of boundary layer blowing/suction for separation prevention . . 7
2.3 Features of turbulent flow behind a backward-facing step 13
2.4 Backward-facing step geometry 15
2.5 Flapping modes in backward-facing step flows. Longitudinal flapping in red, cross-flapping in blue 19
2.6 Generic closed-loop controller block diagram 30
2.7 Block diagram of full state feedback using an observer 36

3.1 Experimental rig 50
3.2 Schematic of experimental setup 51
3.3 Plenum internal assembly 51
3.4 Bell mouth/coupling and test section geometry 52
3.5 Connection of Sensortechnics HCX transducers 55
3.6 Frequency response of Visaton FR 58 4 Ω full range loudspeaker, copied with permission from VISATON GmbH & Co. KG [163]. 58
3.7 Acoustic actuator assembly and internal cavity volumes 59
3.8 Acoustic actuator assembly installation 60
3.9 Actuator response 62
3.10 CFD mesh side profile 65

3.11 RANS and laminar solver mean streamlines. Red triangles show reattachment points calculated from wall shear stress 66
3.12 Instantaneous snapshots of unsteady k-ω SST and laminar solutions with actuation. Mean reattachment point shown by black triangles, instantaneous reattachment points shown by red triangles. 67
3.13 Phase averaged laminar simulation streamlines. Mean reattachment point shown by black triangles, phase averaged reattachment points shown by red triangles 67
3.14 CFD and experimental mean and RMS wall C_p 69
3.15 Baseline hot-wire and CFD mean and RMS velocity profiles 70
3.16 Forced hot-wire and CFD mean and RMS velocity profiles 71
3.17 Point frequency spectra of CFD u-v velocity compared to experimental hot-wire measurements. Baseline flow on left, actuation on right 73
3.18 Point frequency spectra of CFD wall pressure compared to experimental measurements. Baseline flow on left, actuation on right 74

4.1 Mean wall C_p distribution measured using Honeywell SSCDRRD010MDAA5 transducers 76
4.2 RMS measured wall C_p and polynomial fits. Dashed lines indicate peaks of fits 79
4.3 Estimated reattachment lengths based on peak RMS wall pressure location 79
4.4 Static flow response 81
4.5 Traverse plane point locations 82
4.6 Mean u-v velocity at hot-wire traverse planes 83
4.7 RMS u-v velocity at hot-wire traverse planes 84
4.8 Baseline mean and RMS velocity at $x/h = 0.75$, 3, and 6.5 86
4.9 $a = 0.05\,\mathrm{V}$ mean and RMS velocity at $x/h = 0.75$, 3, and 6.5 87
4.10 $a = 0.1\,\mathrm{V}$ mean and RMS velocity at $x/h = 0.75$, 3, and 6.5 87
4.11 $20\,\mathrm{m\,s^{-1}}$ wall-normal mean velocity profiles at $z/h = 0$, 1.5, and 3, $a = 0$ (baseline), 0.05 V, and 0.1 V. $x/h = 0.25$ to $x/h = 4$ 89

4.12 $20\,\mathrm{m\,s^{-1}}$ wall-normal mean velocity profiles at $z/h = 0$, 1.5, and 3, $a = 0$ (baseline), 0.05 V, and 0.1 V. $x/h = 4.5$ to $x/h = 12.5$ 90
4.13 $20\,\mathrm{m\,s^{-1}}$ wall-normal RMS velocity profiles at $z/h = 0$, 1.5, and 3, $a = 0$ (baseline), 0.05 V, and 0.1 V. $x/h = 0.25$ to $x/h = 4$ 91
4.14 $20\,\mathrm{m\,s^{-1}}$ wall-normal RMS velocity profiles at $z/h = 0$, 1.5, and 3, $a = 0$ (baseline), 0.05 V, and 0.1 V. $x/h = 4.5$ to $x = 12.5$ 92
4.15 20 $\mathrm{ms^{-1}}$ spanwise mean velocity profiles at y/h = -0.5, 0, and 0.5, $a = 0$ (baseline), 0.05 V, and 0.1 V, at several x locations 93
4.16 Velocity non-uniformity as a function of streamwise location 94
4.17 Centre span velocity profiles at $x/h = 5$ 96
4.18 NU_y at $x/h = 5$ 96
4.19 Spanwise velocity profiles at $x/h = 5$ for different spanwise actuation configurations 100
4.20 Spanwise velocity profiles at $x/h = 8.5$ for different spanwise actuation configurations 101

5.1 Baseline wall pressure PSDs plot against frequency in Hz (actuation cavities open) 108
5.2 Baseline wall pressure PSDs plot against Strouhal number (actuation cavities open) 109
5.3 Wall Pressure PSDs at $x/h = 2$ and $x/h = 4$, actuation cavity orifices open. Zoomed in to 300 Hz peak 110
5.4 Wall Pressure PSDs cavity orifices open vs taped over 111
5.5 Effect of 200 mm extension on wall pressure frequency content 112
5.6 Streamwise evolution of baseline wall pressure PSD for each velocity (actuation cavities open). Measurement closest to estimated reattachment point in black. Each PSD offset by 2 dB compared to the previous location. 114
5.7 hot-wire measurement points at centre plane ($z = 0$). Estimated reattachment point at $v_\mathrm{in} = 20\,\mathrm{m\,s^{-1}}$ shown by blue triangle 115
5.8 PSDs of hot-wire point measurements at $20\,\mathrm{m\,s^{-1}}$ 117

5.8 PSDs of hot-wire point measurements at $20\,\mathrm{m\,s^{-1}}$. PSD at each location offset for legibility by the amount indicated in the plot line labels. 118
5.9 Pre-multiplied power spectra of hot-wire measurements around expected roll-up location 121
5.10 hot-wire spectra at multiple inlet velocities 123
5.11 $1\,\mathrm{m\,s^{-1}}$ inlet speed pre-multiplied hot-wire spectra 125
5.12 Effect of acoustic actuation on pre-multiplied hot-wire PSD at several query points 128
5.13 Pre-multiplied hot-wire PSD along $y/h = 0.5$ at $v_{in} = 20\,\mathrm{m\,s^{-1}}$ with acoustic forcing 128
5.14 Comparison of pre-multiplied hot-wire spectra with $a = 0.05\,\mathrm{V}$ and $a = 0.1\,\mathrm{V}$ amplitude excitation. PSD at each x location offset by $0.25(x - x_1)/h$, where $x_1/h = 0.25$ (the most upstream measurement location) 130
5.15 Effect of acoustic actuation on hot-wire velocity spectrum at multiple velocities 132
5.16 Effect of acoustic actuation on hot-wire velocity spectrum at multiple velocities, zoomed in peaks at forcing frequency and first sub-harmonic 132
5.17 Baseline CFD vortex roll-up and merging 134
5.18 Actuated CFD vortex roll-up and merging 134
5.19 Baseline CFD vortex merging. 135
5.20 Cumulative POD mode variance 136
5.21 Frequency content of truncated POD reconstruction 138
5.22 First 10 Baseline POD modes. Colour levels show pressure, arrows show velocity direction and magnitude 139
5.23 First 10 Steady Actuation POD modes Colour levels show pressure, arrows show velocity direction and magnitude 140
5.24 Weighting, $\mathbf{W}$, used for DMD. Superimposed on mean streamlines of baseline CFD solution 141
5.25 DMD eigenvalues of baseline and forced flows 143
5.26 Baseline DMD modes. Colour levels show pressure, arrows show velocity direction and magnitude. Red triangle indicates mean reattachment point . 144

5.27 Steady actuation DMD modes. Colour levels show pressure, arrows show velocity direction and magnitude. Red triangle indicates mean reattachment point 145
5.28 u-velocity contours of baseline flow DMD flapping mode + mean. Red triangle indicates instantaneous reattachment point based on wall shear stress. 147
5.29 Wall shear stress of baseline flow DMD flapping mode + mean. Mean shown by black dashed line, instantaneous wall shear stress shown in red. 147
5.30 Spanwise PSD distribution at $y/h = 0.5$ and several streamwise locations . . 150
5.31 Spanwise PSD distribution at $y = 0$ and several streamwise locations 151
5.32 Spanwise PSD distribution at $y/h = -0.825$ and several streamwise locations 151
5.33 Comparison of smoothed and un-smoothed pre-multiplied hot-wire PSD with actuation 153
5.34 Spanwise PSD distribution at $y/h = 0.5$ and several streamwise locations . . 154
5.35 Spanwise PSD distribution at $y = 0$ and several streamwise locations 155
5.36 Spanwise PSD distribution at $y/h = -0.825$ and several streamwise locations 155

6.1 ETFEs at $x/h = 2$ 161
6.2 ETFEs at $x/h = 3$ 162
6.3 ETFEs at $x/h = 4$ 162
6.4 ETFEs at $x/h = 5$ 163
6.5 ETFEs at $x/h = 6$ 163
6.6 ETFEs at $x/h = 7$ 164
6.7 Hot-wire velocity ETFEs. Error bars show one standard deviation 166
6.8 9^{th} order model fits to identified ETFEs 168
6.9 3rd order model fits to identified ETFEs 170
6.10 Pole-zero plots of 3rd order transfer function fits for all velocities at each mean input voltage 171
6.11 C_p at $x/h = 5$ vs actuation amplitude 172
6.12 Difference between mean C_p with amplitude modulated input voltage and steady amplitude input 173
6.13 Simplified block diagram of closed loop gain-sheduling PI controller 175

6.14 Comparison between high and low bandwidth PI tuning at $20\,\mathrm{m\,s^{-1}}$, $0.1\,\mathrm{V}$. 177
6.15 Model vs experimental closed-loop transfer function at $v_{\mathrm{in}} = 20\,\mathrm{m\,s^{-1}}$, $C_{p,\mathrm{ref}} = 0.24$ ($u_{\mathrm{m}} \approx 0.1\,\mathrm{V}$). Input signal $u = u_{\mathrm{m}} + 0.03\sin(2\pi f_{\mathrm{m}} t)$ V with f_{m} from 0.5 to 100 Hz, measured for 100 s per frequency. Error bars show 1 standard deviation 178
6.16 PI controller tunings for all 16 design points 179
6.17 Linearly interpolated gain schedule 180
6.18 Experimental closed loop PI transfer functions at design points 181
6.19 Experimental closed loop PI transfer functions at off-design points 181
6.20 Ensemble averaged experimental step responses of gain scheduled PI controller 183
6.21 Inlet velocity disturbance rejection of open-loop and PI controllers 185
6.22 Effect of PI controller on C_p frequency content 186
6.23 Effect of PI controller on velocity frequency content 187
6.24 Simplified block diagram of closed loop interpolating LQG controller 190
6.25 LQG low-pass filter augmented controller tunings for all 16 design points. Dotted lines = LQR, solid lines = LQG 193
6.26 Experimental closed loop LQG transfer functions at design points 195
6.27 Experimental closed loop LQG transfer functions at off-design points 196
6.28 Ensemble averaged filtered experimental step responses of LQG controller . 197
6.29 Interpolating LQG controller velocity disturbance 198
6.30 Effect of LQG controller on C_p frequency content 199
6.31 Effect of LQG controller on velocity frequency content at $(x, y, z)/h = (3, 0.5, 0)$ 200
6.32 Frequency spectra of input signals 202

Nomenclature

Abbreviations

ADC	Analogue to digital converter
AFC	Active flow control
AIP	Aerodynamic interface plane
AM	Amplitude modulated
AR	Aspect ratio
BFS	backward-facing step
BL	Boundary layer
CFD	Computational fluid dynamics
CTA	Constant temperature anemometry
DAC	Digital to analogue converter
DARE	Discrete algebraic Riccati equation
DBD	Dielectric barrier discharge
DMD	Dynamic mode decomposition
DMDc	Dynamic mode decomposition with control
ER	Expansion ratio
ETFE	Empirical transfer function estimate
FPGA	Field programmable gate array
GM	Gain margin
HEX	Heat exchanger
IATA	International Air Transport Association
ID	Inner diameter
KF	Kalman filter
KH	Kelvin-Helmholtz (instability)
LES	Large eddy simulation
LQG	Linear quadratic Gaussian
LQI	Linear quadratic integrator
LQR	Linear quadratic regulator
LQT	Linear quadratic tracking
LTR	Loop transfer recovery
MIMO	Multi-input multi-output
MPC	Model predictive control
NACA	National Advisory Committee for Aeronautics
NI	National Instruments
PI	Proportional integral
PID	Proportional integral derivative
PIV	Particle image velocimetry
PM	Phase margin
POD	Proper orthogonal decomposition
PSD	Power spectral density
RANS	Reynolds-averaged Navier Stokes
RMS	Root mean squared
ROM	Reduced order model
RT	Real time
SBES	Stress blended eddy simulation
SST	Shear stress transport
URANS	Unsteady Reynolds-averaged Navier Stokes
VR	Velocity Ratio
WMLES	Wall modelled large eddy simulation

Miscellaneous

γ	Ratio of specific heat capacities
δ^*	Displacement thickness (m)
δt	Sample time (s)
η	Integral state cost
θ	Momentum thickness (m)
λ_j	Eigenvalues
$\mathbf{\Lambda}$	Diagonal matrix of eigenvalues
μ	Dynamic viscosity of air ($\mathrm{Pa\,s}$)
ρ	Air density ($\mathrm{kg\,m^{-3}}$)
σ_j	Eigenvalue decay constant
$\mathbf{\Sigma}$	Diagonal matrix of singular values
$\mathbf{\Sigma}_r$	Truncated diagonal matrix of singular values
τ_w	Wall shear stress (µPa)
$\boldsymbol{\phi}_j, \mathbf{\Phi}$	POD/DMD modes
Φ_{uu}	Power spectral density of input signal
Φ_{yu}	Cross spectral density of output and input signals
$\boldsymbol{\psi}_j$	Eigenvectors
$\mathbf{\Psi}$	Matrix of eigenvectors
ω	Angular frequency ($\mathrm{rad\,s^{-1}}$)
a	Actuation amplitude (V)
$a_j(t)$	Temporal coefficients
A	Cross-sectional area ($\mathrm{m^2}$)
A_m	Ratio of acoustic to freestream velocity
A_ref	Reference area ($\mathrm{m^2}$)
$\mathbf{A}$	System matrix
$\mathbf{A}_\mathrm{aug}$	Augmented system matrix
$\tilde{\mathbf{A}}$	Projected DMD operator
b_j,$\mathbf{b}$	DMD mode amplitudes
B	Peak-to-peak amplitude of sinusoid
$\mathbf{B}$	Input matrix
$\mathbf{B}_\mathrm{aug}$	Augmented input matrix
$\tilde{\mathbf{B}}$	Projected DMDc control matrix
c	Speed of sound in air ($\mathrm{m\,s^{-1}}$)
c_p	Specific heat capacity at constant pressure ($\mathrm{J\,kg^{-1}\,K^{-1}}$)
$C(s)$	Controller transfer function
C_a	Equivalent capacitance of acoustic transmission line ($\mathrm{m^4\,s^2\,kg^{-1}}$)
C_D	Drag coefficient
C_L	Lift coefficient
C_p	Pressure coefficient, $\frac{p-p_\infty}{p_0-p_\infty} \equiv \frac{p-p_\infty}{0.5\rho U^2}$
C_{p0}	Steady state pressure coefficient
$C_{p,\mathrm{map}}$	Static mapping from steady state input amplitude to steady state C_p
$C_{p,\mathrm{ref}}$	Control reference pressure coefficient
C_q	Volume flow rate coefficient, $\frac{q}{UA_\mathrm{ref}}$
C_v	Velocity coefficient, $\frac{u}{U}$
$\overline{C}_p$	Mean pressure coefficient
$\mathbf{C}$	Output matrix
$\mathbf{C}_\mathrm{aug}$	Augmented output matrix
$d_\mathrm{i}(t)$	Input disturbance
$d_\mathrm{o}(t)$	Output disturbance
D_h	Hydraulic diameter (m)
$D_\mathrm{i}(s)$	Laplace transform of input disturbance
$D_\mathrm{o}(s)$	Laplace transform of output disturbance
$e(t)$	Error between reference and output
$\mathbf{e}_k$	State estimation error

f	Frequency (Hz)
f_0	Natural frequency of vortex roll-up (Hz)
f_c	Actuation carrier frequency (Hz)
f_m	Actuation modulation frequency (Hz)
f_H	Helmholtz resonance frequency (Hz)
f^+	Non-dimensional frequency, $\frac{f}{f_0}$
$\mathbf{F}$	Process noise matrix
$G(s)$	Plant transfer function
G_TL	Transfer function of transmission line
$\hat{G}$	Empirical transfer function estimate
h	Step height (m)
H	Test section height downstream of step (m)
Id	Input delay (no. of time steps or s)
J	Quadratic cost term
k	Thermal conductivity ($\mathrm{W\,m^{-1}\,K^{-1}}$)
k_d	Derivative gain
k_i	Integral gain
k_p	Proportional gain
$\mathbf{K}_0$	Feed-forward gain
$\mathbf{K}_\mathrm{f}$	Kalman filter gain
$\mathbf{K}_\mathrm{LQR}$	LQR feedback gain
L	Test section length downstream of step (m)
$L(s)$	Open-loop transfer function
L_a	Equivalent inductance ($\mathrm{kg\,m^{-4}}$)
L_c	Channel length (m)
L_crd	Chord length (m)
L_eq	Equivalent length (m)
L_n	Neck length (m)
Ma	Mach number, $\frac{U}{c}$
$n(t)$	Sensor noise
$N(s)$	Laplace transform of sensor noise
NU	Non-uniformity metric defined as spatial standard deviation of time-mean velocity
$NU_\mathrm{y}(x)$	NU evaluated in y-direction along $z = 0$
$NU_\mathrm{yz}(x)$	NU evaluated on y-z plane
p	Pressure (Pa)
p_0	Freestream total pressure (Pa)
p_∞	Freestream static pressure (Pa)
P	Perimeter (m)
$\mathbf{P}$	Solution to DARE
Pr	Prandtl number, $\frac{c_p \mu}{k}$
q	Volume flow rate ($\mathrm{m^3\,s^{-1}}$)
$\mathbf{q}(\mathbf{z})$	Vector field
$\mathbf{Q}$	State weighting matrix
$\mathbf{Q}_\mathrm{aug}$	Augmented state weighting matrix
$\mathbf{Q}_\mathrm{v}$	Process noise covariance
r	Truncation value
$r(t)$,$\mathbf{r}_k$	Controller reference
$R(s)$	Laplace transform of controller reference
R_a	Equivalent resistance ($\mathrm{kg\,m^{-4}\,s^{-1}}$)
$\mathbf{R}$	Control weighting matrix
$\mathbf{R}_\mathrm{w}$	Sensor noise covariance
$\mathbf{R}_\mathrm{xx}$	Spatial (POD) covariance matrix
Re_c	Reynolds number based on chord length, $\frac{\rho U L_\mathrm{crd}}{\mu}$
Re_h	Reynolds number based on step height, $\frac{\rho U h}{\mu}$

s	Test section spanwise width (m)
s_j	Singular values
$S(s)$	Sensitivity transfer function
St_θ	Strouhal number based on momentum thickness, $\frac{f\theta}{U}$
St_c	Strouhal number based on chord length, $\frac{fL_{\mathrm{crd}}}{U}$
St_h	Strouhal number based on step height, $\frac{fh}{U}$
$T(s)$	Closed-loop transfer function
T_d	Delay time (s)
u	x-direction (streamwise) velocity component ($\mathrm{m\,s^{-1}}$)
$u(t)$,$\mathbf{u}_k$	Control input
u_m	Input signal mean
u_map	Static mapping from steady state C_p to steady state input amplitude
$\overline{u}$	Mean streamwise velocity component ($\mathrm{m\,s^{-1}}$)
U	Freestream velocity ($\mathrm{m\,s^{-1}}$)
$U(f)$	Fourier transform of input signal
$\mathbf{U}$	Matrix of left singular vectors
$\mathbf{U}_r$	Truncated matrix of left singular vectors
v	y-direction (wall-normal) velocity component ($\mathrm{m\,s^{-1}}$)
$v(t)$,$\mathbf{v}_k$	Process noise
v_in	Inlet velocity ($\mathrm{m\,s^{-1}}$)
V_0	Static cavity volume ($\mathrm{m^3}$)
$\mathbf{V}$	Matrix of right singular vectors
$\mathbf{V}_r$	Truncated matrix of right singular vectors
$w(t)$,$\mathbf{w}_k$	Sensor noise
$\mathbf{W}$	Spatial (POD) weighting matrix
x	Streamwise direction
x_r	Reattachment position (m)
x_{r0}	Baseline/unforced reattachment position (m)
x_RMS	Location of peak RMS wall pressure (m)
$x_{\mathrm{r_{est}}}$	Estimated reattachment length (m)
x^+	Non-dimensional streamwise wall grid spacing
$\mathbf{x}_k$	State vector
$\mathbf{x}_0$	Steady state state vector
$\mathbf{x}_{\mathrm{aug},k}$	Augmented state vector
$\hat{\mathbf{x}}_0$	Steady state state vector estimate
$\hat{\mathbf{x}}_k$	State vector estimate
$\tilde{\mathbf{x}}_k$	Projected DMD states
$\mathbf{X}$	Matrix of snapshots
$\mathbf{X'}$	Matrix of snapshots shifted forward by one measurement
y	Wall-normal direction
$y(t)$,$\mathbf{y}_k$	System output
y^+	Non-dimensional wall-normal wall grid spacing
$\hat{\mathbf{y}}_k$	System output estimate
$Y(f)$	Fourier transform of output signal
$Y(s)$	Laplace transform of system output
$\mathbf{Y}$	Matrix of snapshots progressed one time step
z	Spanwise direction
z^+	Non-dimensional streamwise-normal wall grid spacing
$\mathbf{z}_k$	Integral state

Chapter 1

Introduction

1.1 Motivation

The global aviation industry currently operates at the largest capacity ever, and continues to grow steadily after having recovered from the 2020-2022 dip during the COVID-19 pandemic [1]. Meanwhile, the urgency of action to combat climate change continues to rise. Current net-zero carbon emissions by 2050 targets, agreed to by International Air Transport Association (IATA) member airlines as of 2021, necessitate immediate investment into novel carbon-free fuel technologies.

One of the main contenders for sustainable aviation is hydrogen combustion (along with fuel cells) [2]. Future hydrogen powered aircraft will have completely redesigned fuel systems compared to current fossil fuel systems, which will likely include multiple compact air-to-X heat exchangers designed to maximise energy recovery and reduce fuel expenditure [3, 4, 5], an example of which is shown in Figure 1.1.

More generally, regardless of fuel type, there are overall weight and aerodynamic advantages to reducing engine length. Furthermore, to increase overall propulsive efficiency requires ever increasing bypass ratios. Shortening the engine axially and increasing bypass ratio will push heat transfer ducts towards the aggressive end, introducing flow separation and non-uniformity that will hamper heat exchanger (HEX) effectiveness [6, 7] and increase pressure losses. Heat transfer from ambient air to cold hydrogen, either bypass air or pre-cooling of the ingested air upstream of the low pressure compressor, will be particularly sensitive to non-uniform HEX flow as the heat transfer load at critical points in the flight

cycle may cause moisture in the air to freeze and block low-flow regions of the HEX. Active flow control (AFC) offers the possibility of opening up the design space by separation control and flow modulation in complex ducts. Engine efficiency at cruise is limited by performance requirements during take off and high-load operation. Active flow control by non-mechanical actuators offers the prospect of lightweight, reliable and adaptable control of separated/non-uniform duct flows [8]. Unlike passive flow control (e.g. vortex generators, duct shaping), AFC is able to be operated only during critical flight cycle stages, allowing heat exchanger ducts to be designed for cruise and the operability extended at off-design points.

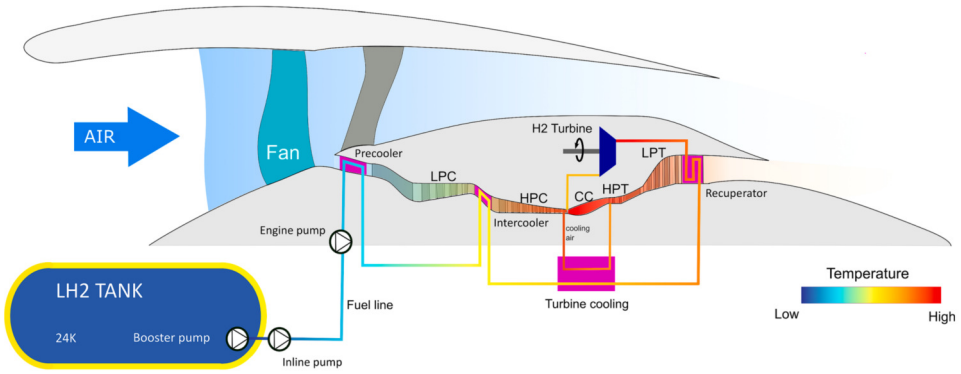


Figure 1.1: Example of a heat management system for a hydrogen combustion turbofan engine featuring pre-cooling, inter-cooling, recuperation, and cooled turbine cooling air, taken from Patrao et al. [4]

The high expansion ratio backward-facing step (BFS) is taken as a canonical example of a highly curved/expanding duct flow, and represents the worst case scenario of complete separation. Beyond this, the BFS demonstrates fundamental features common to many separated/reattaching flows [9], and is often used as a representative example of combustor flows in which the interaction between vortex and thermoacoustic dynamics can significantly affect efficiency and emissions [10].

1.2 Thesis Content

Chapter 2 presents a review of active control strategies for separated flows, with the focus on periodic and acoustic excitation and backward-facing step flows. First, a general introduction to active flow control and periodic excitation is given, followed by a description

of the salient features of backward-facing step flows and examples of active flow control. The fundamentals of control theory and modal decomposition/reduced order modelling are then outlined, and the chapter is concluded with examples of closed-loop flow control.

The experimental backward-facing step and characterisation of the opposite-side acoustic actuation is detailed in Chapter 3. In Chapter 4, the time-averaged wall pressure and hot-wire velocity field of the baseline and forced flows are presented. The effectiveness of actuation is demonstrated, and shown to reduce reattachment length, estimated from the RMS wall pressures at the centre span of the test section, by at least 24%, depending on inlet speed. The chapter is completed by investigation of the effects of spanwise non-uniform actuation on the spanwise velocity distribution and side-wall effects.

In Chapter 5 the dominant acoustic modes of the experimental setup are identified and explained, and the dynamic behaviour of the backward-facing step flow is studied by inspection of wall pressure and hot-wire frequency content. The mechanism by which acoustic excitation affects the flow is also identified as the coupling of natural vortex-structures to the excitation tone. Numerical simulations of the backward-facing step flow, with and without acoustic actuation, are presented and validated against experimental data in Chapter 3. The simulation data are used to confirm the conclusions made from the experimental hot-wire measurements, and the dominant flow structure modes are extracted by Dynamic Mode Decomposition in Chapter 5.

Chapter 6 demonstrates feedback control of the backward-facing step flow, with aims of tracking a reference reattachment length (by proxy of wall pressure coefficient) and the attenuation of periodic disturbances. Finally, conclusions are drawn in Chapter 7.

Chapter 2

Background and Literature Review

2.1 Introduction

This chapter provides a background on flow control strategies and actuators, with a focus on backward-facing step flows (section 2.3) as a canonical example of flow separation in a highly curved/expanding duct flow. A general overview of flow control strategies and the mechanisms is presented in section 2.2, followed by example applications of open-loop active flow control in section 2.4. Sections 2.5 and 2.6 offer introductions to control theory and modal decompositions/reduced order modelling respectively, and the chapter is concluded in section 2.7 with examples of closed-loop active flow control in literature.

2.2 Flow Control

Gad-el-Hak [11] defines flow control generally and concisely as "the attempt to alter the character or disposition of a flow field favourably". Some of the more common aims of aerodynamic flow control are lift enhancement, drag reduction, mixing augmentation, and noise suppression [12]. Separated and free-shear flows are of particular engineering importance, and significant effort has been put into the control of boundary layer separation and wake flow. Flow control of separated/wake flows can be categorised either as boundary layer control or direct wake control [13]. Boundary layer control seeks to manipulate the properties of the boundary layer prior to separation, to delay or prevent separation entirely, or to affect wake/separation bubble characteristics indirectly (e.g. vortex generators, dim-

ples/surface treatments, boundary layer suction/injection). In comparison, direct wake control seeks to favourably alter the wake flow by actuation downstream of (or at) the separation location, for example to avoid or promote coherent vortex trains or to increase base pressure (e.g. splitter plates, base-blowing, trailing edge shaping, unsteady forcing at separation edge).

In addition to the classification of boundary layer or direct wake control, flow control can be either passive or active. Passive flow control is that which does not require energy input, e.g. vortex generators, splitter plates, surface treatments. Active flow control (AFC) is that which does requires energy input, e.g. blowing/suction, dielectric barrier discharge plasma actuators, zero net mass flux actuators. Passive boundary layer flow control often seeks to prevent separation by inducing early transition to turbulence (e.g. vortex generators), which increases skin friction across all operating conditions regardless of whether the control is effective. Similarly, passive direct wake control often requires significant geometric alterations, for instance protruding splitter plates or other structures in the wake or at the separating edge, either spanwise uniform or periodic with fixed spacing.

There are a number of benefits to using AFC over passive control methods, including:

- Active control is able to affect the flow without permanent geometric alteration or obstruction, therefore can be turned off when it is not needed and have no detrimental aerodynamic effects.
- AFC actuators can be used for unsteady/periodic excitation, where a large effect can be achieved from a comparatively small perturbation by coupling to natural flow instabilities.
- AFC can be used in conjunction with open/closed-loop control schemes, allowing adaptation to current operating conditions.
- Many (although not all) AFC actuators inject momentum into the flow, which allows the effect to be greater or have a wider range of application. For example, vortex generating jets can be more effective than passive vortex generators due to the added momentum enhancing the streamwise vortex strength and mixing.

The main drawbacks of active flow control are the added weight, complexity, and energy requirements of the actuators and control systems. Despite the additional constraints imposed by these factors, AFC has the ability to open up the design space of jet engines, and may yield significant efficiency gains in future aircraft designed around active flow control systems from the ground up.

Figure 2.1 illustrates further categorisation of AFC, based on how it is controlled/determined [11]. Reviews of actuators for active flow control and control approaches are provided by Cattafesta & Sheplak [14], Brunton & Noack [15], and Sipp & Schmid [16].

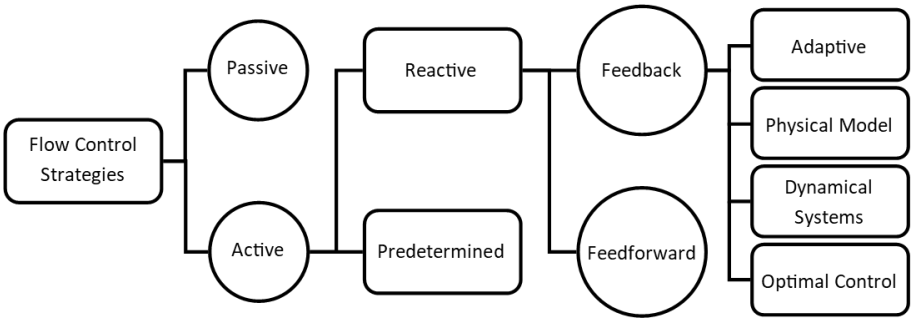


Figure 2.1: Categorisation of Flow Control [11]

2.2.1 Common Actuation Strategies

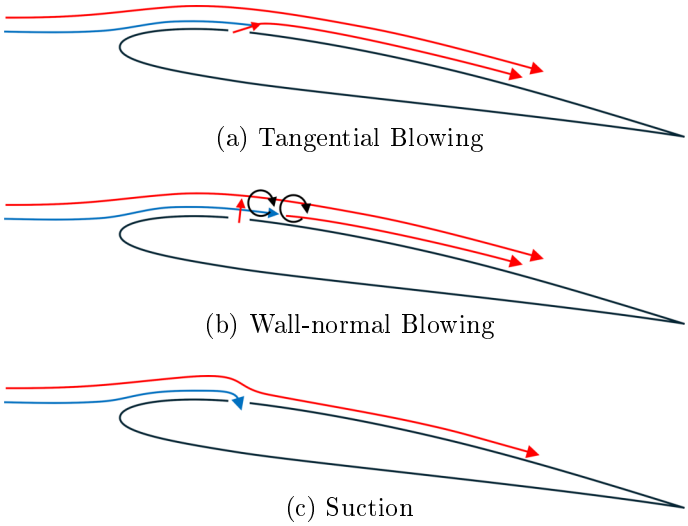
Steady Blowing/Suction

Blowing/suction is defined by the addition or subtraction of mass/momentum. Separation control using steady blowing/suction is most typically applied to the boundary layer just upstream of or at separation, where despite using opposite means, both seek to enhance the near wall momentum and energise the boundary layer to prevent or delay separation. Suction achieves this by ingesting the low-momentum laminar fluid from the boundary layer, allowing it to be replaced by the higher momentum fluid further from the wall [17]. Boundary layer suction has also historically been used to prevent transition in boundary layers by suppressing the development of natural instabilities [18, 19], however this is of less interest for separation control, where the additional momentum and mixing in a turbulent boundary layer is often beneficial.

Blowing, on the other hand, has been used to enhance near-wall momentum either directly,

by tangential blowing, or indirectly, by wall-normal blowing designed to promote mixing in the boundary layer and the exchange of high momentum fluid from the freestream with the low momentum fluid from near the wall [20]. Wall-normal blowing at relatively low mass flow rates effectively acts as a fluidic turbulator. However, adverse effects have been reported at higher mass flow rates due to the blockage effect of the 'fluid wall' [21]. Although steady blowing typically refers to mass injection through a slot or orifice provided by an external source, the fundamental effect is achieved by the addition of momentum, therefore it seems reasonable to conclude that actuators which inject steady momentum using only the working fluid, for example dielectric barrier discharge plasma actuators, can also be used for blowing.

Vortex generating jets [22, 23, 24] and plasma vortex generators [25] can be considered as a subset of blowing, in which an array of jets, or plasma actuators, inject fluid/momentum into a boundary layer such that streamwise vortices are formed. The injection of momentum enhances the streamwise vortex strength and mixing compared to passive vortex generators, which can only energise the boundary layer by extracting energy from the flow.



(a) Tangential Blowing

(b) Wall-normal Blowing

(c) Suction

Figure 2.2: Illustration of boundary layer blowing/suction for separation prevention

In addition to boundary layer control, a number of studies have applied blowing/suction in the wake or recirculation bubble of a separated flow, however these are generally considered to be inefficient 'brute force' methods in which the amplitude of the perturbations are sufficient to alter the flow [14, 12]. For example, several studies have demonstrated that

steady blowing at the rear of a bluff body, largely in the context of road vehicles, can achieve a significant reduction in pressure drag. However, the efficiency (ratio of power saved by drag reduction to actuation power) drops below one at relatively modest drag reductions [26]. This inefficiency can be attributed to the artificial increase in base pressure by the recovery of dynamic pressure from the jets themselves rather than the main flow [13].

Unsteady Actuation

While steady actuation seeks to influence the flow by steady energy input, most often by energising the boundary layer, unsteady actuation is defined by an unsteady (usually periodic) disturbance and typically seeks to leverage natural instabilities in the flow to achieve a large effect with a small perturbation. For many flow control applications, especially those involving a large separated region or transition to turbulence, periodic forcing is as or more effective than steady forcing for a fraction of the total energy/mass input (duty cycle) [27, 28, 29, 30, 31].

It is well understood that shear layers exhibit convective instabilities which amplify small disturbances in certain frequency ranges [32], and can lead to the formation of large coherent structures. The dominant instability in separated and reattaching plane shear layers and jets is the Kelvin-Helmholtz instability, where an initially small amplitude 'wiggle' of the shear layer grows and eventually causes the shear layer to roll-up into a train of discrete plane/ring vortices [33]. There is agreement in the literature that unforced vortex roll-up occurs at a non-dimensional frequency (Strouhal number) of $St_\theta \approx 0.012$ [34, 35, 36, 37, 38, 39, 40, 41, 42], where

$$St_\theta = \frac{f\theta}{U} \tag{2.1}$$

θ is momentum thickness, f is the vortex frequency, and U is the freestream or jet core velocity. Once formed, the shear layer vortices grow and merge, forming larger vortices before eventually breaking up into highly three dimensional structures [43]. These large vortices are largely responsible for significant momentum transfer and vorticity, leading to high Reynolds stresses and spreading/curvature of the shear layer.

Periodic excitation at frequencies the shear layer is responsive to forces the roll-up of vor-

tices at the excitation frequency [44, 45, 46] or, depending on the actuator and excitation frequency, promotes the formation and enhances the strength of larger merged vortex structures [47, 48, 49], which can be used to manipulate the character of the flow without requiring a large amplitude disturbance. A similar effect is seen in attached boundary layers, where the enhanced vorticity and momentum due to discrete forced vortices is stronger than the equivalent steady forcing [50, 31].

Wiltse & Glezer [51] introduced the *demodulating property of shear layers*, that the shear layer responds to the modulation signal when forced by an amplitude modulated carrier signal. They demonstrated that a square jet actuated by piezoelectric flaps driven with an amplitude modulated signal, where the carrier frequency was significantly above the natural frequency of vortex roll-up, responded to the modulation signal. The focus of the study was to use an actuator with resonant frequency well above the frequencies which the flow is responsive to, and it was shown that the the demodulation was due to the merging of smaller vortices shed at the carrier tone into larger structures at the modulation tone. This behaviour was also demonstrated for backward-facing step flows by Vukasinovic et al. [52]. Recently, Nicholls et al, [53] investigated the response of a jet shear layer to an amplitude modulated acoustic tone, and demonstrated that merging of the vortices shed at the carrier tone does not need to occur for the signal to be demodulated. Nicholls et al, [53] asserted that the strength of a vortex depends on the mean amplitude of the excitation waveform during its formation, and that even when vortex merging did not occur or the modulation frequency was low compared to the carrier frequency such that an unfeasibly large number of vortices would have to merge to form a structure at the modulation frequency, demodulation of the excitation signal occurred as a result of the effect of vorticity on shear layer spreading. It seems possible that the two mechanisms of demodulation identified may exist in separate actuation regimes with respect to the carrier tone frequency. Both Wiltse & Glezer [51] and Vukasinovic et al. [52] used carrier frequencies approximately an order of magnitude above the natural roll-up frequencies, while Nicholls et al. [53] used a carrier frequency approximately twice the natural frequency. It has been demonstrated for reattaching shear layer flows that the effect of periodic forcing at the separation location on reattachment length is a function of the reduced frequency

$f^+ = f_a/f_0$, where f_a is the excitation frequency and f_0 is the natural frequency of vortex roll-up, and that there is a transition from actuation reducing the reattachment length to causing a slight increase in reattachment length at around $f^+ = 4$ [41, 54, 55, 45]. This behaviour is attributed to the size/strength of the forced vortices. At lower excitation frequencies larger vortices are formed, which penetrate the shear layer and are responsible for a large amount of momentum transfer, while at higher frequencies the vortices are smaller and weaker, and unable to penetrate the shear layer. The implication of this is that demodulation only occurred in the experiments of Wiltse & Glezer [51] and Vukasinovic et al. [52] once larger structures capable of penetrating the shear layer had formed by the merging of smaller vortices. However, this step was not necessary in the experiments of Nicholls et al. [53] where the shear layer was responsive to the rolled-up vortices.

2.2.2 Flow Control Actuators

In order to implement an active flow control scheme, actuators must have sufficient control authority and bandwidth. Furthermore, to be practically useful actuators must also be robust and efficient. For jet engines the response of the controller must be at least as fast as changes in flight conditions and the spool-up time of the engine disc and shaft, which may be of the order of several seconds, However, a significantly higher actuator bandwidth may be required for unsteady flow control schemes designed to leverage natural flow instabilities, and for the rejection of disturbances. For periodic excitation of separated flows the most effective actuation frequency is often reported to be of the order of $St \sim O(0.1)$ based on geometric characteristic length (e.g. step height, jet nozzle diameter).

A review of actuators used for flow control is provided by Cattafesta & Sheplak [14], who classify actuators by function as either fluidic, plasma, or moving surface. Fluidic actuators are those which operate by injection/suction of fluid (e.g. blowing/suction, steady or pulsed jets [31], fluidic oscillators/switching jets [56, 57, 58, 59], internal oscillators/synthetic jets [60]), plasma actuators effect the flow by either the 'electric wind' or expansion wave of an electrically generated plasma discharge (e.g. dielectric barrier discharge actuators (DBDs) [61], nano-second DBDs [62], SparkJets [63]), and moving surface actuators are those where a moving body or boundary interacts directly with the flow (e.g. vibrating flaps [51, 64] or ribbons [65]). In the current work the additional

category of 'acoustic' actuation is also considered, which denotes that the influence on the flow is due to mechanical acoustic waves propagating through the fluid by particle oscillations, rather than a local velocity perturbation.

Neither actuator development nor optimisation are within the scope of the current work, therefore the interested reader is directed toward the literature for detailed descriptions of the design and operating principles of the various non-acoustic actuators.

Acoustic Actuation

It has been known for some time that acoustic pressure waves are able to initiate boundary layer transition [65], and that there is significant coupling between flow dynamics and acoustic waves causing combustion instabilities [66]. In a brief summary of several key areas in the field of aero-acoustics, Crighton [67] explains how vorticity can be generated by sound and vice-versa, through the action of the non-linear terms in the Navier-Stokes equations or linear coupling of the fields where they are required to satisfy boundary conditions.

A distinction should be made between **'internal oscillators'** and **'external oscillators'**. For example, a number of flow control studies have employed Helmholtz resonator style actuators consisting of an acoustically driven cavity and slot (some of which are summarised in Table 2.1), which have been referred to generally as 'internal oscillators' [9]. Schematically, this actuator configuration is often identical to that of a synthetic jet, and the distinction between the classifications is not always clear. A synthetic jet is defined by a non-zero time averaged net momentum in quiescent flow, which is not necessarily the case for the general 'internal oscillator', however this distinction may be lost in a cross-flow where the expulsed fluid is swept away. Williams et al. [68] demonstrated that although an internal oscillator does produce an acoustic wave, the primary mechanism by which the local flow is affected is the slot velocity. This conclusion is supported by the imaging of Chun & Sung [54] who showed a strong blowing/suction through the slot of an internal oscillator positioned at the separating edge of a backward-facing step. As such, although an internal oscillator is occasionally considered as an acoustic actuator, it is more often classified as oscillatory blowing/suction, or as an oscillatory jet.

External oscillators, on the other hand, are installed some way away from the local flow that is to be controlled, and impose a radiated acoustic field. Typical examples of acoustic actuation by external oscillator embed a loudspeaker in the wall of a wind tunnel or channel some distance from the region of interest [69, 70, 48], or (often the case for periodically exited jet experiments) in a plenum upstream of the test section [44, 71, 72, 53]. Helmholtz resonator style assemblies consisting of one or more loudspeaker-cavity-neck units have also been used for external acoustic actuation as an alternative to placing a loudspeaker directly in the wall of a plenum or wind tunnel [73, 74, 75, 76]. This approach may be beneficial where the most effective excitation frequency is known a priori, as the resonance of the assembly can be used to maximise efficiency across a fairly narrow frequency range. Unlike the other actuators outlined in this section, which have output depending on fluid properties and actuator parameters, the response of external acoustic actuation depends also on acoustic resonances of the tunnel or test section geometry [48, 77]. It has been noted that the excitation level required from acoustic forcing of external aerodynamics (e.g. wings) is unreasonably high [20]. However, it seems that acoustic excitation could be ideal for the control of duct flows, where matching of acoustic driver/loudspeaker, actuator cavity, and duct resonance frequencies to flow instabilities could yield highly efficient control.

2.3 Backward-facing Step Flow

The backward-facing step (BFS) has been and remains a popular choice of canonical separated flow since the 1960s. The natural flow and mechanisms by which forcing affects the flow are well understood, therefore it is an appropriate choice for the testing of novel actuators or flow control strategies without introducing unknowns relating to new geometry. Despite its simple geometry, the BFS exhibits the most important features of separated flows: free shear layer; vortex formation and evolution; and reattachment. In the context of engine heat exchanger flows, the BFS represents the worst-case scenario of separation in a diverging/highly curved duct.

Backward-facing step flows are often described by reference to five regions:

- Sharp separation due to the sudden expansion at the step edge

- The separated shear layer, starting at the edge and gradually spreading and curving towards the wall below the step
- The reattachment region, where the shear layer impinges on the wall behind the step
- The separation (or recirculation) bubble encapsulated between the dividing streamline and the step, consisting of the primary recirculation and secondary recirculation (corner vortex)
- The attached/recovery region downstream of reattachment, where a new boundary layer forms and the flow realigns to the streamwise direction

Figure 2.3 shows a simplified depiction of the flow featured behind a backward-facing step.

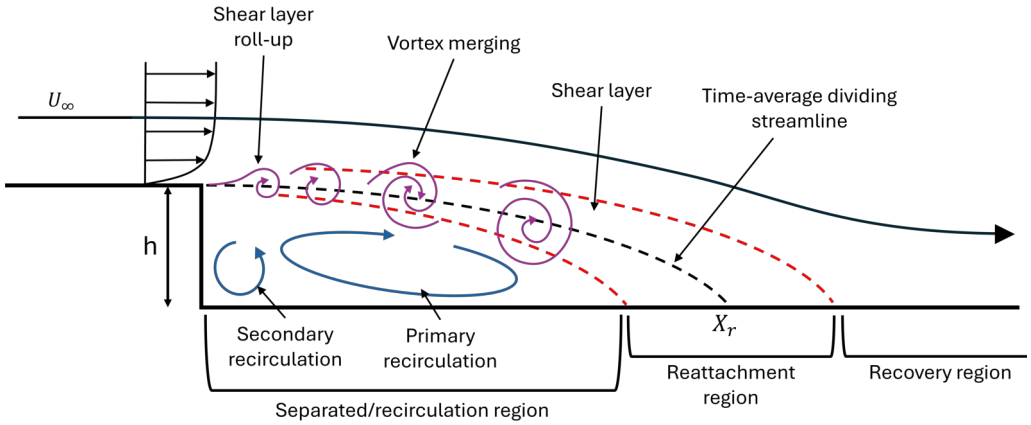


Figure 2.3: Features of turbulent flow behind a backward-facing step

Immediately after separation and up to around halfway through the separated region, the shear layer is only slightly curved and behaves as an unconstrained plane mixing layer [78], after which it curves sharply toward and impinges on the step-side wall. The behaviour of the reattaching shear layer differs significantly from that of an ordinary plane mixing layer due to interaction with the wall and the turbulent recirculating flow in the separation bubble [79]. The curvature of the shear layer towards the wall can be explained by the entrainment of fluid below the step by the shear layer resulting in a low pressure region, which pulls the shear layer towards the wall. The reattaching shear layer splits at the wall with some of the fluid (in steady state necessarily equal to the amount entrained)

deflected upstream due to the adverse pressure gradient, hence driving the recirculation in the separation bubble [79]. This is often referred to as the Coandă effect [80], although strictly speaking the Coandă effect pertains to an attaching free jet rather than a shear layer.

Although many of the important aspects of BFS flows can be explained by the steady-state or time-averaged flow field, it is important to remember that there is a great deal of unsteadiness instantaneously, especially in the separated shear layer where large turbulent structures of scales comparable to the step height prevail.

The BFS flow is most often characterised by reattachment position x_r, and occasionally by the recirculation area bounded by the dividing streamline. A number of different but equivalent definitions are used for x_r, depending on available data, including but not limited to: where the mean dividing streamline originating at the step edge terminates on the wall; the point at which mean wall shear stress is zero, or the streamwise mean velocity component just above the wall is zero; where the time forward fraction of flow near the wall is equal to 0.5, i.e. the instantaneous streamwise velocity is equally likely to be forwards or backwards. The exact reattachment length and dividing streamline shape are functions of inlet conditions, expansion ratio (ER $= H/h$), and aspect ratio (AR $= s/h$) of the step geometry, where h is the step height, H is the channel height downstream of the step, and s is the spanwise width of the channel as illustrated in Figure 2.4. The effects of each parameter have been well studied [81, 82, 83, 84, 85]. The extent to which the flow can be considered two-dimensional also depends on the aspect ratio of the step. de Brederode & Bradshaw [86] demonstrated that for aspect ratios greater than AR = 10 the centre channel flow can be considered nominally 2D, while for lower values of AR the side wall effects alter the flow across the entire spanwise width.

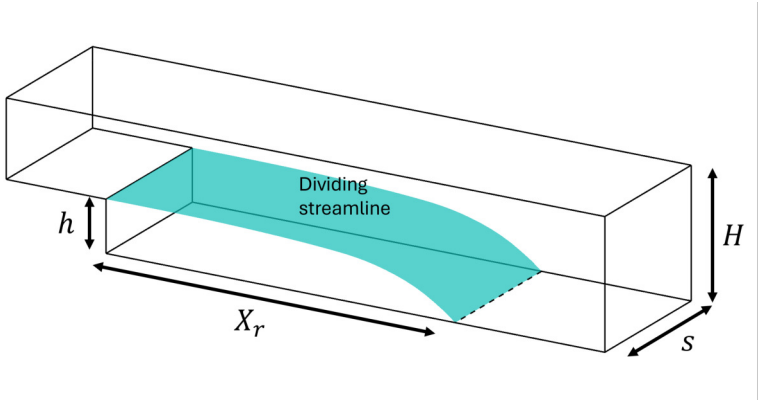


Figure 2.4: Backward-facing step geometry

2.3.1 Dynamical Modes/Flow Structures

For moderate to high Reynolds number transitional and fully turbulent flow, which is of greater practical relevance than fully laminar, the dynamical behaviour of the BFS flow is dominated by several periodic modes or 'coherent structures'. Namely, in order of decreasing frequency: the 'shear layer mode'; the 'step mode'; the 'shedding mode'; and the 'flapping mode'.

Shear layer mode

Shortly after separation, the Kelvin-Helmholtz (KH) instability leads to spanwise roll-up of the shear layer into discrete plane vortices, typically referred to as the 'shear layer mode' [39]. Hasan [39] identified that, as for unconstrained mixing layers, the shear layer mode frequency scales with momentum thickness rather than step height, with both having non-dimensional frequency $St_\theta \approx 0.012$. Although the shear layer mode was initially characterised for a laminar boundary layer at the point of separation, Hasan & Khan [40] demonstrated the exact same behaviour for a turbulent boundary layer, with the only difference being that the peaks in the frequency spectrum of the initially turbulent flow corresponding to the roll-up and subsequent merging of vortices were broader due to greater unsteadiness and phase drift.

Step Mode

The shear layer vortices grow and merge as they travel downstream, leading to a thickening of the shear layer and a reduction in the vortex passing frequency, the mechanisms of which are explained in detail by Winant & Browand [33]. Unlike unconstrained mixing layer flows, the presence of the wall limits the scale of the largest structures in the separated shear layer to that of the step height. Hasan [39] observed that this dominant scale of vortex, the so-called 'step mode', occurred at a Strouhal number based on step height of $St_h \approx 0.18$, and is analogous to the 'preferred' mode of a free jet [44].

Although nominally periodic, Winant & Browand [33] explain that the growth and pairing of vortices does not in fact occur perfectly consistently. Pairing is promoted by small variations in vortex spacing and strength, therefore does not always occur at the same point in space and occasionally an odd vortex is 'dropped out', leaving it to merge with a later pairing. This intermittency in pairing manifests in the frequency spectrum of a point measurement as a broad peak with frequency gradually decreasing in the streamwise direction, rather than sharp peaks at the shedding frequency and its subharmonics which would be expected from perfectly periodic shedding and pairing. A similar effect was seen across the shear layer, where the peaks shifted to lower frequencies on the low velocity side of the shear layer.

Shedding Mode

The 'shedding' mode refers to the shedding of a vortex from the entire separation bubble at the point of reattachment, which is most often reported at a frequency $St_h \approx 0.07$. [35, 87, 88, 89, 90, 55, 91]. That this is approximately one third to half of the 'step mode' frequency suggests that additional amalgamation of the large shear layer vortices occurs around reattachment. Troutt et al. [92] demonstrated a drop in the Strouhal number of the dominant spanwise mode from $St_h \approx 0.2$ (the 'step mode') just upstream of reattachment to $St_h \approx 0.12$ downstream of reattachment. No additional mergings were observed further downstream, with the frequency peak remaining at $St_h \approx 0.12$ until at least 9 step heights downstream of reattachment.

Hu et al. [91] used the Dynamic Mode Decomposition (DMD) algorithm to identify domi-

nant modes in a numerical backward-facing step simulation, and concluded that the 'shedding' phenomena is multi-scale, with DMD mode frequencies from $St_h = 0.03$ to 0.1.
Contrary to the common understanding that vortex pairing occurs in tandem with streamwise propagation, Wee at al. [90] and Hudy at al. [93] found that for moderate Reynolds numbers ($Re_h < 10000$) the largest coherent structures grew in place at around half the streamwise reattachment length before shedding once their size reached the step height, and accelerating to the observed convection speed, with $St_h = 0.067$. In both cases, the large 'shed' vortices propagated well downstream of reattachment, consistent with the findings of Troutt et al. [92]. This behaviour was likened to the shedding mode of a bluff body in cross flow, and linked to an absolute instability in the flow. *Absolute instability* refers to a disturbance which propagates both upstream and downstream to effect the entire flow, in contrast to a *convective instability*, where the disturbance is swept away from its source [32].

Flapping mode

There is agreement amongst the literature on the existence of a low frequency 'flapping' mode, where the reattachment position drifts back and forth by as much as one step height, although the mechanism by which this occurs has been debated for some time [94]. The flapping mode is often described as a random, or non-periodic, vertical motion of the shear layer having time and length scales much larger than those of the typical shear layer vortex, with $St_h = \mathcal{O}(0.01)$ [95, 96, 97, 89, 55, 98, 99, 100].
Several alternative or complementary explanations for the longitudinal flapping mode have been proposed, summarised by Ma & Schröder [94]. The two most widely accepted are outlined below:

> **Flow Imbalance:** Eaton & Johnson [95] suggested that the breakdown of spanwise vortices causes an instantaneous imbalance between the fluid entrained from the recirculation region and the fluid reinjected into the recirculation by the splitting of the shear layer at reattachment. That the flapping relates to the entrainment of fluid into the recirculation bubble is supported by Heenan and Morrison [97], who found that replacing the reattachment wall behind the step with a permeable surface,

below which was a nominally airtight chamber, stabilised reattachment and prevented the flapping motion. The permeable wall configuration provided a steady route for upstream convection, hence preventing an imbalance between the flow entrained by the shear layer and that reingested into the recirculation bubble.

Coherent Structures: Troutt et al. [92] found that the unsteadiness could be due to the interaction of the recirculation region with large scale vortices. Driver et al. [96] proposed that the occasional higher than average momentum vortical structure might escape the reattachment region without much of its mass being re-ingested by the recirculation bubble, causing the momentary collapse of the bubble. The larger adverse pressure gradient on account of the increased shear layer curvature would then re-inflate the bubble.

Statnikov et al. [99] identified two flapping-type shear layer modes, the longitudinal flapping, or 'pumping', mode with $St_h \approx 0.01$, and the 'cross-flapping' mode, with $St_h \approx 0.07$, for a high Reynolds number and Mach number backward-facing step flow ($Re_h = 1.8 \times 10^5$, $Ma = 0.8$). Figure 2.5 demonstrates the motion of both flapping modes. The lower-frequency longitudinal flapping involves the periodic elongation and contraction of the recirculation bubble with little vertical motion of the shear layer, while cross-flapping involves a vertical a snaking motion of the shear layer without significantly affecting the reattachment length. Given that the frequency of the cross-flapping mode agrees with that of the more commonly identified shedding mode, it seems possible that the cross-flapping is the displacement of the shear layer by the passing of the largest coherent structures.
The flapping motion is sometimes described as roughly 2D in nature but, as it is most often identified from either frequency data or flow field measurements on a single spanwise normal slice, it is not clear that it is necessarily 2D. Statnikov et al. [99] found that both the 'cross-flapping' and 'pumping' modes were highly three-dimensional, with spatially periodic phase in the spanwise direction of wavelength approximately two step heights. This finding is consistent with the spanwise width of the largest structures identified by Lee et al. [101], and further suggests that the mechanism of flapping may be linked with the largest vortical structures in the flow.

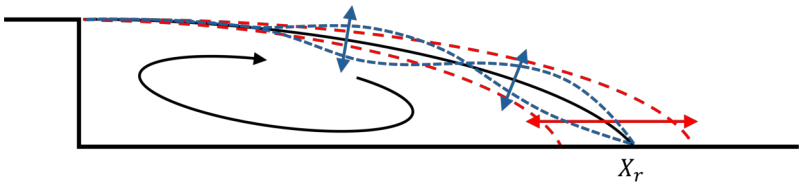


Figure 2.5: Flapping modes in backward-facing step flows. Longitudinal flapping in red, cross-flapping in blue

2.3.2 Vortex Break-up and Recovery Region

Shear layer roll-up and vortex structures are initially two-dimensional in character. However, the spanwise coherence begins to break down about three step heights downstream of separation, with the turbulent structures becoming fully three-dimensional somewhere upstream of reattachment [79]. A conceptual explanation of the breakup of spanwise structures in a separated shear layer is provided by Müller & Gyr [102]. Bending of a vortex tube produces self induced velocities according to the Biot-Savart law, hence an initially small streamwise disturbance is effectively amplified by interaction with velocity gradients in the flow, and results in the stretching of the spanwise vortex tube to form elongated hairpin vortices [43]. Lee et al. [101] used three component hot-wire measurements combined with a microphone array on the wall to identify large structures in the separated and reattachment regions of a backward-facing step flow, and found that the spanwise width of large vortices in the recirculation and reattachment regions were 2 and 2.5 step heights, respectively.

Troutt et al. [92] observed that there is significant correlation of spanwise positioned hot-wire measurements as far as two reattachment lengths (16 step heights) downstream of the step, indicating the persistence of large spanwise organised structures. Although this initially seems at odds with the breakdown of spanwise coherence well upstream of reattachment, an explanation may be provided by the flow imaging of Bernal & Roshko [43] which shows that despite the transition of the spanwise vortex tubes to highly unsteady three-dimensional structures, the vortices appear to continue to travel as a spanwise packet rather than dispersing.

Studies have typically focused on the separated and reattachment regions of the backward-

facing step; consequently there is comparatively little information available about flow dynamics far downstream of reattachment. An abrupt drop in Reynolds stresses and turbulence intensity in the reattachment region and continued decay downstream has been reported, attributed to the stabilising effects of curvature and the suppression of vortex merging by proximity to the wall [78]. Troutt et al. [92] did not observe any merging of coherent structures downstream of reattachment, with Strouhal number staying constant at $St_h \approx 0.12$ from reattachment to two reattachment lengths downstream of the step. The persistence of large structures far downstream of reattachment is consistent with the finding of Bradshaw & Wong [103] that the flow was not fully recovered even 50 step heights downstream of separation.

2.3.3 Influence of Inlet Conditions and Channel Geometry

Nadge & Govardhan [84] performed a systematic study of the effects of Reynolds number and expansion ratio on the mean separation bubble behind a backward-facing step, for expansion ratios between 1.1 and 2.5, and Reynolds numbers between 6000 and 67000. It was found that reattachment length (x_r) increased roughly linearly with Re_h, up to around $Re_h = 20000$ after which x_r remained constant. Similarly, x_r increased approximately linearly with ER up to ER ≈ 1.80, after which x_r saturated at about $8.5h$ for high Re_h. Although reattachment length saturated for $Re_h \gtrsim 20000$, the structure of the separation bubble continued to change up to $Re_h \gtrsim 36000$, with the size of the secondary recirculation being larger at lower Re_h. The variation in mean bubble structure was attributed to the transitional state of the separating boundary layer at lower Reynolds numbers. The finding that reattachment length saturated above a critical Re_h regardless of boundary layer thickness is consistent with those of Adams & Johnston [104], who observed that for fully developed incoming flow the state and thickness of the boundary layer had little effect on reattachment length. Expansion ratio did not significantly impact the structure of the mean recirculation bubble, except for at the highest ER of 2.5 where the flow begins to tend towards a wall-jet.

A similar study was performed by Otugen & Muckenthaler [82] in which the dynamic behaviour of the separated region was also investigated. At lower Reynolds numbers and the smallest expansion ratio ($Re_h \lesssim 10000$, ER = 1.5), no pairing of the shear layer vortices

was observed. Conversely, multiple pairing events were observed only for larger Reynolds numbers and expansion ratios ($Re_h \gtrsim 16600$, ER $\gtrsim 2$). For intermediate Reynolds number/expansion ratio cases, a single pairing of the shear layer vortex structures was seen.

The effect of aspect ratio on the two-dimensionality of the BFS flow was investigated by de Brederode & Bradshaw [86] using oil film visualisation. It was found that reattachment length changed significantly with aspect ratio due to the effects of the side wall flow up to AR ≈ 10, after which the centre plane flow could be considered 2D. At lower aspect ratios the variation of reattachment length with AR was opposite depending on whether the boundary layer at separation was laminar or turbulent: For a laminar BL the reattachment length decreased with AR, while for a turbulent BL it increased. de Brederode [105] also observed wall-normal aligned vortex traces on the lower wall at the edges of the secondary recirculation, which were of alternate direction for laminar and turbulent boundary layers at separation.

Lim et al. [106] investigated the flow behind a low aspect ratio (AR = 3.3) backward-facing step without varying AR as a parameter. As for the study of de Brederode [105], Lim et al. [106] observed a much shorter reattachment length than for the 2D BFS flow, with a wavy reattachment line, and found significant 3D effects relating to the secondary recirculation below the step. Large scale streamwise aligned vortices were identified downstream of the reattachment region, originating from horseshoe-like vortices which emerged from the corner between the side wall and the step face. The formation of the horseshoe vortices at the junctions between the step and side walls is explained by de Brederode [105].

More recently, Zheng et al. [85] studied the effect of aspect ratio on the flow behind a backward-facing step with external corners and a well developed turbulent boundary layer, although the conclusions may be of limited relevance due to the majority of BFS studies being conducted with the step extending across the full channel/tunnel width. Zheng et al. [85] found that the reattachment length increased with AR and that the presence of corner vortices affected the centre plane flow up to a value of AR between 8 and 16. They also noted that low aspect ratios limited the scale of vortical structures.

2.4 Open-Loop Flow Control Examples

2.4.1 Backward-facing Step Flow Control

Given its prevalence as a choice of canonical flow, a significant number of studies have investigated active control of backward-facing step flows at practically relevant Reynolds numbers. The majority of the literature, along with the work presented in this thesis, approach BFS flow control with the aim of reducing the reattachment length/separation bubble size. This aim is consistent with the intent to recover the flow in the shortest distance possible after separation and mitigate the effects of highly non-uniform flow due to separation on downstream components or processes. However, it is worth noting that reducing the extent of the separation bubble is contrary to the aim of total drag reduction, where an increase in streamline curvature results in decreased base pressure.

Studies available in the open literature somewhat favour periodic excitation over steady control methods, due to the practical considerations of supplying a mass flow in target applications and the improved efficiency of periodic excitation gained by leveraging natural instabilities.

Steady Excitation

de Brederode [105] investigated 'brute force' steady blowing and suction through perforations in the side walls on either side of the recirculation bubble, and found that blowing caused both reattachment length and base pressure to increase, while suction caused a comparatively smaller decrease in x_r and increase in base pressure. This discrepancy in the sign of the effect was explained by the lower pressure in the separation bubble compared to the freestream, resulting in the majority of the suction mass flow being extracted from the freestream flow rather than the bubble. The percentage reduction/increase in reattachment length for blowing and suction with volume flow rate coefficient $C_q \equiv q/(UA_\mathrm{ref}) = 5\times10^{-2}$ (where q is actuation volume flow rate, U is the freestream velocity, and A_ref is the area of the step face) at $Re_h = 50000$ were:

	Laminar BL	Turbulent BL
Blowing	+8%	+11%
Suction	-1.7%	-2%

Uruba et al. [107] also used blowing and suction to control the separation bubble, but through a slot/orifices at the foot of a low aspect ratio BFS (AR = 4). Volume flow rate coefficients of $-0.35 \leq C_q \geq 0.35$ were tested at a Reynolds number of $Re_h = 35000$, and they found that both blowing and suction were effective in terms of reattachment length reduction, reducing x_r by as much as two thirds. The authors observed that blowing was most effective at higher velocities, even when flow rate was kept constant, while suction depended only on C_q. The authors suggest that the mechanism of control by blowing was the entrainment of recirculation zone fluid by the wall-jet, while for suction it was the removal of low momentum fluid, however it is noted that the power requirements of continuous blowing/suction are relatively large.

Gautier & Aider [21] used normal blowing/suction just upstream of a step to control the recirculation area, at $Re_h = 2900$. The experimental configuration used had a significant bias towards blowing, with the achievable velocity ratios being $-0.25 <$VR< 1.8. Suction caused the recirculation area to shrink, with a maximum reduction of about 30%. However, no evidence of the effectiveness beginning to saturate at the suction amplitudes tested is seen, implying that stronger suction would achieve a greater reduction in bubble size. Increasing blowing velocity above a minimum threshold initially caused the recirculation area to reduce, with a maximum reduction of about 50% for VR ≈ 1, before increasing recirculation size at higher velocities, reaching a maximum of about 30% above the baseline at VR ≈ 1.65. At the most effective blowing ratio, the authors observed that the shear layer was thickened and instabilities appeared sooner, while at higher blowing velocities the jet acted as a barrier to the oncoming flow.

Morioka & Honami [108] used vortex generating jets to control the reattachment length behind a step at $Re_h = 27000$ ($Re_\theta = 2600$). They found that reattachment length very slightly increased at low velocity ratios (0.6% increase at VR = 1), but decreased with jet velocity at higher velocity ratios. The largest reduction of 21% was achieved at the

maximum VR of 9, although the trend of x_r with velocity ratio showed diminishing return as jet velocity increased, indicating that VR = 9 may be close to maximum effectiveness.

Periodic Excitation

The majority of periodic forcing studies have found the most effective forcing frequency in terms of reattachment length reduction to be close to the natural shear layer vortex frequency, which is typically able to reduce reattachment length by at least 20% at moderate Reynolds numbers, regardless of actuator type [9]. Numerous studies have investigated periodic excitation by pulsed or oscillating jets (internal oscillators) and DBD plasma actuators at or just upstream of the separating edge. However, to the best knowledge of the present author, only Bhattacharjee et al. [69] and Marrot et al. [42, 109, 48] employed non-local acoustic excitation using loudspeakers embedded in the tunnel walls.
Berk et al. [45] explain that periodic excitation at the step edge causes the roll-up of shear layer vortices at the forcing frequency, which affects shear layer spreading/curvature via the transfer of momentum from the freestream flow into the recirculation bubble, hence reattachment length scales with circulation. Chun & Sung [41, 54] identified two regimes of periodic forcing depending on the ratio of forcing frequency to the frequency of the shear layer mode (f^+), and more recently both Berk et al. [45] and D'Adamo et al. [110] identified a third regime at lower forcing frequencies:

A. For $f^+ \lesssim 1$ large vortices are formed, but roll-up time/length is long compared to recirculation bubble length (roll-up scales with $1/f$), resulting in a lower reduction in reattachment length compared to $f^+ \approx 1$. x_r decreases with increasing f^+

B. For $1 \lesssim f^+ \lesssim 4$ a train of reasonably large vortices is formed, with roll-up occuring closer to the step than in the unforced flow, individual vortex circulation decays with $(tf)^{-2}$. x_r increases with increasing f^+

C. For $f^+ \gtrsim 4$ a train of small close together vortices is formed, having lower circulation and unable to penetrate across the shear layer, resulting in a slight increase in reattachment length compared to unforced flow. $x_r \to x_{r0}$ as $f^+ \to \infty$

McQueen et al. [111] demonstrated that this forced vortex behaviour remains unchanged

even for high Reynolds numbers up to 472000. The behaviour also seems to be somewhat insensitive to actuator geometry/type, with internal oscillators [41, 54, 55, 45, 111], and DBD plasma actators on the vertical step face [110] producing similar curves of reattachment length against forcing frequency. There are, however, some notable examples which demonstrate different forced vortex behaviour with different actuator type/arrangement [42, 109, 48, 47].

Of particular relevance to the current work are the studies of Marrot et al. [42, 109, 48], who investigated the effect of external acoustic excitation on the BFS flow over a range of excitation frequencies. Although a relationship between vortex roll-up and excitation frequency is not explicitly stated, the data presented indicate that the acoustic actuation couples to the vortex structure closest to the actuation frequency, rather than exclusively to roll-up. Marrot et al. [42, 109, 48] found that the most effective actuation frequency in terms of reattachment length reduction at lower excitation amplitudes was around $f^+ \approx 0.4$ ($St_h \approx 0.61$), which corresponded to the second longitudinal acoustic mode of the tunnel, and $f^+ \approx 0.17$ ($St_h \approx 0.25$) at higher amplitudes, corresponding to the first longitudinal mode, with frequencies between these values comparatively ineffective regardless of actuation amplitude. A slight increase of reattachment length was seen for excitation frequencies exceeding around $f^+ \approx 1.2$. Although frequency spectra suggest that excitation at $f^+ = 1$ enhances the strength and periodicity of vortex roll-up and the first pairing, only a small reduction in reattachment length was observed. While the effectiveness appears to depend strongly on tunnel resonances, the shear layer mode frequency was also identified as the fifth longitudinal resonance mode, so the ineffectiveness of control at $f^+ = 1$ is surprising and suggests that acoustic forcing is more effective when larger structures are targeted.

Duriez et al. [47], investigated actuation by a pulsed DBD actuator just upstream of the step edge, and found that multiple vortices rolled up per actuation period when forced at a frequency $f^+ \lesssim 0.73$. This behaviour was explained as the flow reverting to its natural behaviour between pulses.

Table 2.1 provides a summary of the experimental configuration, reattachment length reduction ($\Delta x_\mathrm{r}/x_\mathrm{r0}$), and optimal forcing Strouhal number based on step height ($St_{h,\mathrm{opt}}$) of some of the backward-facing step control studies using periodic excitation at moderate

to high Reynolds numbers. The relatively small spread in the optimal values of St_h despite the complicated multi-scale nature of backward-facing step flows is likely indicative that the ratios of the important scales (momentum thickness, step height, reattachment length) are often similar between studies.

Reference	**Actuator type**	**ER**	**AR**	$\mathbf{Re_h}$	$\mathbf{\Delta x_r/x_{r0}}$	$\mathbf{St_{h,opt}}$
Bhattacharjee et al. 1986 [69]	Acoustic on opposite to step wall	1.1	16.25	26000-76000	10-15%	0.2-0.4
Marrot et al. 1998-2005 [42, 109, 48]	Acoustic far downstream of step	1.33	10	38000	20%	0.25
Chun & Sung 1996 [41], Liu et al. 2005 [55]	45° oscillating jet at step edge	1.5	12.5	13000, 23000, 33000	22%, 34%, 37%	0.27
Chun & Sung 1998 [54]	45° oscillating jet at step edge	1.087	12.5	1200	66%	0.477
Yoshioka et al. 1999 [112], Yoshioka et al. 2001 [113]	45° oscillating jet at step edge	1.5	12	3700	31%	0.19
Henning & King 2007 [114]	45° oscillating jet at step edge	1.27	20	25000	30%	0.3
Berk et al. 2017 [45]	45° oscillating jet at step edge	1.09	18	41000	29%	0.21
McQueen et al. 2022 [111]	45° synthetic jet at step edge	1.1	10	118000-472000	36%	0.27
Gautier & Aider 2014 [115]	Burst modulated wall-normal jet upstream of step edge	1.22	10	2070, 2900	$\approx 40\%$	0.258, 0.272
Chovet et al. 2019 [116]	Pulsed microblowers just upstream of step edge	1.04	24	30450	4.8%	0.226
D'Adamo et al. 2014 [110]	DBD on vertical face behind step	1.1	9	1520	37%	0.17
Duriez et al. 2014 [47]	DBD upstream of step edge	1.2	5	4400	35%	0.305
Pouryoussefi et al. 2015 [117]	Streamwise directed DBD at step edge	1.08	10.2	18000-54000	-	0.27
Sujar-Garrido et al. 2015 [118], Benard et al. 2016 [119]	Streamwise directed DBD at step edge	1.11	10	30000	22%	0.25

Table 2.1: Summary of BFS control by periodic excitation studies

2.4.2 S-duct Flow Control

The diffusing nature of S-ducts often leads to flow separation and blockage [8], and duct curvature causes pressure gradients which force the higher velocity fluid to the inner radius side, resulting in the formation of counter rotating vortices. Secondary flows of bulk swirl and those associated with switching of swirl direction are also seen in unsteady S-duct flow [120]. Several examples of active flow control in S-ducts are summarised below. A more detailed review of passive and active S-duct flow control is presented by Wojewodka et al. [8].

Burrows et al. [121, 122] used fluidic actuation to mitigate total pressure distortion arising from secondary vortices and separation in an aggressive double-offset diffuser. A spanwise array of 3 to 13 oscillating jets was located upstream of separation in the second turn of the duct, with jets on either side of the centreline oriented slightly towards the sidewalls. Oscillation frequencies were 7-9 kHz and mass flux 0.44% of the diffuser flow. The streamwise vorticity introduced by the jets diminished separation and weakened the counter-rotating vortices, with the strongest effect using all 13 actuators, reducing aerodynamic interface plane (AIP) distortion by over 60%. In addition to time averaged measures, the instantaneous variation in circumferential pressure distortion was reduced by more than 25%.

Rabe [123] assessed the performance of a microjet array on the inner curve of a highly curved S-duct with non-constant cross section shape. This actuation was shown to be successful at reducing total pressure distortion at the AIP and improving compressor stability margin at design and off-design conditions, with jet mass flux 1% of inlet mass flow.

Gissen et al. [124, 125] applied synthetic jets and passive vanes together to suppress total pressure distortion in a boundary layer ingesting offset diffuser without natural separation. The combination of passive and active control was designed such that active control increased authority in conditions where flow distortions would be highest, however safe operation would be maintained if the active component fails. The actuators consisted of 6 vanes and, just downstream, an array of 30 synthetic jet orifices arranged in 3 rows of 10. Vanes and synthetic jets alone were both able to reduce the circumferential distortion measure by around 20%, and together reduced distortion by up to 35%. The authors noted however that some configurations of the hybrid scheme had a detrimental effect compared

to baseline.

2.4.3 Non-BFS Acoustic Flow Control

Although to the knowledge of the present author only Bhattacharjee et al. [69] and Marrot et al. [42, 109, 48] used non-local acoustic forcing for the control of flow over a backward-facing step, a number of studies have investigated acoustic control on problems exhibiting similar flow physics, especially the acoustic forcing of free jets, and post-stall aerofoils. Historically, a significant proportion of the research on jet excitation has made use of acoustic disturbances, most often introduced in the plenum or jet nozzle upstream of the exit [44, 71, 36, 73, 126, 75, 76, 72, 53], and occasionally emanating from downstream of the jet exit [127]. Although the majority of research has considered unbounded jets, the similarity between free shear layers and the initial section of a reattaching shear layer [79] implies that acoustic actuation of equivalent configuration will excite similar instabilities/flow dynamics for reattaching shear layer flows.

Collins & Zelenevitz [128] demonstrated the ability of acoustic excitation by a downstream loudspeaker in the wall of the wind tunnel to either partially or fully reattach the flow over a stalled aerofoil from $Re_c = 2.5 \times 10^5$ to 5.3×10^5, which was concluded to be due to premature transition to turbulence of the upstream boundary layer. A similar experiment was conducted by Zaman & McKinzie [129], in which acoustic excitation was used to suppress a laminar separation bubble on the suction side of airfoils at Reynolds numbers from $Re_c = 2.5 \times 10^4$ to 1×10^5. The authors were able to reduce but not completely suppress the separation, and found that the most effective excitation frequency was $St_c/Re_c^{1/2} \approx 0.025$.

Coskun et al. [130] investigated the effectiveness of acoustic excitation on high Reynolds number turbulent separation over an NACA0015 aerofoil at $Re_c = 1 \times 10^6$ numerically, where natural separation occurred approximately at the mid-chord. It was confirmed that forcing was most effective at $f^+ = 1$. The effectiveness was strongly asymptotic with amplitude due to the nearing of complete suppression of separation at higher amplitudes. A maximum increase in C_L/C_D of 120% compared to the baseline was achieved for excitation amplitudes above $A_\mathrm{m} = 5\%$, where A_m is the ratio of acoustic velocity to freestream velocity. Coskun et al. [130] also found that the effectiveness of acoustic excitation improved

with increasing freestream turbulence level.

Nishioka et al. [70] investigated the control of separation at the sharp edge of a flat plate aerofoil by low amplitude acoustic forcing from a loudspeaker mounted in the wind tunnel wall at $Re_c = 4 \times 10^4$. The forced roll-up of vortices was demonstrated, which enhanced entrainment and caused the separated shear layer to reattach earlier (or at all) compared to the unexcited case. Nishioka et al. [70] found that excitation was most effective when the scale of the forced vortices matched that of the separation bubble, hence the most effective frequency decreased with angle of attack and was always lower than the natural shedding frequency, which depends on the thickness of the shear layer. The findings of Nishioka et al. [70] were corroborated by Zaman [77], who performed a similar study on a post stall aerofoil. Interestingly, Zaman [77] also identified a saturation and shortly after a break down of effectiveness as excitation amplitude increased, which was attributed to the bursting of the separation bubble.

Recently, it has also been demonstrated that acoustic forcing is an effective mechanism of controlling fluidic diverters and other Coandă effect devices [58, 59, 57, 131, 132]. Mair et al. [58, 59] used Helmholtz resonator/internal oscillator type acoustic actuators driven by piezoelectric diaphragms on either side of a bistable diverter, and found that while actuation from either side was able to switch the jet, it was several times more effective from the unattached side. This is partly the motivation for the canonical setup studied in this thesis.

2.5 Fundamentals of Closed-loop Control

The examples of control cited so far have all been open-loop (or conducted an open-loop characterisation prior to closed-loop control), which refers to the absence of feedback, i.e. predetermined or feed-forward. In many cases open-loop control is perfectly adequate, and it has been demonstrated that for free-shear flows dominated by the Kelvin-Helmholtz instability that the most effective control input depends on inlet conditions, implying that adaptive control strategies need only be feed-forward. However, closed-loop control, in which the input is adjusted based on downstream measurements, guarantees both robustness and minimum energy expenditure for a given minimum output.

A generic block diagram of feedback control is shown in figure 2.6, with plant transfer function $G(s)$, and controller $C(s)$. The generic system has one output, y, and four external inputs: the reference, r, which the output is intended to track; input disturbance, d_{i}, and output disturbance, d_{o}, which the controller is intended to counteract; and sensor noise noise, n, which should be ignored. The choice of modelling plant uncertainties as either input or output disturbances is somewhat arbitrary, and often systems are considered to have only one disturbance. From the perspective of a fluid system, uncertainty in plant dynamics (e.g. non-linearity, high order behaviour) might be modelled as an input disturbance, while random unsteadiness/turbulence could be considered an output disturbance. The purpose of controller, $C(s)$, is to reduce uncertainty in the presence of noise and disturbances, and ensure that the system is stable, i.e. that all signals remain bounded.

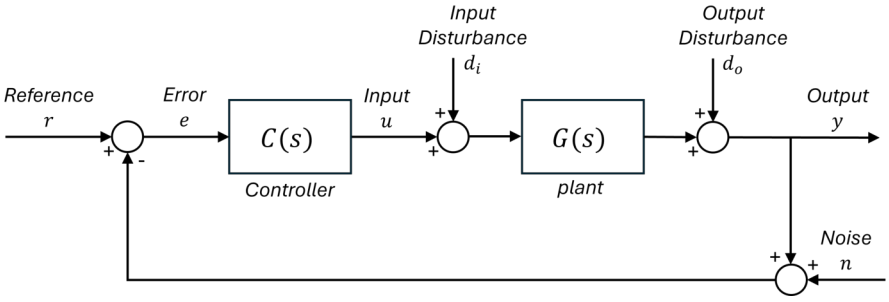


Figure 2.6: Generic closed-loop controller block diagram

The input-output behaviour of the system can be described by transfer functions relating the Laplace transforms of the signals

$$Y(s) = \frac{G(s)C(s)}{1+G(s)C(S)}[R(s) - N(s)] + \frac{G(s)}{1+G(s)C(s)}D_{\mathrm{i}}(s) + \frac{1}{1+G(s)C(s)}D_{\mathrm{o}}(s) \quad (2.2)$$

The (output) **sensitivity** transfer function, $S(s)$, and **complimentary sensitivity** transfer function (also called the closed-loop transfer function), $T(s)$ are defined as:

$$S(s) = \frac{1}{1+G(s)C(S)}, \quad (2.3)$$

and

$$T(s) = I - S(s) = \frac{G(s)C(s)}{1 + G(s)C(S)}, \tag{2.4}$$

which allows 2.2 to be rewritten as

$$Y(s) = T(s)[R(s) - N(s)] + S(s)[G(s)D_{\mathrm{i}}(s) + D_{\mathrm{o}}(s)]. \tag{2.5}$$

An ideal controller would be able to achieve $Y(s) = R(s)$ at all frequencies, however it is clear that this is not practically achievable. Rejection of disturbances requires that the controller gain be as large as possible, such that $S(s) \to 0$, however if this were the case then $T(s) \to 1$ and the sensor noise will be completely be fed through to the output y. Fortunately, each of the terms in the above equations are a function of frequency, therefore $C(s)$ can be designed in such a way that the sensitivity transfer function is large over some frequency ranges and small over others.

Physical systems are strictly proper, meaning that their transfer functions contain more poles than zeros, therefore both $|G(s)| \to 0$ and $|C(s)| \to 0$ as $|s| = \omega \to \infty$. It follows that $\lim_{\omega\to\infty} S(j\omega) = 1$, and $\lim_{\omega\to\infty} T(j\omega) = 0$, which along with 2.5 indicate that the bandwidth of the closed-loop system cannot be made arbitrarily high, and that at high frequencies noise will be filtered out but disturbances will not be. However, disturbances typically occur at low frequencies, while a good sensor will have very little noise at low frequencies, so it would seem that this behaviour is no problem at all. The task of a control engineer is then to design a controller $C(s)$ such that the 'cross over' point between $S(s)$ and $T(s)$ is an acceptable compromise between the disturbance rejection/tracking bandwidth and the noise rejection of the system.

In addition to being the transfer function from $D_{\mathrm{o}}(s)$ to $Y(s)$, the sensitivity function also gives the ratio of fractional change in closed-loop transfer function gain to the fractional change in plant gain,

$$S(s) = \frac{\delta T(s)/T(s)}{\delta G(s)/G(s)}. \tag{2.6}$$

For example, if $|S(j\omega)| = 0.1$, then a deviation in plant gain of 10% from the modelled gain at ω will cause only a 1% deviation of the closed-loop gain. The magnitude of the

sensitivity transfer function is therefore particularly important when the physical plant contains unmodelled dynamics, or dynamics which vary with time/operating point, as in either case a high value of $|S|$ may result in a closed-loop response which differs significantly from designed.

Bode's Sensitivity Integral

Bode's sensitivity integral, sometimes referred to as the 'waterbed effect', states that for a single-input, single-output (SISO) system,

$$\int_0^\infty \ln|S(j\omega)|\, d\omega = \pi \sum_k \Re(p_k) - \frac{\pi}{2} \lim_{s\to\infty} sL(s) \tag{2.7}$$

where $L(s) = G(s)C(s)$ is the open-loop transfer function, and p_k are the unstable (right half plane) poles of $L(s)$. If $L(s)$ is stable and has at least two more poles than zeros, then 2.7 simplifies to

$$\int_0^\infty \ln|S(j\omega)|\, d\omega = 0. \tag{2.8}$$

These equalities demonstrate that any suppression of $S(j\omega)$ over some frequency range is necessarily accompanied by an increase at other frequencies. Additional design constraints are imposed by unstable open-loop poles or minimum phase zeros, and by the directionality properties of multi-input, multi-output (MIMO) systems [133], the details of which are beyond the scope of the current section.

Stability Margins

As has been briefly discussed in relation to the sensitivity transfer function, it is important that a controller be robust to uncertainties in modelled system dynamics and noise/disturbances without becoming unstable. Robustness is typically quantified by the gain and phase margins of the open-loop system. Gain margin (GM) is the factor of gain (in dB) required to increase the open-loop gain to unity at the frequency where phase is $-180°$, i.e. GM $= -20\log_{10}(|L(j\omega_\mathrm{g})|)$, where $\angle L(j\omega_\mathrm{g}) = -180°$, and corresponds to the the amount of gain that can be added before the closed-loop system becomes a positive feedback loop. Similarly, phase margin (PM) is the difference between the phase and $-180°$ at the frequency where open-loop gain is unity, i.e. PM $= \angle(L(j\omega_\mathrm{p}))+180°$, where

$20\log_{10}(|L(j\omega_\mathrm{p})|) = 0\,\mathrm{dB}$, which corresponds to the amount of phase lag that can be added before a positive feedback loop forms. In the case where there are multiple possible values of ω_g or ω_p, then the gain and phase margins of the system are taken as the the smallest values. GM $> 3\,\mathrm{dB}$ and PM $> 30^\circ$ are often taken as an acceptable compromise between bandwidth and stability.

2.5.1 Optimal Control: Linear Quadratic Regulator

Unlike the PID controller, which was arrived at empirically by trial and error and then subsequently formalised into modern control frameworks, optimal control is a design methodology based on defining a cost function which is to be minimised by the feedback gain.
First, it is necessary to transition from transfer function representation to the state-space representation of dynamic systems. Plant dynamics can be expressed in terms of a (discrete) state-space system as

$$\begin{aligned} \mathbf{x}_{k+1} &= \mathbf{A}\mathbf{x}_k + \mathbf{B}\mathbf{u}_k \\ \mathbf{y}_k &= \mathbf{C}\mathbf{x}_k + \mathbf{D}\mathbf{u}_k \end{aligned} \tag{2.9}$$

where $\mathbf{x}_k$ are the system states, $\mathbf{u}_k$ are the inputs, $\mathbf{y}_k$ are the outputs, $\mathbf{A}$ is the system matrix governing the internal dynamics, $\mathbf{B}$ is the input matrix, $\mathbf{C}$ is the output matrix, and $\mathbf{D}$ is the feed-through matrix. For many systems there is no direct feed through of input to output, so for convenience the $\mathbf{D}$ matrix will be omitted from this point forward.

In the case of the *Linear Quadratic Regulator* (LQR), the cost to be minimised is chosen to be a quadratic function of the form

$$J = \sum_{k=0}^{\infty} (\mathbf{x}_k^\mathrm{T}\mathbf{Q}\mathbf{x}_k + \mathbf{u}_k^\mathrm{T}\mathbf{R}\mathbf{u}_k), \tag{2.10}$$

where $\mathbf{Q}$ and $\mathbf{R}$ are the (symmetric) state and control weighting matrices, respectively. It is the task of the control engineer to tune these cost matrices to achieve the desired system performance. The state weighting matrix, $\mathbf{Q}$, can be thought of as an energetic cost of the deviation of system states from the origin (or their steady state values in the tracking problem), while the control weighting matrix, $\mathbf{R}$, can be thought of as the cost of actuation, for which the designer will consider both energy input and the physical limitations of the

actuators used. A typical starting point is to choose $\mathbf{Q} = \mathbf{C}^{\mathrm{T}}\mathbf{C}$, i.e. the states are costed equivalently to the output, then to tune $\mathbf{R}$ to achieve an acceptable compromise between transfer functions $T(s)$, $S(s)$, and the input signal $\mathbf{u}$. Parameter tuning can be done this way because the important quantity is the ratio $\mathbf{Q}/\mathbf{R}$ and not the absolute values of the matrices.

The linear state feedback control law is given by

$$\mathbf{u}_k = -\mathbf{K}_{\mathrm{LQR}}\mathbf{x}_k, \tag{2.11}$$

where the feedback gain $\mathbf{K}_{\mathrm{LQR}}$ is given by the solution to the LQR problem:

$$\mathbf{K}_{\mathrm{LQR}} = (\mathbf{R} + \mathbf{B}^{\mathrm{T}}\mathbf{P}\mathbf{B})^{-1}\mathbf{B}^{\mathrm{T}}\mathbf{P}\mathbf{A} \tag{2.12}$$

where $\mathbf{P}$ is the positive definite solution to the *Discrete Algebraic Riccati Equation* (DARE):

$$\mathbf{P} = \mathbf{A}^{\mathrm{T}}\mathbf{P}\mathbf{A} - (\mathbf{A}^{\mathrm{T}}\mathbf{P}\mathbf{B})(\mathbf{R} + \mathbf{B}^{\mathrm{T}}\mathbf{P}\mathbf{B})^{-1}\mathbf{B}^{\mathrm{T}}\mathbf{P}\mathbf{A} + \mathbf{Q} \tag{2.13}$$

Linear Quadratic Tracking problem

The regulator problem is formulated to drive the output $\mathbf{y}_k = \mathbf{C}\mathbf{x}_\mathbf{k}$ to zero. However, it is often desirable to have the controller track a requested output The LQR can be converted to a *Linear Quadratic Tracking* problem (LQT) by setting the steady state output equal to reference value $\mathbf{r}$, resulting in feedback $\mathbf{u}_k$ [134]:

$$\mathbf{u}_k = (\mathbf{I} - \mathbf{K}_{\mathrm{LQR}}(\mathbf{A} - \mathbf{I})^{-1}\mathbf{B})(\mathbf{C}(\mathbf{A} - \mathbf{I})^{-1}\mathbf{B})^{-1}\mathbf{r} - \mathbf{K}_{\mathrm{LQR}}\mathbf{x}_k \tag{2.14}$$

Exact tracking of the reference using feedback of this form will only happen if the system model matrices $\mathbf{A}$ and $\mathbf{B}$ are exact, which will not be the case. Therefore, an integrator is typically added to achieve acceptable steady state performance [134].

The *linear quadratic integrator* (LQI) problem is adapted from the LQR by augmenting the state vector to include an integrator term, such that $\mathbf{x}_{\mathrm{aug},k} = \begin{bmatrix}\mathbf{x}_k^{\mathrm{T}} & \mathbf{z}_k^{\mathrm{T}}\end{bmatrix}^{\mathrm{T}}$, where $\mathbf{z}_{k+1} = \mathbf{z}_k + \delta t(\mathbf{r} - \mathbf{C}\mathbf{x})$ is the integrator. The LQI gain, $\mathbf{K}_{\mathrm{LQI}} = \begin{bmatrix}\mathbf{K}_{\mathrm{LQI,x}} & \mathbf{K}_{\mathrm{LQI,i}}\end{bmatrix}$, can then be found by solving the DARE as normal with system and cost matrices replaced

with augmented matrices:

$$\mathbf{A}_{\text{aug}} = \begin{bmatrix} \mathbf{A} & \mathbf{0} \\ \delta t\mathbf{C} & \mathbf{I} \end{bmatrix}, \ \mathbf{B}_{\text{aug}} = \begin{bmatrix} \mathbf{B} \\ \mathbf{0} \end{bmatrix}, \ \mathbf{C}_{\text{aug}} = \begin{bmatrix} \mathbf{C} & \mathbf{0} \end{bmatrix}, \ \mathbf{Q}_{\text{aug}} = \begin{bmatrix} \mathbf{Q} & \mathbf{0} \\ \mathbf{0} & \eta \end{bmatrix} \tag{2.15}$$

where η is a weighting determining the importance of the integral term.

Robustness Guarantees

The poles of the closed-loop system with the control law 2.11 are given by the eigenvalues of $\mathbf{A} - \mathbf{B}\mathbf{K}_{\text{LQR}}$, which are guaranteed to be in the left-half-plane, guaranteeing that the closed loop system is stable. Furthermore, it can be shown by frequency domain arguments that the continuous-time LQR has a guaranteed gain margin of at least 6 dB, and phase margin of at least 60°. It is worth noting that while performance guarantees do exist for the discrete-time LQR, they are not as good [135].

2.5.2 Kalman Filter

In the previous section, in which the LQR was introduced, it was assumed that the controller has full knowledge of the system states, $\mathbf{x}$, so that a full state feedback control law, $\mathbf{u} = -\mathbf{K}\mathbf{x}$, could be used. While in some cases the system states represent physical quantities that can be measured, it is often the case that they are not or can not be directly measured, and only the output $\mathbf{y} = \mathbf{C}\mathbf{x}$ is available. However, full state feedback is a powerful control law which it would be unfortunate to give up due to lack of measurements. The solution to this dilemma is to use an **observer** to estimate the system states. An observer is effectively a real-time simulation of a physical system, which takes the measured outputs and uses them to correct the simulated state estimates.

An observer can be used to estimate the internal states of a system from a single or very few measurements $\mathbf{y} = \mathbf{C}\mathbf{x}$, so long as the system is observable. The observer is its own dynamical system with inputs $\mathbf{u}$ and $\mathbf{y}$ and output full state estimates $\hat{\mathbf{x}}$ (and optionally $\hat{\mathbf{y}}$) designed to converge to the true internal system states and output,

$$\begin{aligned} \hat{\mathbf{x}}_{k+1} &= (\mathbf{A} - \mathbf{K}_{\text{f}}\mathbf{C})\hat{\mathbf{x}}_k + \begin{bmatrix} \mathbf{B} & \mathbf{K}_{\text{f}} \end{bmatrix} \begin{bmatrix} \mathbf{u}_k \\ \mathbf{y}_k \end{bmatrix}, \\ \hat{\mathbf{y}}_k &= \mathbf{C}\hat{\mathbf{x}}_k \end{aligned} \tag{2.16}$$

which has error dynamics

$$\mathbf{e}_{k+1} = (\mathbf{A} - \mathbf{K}_\mathrm{f}\mathbf{C})\mathbf{e}_k \tag{2.17}$$

where $\mathbf{e}_k = \mathbf{x}_k - \hat{\mathbf{x}}_k$ is the error between the true and estimated states.

Figure 2.7 shows the block diagram of a state feedback controller using an observer.

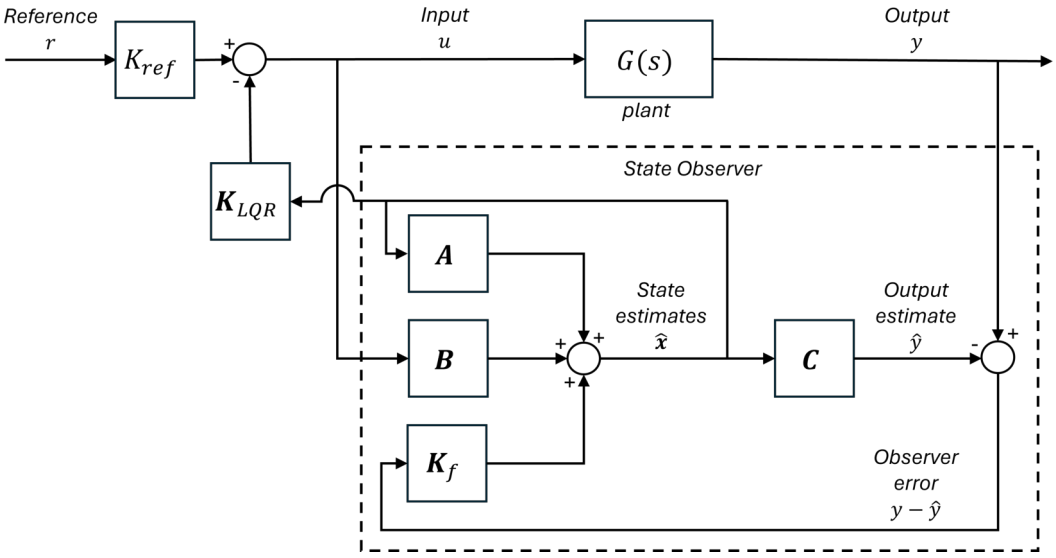


Figure 2.7: Block diagram of full state feedback using an observer

$\mathbf{K}_\mathrm{f}$ must be chosen so that $\mathbf{A} - \mathbf{K}_\mathrm{f}\mathbf{C}$ is stable, i.e. its eigenvalues are within the unit circle. While it may initially seem desirable to set the observer bandwidth as high as possible, in practice this will result in feeding sensor noise through to the state estimates. A *Kalman filter* (the sensing equivalent of the LQR) is the most optimal estimator in a minimum variance sense, under the assumption that sensor and process noise are Gaussian [136]. For the system with disturbances and sensor noise

$$\begin{aligned} \mathbf{x}_{k+1} &= \mathbf{A}\mathbf{x}_k + \mathbf{B}\mathbf{u}_k + \mathbf{F}\mathbf{v}_k \\ \mathbf{y}_k &= \mathbf{C}\mathbf{x}_k + \mathbf{w}_k \end{aligned} \tag{2.18}$$

where $\mathbf{v}$ and $\mathbf{w}$ are Gaussian white noise signals to represent process noise and sensor noise respectively, and $\mathbf{F}$ is the mapping of $\mathbf{v}$ onto the states. The covariances of $\mathbf{Fv}$ and $\mathbf{w}$ are denoted as $\mathbf{Q}_\mathrm{v}$ and $\mathbf{R}_\mathrm{w}$, respectively. The simplest choice of $\mathbf{F}$ is to set $\mathbf{F} = \mathbf{B}$, i.e. the process noise is modelled as an input disturbance. The optimum value of $\mathbf{K}_\mathrm{f}$ to minimize

the prediction error variance is then is given by the solution to

$$\min_{\mathbf{K}_\mathrm{f}} \mathbb{E}[\mathbf{e}_k \mathbf{e}_k^\mathrm{T}] \tag{2.19}$$

where the error dynamics with disturbance and noise are now

$$\mathbf{e}_{k+1} = (\mathbf{A} - \mathbf{K}_\mathrm{f}\mathbf{C})\mathbf{e}_k + \mathbf{F}\mathbf{v}_k + \mathbf{K}_\mathrm{f}\mathbf{w}_k. \tag{2.20}$$

Once again, the optimal gain is given by the solution to the DARE:

$$\begin{aligned} \mathbf{P} &= \mathbf{A}\mathbf{P}\mathbf{A}^\mathrm{T} - (\mathbf{A}\mathbf{P}\mathbf{C}^\mathrm{T})(\mathbf{R}_\mathrm{w} + \mathbf{C}\mathbf{P}\mathbf{C}^\mathrm{T})^{-1}\mathbf{C}\mathbf{P}\mathbf{A}^\mathrm{T} + \mathbf{Q}_\mathrm{v} \\ \mathbf{K}_\mathrm{f} &= \mathbf{A}\mathbf{P}\mathbf{C}^\mathrm{T}(\mathbf{R}_\mathrm{w} + \mathbf{C}\mathbf{P}\mathbf{C}^\mathrm{T})^{-1} \end{aligned} \tag{2.21}$$

The duality of the LQR and the Kalman filter is evident from the equations, which are identical except for the interchange of $\mathbf{A}$ with $\mathbf{A}^\mathrm{T}$, $\mathbf{B}$ with $\mathbf{C}^\mathrm{T}$, $\mathbf{Q}$ with $\mathbf{Q}_\mathrm{v}$, $\mathbf{R}$ with $\mathbf{R}_\mathrm{w}$, and $\mathbf{K}_\mathrm{LQR}$ with $\mathbf{K}_\mathrm{f}^\mathrm{T}$.

In theory the covariances $\mathbf{Q}_\mathrm{v}$ and $\mathbf{R}_\mathrm{w}$ can be measured, although in practice a similar approach to the tuning of LQR gains is usually taken, with a control engineer tuning the ratio $\mathbf{R}_\mathrm{w}/\mathbf{Q}_\mathrm{v}$ to achieve a satisfactory balance of tracking response and noise rejection. The process noise covariance, $\mathbf{Q}_\mathrm{v}$, represents both the magnitude of disturbances and the degree of plant uncertainty, while the standard definition of $\mathbf{R}_\mathrm{w}$ is that it represents sensor noise. However, given the positioning of the noise input, $\mathbf{w}$, at the measured output, it must also account for any output disturbances. This is important to note for fluid systems with high turbulence levels, where the most significant contribution to $\mathbf{R}_\mathrm{w}$ is likely to be from small scale unsteadiness which does not interact with any observable/controllable dynamics. Increasing the value of $\mathbf{R}_\mathrm{w}$ relative to $\mathbf{Q}_\mathrm{v}$ tells the Kalman filter that the measurement uncertainty is larger than the model uncertainty, causing it to follow the measurement less, and vice versa.

As would be expected, the Kalman filter has equivalent stability and robustness guarantees to the LQR.

2.5.3 Linear Quadratic Gaussian (LQG)

The combination of linear quadric control law and Kalman filter (linear quadratic estimator) is called the *Linear Quadratic Gaussian* (LQG) controller. The separation principle states that the LQR and Kalman filter can be designed independently of each other. However, despite the individual robustness guarantees of the LQR and Kalman filters, there is no guarantee that the combination will be robust [137].

Substituting the control law $u_k = -\mathbf{K}_{\text{LQR}}\hat{\mathbf{x}}_k = -\mathbf{K}_{\text{LQR}}(\mathbf{x}_k - \mathbf{e}_k)$ into 2.18 and combining with 2.20 allows for the closed-loop combined Kalman filter and LQR system dynamics to be written as

$$\begin{bmatrix}\mathbf{x}_{k+1}\\ \mathbf{e}_{k+1}\end{bmatrix} = \begin{bmatrix}\mathbf{A}-\mathbf{B}\mathbf{K}_{\text{LQR}} & \mathbf{B}\mathbf{K}_{\text{LQR}}\\ 0 & \mathbf{A}-\mathbf{K}_{\text{f}}\mathbf{C}\end{bmatrix}\begin{bmatrix}\mathbf{x}_k\\ \mathbf{e}_k\end{bmatrix} + \begin{bmatrix}\mathbf{F} & \mathbf{0}\\ \mathbf{F} & -\mathbf{K}_{\text{f}}\end{bmatrix}\begin{bmatrix}\mathbf{v}_k\\ \mathbf{w}_k\end{bmatrix} \tag{2.22}$$

Which has closed-loop poles given by the eigenvalues of $\mathbf{A}-\mathbf{B}\mathbf{K}_{\text{LQR}}$ (the closed-loop poles of the deterministic system with LQR controller) and $\mathbf{A}-\mathbf{K}_{\text{f}}\mathbf{C}$ (the closed-loop poles of the Kalman filter). The robustness of the LQR can therefore be recovered by ensuring that the closed-loop poles of the Kalman filter are significantly faster than the LQR poles, such that the LQG transfer function approximates the LQR. While this may suggest that all one needs to do to guarantee robustness is to make the Kalman filter as fast as possible by setting $\mathbf{Q}_{\text{v}}/\mathbf{R}_{\text{w}} \to \infty$, the reality is that this increases the sensitivity to sensor noise/output disturbance. A compromise must be made between noise filtering, closed loop bandwidth (i.e. de-tuning the LQR to be slower relative to the Kalman Filter), and gain/phase margins. An iterative method for the design on an LQG controller was formalised by Doyle & Stein [138], referred to as the *Loop Transfer Recovery* (LTR) procedure.

2.6 Reduced Order Modelling

Many complex fluid flows display low-dimensional behaviour [139], i.e. the behaviour is dominated by a relatively small number of dynamic 'modes' often corresponding to large coherent structures. The identification of a low-dimensional basis set of physically interpretable modes and their corresponding dynamics from high dimensional experimental visualisation or simulation data can be an invaluable method for both the analysis and

modelling of fluid flows. The following section outlines the most common modal decomposition methods, **Proper Orthogonal Decomposition (POD)**, and **Dynamics Mode Decomposition (DMD)**.

2.6.1 Proper Orthogonal Decomposition

Proper Orthogonal Decomposition is a modal decomposition technique for extracting orthogonal basis functions (modes) which optimally express data in an energetic sense. Extracted POD modes identify coherent structures in fluid flows [140], and can be used for analysis or as a reduced-order basis for dynamic models.

Assuming that realisations of a process belong to a Hilbert space, the Karhunen-Loeve theorem [141] states that mean-subtracted field $\mathbf{q}$ can be expressed as an expansion along mutually orthogonal basis functions $\boldsymbol{\phi}_j(\mathbf{z})$.

$$\mathbf{q}(\mathbf{z}) = \sum_{j=1}^{\infty} a_j \boldsymbol{\phi}_j(\mathbf{z}) \tag{2.23}$$

where $\mathbf{z}$ are the independent variables of $\mathbf{q}$, typically position $\mathbf{x}$ and time t, and a_j are basis functions coefficients. *Spatial POD* further assumes that spatial and temporal dynamics are separable

$$\mathbf{q}(\mathbf{x}, t) = \sum_{j=1}^{\infty} a_j(t) \boldsymbol{\phi}_j(\mathbf{x}) \tag{2.24}$$

The basis vectors optimally representing the field (POD modes) are the eigenvectors of the spatial covariance matrix, which for discrete data is

$$\mathbf{R}_{\mathrm{xx}} = \frac{1}{N-1} \mathbf{X}\mathbf{X}^{\mathrm{T}}\mathbf{W} \quad \in \mathbb{R}^{n \times n} \tag{2.25}$$

where $\mathbf{X}$ is the matrix of snapshots,

$$\mathbf{X} = [\mathbf{q}(t_1) \quad \mathbf{q}(t_2) \quad \ldots \quad \mathbf{q}(t_m)] \quad \in \mathbb{R}^{n \times m} \tag{2.26}$$

and $\mathbf{W}$ is the (symmetric, positive definite) weighting through which the inner product in the finite dimension vector Hilbert space is defined

$$\langle \mathbf{q}_1, \mathbf{q}_2 \rangle = \mathbf{q}_1^{\mathrm{T}} \mathbf{W} \mathbf{q}_2 \tag{2.27}$$

$\mathbf{W}$ determines the orthogonality and optimality properties of the POD modes [142]. Typically, $\mathbf{W}$ is set to the identity matrix, $\mathbf{I}$, although it can also be set so that the POD modes calculated are optimal in turbulent kinetic energy or a compressible energy norm, for example.

Method of Snapshots - When a large dataset is used the size of $\mathbf{R}_{\mathrm{xx}}$ $(n \times n)$ becomes prohibitive. Sirovich [143] showed that the (often much smaller) $m \times m$ temporal correlation matrix can be used in place of the $n \times n$ spatial correlation matrix. The eigenvalue problem

$$\left(\mathbf{R}_{\mathrm{xx}} = \frac{1}{N-1} \mathbf{X}^{\mathrm{T}} \mathbf{W} \mathbf{X} \right) \boldsymbol{\psi}_j = \lambda_j \boldsymbol{\psi}_j, \quad \boldsymbol{\psi}_j \in {\mathbb{R}_{\mathrm{xx}}}^m \tag{2.28}$$

is then solved. $\mathbf{X}\mathbf{X}^{\mathrm{T}}\mathbf{W}$ and $\mathbf{X}^{\mathrm{T}}\mathbf{W}\mathbf{X}$ share the same nonzero eigenvalues, and the POD modes can be recovered by

$$\boldsymbol{\phi}_j = \mathbf{X} \boldsymbol{\phi}_j \frac{1}{\sqrt{\lambda_j}} \tag{2.29}$$

or in matrix form

$$\boldsymbol{\Phi} = \mathbf{X} \boldsymbol{\Psi} \boldsymbol{\Lambda}^{-1/2} \in \mathbb{R}^{n \times m} \tag{2.30}$$

Relation to SVD - The spatial POD modes $\boldsymbol{\Phi}$ and temporal POD modes $\boldsymbol{\Psi}$ are equivalent (when $\mathbf{W} = \mathbf{I}$) to the left singular vectors $\mathbf{U}$ and right singular vectors $\mathbf{V}$, respectively, of the singular value decomposition $\mathbf{X} = \mathbf{U}\boldsymbol{\Sigma}\mathbf{V}^{\mathrm{T}}$. Singular values and POD eigenvalues are related by $s_j^2 = \lambda_j$.

POD eigenvalues give the amount of energy captured by their corresponding POD modes, and can be ordered to rank the modes based on their energetic importance. The number of modes needed to capture the fluctuations of the data is generally much less than the

dimension of the data [139], therefore typically only r modes are retained such that

$$\sum_{j=1}^{r} \lambda_j / \sum_{j=1}^{n} \lambda_j \approx 1 \tag{2.31}$$

POD modes are optimal, in the energetic sense determined by weighting $\mathbf{W}$, at representing the data for any number r of retained modes. They are therefore useful for constructing reduced-order approximations of high dimensional data. Incoherent noise in the data is usually accounted for by high-order modes, so the truncation is also beneficial in that it essentially de-noises the data.

$$\mathbf{q}(\mathbf{x}, t) \approx \sum_{j=1}^{r} a_j(t) \boldsymbol{\phi}_j(\mathbf{x}) \tag{2.32}$$

Temporal coefficients of the POD modes can be found by the inner product $a_j(t) = \langle \mathbf{q}(t), \boldsymbol{\phi}_j \rangle$.

Some of the drawbacks of POD analysis are [139]:

- POD modes are the most optimal in an energetic sense, but do not necessarily represent relevant dynamics well. This is addressed by balanced POD and DMD.
- It is not always clear what value to truncate the POD at, and multiple criteria exist.
- POD modes are calculated from a second-order statistic. As a result the modes do not inherently contain any dynamics, and higher order correlations are not captured.
- Each POD mode contains multiple frequency components, which is not necessarily helpful for analysis and complicates reduced order modelling using POD modes. Spectral POD and DMD address this.

2.6.2 Dynamic Mode Decomposition

Since its proposal by Schmid [144] in the late 2000s, dynamic mode decomposition (DMD) has been widely used in the fluids community as a powerful tool for analysis and reduced-order modelling. DMD extracts dynamical modes corresponding to coherent spatial structures, each with a single oscillation frequency and decay rate, from high-dimensional data

snapshots, along with a low-dimensional linear approximation of the system evolution. DMD can be viewed as an approximation of Koopman operator theory [145, 146, 147], which states that a nonlinear system can be represented by an infinite-dimension linear operator on a Hilbert space of system observables. DMD analysis requires *spatially* and *temporally* resolved field data, and is suited to time-resolved particle image velocimetry (trPIV), unsteady CFD data, and sensor array measurements among other data acquisition methods.

DMD assumes the system of measurements can be approximated by a linear operator $\mathbf{A}$ stepping the measurements at one timestep, $\mathbf{x}_k$ to the measurements at the next, $\mathbf{x}_{k+1}$.

$$\mathbf{x}_{k+1} = \mathbf{A}\mathbf{x}_k \tag{2.33}$$

or

$$\mathbf{Y} = \mathbf{A}\mathbf{X} \tag{2.34}$$

where

$$\mathbf{X} = [\mathbf{x}(t_1) \quad \mathbf{x}(t_2) \quad \cdots \quad \mathbf{x}(t_n)] \quad \text{and} \quad \mathbf{Y} = [\mathbf{x}(t_1 + \delta t) \quad \mathbf{x}(t_2 + \delta t) \quad \cdots \quad \mathbf{x}(t_n + \delta t)] \tag{2.35}$$

where δt is the time between each of the snapshots in a pair. Often the data used is a single series of snapshots with equal time spacing and $\mathbf{Y} = \mathbf{X}'$, the matrix of snapshots shifted by one measurement.

$$\mathbf{Y} = \mathbf{X}' = [\mathbf{x}(t_2) \quad \mathbf{x}(t_3) \quad \cdots \quad \mathbf{x}(t_{n+1})]. \tag{2.36}$$

$\mathbf{x}(t_k)$ is arranged as the stacked vector of spatial measurements at time t_k,

$$\begin{aligned}\mathbf{x}(t_k) = [&m_1(p_1) \quad m_1(p_2) \quad \cdots \quad m_1(p_\nu) \quad m_2(p_1) \quad m_2(p_2) \quad \cdots \quad m_2(p_\nu) \\ &\cdots \quad m_\mu(p_1) \quad m_\mu(p_2) \quad \cdots \quad m_\mu(p_\nu)]^T\end{aligned} \tag{2.37}$$

where there are μ measurement quantities m_i and ν spatial points at which measurements p_j are taken. For example, measurements might be velocity components and pressure taken from a CFD simulation.

$\mathbf{A}$ can be calculated by a least-squares regression fit using the Moore-Penrose pseudoinverse of $\mathbf{X}$, denoted by †, $\mathbf{A} = \mathbf{Y}\mathbf{X}^\dagger$. However, in most cases the dimension of the data is too large for $\mathbf{A}$ to be computed explicitly. The DMD algorithm overcomes this by the projection of $\mathbf{A}$ onto a reduced-dimension basis, typically the r dominant left singular vectors of the data matrix $\mathbf{X}$ (the first r POD modes).

The eigenvectors of $\mathbf{A}$ are the directions along which the state evolves, which can be interpreted as coherent spatial structures (DMD modes) and the eigenvalues represent the temporal growth rates and frequencies along these directions (DMD eigenvalues). These are calculated from the projected operator $\tilde{\mathbf{A}}$. The **exact DMD** algorithm [148] is summarised as follows:

$$\begin{aligned} &\mathbf{X} = \mathbf{U}\mathbf{\Sigma}\mathbf{V}^{\mathrm{T}} \quad \mathbf{Y} = \mathbf{A}\mathbf{U}\mathbf{\Sigma}\mathbf{V}^{\mathrm{T}} \\ &\tilde{\mathbf{A}} = \mathbf{U}_r^{\mathrm{T}}\mathbf{A}\mathbf{U}_r = \mathbf{U}_r^{\mathrm{T}}\mathbf{Y}\mathbf{V}_r\mathbf{\Sigma}_r^{-1} \\ &\tilde{\mathbf{A}}\mathbf{\Psi} = \mathbf{\Psi}\mathbf{\Lambda} \\ &\mathbf{\Phi} = \mathbf{Y}\mathbf{V}\mathbf{\Sigma}^{-1}\mathbf{\Psi} \end{aligned} \tag{2.38}$$

where $\mathbf{\Phi}$ and $\mathbf{\Lambda}$ are the first r DMD modes and nonzero eigenvalues, respectively.

The DMD algorithm was originally designed to be applied to a single time series of data. However, under the exact DMD definition, the data snapshots are required only to be ordered into pairs. Applying the DMD to snapshot pairs from multiple system realisations, discussed by Tu et al. [148] can be used as a means of averaging multiple experimental trajectories to reduce the effect of noise on the DMD operator fit.

DMD suffers from several drawbacks, including:

- Standard DMD does not allow for control inputs, a limitation which is overcome by DMD with control (DMDc) [149]. DMDc by default also provides a reduced order model of the form $\tilde{\mathbf{x}}_{k+1} = \tilde{\mathbf{A}}\tilde{\mathbf{x}}_k + \tilde{\mathbf{B}}u_k$, where $\tilde{\mathbf{x}}$ are the temporal coefficients of the POD modes used for projection.
- The best-fit linear approximation means that future state prediction is likely to be inaccurate for anything but short times.

- The DMD is only able to capture dynamics which are represented by the reduced-order basis projected onto. As discussed in relation to POD, the basis set most optimal from an energetic perspective is not necessarily optimal for representing dynamics of interest.
- DMD is appropriate for slightly nonlinear systems, but the linear propagator model is not well suited to highly nonlinear system.

Prediction using DMD modes

DMD assumes that there is a linear operator $\mathbf{A}$ which advances measurements at one time step to the next, $\mathbf{x}_{k+1} = \mathbf{A}\mathbf{x}_k$. The DMD modes $\boldsymbol{\phi}_j$ are the eigenvectors of $\mathbf{A}$ and corresponding eigenvalues $\lambda_j = e^{(\sigma_j + i\omega_j)}$ give the temporal behaviour. The flowfield can then be reconstructed approximately as

$$\mathbf{x}_k = \boldsymbol{\Phi}\boldsymbol{\Lambda}^k\mathbf{b}, \quad \mathbf{b} = \boldsymbol{\Phi}\backslash\mathbf{x}(0) \tag{2.39}$$

or in summation form

$$\mathbf{x}_k = \sum_{j=1}^{r} b_j \boldsymbol{\phi}_j \lambda_j^k \tag{2.40}$$

where b_j is the contribution from each mode to the initial state vector $\mathbf{x}(0)$. The amplitudes $\mathbf{b}$ can alternatively be calculated so that the DMD approximation expresses the data optimally for the number of modes kept [150].

That the DMD modes contain individual dynamics and represent a linear approximation of the system may be a significant advantage compared to the POD, both for modelling/control and the identification of coherent structures in cases like the BFS flow where there is a fairly consistent relationship between vortex scale and frequency. However, whether the DMD (or the POD) are practically useful for future state prediction and feedback control of fluid flows is somewhat dependent on the flow of interest. In particular, the least-squares regression fit in the DMD results in modes representing dynamics with phase drift having large decay rates and therefore little influence in the reduced order model/prediction. The DMD, and to some extent reduced order modelling in general, is

more likely to be suitable for prediction/control of flows where the dominant structures are large and have consistent phase (e.g. cylinder shedding), or where the aims of control can be quantified by a slow varying bulk effect (e.g. reattachment length, quasi-steady drag reduction). The compactness of the DMD model also depends on the variables used and the optimality of the projection basis (the POD modes) for representing the important behaviour. For example, turbulence energy does not always correlate with force/pressure, but can account for a large proportion of the velocity field variance, so the leading POD modes may not be the most important to the control aim and a greater number of modes will need to be kept. Regardless of its suitability for feedback control, DMD is a valuable tool for the identification and analysis of flow dynamics.

2.7 Closed-loop Control of Separated Flows

A number of studies have investigated feedback control of separated flows, typically with the aim of reducing reattachment length/recirculation bubble size, or suppressing velocity/pressure fluctuations. Both classical and novel control methodologies have been used, although relatively few studies have reported the closed loop bandwidth achieved and flow configurations often differ, therefore is it difficult to make direct comparisons.

2.7.1 Model-based Approaches

Morioka & Honami [108] investigated the control of reattachment length behind a BFS actuated by vortex generating jets just upstream of separation. Closed-loop control was accomplished by a PI controller with wall pressure measurement in the reattachment zone as feedback, which achieved a closed-loop response time of the order of 0.1 s at $Re_h = 27000$ ($St_h \approx 0.04$).

Henning & King [114] used a robust $\mathcal{H}_\infty$ controller to control the spanwise variable reattachment length downstream of a backward-facing step actuated by an array of amplitude modulated internal oscillators at the step edge. The location of maximum RMS pressure fluctuation measured by four streamwise arrays of microphones embedded in the wall at different spanwise positions were used for feedback, as a proxy for reattachment length. A closed-loop bandwidth of approximately 0.1 Hz at $Re_h = 25000$ ($St_h \approx 1.2 \times 10^{-4}$)

was achieved, however this was limited by the RMS window length of 1.5 s. In a separate study, Becker, Garwon, & King [151] showed that the response time could be reduced by around one magnitude by sensing reattachment length via a model based sensor making use of the pressure signals of passing vortices instead of using RMS wall pressures. A step response time of the order of 0.5 s was achieved at $Re_h = 4000$ using the model based sensor, corresponding to $St_h \approx 0.01$. In comparison, the moving-window RMS sensor with window length 3 s achieved a step response around $St_h \approx 0.002$ at $Re_h = 4000$.

Marrot et al. [48] used an array of internal oscillators on the vertical face of a backward-facing step to counteract the disturbance from acoustic forcing by downstream loudspeakers. The control loop used an adaptive recursive least-mean-squares algorithm applied to the signal from either a microphone or a hot-wire probe in the shear layer downstream of separation. It was found that the control was ineffective for the natural flow due to lack of coherence, but was able to damp the effects of the acoustic disturbance, both when the disturbance was periodic and when it was coupled to the hot-wire measurement to model the effects of combustion instabilities.

Morgans et al. [152] investigated the closed-loop control of the wake behind a backward-facing step at Reynolds numbers based on momentum thickness from 280 to 3000. Actuation was provided by oscillatory blowing/suction through a 45° angled slot at the step edge (equivalent to the standard internal oscillator), and the fluctuating component of base pressure was used as feedback. The premise of the control strategy used was that decreasing base pressure fluctuations leads to an increase in mean base pressure. The authors found that linear second or third order state-space models provided a good fit to identified system dynamics, and controllers were designed using $\mathcal{H}_\infty$ loop-shaping to achieve a sensitivity magnitude smaller than unity over the dominant frequency range of the Kelvin-Helmholtz instability. The controller succeeded in suppressing the KH instability and vortical structures in the initial stages of the shear layer at all Reynolds numbers, resulting in an elongated separation bubble and increased base pressure, although was significantly more effective for laminar flow.

Nicholls and Bacic [131] controlled the switching of a bi-stable fluidic diverter with piezoelectric internal oscillators embedded in the sides of the device. The actuators were amplitude modulated and the total pressure in the initially unattached side channel was used

as feedback measurement. The device was modelled by a Hammerstein model, in which non-linear behaviour is incorporated into a static non-linearity at the input, followed by linear plant dynamics. Closed-loop control was achieved by an LQG controller, which was effective at tracking desired total pressure in the side channel and rejecting disturbances. A closed-loop bandwidth of approximately $St_{D_\mathrm{h}} \approx 1 \times 10^{-3}$ was achieved, where D_h is the hydraulic diameter of the jet entering the device.

Raibaudo & Kerhervé [153] investigated the use of PI, LQR, LQG, and $\mathcal{H}_\infty$ controllers for the control of separated flow behind a backward-facing ramp in a diverging channel. Actuation was achieved by modulating the duty cycle of a spanwise array of burst modulated co-rotating vortex generating jets just upstream of separation, with measurements from hot film sensors positioned on the ramp as feedback. The authors found that a first order model with delay was a good fit to the experimental response, and a Kalman filter could be used to obtain a real time estimate of separation length from the hot film sensor measurements. All four controllers were effective at reference tracking, however the $\mathcal{H}_\infty$ controller demonstrated the fastest response time and improved disturbance rejection compared to the other controllers, and was able to maintain the flow in the attached state despite large disturbances and sensor noise. Non-dimensional step response times, tU_∞/h, were 28.1 for the PI and LQG controllers, and 15.5 for the $\mathcal{H}_\infty$ controller.

Deem et al. [154] used Online-DMD for adaptive closed-loop control of laminar separated boundary-layer on a canonical flat plate model with an imposed adverse pressure gradient, at Reynolds numbers from 9×10^4 to 1.25×10^5. It was concluded that a reduced order model constructed using data of the autonomous flow was no longer valid when control was applied. To overcome this, online DMDc was used on an array of 13 flush-mounted unsteady pressure sensors (microphones) to construct a time-varying estimate of the dynamics. Control was achieved by a burst modulated synthetic jet located upstream of separation on the upper surface of the plate. Adaptive feedback control was implemented by recursively computing LQR feedback gains based on the current online DMD estimate. The control was robust to varying flow conditions and required approximately 30% less actuation authority than non-adaptive control for similar reductions in separation bubble size. The control consistently reduced or eliminated separation in under 10 characteristic periods of the shear layer vortex shedding.

Fonzi et al. [155] implemented an algebraic DMDc model into an model predictive control (MPC) framework for gust-load alleviation and lift tracking of a flexible wing across multiple operating conditions. An interpolation between the states calculated by several reduced order models (ROMs), each determined at a different freestream velocity, was used to account for non-linearities of the system with freestream velocity. The interpolated ROM agreed very well with full order numerical simulations, with errors below 2% for lift and drag and below 5% for moments across a range of conditions, and MPC was effective at alleviating gust-induced wing load.

2.7.2 Model-free Approaches

Model-free control seeks to minimise a cost function based on system perturbations and local response, without involving or producing a model of the system. The most commonly used model-free approaches are extremum-seeking and slope-seeking control [156], which seek local maximum and specific slope of an objective function, respectively, under the assumption of a static input-output mapping. Model-free control is an attractive option for complex flow control problems where representative dynamical models are not necessarily easy to identify or where limited data are available, although these methods may be slow to respond due to repeatedly perturbing the system and waiting for feedback to determine which direction the input should move.

Examples include using extremum-seeking control to reduce the effects of separation over a backwards facing step and in a diffuser [157], and slope-seeking control to increase base pressure on a bluff body, noise reduction in turbomachines and the prevention of separation over a high-lift wing flap [158]. Slope-seeking control combined with an extended Kalman filter has also shown to be effective for controlling axial compressor stall with tip blowing [159].

Gautier & Aider [21] used a gradient descent algorithm on the recirculation area behind a BFS to control the amplitude of a wall-normal jet just upstream of separation. The controller was able to arrive at the most effective actuation amplitude automatically, although the authors did not demonstrate its ability to track a reference or reject disturbances.

Garwon et al. [157] used an extremum-seeking controller to determine the optimal periodic excitation frequency in a BFS flow with actuation by an internal oscillator at the step

edge, while the amplitude was determined by an adaptive integral controller. The coupled controller was able to track a reference (the location of maximum RMS wall pressure fluctuation) and reject disturbances while minimising actuation amplitude. However, the transient time of the extremum-seeking controller was long.

For flows dominated by unsteady vortex shedding (for example bluff bodies at low Reynolds numbers) it has been shown that very simple control schemes intended to oppose the natural shedding can be effective. Both Ffowcs Williams & Zhao [160] and Roussopoulos [161] were able to suppress the shedding behind circular cylinders at low Reynolds numbers by external acoustic actuation fed with the phase shifted signal measured by a hot-wire probe in the cylinder wake.

Chapter 3

Experimental and Numerical Setup

3.1 Experimental Setup

The experimental rig, shown in Figure 3.1, consists of a large cylindrical plenum, a bell-mouth/coupling section, an acrylic test section, and a two axis traverse able to position a total pressure/hot-wire probe inside the test section, as illustrated by the simplified schematic shown in figure 3.2. Air is supplied to the plenum by a centrifugal blower controlled via a variable frequency inverter driver.

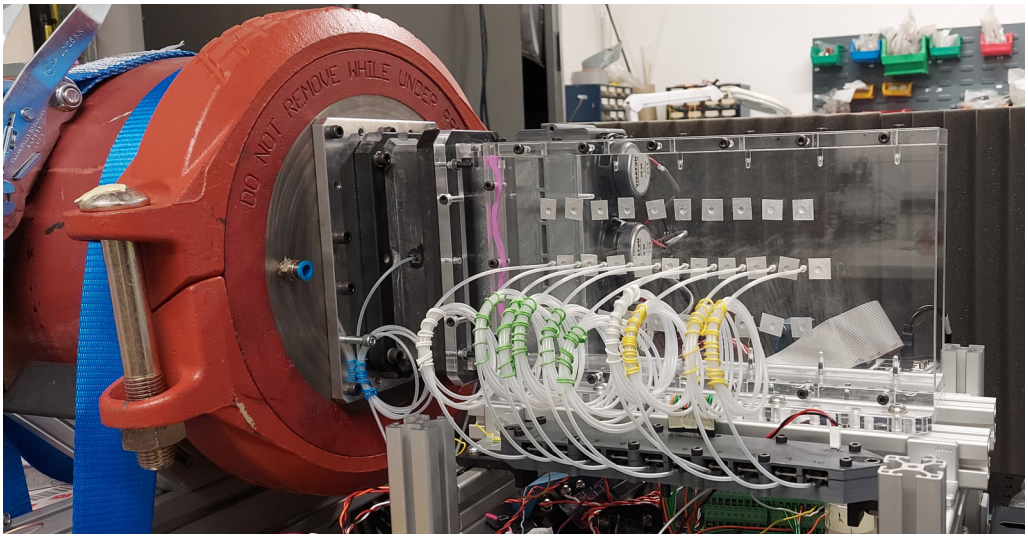


Figure 3.1: Experimental rig

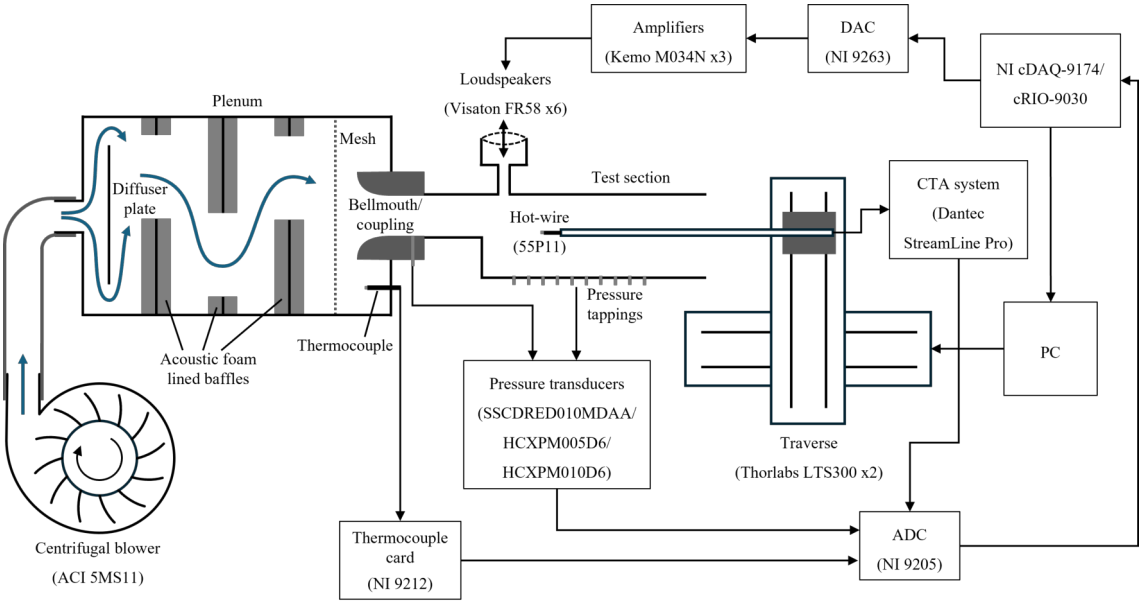


Figure 3.2: Schematic of experimental setup

The plenum is approximately 600 mm long by 300 mm in diameter, with internals consisting of a 250 mm diameter diffusing plate followed by three baffle plates lined with 25 mm acoustic foam, a fine wire mesh, and finally a bell-mouth designed to provide the smoothest possible transition to the test section inlet flow given the dimensions of the plenum end plate cut-out. A simplified depiction of the plenum internals is given in Figure 3.3. The plenum internals, designed to slow and smooth the incoming flow, and the large contraction from plenum to test section inlet channel ensure that the inlet flow is well conditioned.

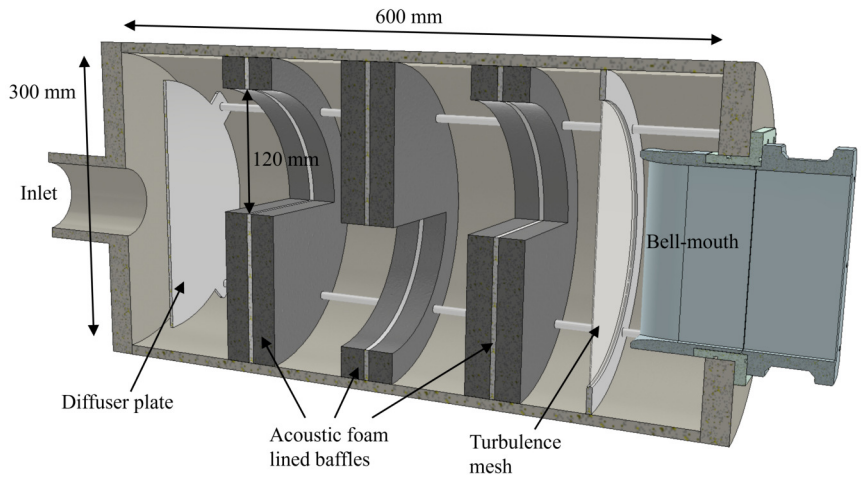


Figure 3.3: Plenum internal assembly

The backward-facing step test section, illustrated in Figure 3.4, has dimensions (summarised in Table 3.1): step height $h = 20\,\text{mm}$, channel height downstream of the step $H = 40\,\text{mm}$, length downstream of step $L = 300\,\text{mm}$, and spanwise width $s = 150\,\text{mm}$. The resulting channel aspect ratio and step expansion ratio are $\text{AR} = s/h = 7.5$ and $\text{ER} = H/h = 2$, respectively.

For aspect ratios below $\text{AR} \approx 10$ the flow at the centre plane is affected by the endwalls [86], therefore cannot be considered 2D, however a much larger aspect ratio is not reasonably achievable using this rig. All positions are given with respect the the origin at the centre-span of the step edge, and x, y, and z-axes being defined as in the streamwise, wall-normal, and spanwise directions respectively, as indicated in Figure 3.4. The test section is oriented physically with the z-axis vertical, so that both the pressure tappings on the step-side wall and acoustic actuator on the opposite-to-step side are easily accessible. Inlet velocity, measured at the centre channel upstream of the step, can be set in the approximate range $v_{\text{in}} = 17\,\text{m}\,\text{s}^{-1}$ to $34\,\text{m}\,\text{s}^{-1}$, corresponding to Reynolds numbers based on step height $Re_h = 21000$ to $Re_h = 42000$ respectively.

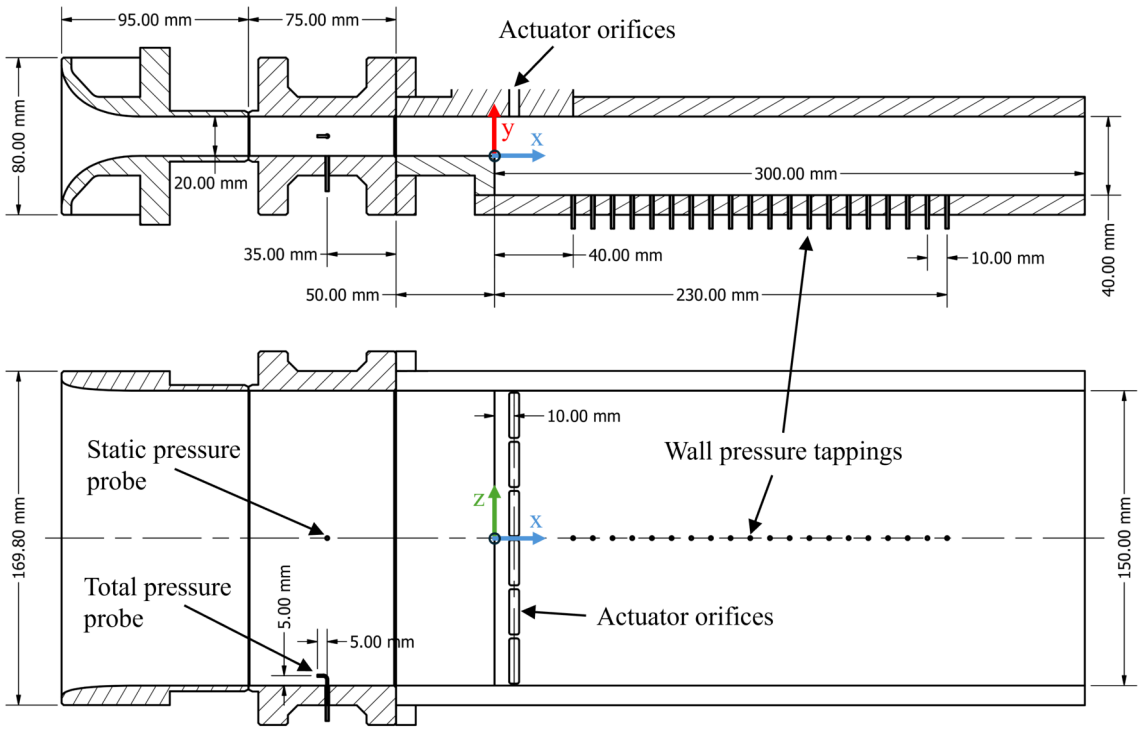


Figure 3.4: Bell mouth/coupling and test section geometry

Abbreviation	Value	Description
h	20 mm	Step height
H	40 mm	Channel height downstream of step
L	300 mm	Length downstream of step
s	150 mm	Spanwise width
AR	7.5	Aspect ratio (s/h)
ER	2	Expansion ratio (H/h)
v_{in}	$\sim$ 17-34 m s^{-1}	Inlet velocity
Re_h	$\sim$ 21000-42000	Reynolds number based on step height

Table 3.1: Backward-facing step test section specifications

Acoustic actuation on the opposite-to-step side was achieved by six 10 W Visaton FR58 4 Ω full range loudspeaker drivers, each mounted to the side of an individual Helmholtz-resonator type cavity with resonance frequency around 300 Hz. The actuation cavities are connected to the test section by a row of 6 rectangular orifices on the side opposite the step, measuring 23 mm by 5 mm with the long axis aligned with the spanwise direction, and centreline 10 mm downstream of the step edge, as illustrated in Figure 3.4.

The Visaton FR 58 transducers are powered by three Kemo M034N power amplifiers with two drivers connected in series to each amplifier. The signal input to the amplifiers is connected via 10 kΩ potentiometers adjusted such that each amplifier has an effective voltage gain of 20.

The traverse consists of two Thorlabs LTS300 translation stages, with maximum movement 300 mm, which can be set up to move in either the horizontal (x-y), or vertical (y-z) planes. Hot-wire velocity measurements were taken using a Dantec 55P11 miniature straight hot-wire probe, with the wire aligned in the z (spanwise) axis, so that x-y plane velocity is measured, connected to a Dantec StreamLine Pro CTA system. Preliminary measurements were also performed with the hot-wire probe rotated 90° so that the measured velocity was in the x-y plane. However, the frequency content of the x-z plane velocity was not discernable different from the x-y plane velocity and it is not possible to extract individual velocity components of unsteady flows using a single wire probe. Measurements were therefore conducted with the single probe orientation only. The hot-wire probe was fixed

into a nominally 6 mm diameter sting to extend the length of the probe and allow the hot-wire to be traversed into the test section. The diameter of the support limits the minimum distance of the hot-wire to the test section walls in flow-normal directions to 3.5 mm.

Pressure tappings were located in the step-side wall from $x = 40\,\text{mm}$ to $x = 230\,\text{mm}$ ($x/h = 2$ to 11.5) downstream of the step, spaced every 10 mm. The number and positions of the tappings connected to transducers depend on the particular measurement set. Pressure measurements were taken with either Honeywell SSCDRRD010MDAA5 $\pm 10\,\text{mbar}$ transducers, or transducers from the Sensortechnics HCX range, as stated in the relevant sections. The accuracy of each pressure transducer is $\pm 0.5\%$ of the full span. The Honeywell transducers were not used for time-resolved pressure measurements, as the 1 kHz internal digital sampling of the acoustic tone caused significant artefacts in the form of a Moiré pattern.

Unless otherwise stated the pressure tappings were connected to transducers via 1 m lengths of semi-flexible 1.5 mm inner diameter nylon tubing. The long tubes act as a second order low-pass filter, which was necessary to avoid saturation of the transducers by the acoustic forcing pressure. The port barbs of the SSCDRRD010MDAA5 transducers are compatible with the 1.5 mm ID tubing and were connected directly, however the larger diameter barbs of the HCX transducers requires the use of an adapter and a short length of $\sim$4 mm ID flexible tubing connected to the transducer, illustrated in Figure 3.5.

Reference total and static pressure measurements were taken in the coupling section upstream of the test section at the locations shown in Figure 3.4. The static pressure probe was embedded in the channel wall at approximate position $(x, y, z) = (-85, 0, 0)\,\text{mm}$ ($(x, y, z)/h = (-4.25, 0, 0)$), while the total pressure probe, a 90° bent 1.2 mm outer diameter steel tube was installed in the lower wall of the coupling section with opening at approximately $(x, y, z) = (-90, 10, -70)\,\text{mm}$ ($(x, y, z)/h = (-4.5, 0.5, -3.5)$). The position of the total pressure probe was chosen to be just outside the boundary layer and the thinnest possible tube was used to minimize the effect of the probe interference on the test section flow. Both upstream probes were connected to pressure transducers by 2 m lengths of semi-flexible 1.5 mm inner diameter nylon tubing.

Traverse measurements were recorded using a National Instruments cDAQ-9174 chassis with a NI 9205 analogue input card, NI 9263 analogue output card, and NI 9212 thermo-

couple card, at a sample rate of 10 kHz unless specified otherwise. System identification and control were performed using an NI CompactRIO-9030 (cRIO) controller with the same set of cards at a sample rate of 4 kHz. The cRIO is comprised of two parts running in parallel: a real-time (RT) processor, and a field programmable gate array (FPGA) for fast execution of smaller tasks and input-output control. Measurement and feedback control is performed by the FPGA, while data processing and logging is performed by the RT module.

The pressure transducers and loudspeaker amplifiers were powered by an RS Pro IPS2303 two channel laboratory power supply.

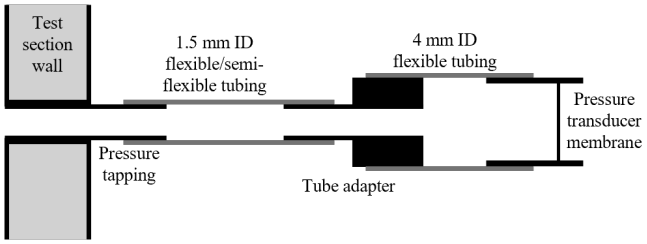


Figure 3.5: Connection of Sensortechnics HCX transducers

3.1.1 Effect of measurement tube length

One of the main challenges of using static pressure measurements as feedback for closed loop control with acoustic forcing is the saturation of pressure transducers by the acoustic pressure. The simplest solution to this problem would be to size up the pressure transducers, however this was not done for two reasons: first, that the larger span transducers do not provide sufficient resolution of pressure fluctuations of interest; and secondly, that the acoustic pressures also necessitates the use of double sided transducers capable of measuring negative pressures, which were not available with a span greater than ± 10 mbar. Therefore, some method of attenuating the acoustic pressure prior to measurement by the transducers was required, for which the simplest and most effective approach was to exploit the low-pass filtering effect of the tubes used to connect the transducers to pressure tappings.

In the case where wavelength is much greater than the cross sectional dimension of a tube, the acoustic behaviour is analogous to an electrical transmission line with equivalent capacitance C_a, inductance L_a, and resistance R_a given by [162]:

$$C_{\mathrm{a}} = \frac{A}{\rho c^2} l, \quad L_{\mathrm{a}} = \frac{\rho}{A} l, \quad \text{and,} \quad R_{\mathrm{a}} = \frac{P\sqrt{2\mu\rho\omega}}{2A^2}\left(1 + \frac{\gamma - 1}{\sqrt{Pr}}\right) l \tag{3.1}$$

where A is the cross sectional area, P is the perimeter, ρ is air density, c is the speed of sound, μ is the dynamic viscosity of air, ω is angular frequency, γ is the adiabatic index of air (taken to be $\gamma = 1.4$), Pr is the Prandtl number (taken as $Pr = 0.71$), and l is the length of the tube. All properties are evaluated at standard atmospheric pressure, 101 325 Pa, and 30 °C (the approximate air temperature measured inside the plenum during experiments). The transfer function of the equivalent transmission line model, is then:

$$G_{\mathrm{TL}}(j\omega) = \frac{1}{1 + R_{\mathrm{a}} C_{\mathrm{a}} j\omega + L_{\mathrm{a}} C_{\mathrm{a}} (j\omega)^2} \tag{3.2}$$

which for a 1 m long tube of diameter 1.5 mm, gives resonant frequency 48.7 Hz, −3 dB cut-off 78.5 Hz, and attenuation at the actuation frequency (300 Hz) 29 dB.

3.1.2 Acoustic Actuator Design

In 1986 Bhattacharjee et al. [69] demonstrated the effective control of a backward-facing step flow by acoustic actuation from the opposite-to-step side, but this configuration has hardly been investigated since, with the literature instead favouring actuation at or close to the edge of the step. The site of forcing is an issue of receptivity, so the logical choice for actuation location is at the step edge, where the velocity gradient is maximum and velocity changes due to forcing are most likely to occur. However, external acoustic forcing has been demonstrated to achieve a reasonable effect without being localised to the separation point by coupling to the larger scale vortex structures in separated shear layer flows [70, 48, 59, 130]. Although local forcing of the boundary/shear layer at or just before separation by velocity perturbations (oscillating blowing/suction, vortex generating jets, DBD actuators etc.) has undoubtedly been shown to be effective, and may in many cases be the best choice, there are several potential benefits of opposite-side acoustic actuation:

- **Packaging/maintenance** - Highly curved diffusing ducts in a real engine may be oriented such that the separated side is less accessible than the attached flow side. Having the actuation equipment installed on the attached side would reduce down

time and maintenance cost.

- **Fouling** - In comparison with synthetic jet or oscillating blowing/suction style actuators, which typically require thin orifices to achieve reasonable jet velocities, acoustic actuators can be designed with orifices of significantly larger cross sectional area or none at all, reducing the relative effects of fouling and minimising the likelihood of blockage.

- **Insensitivity to separation point** - While the backward-facing step geometry in this study has fixed separation at the step edge, for ducts/diffusers with adverse pressure gradient driven separation the effectiveness of local actuation on the separating side may depend on position relative to the separation point. However, this is not the case for acoustic actuation, which has been shown to be effective even when the actuator is placed far from the separated shear layer [69, 48].

Recently, work undertaken at the Oxford Thermofluids Institute by Mair [59, 58] and Nicholls [57] has demonstrated that acoustic actuation from the side opposite to reattachment can be effective at controlling reattaching jets in fluidic devices. Switching of a bistable device with opposite-side actuation was achieved with an amplitude reduction up to 90% compared to the amplitude needed to initiate switching from inside the recirculation bubble. The observations in this work provide a secondary motivation for studying the backward-facing step flow with acoustic excitation, given the similar physics of reattaching jets and shear layers.

Visaton FR 58 transducers were chosen due to their compact size and flat frequency response, shown in Figure 3.6, however a limitation of smaller size dynamic drivers is the inability to reproduce low frequencies, in this case the FR 58 has a resonant frequency of 190 Hz, below which the response rolls off.

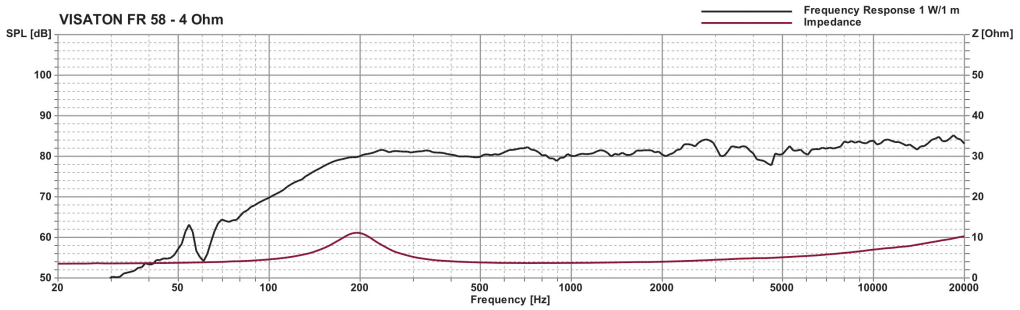
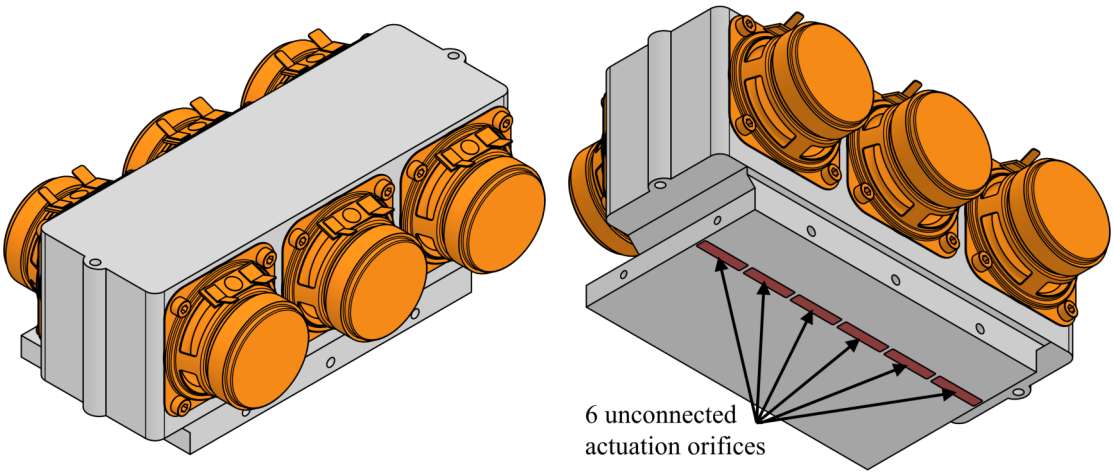


Figure 3.6: Frequency response of Visaton FR 58 4 Ω full range loudspeaker, copied with permission from VISATON GmbH & Co. KG [163].

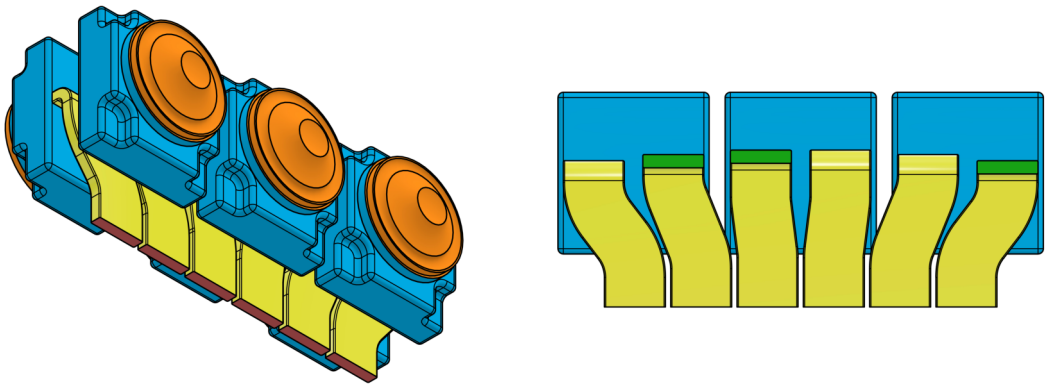
Figure 3.7a shows the acoustic actuator assembly, consisting of a 3D-printed (FDM) cavity/neck part printed in tough PLA and 6 Visaton FR58 4 Ω transducers. The internal volumes of the actuation cavities are shown in Figure 3.7b, colour coded for clarity. Each transducer is mounted on the side of an individual cavity which is connected to the test section via a neck with constant cross sectional area 23 by 5 mm. The cavity volume and neck length were chosen such that the theoretical Helmholtz resonance is approximately 260 Hz, which was identified as the most effective actuation frequency in preliminary experiments with simple funnel-shaped actuator cavities [164]. The Helmholtz resonance is given by

$$f_{\mathrm{H}} = \frac{c}{2\pi}\sqrt{\frac{A}{V_0 L_{\mathrm{eq}}}}, \tag{3.3}$$

where c is the speed of sound, A is the cross sectional area of the neck, V_0 is static cavity volume, and $L_{\mathrm{eq}} = L_{\mathrm{n}} + 0.3D_{\mathrm{h}}$ is the equivalent length of the neck with end correction, equal to the neck length, L_{n}, plus the hydraulic diameter of the opening, D_{h}. The exact geometry was then determined by the physical sizes of the transducers and test section, resulting in two rows of three cavity volumes and curved necks connecting the actuation orifices to cavities on alternating sides.



(a) Actuator assembly



(b) Internal volume

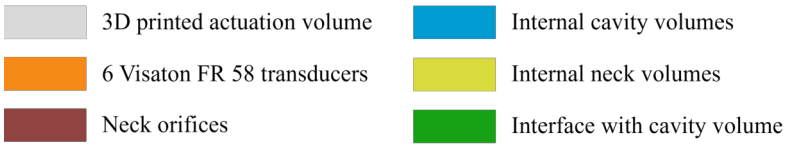


Figure 3.7: Acoustic actuator assembly and internal cavity volumes

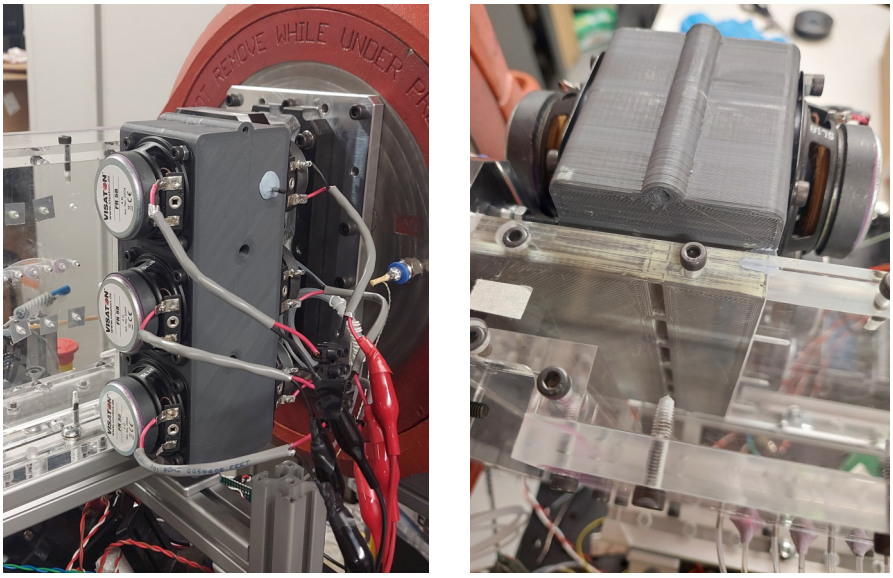


Figure 3.8: Acoustic actuator assembly installation

3.2 Characterisation of Acoustic Actuation

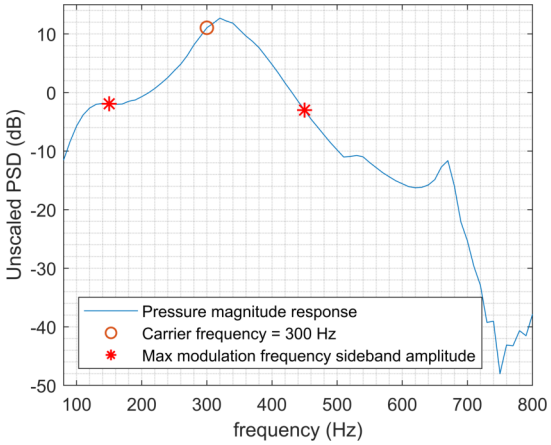
While the calculated resonance frequency of the cavities would be expected to be accurate in the case of a rigid walled cavity with the orifices exiting into free air, in practice the observed resonant frequency of the acoustic actuator assemblies will depend also on the mechanical and electrical properties of the transducers, and the test section geometry.

The acoustic response of the actuator-test section system was characterised with no flow through the test section by performing a sweep of frequencies from 80 Hz to 800 Hz with 10 Hz spacing and input voltage amplitude 0.1 V to the amplifiers (2 V to the loudspeakers), for a measurement time of 2 s per frequency. Pressure measurements were taken with a Kulite XCQ-062 series transducer embedded in the step-side wall of the test section at $x = 100$ mm, recorded at a sampling frequency of 10 kHz. The Kulite transducer was used for this characterisation as it has a large span and also high resolution, allowing the acoustic response to be evaluated without needing to correct for the measurement tube response, but was not available for any of the other experiments presented in this thesis. Figure 3.9a shows the measured frequency response of the actuator-test section system, which has resonant frequency ∼320 Hz and a Q-factor of approximately 4.4.

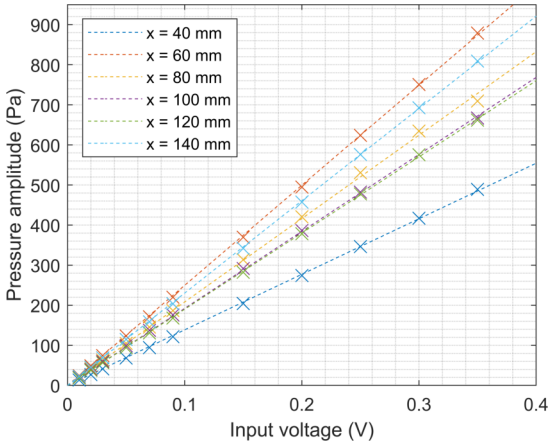
The actuation carrier frequency, f_c, was chosen to be 300 Hz as this is both approximately the frequency of the strongest vortex mode seen in the natural (unforced) flow at 20 m s^{-1}

inlet velocity, and the dominant acoustic resonance of the test section, along with being close to the maximum volume response of the actuator.

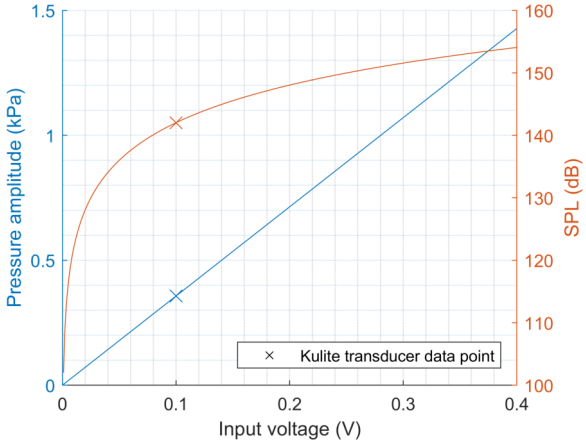
The linearity of volume response with input voltage was confirmed by performing a sweep of input voltage amplitudes from 0.01 V to 0.35 V at 300 Hz, and measuring the wall pressure amplitudes from $x = 40$ mm to 140 mm, spaced every 20 mm, shown in Figure 3.9b. The HCX transducers with 1 m long measurement tubes were used for these measurements, therefore while Figure 3.9b does demonstrate linearity, the pressure amplitudes shown are significantly lower than the actual acoustic pressures in the test section. The relative slopes of pressure amplitude against voltage for each transducer/position are also not necessarily representative of the spatial distribution of acoustic amplitude, as slight differences in the measurement connections of each transducer result in unequal attenuation. The Kulite transducer measurement on the step side wall at $x/h = 5$ was used to calculate the slope of pressure amplitude against input voltage as 3.5695×10^3 Pa/V at $f_c = 300$ Hz. The corresponding sound pressure level (SPL) at $x/h = 5$, based on a reference pressure of 20 µPa, is shown in Figure 3.9c.



(a) Acoustic pressure frequency response (Kulite XCQ-062 transducer)



(b) Acoustic pressure amplitude with voltage at $f_c = 300\,\text{Hz}$ (Sensortechnics HCX transducers)



(c) Sound pressure level with voltage at $f_c = 300\,\text{Hz}$

Figure 3.9: Actuator response

3.3 Numerical Setup

CFD simulations were performed using the commercial CFD solver ANSYS CFX 2021 R2 and run on the University of Oxford Advanced Research Computing (ARC) facility [165]. The motivation for conducting numerical simulations was to provide a qualitative view of the flow dynamics which are not well resolved by the available experimental measurements, particularly the large scale coherent structures and how they are affected by the acoustic excitation.

Preliminary simulations indicated that it is necessary to use a scale resolving model [166] to

capture vortex-roll up and merging in the shear layer, and hence the effects of actuation. Four turbulence treatments were initially tested: The k-ω shear stress transport model (SST); Wall modelled large eddy simulation (WMLES); Stress blended eddy simulation (SBES); and the laminar solver, i.e. turbulence model free. SST is a Reynolds-averaged Navier-Stokes (RANS) model and does not resolve the shear layer vortices, but provided a reasonable fit to the mean baseline flow and was therefore used to initialise the unsteady simulations using the other three models. The SBES model is a hybrid RANS-LES approach, in which the solver automatically assigns the RANS and LES regions. However, the fit of the preliminary SBES simulations to the experimental velocity profiles was unsatisfactory. The decision to use the laminar solver was initially made with the hope that it would provide some insight into the damping effect of turbulence, however the solution was found to be a surprisingly good match to the experimental data, and differed only slightly from the WMLES solution, with the turbulence model-free solution appearing to be a slightly better match to experimental velocity measurements. It should be noted that although the laminar solver directly solves the Navier-Stokes equations without any turbulence model, the current approach should not be classified as direct numerical simulation as the grid and timescale requirements to resolve the Kolmogorov micro scales are not met [167].

Only two cases are presented: the baseline flow at $20\,\mathrm{m\,s^{-1}}$ inlet velocity; and forced flow at $20\,\mathrm{m\,s^{-1}}$ inlet velocity with an actuation amplitude very approximately equal to an experimental amplitude of $0.05\,\mathrm{V}$.

3.3.1 Mesh and Boundary Conditions

Simulations were conducted on a spanwise slice of the test section domain, of width equal to the step height. Although the AR > 10 condition for nominally 2D flow [86] has not been met in the experimental flow, the decision to simulate only the central slice of the domain under the assumption of nominally 2D flow was made to reduce the computational cost of simulation. Although side-wall effects likely account for some of the discrepancy between the simulated and experimental flowfields at the centre of the channel, the numerical study is primarily conducted to better understand the unsteady flow dynamics and mechanism of acoustic control, neither of which are expected to be significantly effected by side-wall

effects for the aspect ratio in question.

A structured hexahedral mesh with 6.5×10^6 elements was used, shown in Figure 3.10, measuring 90 by 100 cells upstream of the step in the x and y directions respectively, and 590 by 200 cells downstream, by 50 cells in the spanwise (z) direction. Grid spacing was defined geometrically to refine the separated shear layer and boundary layer regions. The maximum values of x^+, y^+, and z^+ were approximately 75, 3, and 50, respectively. However, typical values of y^+ and z^+ did not exceed 1 and 20, respectively.

The inlet velocity profile was derived from the k-ω SST solution of a straight rectangular channel flow with uniform inlet velocity. The channel length and inlet velocity were chosen so that the simulated velocity profile approximately matched the experimental inlet velocity profile and momentum thickness. An opening boundary condition was used for the test section exit, a smooth no-slip wall condition was used for the walls, and a periodic condition was set on the spanwise normal sides of the simulation domain to avoid having to capture side-wall effects.

The actuation is modelled as a spatially uniform, temporally sinusoidal, velocity at the end of a short neck of length 5 mm, which preliminary simulations determined was a sufficient representation of the actuator cavities despite the significant simplification. For the baseline simulation the actuator slot boundary was set to a solid wall rather than a velocity condition to prevent entrainment of fluid through the slot. The magnitude of the oscillating velocity was chosen empirically based on preliminary simulations to achieve an upstream shift of the mean wall pressure curve roughly equivalent to the effect of an experimental input amplitude of 0.05 V, and was equal to $3\,\mathrm{m\,s^{-1}}$.

A high resolution advection scheme and second order backwards Euler transient scheme were used. A time step of 5×10^{-5} s was chosen, with seven inner iterations per step, and results were saved every fifth timestep, giving 66.6 simulation timesteps and 13.3 saved samples per actuation period.

The unsteady simulations were initialised from a well converged steady k-ω SST solution. Both baseline and actuation simulations were run for an initial time of 0.1 s to allow the flow to develop/settle, before being recorded for 0.25 s each, which was long enough for the mean velocity at several query points to be well converged.



Figure 3.10: CFD mesh side profile

3.3.2 Comparison of Laminar Simulation to URANS

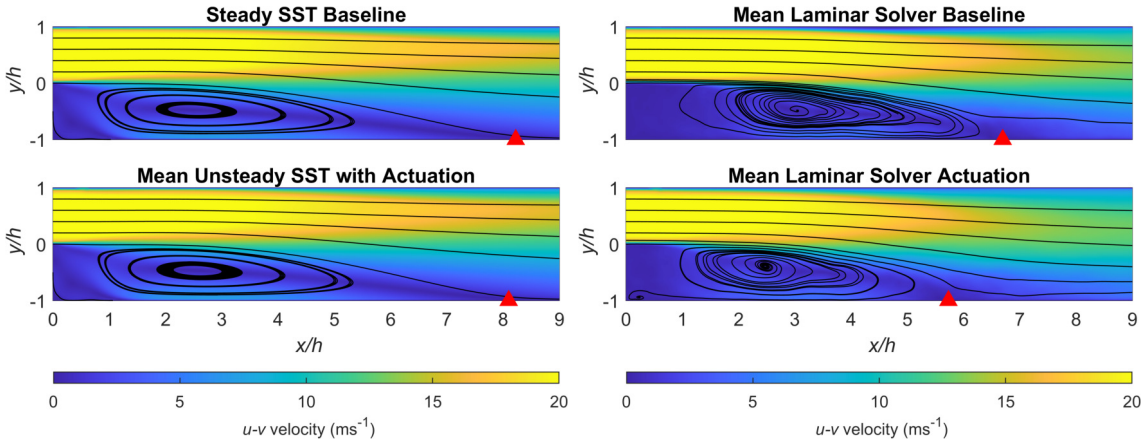
It was briefly mentioned in Section 3.3 that a scale resolving turbulence treatment [166] is necessary to capture the effects of actuation. This is demonstrated in Figures 3.11 and 3.12, which show centre-plane streamline plots of preliminary k-ω SST simulations with and without actuation compared to the laminar simulations. Figure 3.11 shows the time-mean streamlines (or the steady state solution in the case of the baseline SST simulation), while Figures 3.12a and 3.12b show instantaneous streamline plots of the SST and laminar simulations at several phases relative to the excitation signal, respectively.

It is immediately obvious from the streamline plots that unsteady RANS is unsuitable for the current problem. Despite the actuation having a reasonable instantaneous effect on the streamlines and the structure of the recirculation bubble, there is almost no change in the mean reattachment length (actuation causes a reduction of $\sim$2.5 mm or $\sim$1.5%). This is not a particularly surprising result given that periodic excitation affects mean flow by interaction with shear layer vortices, and RANS models do not resolve individual vortices in the BFS flow. In direct comparison, actuation reduces the mean reattachment point in the laminar simulation by 14.4%, from $x_\mathrm{r}/h = 6.70$ to $x_\mathrm{r}/h = 5.73$ (The experimental reattachment length reduction at $v_\mathrm{in} = 20\,\mathrm{m\,s^{-1}}$ and $a = 0.05\,\mathrm{V}$, estimated in Chapter 4, is $\sim$ 14.5%). The instantaneous streamline plots of the laminar solution, displayed in Figure 3.12b also demonstrate that the laminar solver resolves individual shear-layer vortices and vortex merging/breakdown.

The lack of individual vortices and eddies in the unsteady RANS simulation means that an instantaneous reattachment point can be identified, shown in Figure 3.12a. However,

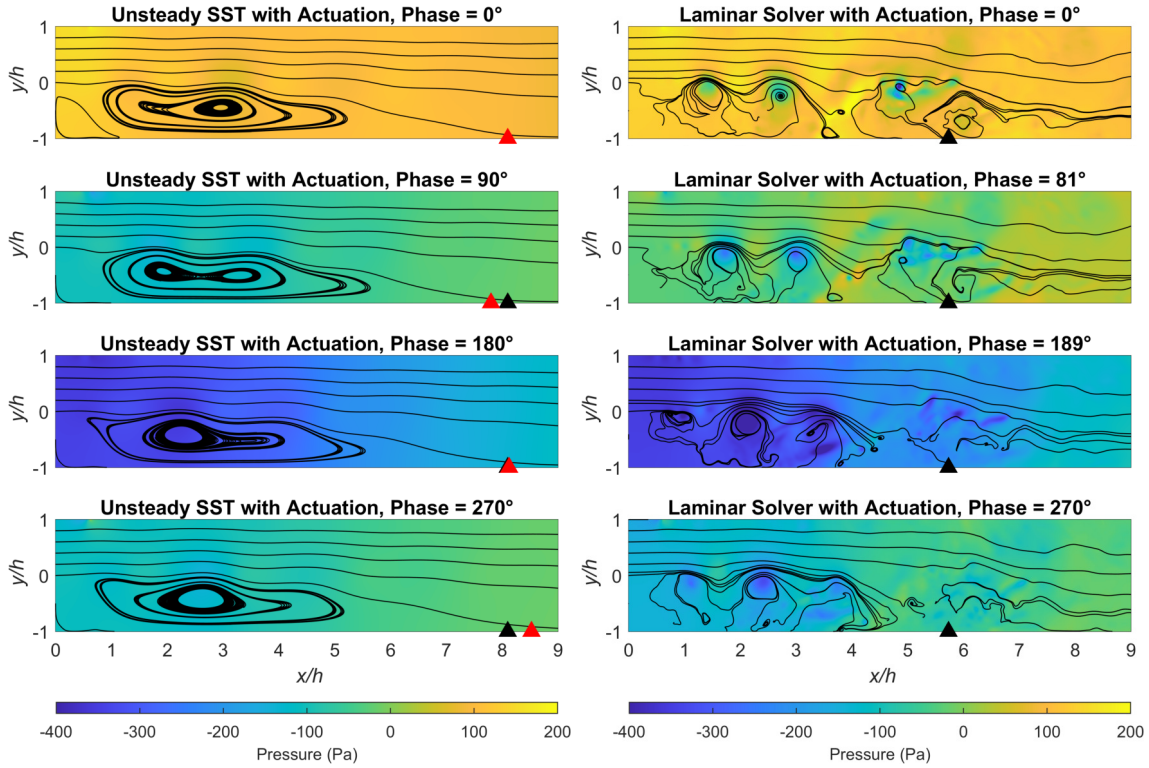
reattachment cannot be defined instantaneously for either the real flow or the laminar simulation, and only exists in an average sense once the individual shear layer vortices and random eddies have been filtered out. For the sake of interest, the phase averaged laminar CFD solution is shown in Figure 3.13. First the pressures and velocities were band-pass filtered by a 4^{th} order zero-phase filter with bandwidth 290 Hz to 310 Hz, then sorted into 10 Hz wide phase bins and the mean calculated for each bin. The vertical 'wiggling' of the 'jet' flow due to the forcing appears to be broadly similar between the URANS and the phase averaged laminar simulations, although where the URANS simulation predicts that the reattachment length drifts back and forth by a small amount at the actuation frequency, the phase averaged reattachment position in the laminar solution is almost stationary.

In summary, unsteady RANS models predict that the acoustic excitation causes the shear layer/streamlines to 'wiggle', but fails to predict the important vortex dynamics and hence the demodulating property of the shear layer, both of which appear to be captured by the laminar solver.



(a) Steady/Mean k-ω SST (b) Mean laminar solution

Figure 3.11: RANS and laminar solver mean streamlines. Red triangles show reattachment points calculated from wall shear stress



(a) k-ω SST streamlines

(b) Laminar streamlines

Figure 3.12: Instantaneous snapshots of unsteady k-ω SST and laminar solutions with actuation. Mean reattachment point shown by black triangles, instantaneous reattachment points shown by red triangles.

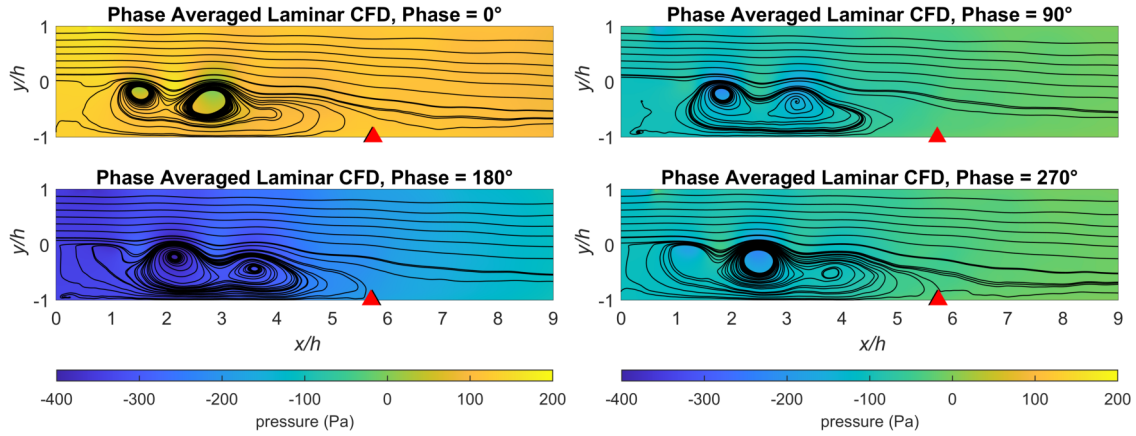


Figure 3.13: Phase averaged laminar simulation streamlines. Mean reattachment point shown by black triangles, phase averaged reattachment points shown by red triangles

3.4 Validation of Numerical Simulations

3.4.1 Mean and RMS Wall Pressure

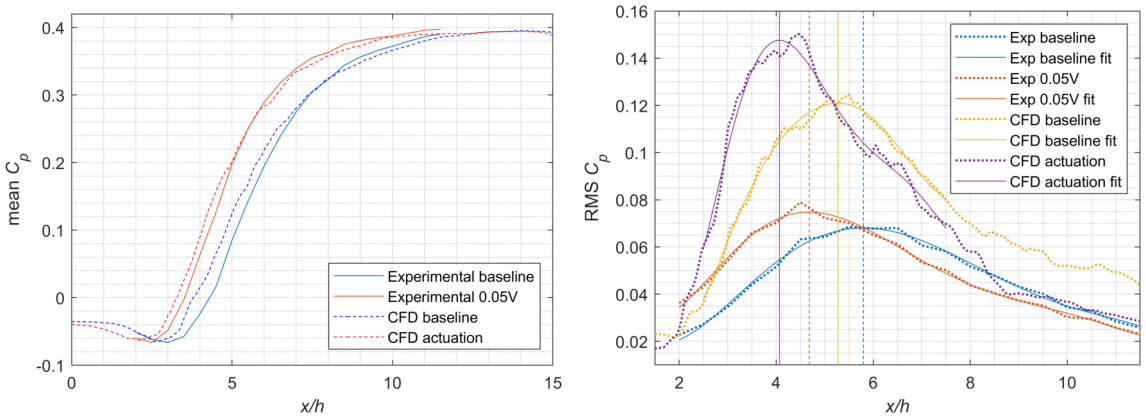
Wall pressure coefficients were calculated for the laminar CFD data based on the velocity and static pressure at the centre of the inlet channel. Figures 3.14a and 3.14b show the mean and RMS wall C_p, respectively, of the CFD cases and experimental baseline and 0.05 V actuation amplitude measurements (detailed in Section 4.2). Prior to calculating the RMS values for the CFD data, the C_p data were filtered equivalently to the experimental wall pressures to remove the actuation tone, first by the theoretical transfer function of the 1 m long measurement tubes, then by a fifth order low pass filter with cut-off frequency 70 Hz to remove the remainder of the acoustic pressure.

The CFD and experimental mean C_p curves agree reasonably well, although the CFD data are offset slightly upstream compared to the experimental data, indicating that the reattachment lengths are slightly shorter. CFD is not expected to perfectly predict reattachment length, especially given the absence of turbulence treatment in the laminar solver, although the effectively infinite span of the numerical domain compared to the relatively low aspect ration of the real flow likely also has some influence.

A similar trend is seen for the RMS C_p distributions, where the CFD and experimental curves have similar shapes with the CFD distributions offset approximately half a step height upstream compared to the experimental data. The correlation of Mabey [168] states that the peak in RMS wall pressure occurs slightly upstream of the reattachment position, hence the approximate equivalence of the CFD actuation amplitude to an experimental amplitude of 0.05 V is demonstrated by the similar distance between the baseline and actuated peak C_p for both CFD and experimental data. The reattachment points of the CFD simulations are calculated from the zero intercept of the wall shear stress, and compared to the position of the peak in RMS C_p, x_{RMS}, in Table 3.2.

Although the shapes are similar, the peak magnitude of CFD RMS wall pressure coefficient is approximately twice that of the experimental data. This is likely due to the lack of turbulence model (therefore lack of eddy viscosity) in the laminar simulations inhibiting the dissipation of energy and resulting in a greater amount of low frequency content compared

to the experimental flow. Despite the discrepancies between experimental data and the numerical simulations, the matching of C_p and RMS C_p distribution shapes indicates that the time mean flow fields and response to actuation are generally similar.



(a) Mean C_p (b) RMS C_p

Figure 3.14: CFD and experimental mean and RMS wall C_p

Case	x_r/h	x_{RMS}/h
Baseline	6.70	5.27
Actuation	5.73	4.07

Table 3.2: CFD reattachment point and max RMS C_p location

3.4.2 Mean and RMS Velocity Field

Figures 3.15 and 3.16 show the laminar CFD and experimental centre plane mean and RMS u-v velocity profiles at several streamwise locations, for the baseline and actuated flows, respectively, plot as velocity coefficient $C_v = v/v_{in}$. The profiles show that the CFD simulations generally agree well with the experimental data. CFD initially underestimates shear layer spreading and the fluctuations in the shear layer for both unforced and forced flow at $x/h = 0.25$, however by $x/h = 2$ for the baseline flow and $x/h = 1.25$ for the forced flow the profiles are a close to exact match. This discrepancy can be explained by the lack of turbulence in the simulated inlet boundary layer. Further downstream, by $x/h = 8.5$, CFD slightly underestimates the mean velocity near to both the step side and attached side-walls, overestimates the RMS velocity near the attached-side wall, and underestimates the RMS

velocity in the centre of the channel. However, overall the laminar CFD and experimental profiles match well and appear to follow similar trends of evolution, providing confidence that the simulated flow field correctly captures the key physical character of the real flow, despite the inaccuracies in the numerical model/setup.

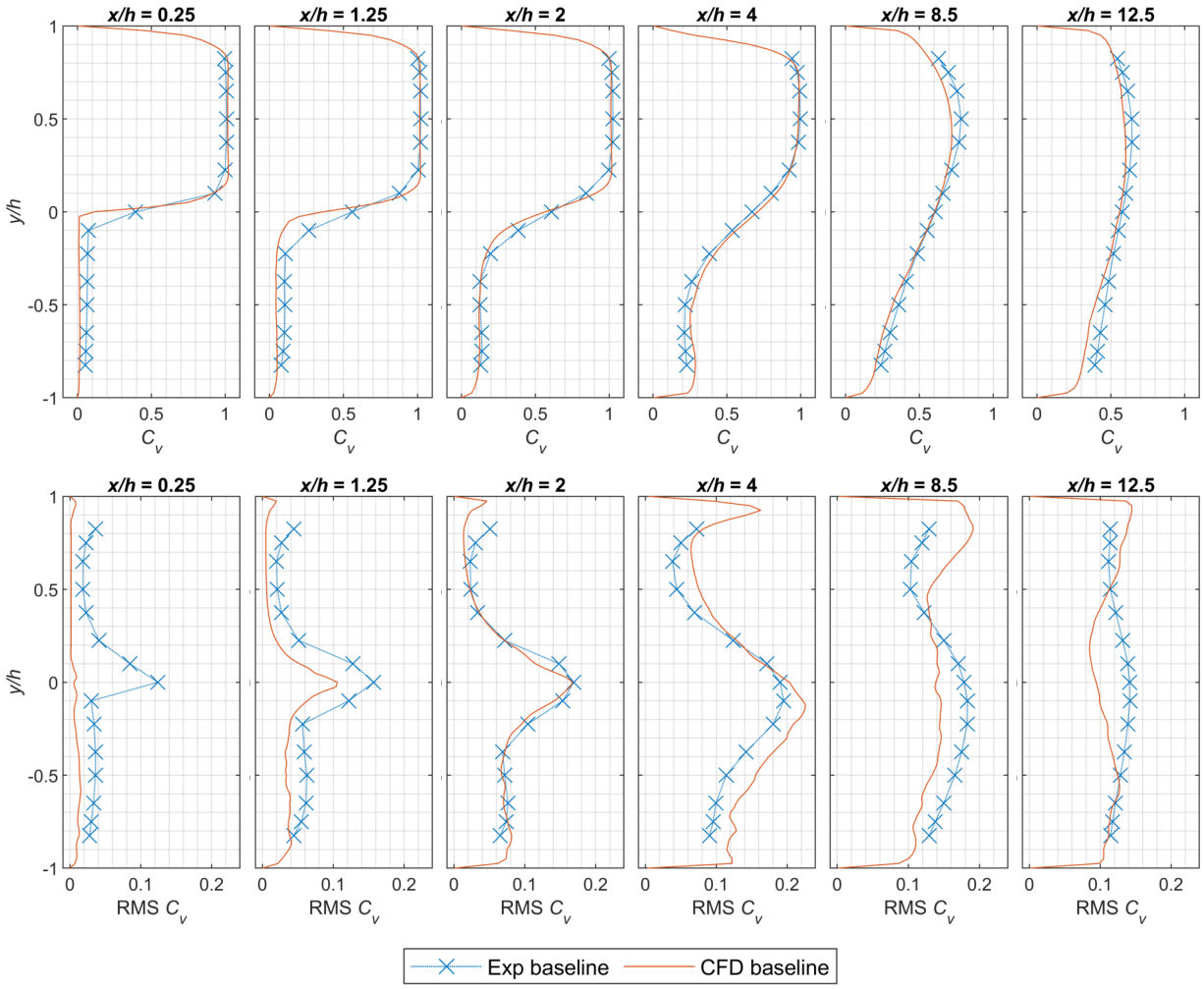


Figure 3.15: Baseline hot-wire and CFD mean and RMS velocity profiles

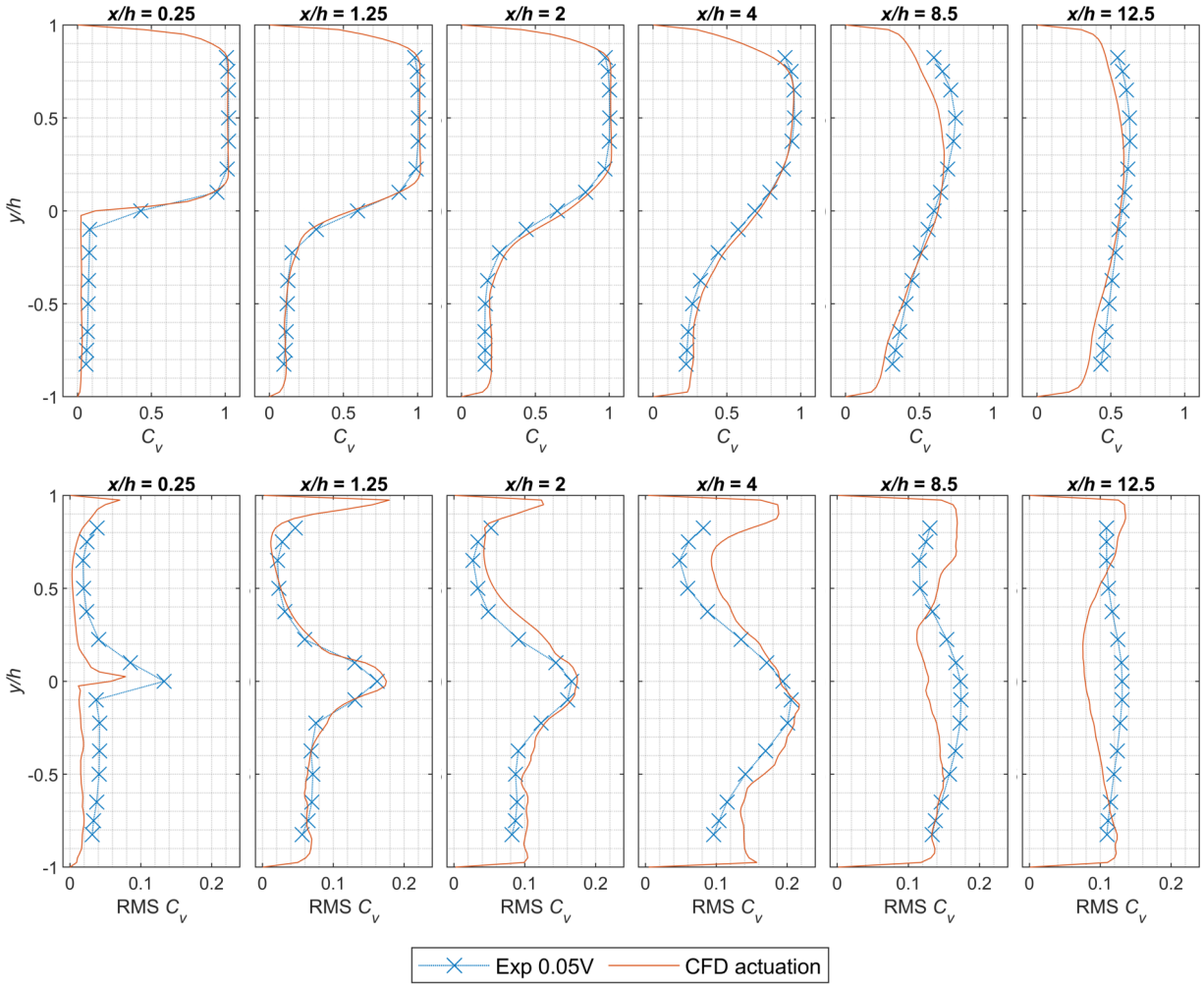


Figure 3.16: Forced hot-wire and CFD mean and RMS velocity profiles

3.4.3 Frequency Spectra

Figure 3.17 shows a comparison of CFD and experimental velocity frequency spectra for both unforced and forced flow at comparison points $(x, y)/h = (1, 0.5)$, $(1.5, 0.25)$, $(3, 0.5)$, and $(5, -0.5)$.

Comparison of the frequency spectra a relatively short distance downstream of separation at $(x, y)/h = (1, 0.5)$ and $(x, y)/h = (1.5, 0.25)$ confirm that the laminar CFD initially underestimates broadband unsteadiness, however the magnitude of content associated with vortex roll-up and merging matches experimental data well for the point close to the shear layer. Unlike the experimental hot-wire measurements, which show a single vortex roll-up/merging peak in the unforced flow that gradually shifts to lower frequencies as streamwise distance from the step increases, the CFD spectra show two distinct (although

not necessarily sharp) peaks, one at half the frequency of the other, implying that pairing is more consistent in the laminar CFD than the experimental flow.

Slightly further downstream at $(x, y)/h = (3, 0.5)$ both magnitude and vortex peaks match reasonably well, although the CFD slightly overestimates low frequency content and the prominence of the vortex pairing peak at the first sub-harmonic of the actuation frequency in the forced case. At $(x, y)/h = (5, -0.5)$, in the shear layer just upstream of reattachment, CFD frequency content agrees well with both the magnitude and decay slope of the hot-wire data, mirroring the particularly good fit of velocity profiles in this range.

3.4.4 Conclusion

In this section a comparison has been made between the numerical simulation results and experimental measurements. In the absence of experimental flow visualisation, the CFD simulations were intended to give a qualitative representation of the formation and evolution of coherent structures in the backward-facing step flow, and how these structures are influenced by acoustic forcing from the opposite side. However, given the seemingly questionable approach of using a laminar solver, it was important to carefully verify the CFD against experimental data.

While there are some discrepancies, primarily the lack of unsteadiness in the shear layer immediately after separation, higher RMS wall C_p magnitude, and shorter reattachment length than the real flow, both the mean flow field and frequency content generally agree well. That the laminar simulations display similar spatial evolution of peaks in frequency content to the real flow, particularly with actuation, is a reasonably convincing justification to use the laminar CFD data to back up conclusions made from the experimental measurements and gain additional insight into the dynamics of the flow.

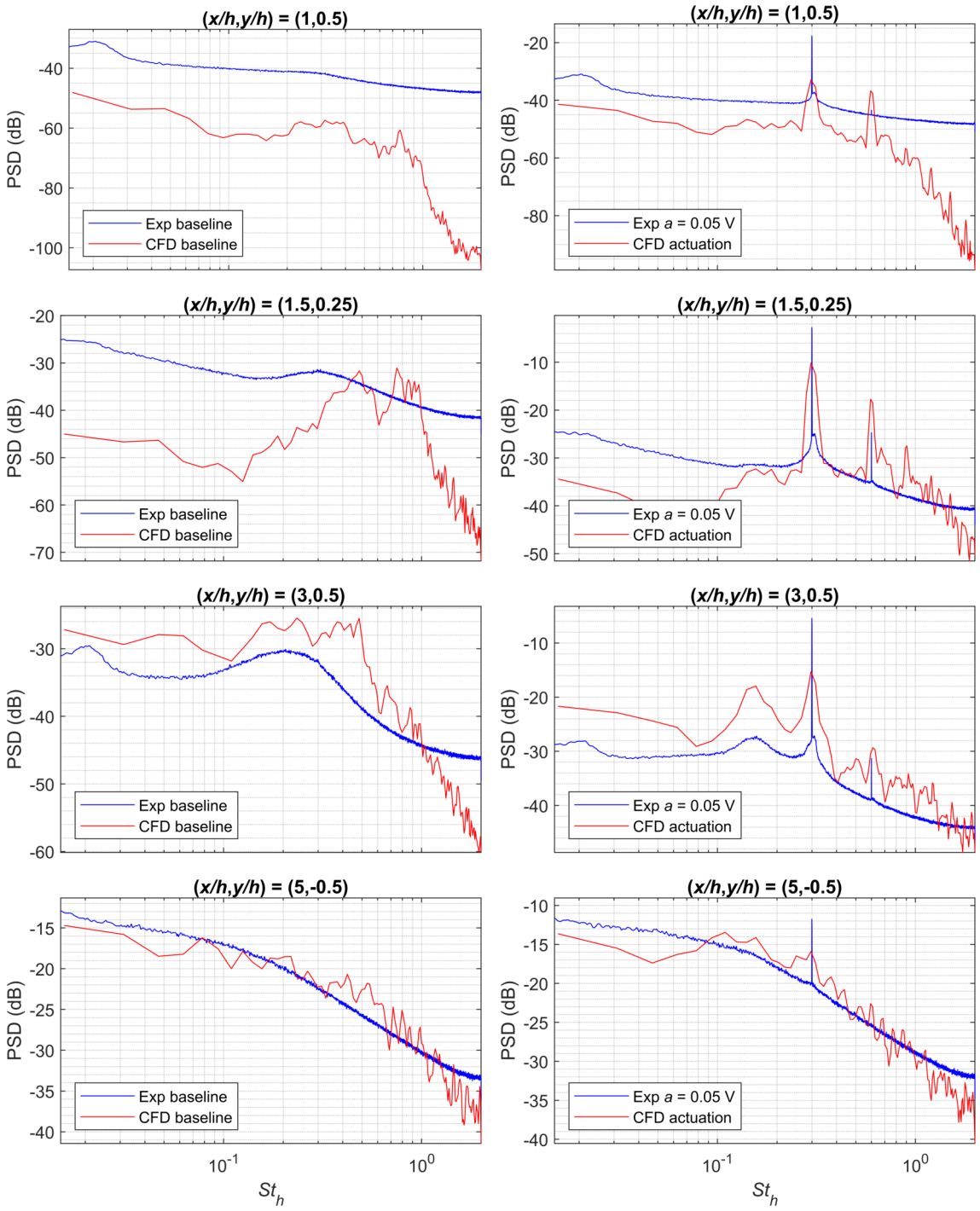


Figure 3.17: Point frequency spectra of CFD u-v velocity compared to experimental hot-wire measurements. Baseline flow on left, actuation on right

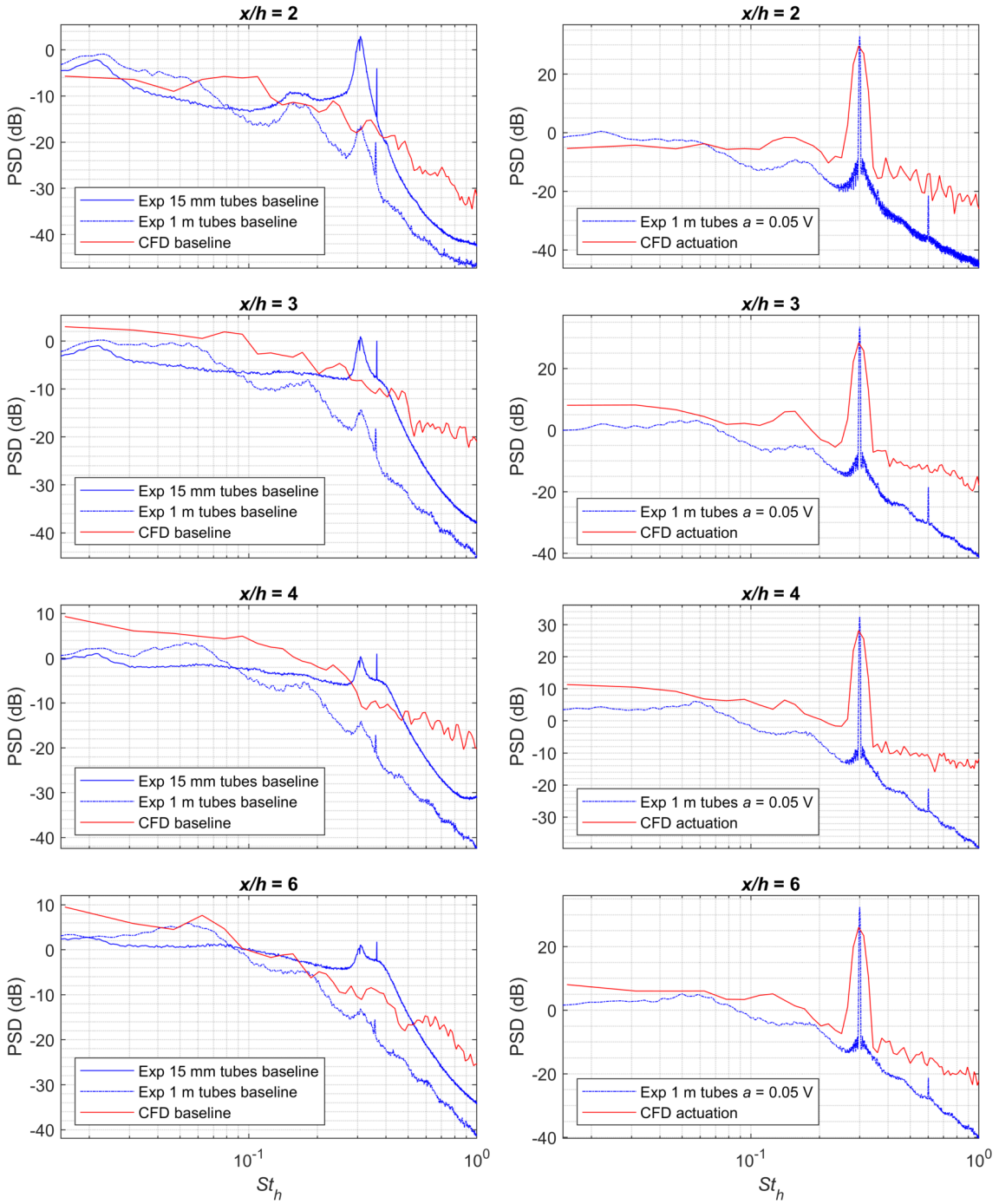


Figure 3.18: Point frequency spectra of CFD wall pressure compared to experimental measurements. Baseline flow on left, actuation on right

Chapter 4

Effect of Actuation on Time-mean Flow

4.1 Introduction

In this chapter, the mean effects of opposite-side acoustic actuation on the backward-facing step flow are quantified by wall pressure and hot-wire measurements.

In Section 4.2 the effect of actuation on mean and RMS wall pressures is investigated, and the reattachment length is estimated from the location of peak RMS wall pressure. Hot-wire traverses of the baseline and actuated flows at inlet speed $v_{\text{in}} = 20\,\text{m}\,\text{s}^{-1}$ are presented in Section 4.3, and the effects of actuation on mean shear layer evolution with distance downstream of the step are studied. Secondary side-wall vortices are also identified, consistent with observations made in previous studies [105, 106, 169]. A metric for flow non-uniformity is introduced and used to quantify the effectiveness of acoustic actuation in a manner more relevant to relevant to heat exchanger performance than reattachment length.

Finally, in Section 4.4 spanwise non-uniform distributed actuation is investigated, in the interest of improving the spanwise uniformity of the mean flow downstream of the step.

4.2 Wall Pressures and Reattachment Length Estimation

Figure 4.1 shows the mean wall pressure coefficient for inlet speeds 20, 25 and 30 $\mathrm{m\,s^{-1}}$, and actuation amplitudes $a = 0$ to 0.3 V in increments of 0.05 V, where pressure coefficient, C_p, is defined as:

$$C_p = \frac{p - p_\infty}{p_0 - p_\infty} \equiv \frac{p - p_\infty}{\frac{1}{2}\rho v_{\mathrm{in}}^2} \tag{4.1}$$

where p_0 and p_∞ are total and static pressure measured in the upstream section of the inlet channel.

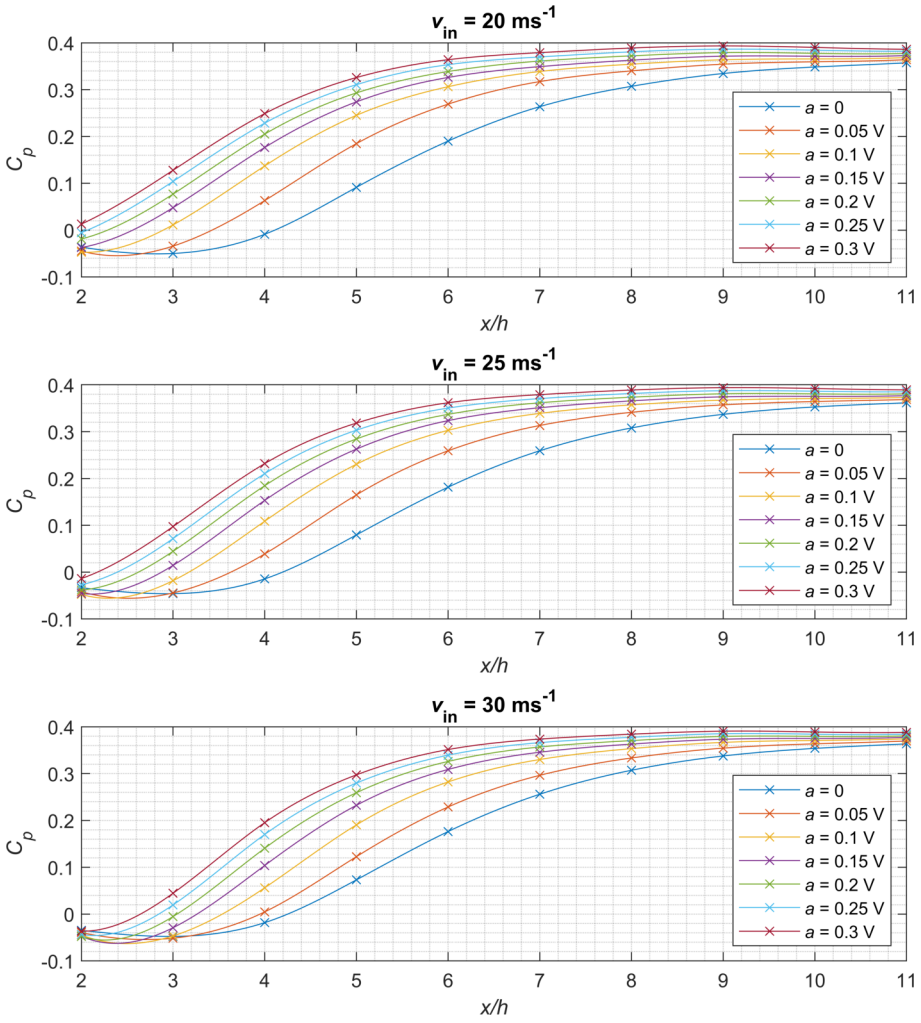


Figure 4.1: Mean wall C_p distribution measured using Honeywell SSCDRRD010MDAA5 transducers

Figure 4.2 shows the calculated RMS wall pressure fluctuations and 7$^{\mathrm{th}}$ order polynomial

curves fit to the measured data. RMS pressure measurements were recorded in sets of up to 6 tappings at a time, using two Sensortechnics HCXPM010D6V ±10 mbar and four Sensortechnics HCXPM005D6V ±5 mbar transducers, for 60 s at a sample rate 10 kHz for each set of tapping locations, at $v_{\text{in}} = 17.5$, 20, 25, and 30 m s^{-1} inlet velocities and forcing amplitudes $a = 0$, 0.05 V, 0.1 V, 0.15 V, and 0.2 V. RMS wall pressures were not calculated for forcing amplitudes above 0.2 V due to saturation of the ±5 mbar transducers by the acoustic pressure at higher amplitudes.

It is necessary to filter out the acoustic tone prior to calculating RMS values, for which a 5^{th} order low pass filter with cut-off frequency 70 Hz was used, as this is approximately the cut-off frequency of the filtering from the measurement tubes connecting transducers and wall tappings. The polynomial fits were used to estimate the peak x position of the RMS pressure, which moves upstream with forcing amplitude. Mabey [168] observed that the peak in RMS wall pressure behind a backward-facing step occurs slightly upstream of reattachment, which has been confirmed by Lee & Sung [89] among others. How far upstream of reattachment the peak in RMS wall pressure occurs is difficult to quantify without an accurate measurement of reattachment length, however an approximation can be made from the CFD data, which suggests that the peak in RMS wall pressure is around 1.5 step heights upstream of the reattachment length. Reattachment length is estimated from the experimental measurements on the assumption that this relationship holds for the experimental flow, i.e. $x_{\text{r}_{\text{est}}} = x_{\text{RMS}} + 1.5h$, where x_{RMS} is the location of the peak RMS wall pressure.

Estimated reattachment length is plotted as a function of input amplitude for each of the four flow speeds, shown in Figure 4.3a. The percentage reductions in reattachment length at the maximum excitation amplitude, $a = 0.2$ V, for each flow speed are given in table 4.1. The estimated maximum reduction in reattachment length based on RMS wall pressures is 28.5% at $v_{\text{in}} = 20\,\text{m s}^{-1}$, which is consistent with typical values stated in literature, summarised in table 2.1. Despite being an unremarkable result when compared to BFS flow control studies which employed local periodic excitation at or close to the step edge, the currently achieved reattachment length reduction is an improvement on the examples of external acoustic excitation in literature, which achieved between 10-20% reduction [69, 48]. It should also be pointed out that the mean wall pressure curves, shown in Figure 4.1

demonstrate that the authority of actuation has not yet saturated by $a = 0.3\,\mathrm{V}$, therefore the maximum possible effectiveness is expected to be greater than the values stated in table 4.1.

$v_{\mathrm{in}}(\mathrm{m\,s^{-1}})$	$x_{\mathrm{r_{est}}}/h$, $a = 0$	$x_{\mathrm{r_{est}}}/h$, $a = 0.2\,\mathrm{V}$	Reduction (%)
17.5	7.15	5.24	26.72
20	7.26	5.19	28.48
25	7.46	5.38	27.97
30	7.51	5.69	24.25

Table 4.1: Estimated reattachment length reduction at $a = 0.2\,\mathrm{V}$

While the location of peak RMS wall pressure, x_{RMS}, can be used as the feedback measurement for control [114], it may not be a suitable choice for a number of reasons. The most obvious of which for the current problem are that the spatial resolution and span of wall pressure measurements required to reliably determine the maximum RMS location necessitates a potentially non-trivial number of pressure transducers, and that the moving window over which the RMS pressures are calculated may limit the controller bandwidth. The simplest and most convenient choice of feedback measurement would be a single wall pressure measurement, however for this to be a viable choice the measured C_p value should be at the least monotonic, and ideally linear, with reattachment length. Figure 4.3b shows the mean wall C_p at several streamwise locations plotted against estimated reattachment length, $x_{\mathrm{r_{est}}}$. Conveniently, the C_p value at $x/h = 5$ is approximately linear with reattachment length, therefore can be used as a simple proxy for reattachment/control effectiveness. The equation of the linear fit between mean C_p at $x/h = 5$, $\overline{C}_p|_{x/h=5}$, is:

$$x_{\mathrm{r_{est}}} = -9.5054\overline{C}_p|_{x/h=5} + 8.0958 \tag{4.2}$$

Applying this linear relationship to the wall pressure measurements taken using the Honeywell transducers, displayed in Figure 4.1, suggests that the maximum possible reattachment length reduction is around or just above 30% for inlet velocities between 20 and $30\,\mathrm{m\,s^{-1}}$, only slightly greater than the reduction at $a = 0.2\,\mathrm{V}$.

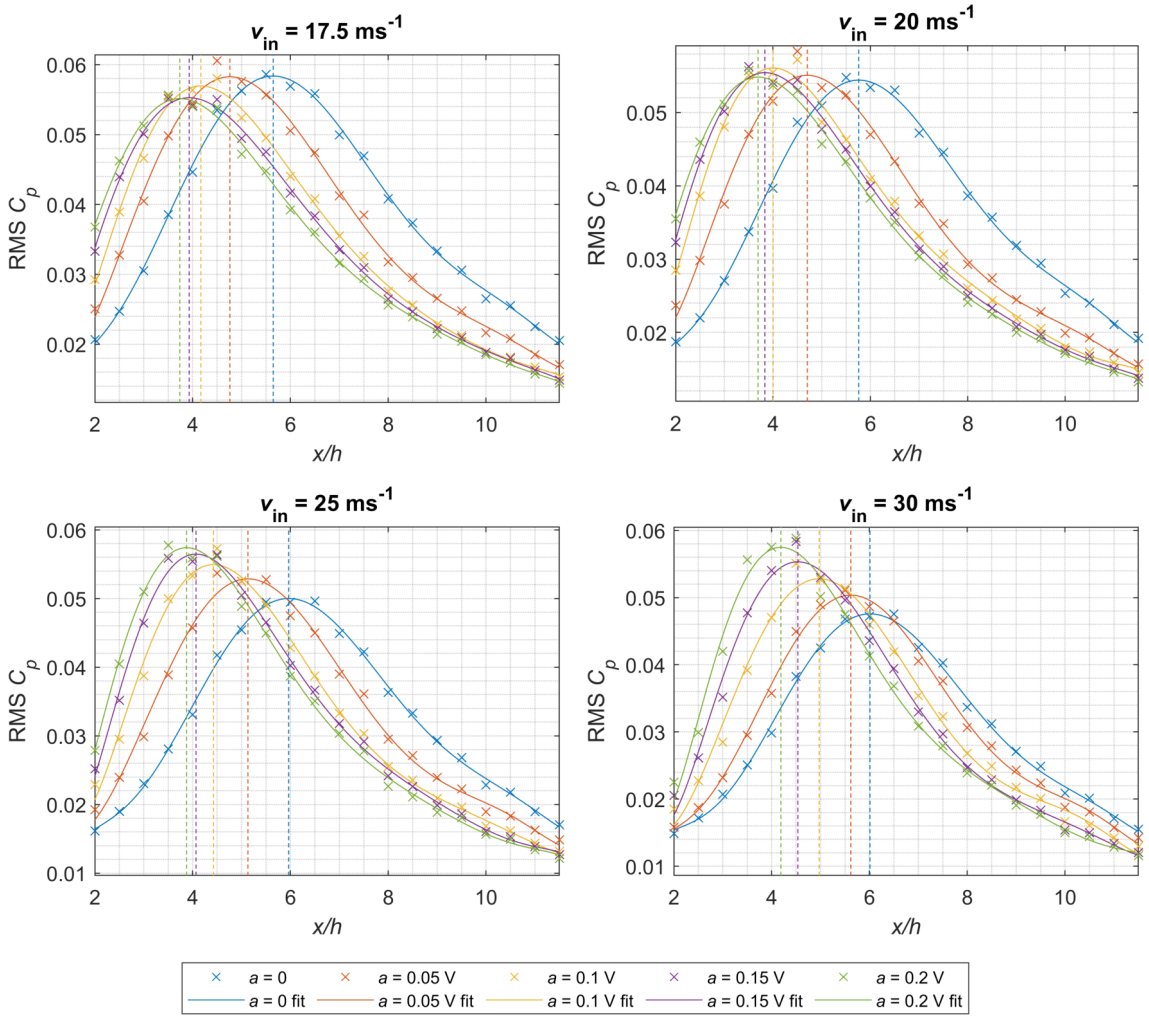
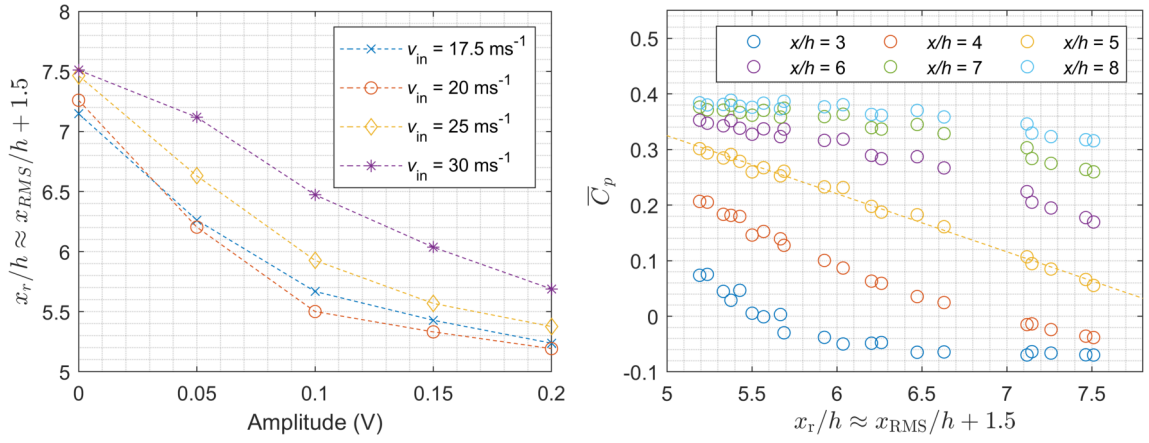


Figure 4.2: RMS measured wall C_p and polynomial fits. Dashed lines indicate peaks of fits



(a) $x_{r_{est}}$ with input voltage

(b) Mean C_p against $x_{r_{est}}$

Figure 4.3: Estimated reattachment lengths based on peak RMS wall pressure location

4.2.1 Static response of flow with actuation frequency

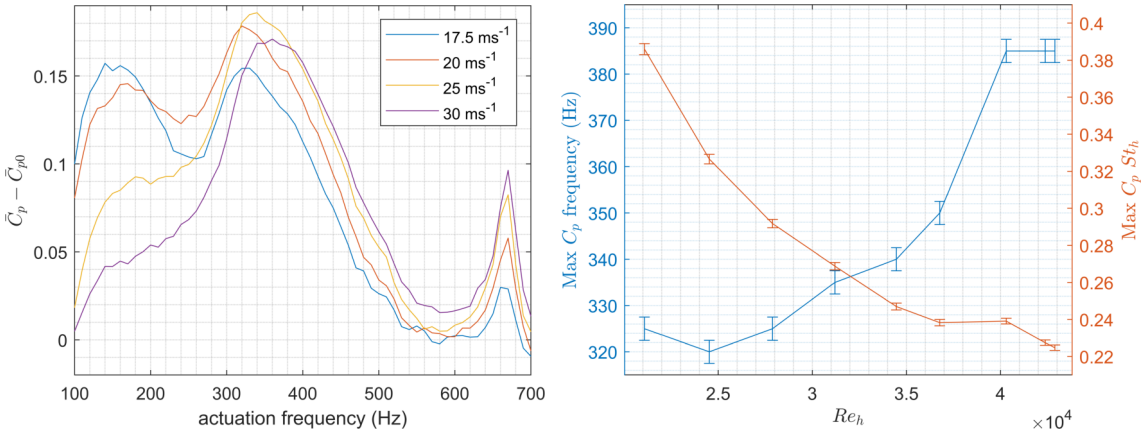
For the experiments presented in this thesis, the actuation frequency (carrier frequency when actuation is amplitude modulated) is set to 300 Hz, equal to the first longitudinal resonance frequency of the test section. Despite this, it is still of interest to investigate the effects of varying actuation frequency, which may inform about the mechanism through which forcing interacts with the flow or present research questions to be addressed in further work.

A frequency sweep from 100 Hz to 700 Hz with spacing 10 Hz and amplitude 0.1 V was performed with the flow on for inlet velocities 17.5 $\mathrm{m\,s^{-1}}$, 20 $\mathrm{m\,s^{-1}}$, 25 $\mathrm{m\,s^{-1}}$ and 30 $\mathrm{m\,s^{-1}}$ and the mean wall pressure coefficient at $x/h = 5$ recorded, which is demonstrated to be a suitable proxy for reattachment length above, shown in Figure 4.4a. At lower flow speeds the static flow response exhibits two peaks (corresponding to reduced reattachment length) at around 160 Hz and 320 Hz, while the response at higher speeds has only a single peak at the higher frequency. A smaller local peak which does not shift with velocity is also present at 670 Hz, consistent with the local peak at the same frequency seen in the acoustic response in Figure 3.9a.

The mean pressure responses shown in Figure 4.4a are a clear demonstration that the most effective steady-state actuation frequency is a function of both flow speed and the acoustic response of the combined actuator-test section system. That the primary peak at around 320 Hz, corresponding to the peak in acoustic response, shifts only slightly with velocity demonstrates that this peak is predominantly a function of the actuation. The ∼160 Hz peak appears to be a sub-harmonic of the ∼320 Hz resonance which couples to a flow mechanism at the lower two velocities, but not as the speed increases. It is interesting that the exact same static response with actuation frequency and flow speed was observed by Nicholls [57] for a fluidic diverter, suggesting that this behaviour is fundamental to reattaching jet/shear layer flows with acoustic actuation, and not merely a quirk of the current BFS setup.

A second sweep with actuation frequencies 250 Hz to 450 Hz spaced every 5 Hz was performed at several inlet velocities from 16.8 $\mathrm{m\,s^{-1}}$ to 34.3 $\mathrm{m\,s^{-1}}$. The most effective frequency in terms of reattachment length reduction, corresponding to the maximum wall

pressure at $x/h = 5$, was then found and plotted against velocity in Figure 4.4b, both as raw frequency and Strouhal number based on step height.



(a) Static flow response with actuation frequency, measured by C_p at $x/h = 5$

(b) Most effective steady-state actuation frequency. Error bars of half the frequency resolution

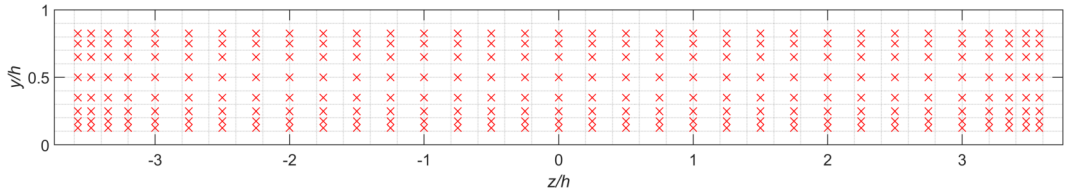
Figure 4.4: Static flow response

The actuation frequency, f_c, was chosen to be constant at 300 Hz. However, Figure 4.4a demonstrates that from a steady-state perspective around 330 Hz may have been a more appropriate choice, as this remains close to the peak effectiveness across the range of achievable inlet velocities.

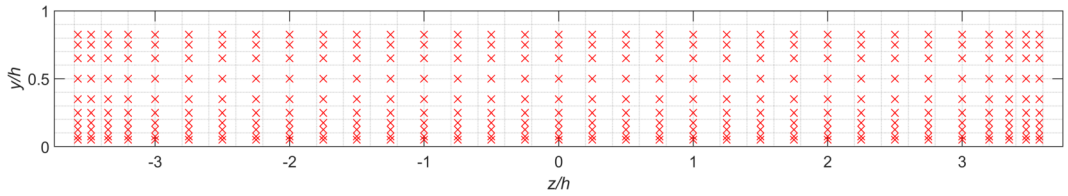
4.3 Velocity Field

A set of hot-wire traverses in the transverse (y-z) plane were taken at a range of streamwise locations in the BFS to build up an image of the mean flow field. The single wire hot-wire probe was oriented in the z-direction, therefore measured velocity magnitude in the x-y plane (i.e. the u-v velocity component). Measurements were taken at a sample rate of 10 kHz for 10 s per point for $a = 0$ (baseline), $a = 0.05$ V, and $a = 0.1$ V actuation amplitudes. It was determined from preliminary data that 10 s is long enough for the cumulative mean to settle, and for the calculated power spectral density to be of sufficient fidelity to show the strongest dynamics. Measurements were spaced on a non-uniform grid of 33 by 8 points upstream of the step, 33 by 10 points in-line with the step edge, and 33 by 15 points downstream of the step, in the z (spanwise) and y (wall-normal) directions

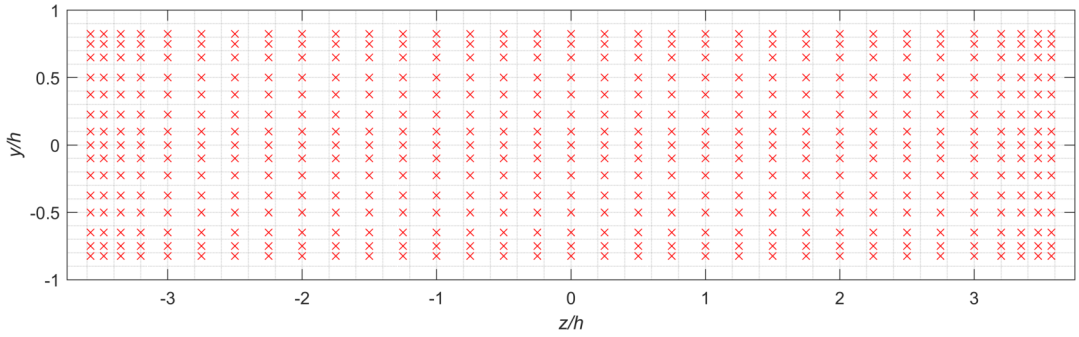
respectively, shown in Figure 4.5. A total of 21 traverse planes were measured for each actuation amplitude: one upstream of the step at $x/h = -2.5$, one in line with the step at $x/h = 0$, and 19 downstream of the step at streamwise locations $x/h = 0.25$, 0.75, 1.25, 1.5, 1.75, 2, 2.5, 3, 3.5, 4, 4.5, 5, 5.5, 6, 6.5, 7, 8.5, 10, and 12.5. The streamwise traverse locations were concentrated in the separated region upstream of reattachment, with additional planes shortly after separation to capture the evolution and merging of shear layer vortices. The resulting total number of measurement points per full traverse was 9999.



(a) Point locations upstream of step



(b) Point locations at step



(c) Point locations downstream of step

Figure 4.5: Traverse plane point locations

Each set of traverses took 30-40 hours, therefore, the full set of traverses were only measured for $20\,\mathrm{m\,s^{-1}}$ inlet speed and three actuation amplitudes (including baseline). It was found that full velocity field measurements at a single velocity were sufficient to characterise the flow features, and this was confirmed by the similarity of features in the frequency spectra at different inlet velocities.

Figures 4.6 and 4.7 shows the mean and RMS of velocity measurements plot on all of the

traverse planes for baseline flow ($a = 0$), $a = 0.05\,\mathrm{V}$, and $a = 0.1\,\mathrm{V}$ actuation amplitudes.

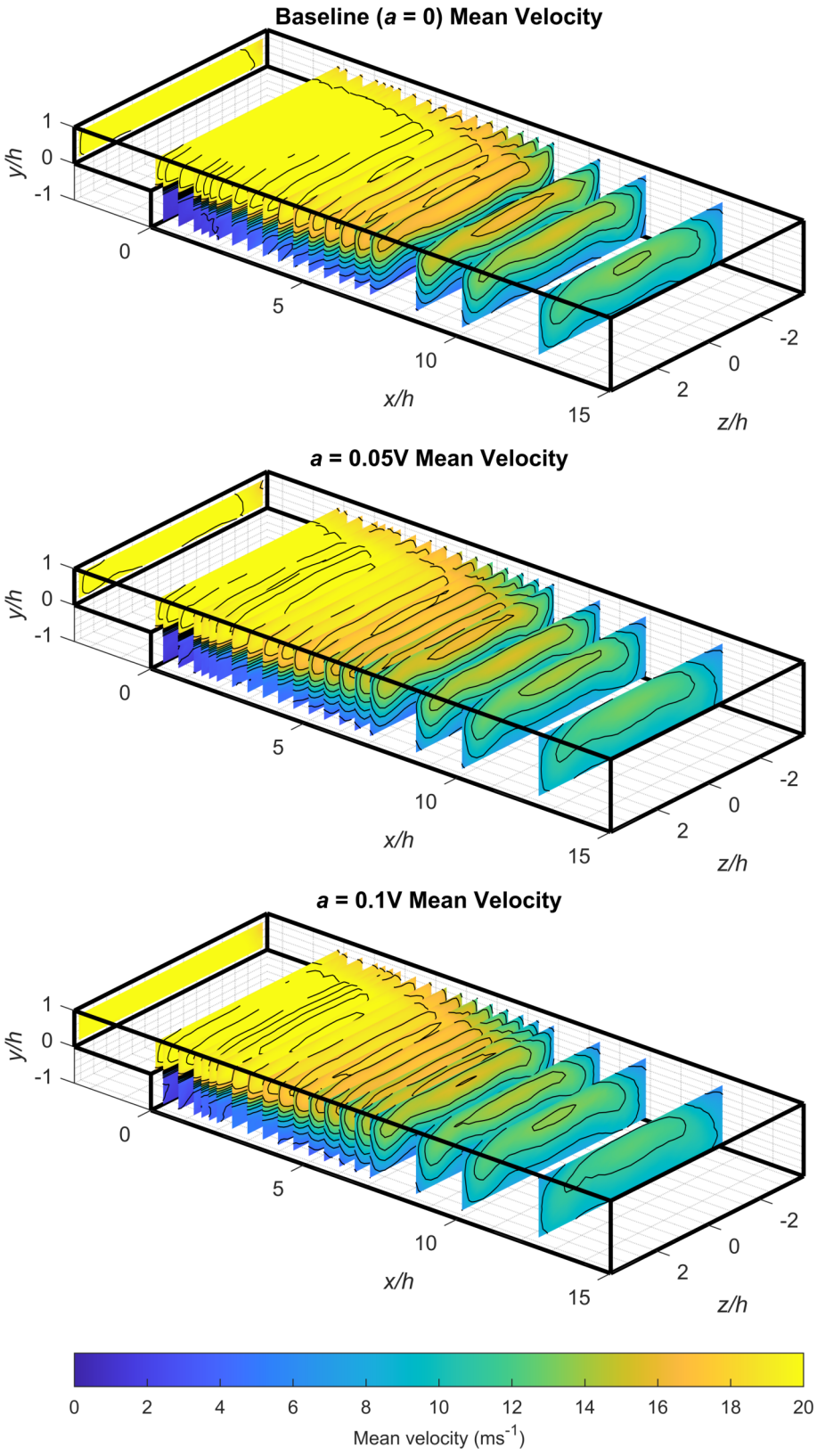


Figure 4.6: Mean u-v velocity at hot-wire traverse planes

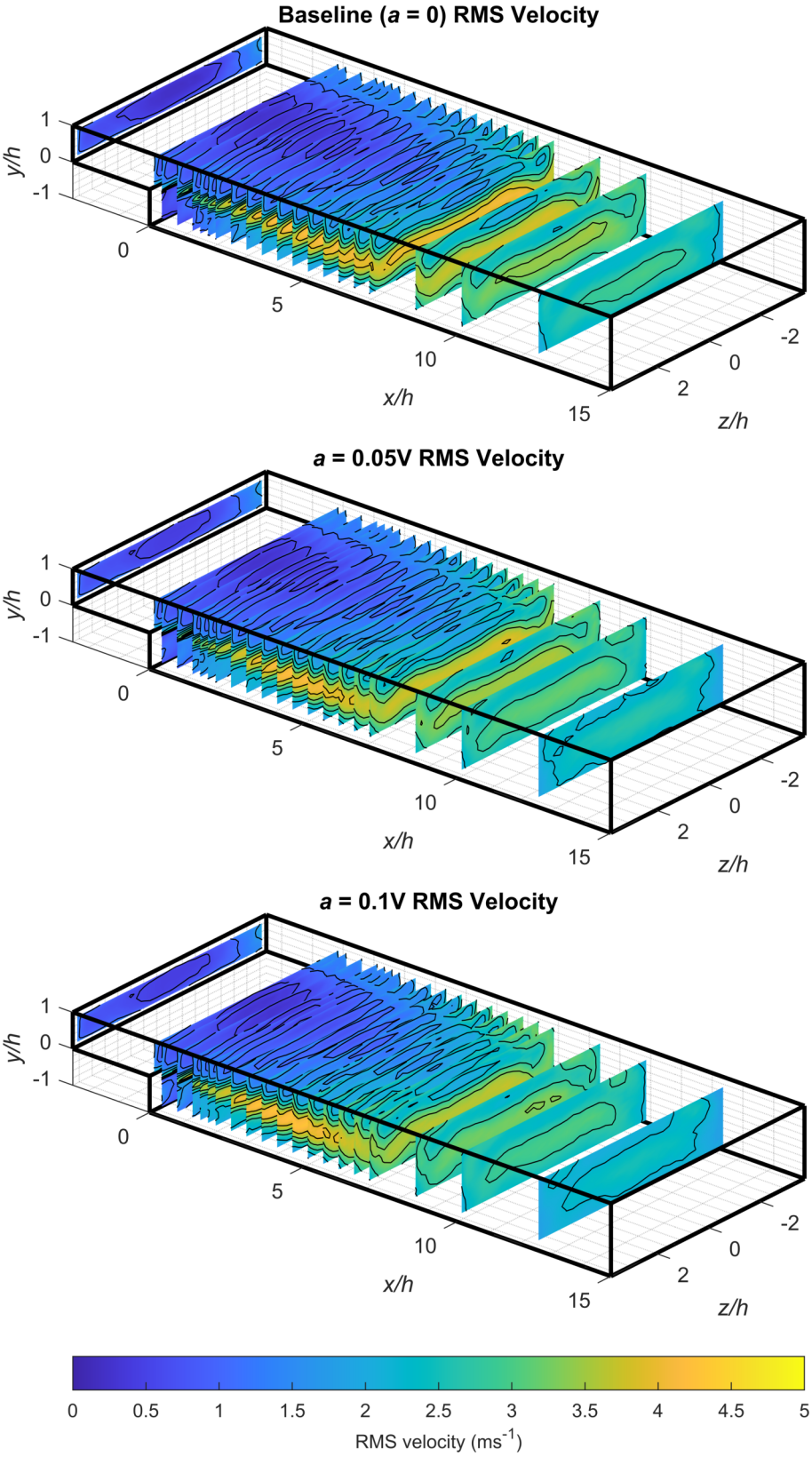


Figure 4.7: RMS u-v velocity at hot-wire traverse planes

Displacement thickness, δ^*, and momentum thickness, θ, at $x = 0$, based on the freestream velocity at $y/h = 0.5$, are calculated from the average velocity profile between $z/h = -1.5$ and $z/h = 1.5$ and given below in table 4.2.

a (V)	δ^* (mm)	θ (mm)
0	0.80	0.39
0.05	0.65	0.37
0.1	0.65	0.37

Table 4.2: Displacement and momentum thickness at $x = 0$ for $v_{\text{in}} = 20\ \text{m}\,\text{s}^{-1}$

Figures 4.8, 4.9, and 4.10 show contour plots of the mean and RMS velocity at several of the cross-section planes, for $a = 0\,\text{V}$, $a = 0.05\,\text{V}$, and $a = 0.1\,\text{V}$ V respectively. Contour plots at three streamwise locations are displayed shortly after separation at $x/h = 0.75$, around half way through the separated region at $x/h = 3$, and slightly upstream of/around reattachment (depending on actuation amplitude) at $x/h = 6.5$. These contours provide a relatively clear qualitative depiction of shear layer spreading and the effect of secondary flows on spanwise velocity distribution with distance downstream of the step [1].
Both the mean and RMS velocity plots show the expansion of the shear layer as the flow travels downstream, with a clear correlation between the region with highest spatial rate of change of velocity and the region of highest RMS velocity. A slight asymmetry in the spanwise direction is also observed, originating from the disturbance caused by the total pressure probe upstream of the test section, placed 5 mm from the side wall and 35 mm upstream of the test section inlet at $(x, y, z)/h = (-2.75, 0.5, -3.5)$, shown in figure **??**.

Velocity contours in Figures 4.8 to 4.10 show that the flow is reasonably spanwise-uniform initially. However, by the point of flow reattachment it can only be considered as approximately 2D in nature for a slice between about $z/h = \pm 1$. Travelling from the centre of the channel to either of the side-walls, a decrease in spreading/uniformity in the y-direction of the mean velocity is apparent at around $z/h = 2$ from the centre, before an increase in

[1] It should be noted that single wire hot-wire probes are unable to resolve the flow direction, and are poorly suited to reverse or zero-mean flows, due to which it is not possible to determine the reattachment length with confidence from the traverse data. Additionally, the reliability of the technique is reduced at low mean flow speeds, and so the velocity magnitude measured in the recirculation bubble is potentially inaccurate. Regardless, hot-wire traverses provide an invaluable qualitative picture of the mean velocity field.

spreading/uniformity at around $z/h = 3$, irrespective of streamwise locations and actuation amplitude. The spanwise variation of mean velocity is accompanied by an increase in the RMS velocity magnitude across the shear layer between roughly $z/h = 2$ and $z/h = 3$ from the centre.

This spanwise distribution is indicative of the redistribution of momentum from the quarter span towards the side-walls by streamwise aligned longitudinal vortices, which form due to the interaction of shear layer vorticity with the side-wall boundary layers. A number of studies, including those of Lim et al. [106], de Brederode [105], and Hall et al. [169], have identified the presence of streamwise aligned vortices originating from the corners of the step.

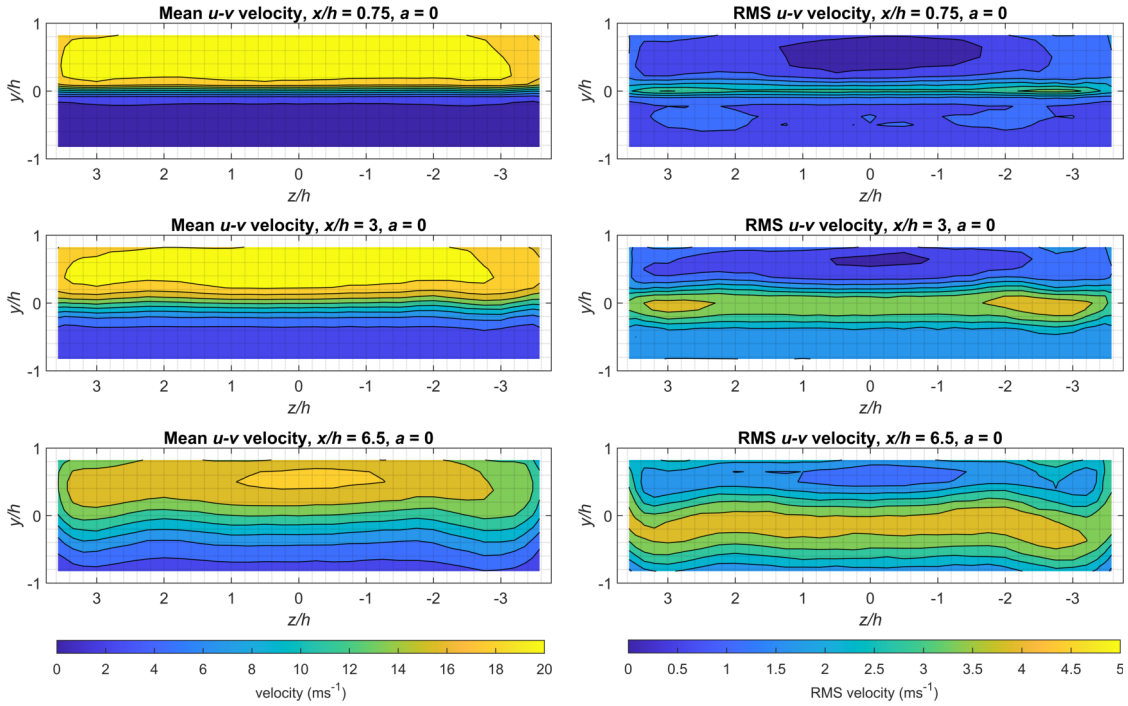


Figure 4.8: Baseline mean and RMS velocity at $x/h = 0.75$, 3, and 6.5

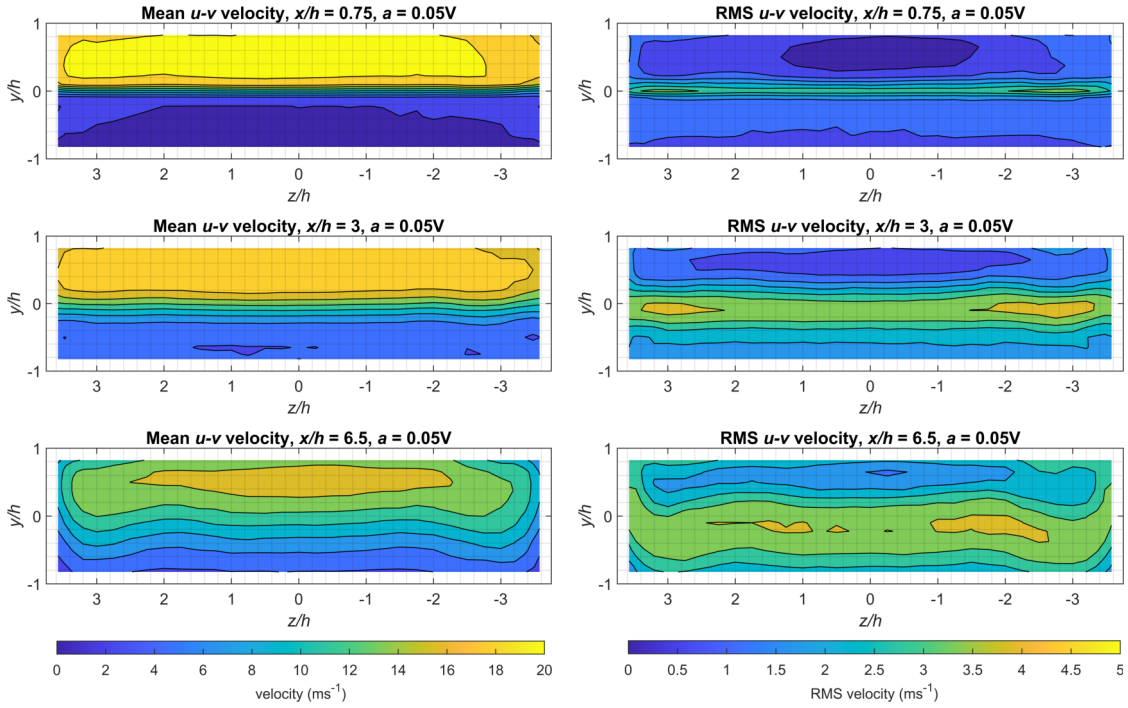


Figure 4.9: $a = 0.05\,\mathrm{V}$ mean and RMS velocity at $x/h = 0.75$, 3, and 6.5

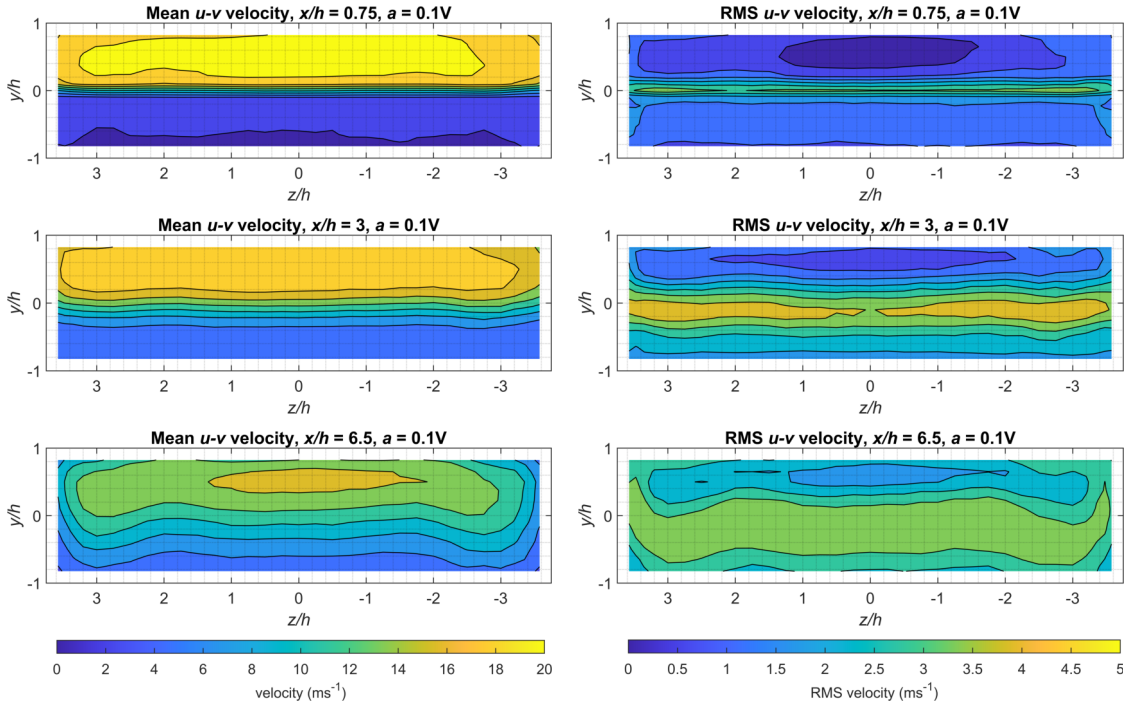


Figure 4.10: $a = 0.1\,\mathrm{V}$ mean and RMS velocity at $x/h = 0.75$, 3, and 6.5

A comparison of the baseline and unactuated flows is presented in Figures, 4.11 and 4.12, and 4.13 and 4.14, which show the mean and RMS velocity profiles at the centre plane,

$z/h = 1.5$, and $z/h = 3$ from the centre at each of the streamwise traverse locations. Immediately after separation at $x/h = 0.25$, actuation does not significantly affect either the mean or RMS velocity profiles. As the flow develops downstream, actuation results in more uniform velocity profiles, with lower maximum and higher minimum velocities. The same effect can be seen in the RMS velocity profiles, where actuation enhances the spreading of the peak in v_{RMS}.

The profiles also show that the mean velocity is essentially spanwise-uniform just after separation, then develops to have a significantly non-uniform spanwise distribution far downstream of the step. The RMS velocity profiles are initially somewhat spanwise non-uniform, having larger magnitude close to the side walls of the test section than the centre, with this non-uniformity continuing to develop downstream.

An alternative view of the hot-wire traverse data is given by Figure 4.15, which shows spanwise profiles of mean velocity at several fixed heights (y positions) and streamwise positions. The spanwise velocity profiles at heights $y/h = -0.5$ and $y/h = 0$ clearly show the effects of secondary flow, as a slight dip from around $z/h = \pm 1.5$ to $z/h = \pm 2.5$ and a peak at around $z/h = \pm 3$.

Although actuation increases shear layer spreading and promotes the early development of the flow, which is particularly apparent from the increase in mean velocity at $y/h = -0.5$ and decrease at $y/h = 0.5$ for streamwise locations downstream of $x/h = 5$, the profile shapes remain similar to the baseline flow. The similarity of spanwise velocity distribution implies that acoustic excitation does not significantly affect the structure of the secondary flow/streamwise vortices beyond the general increase in spreading.

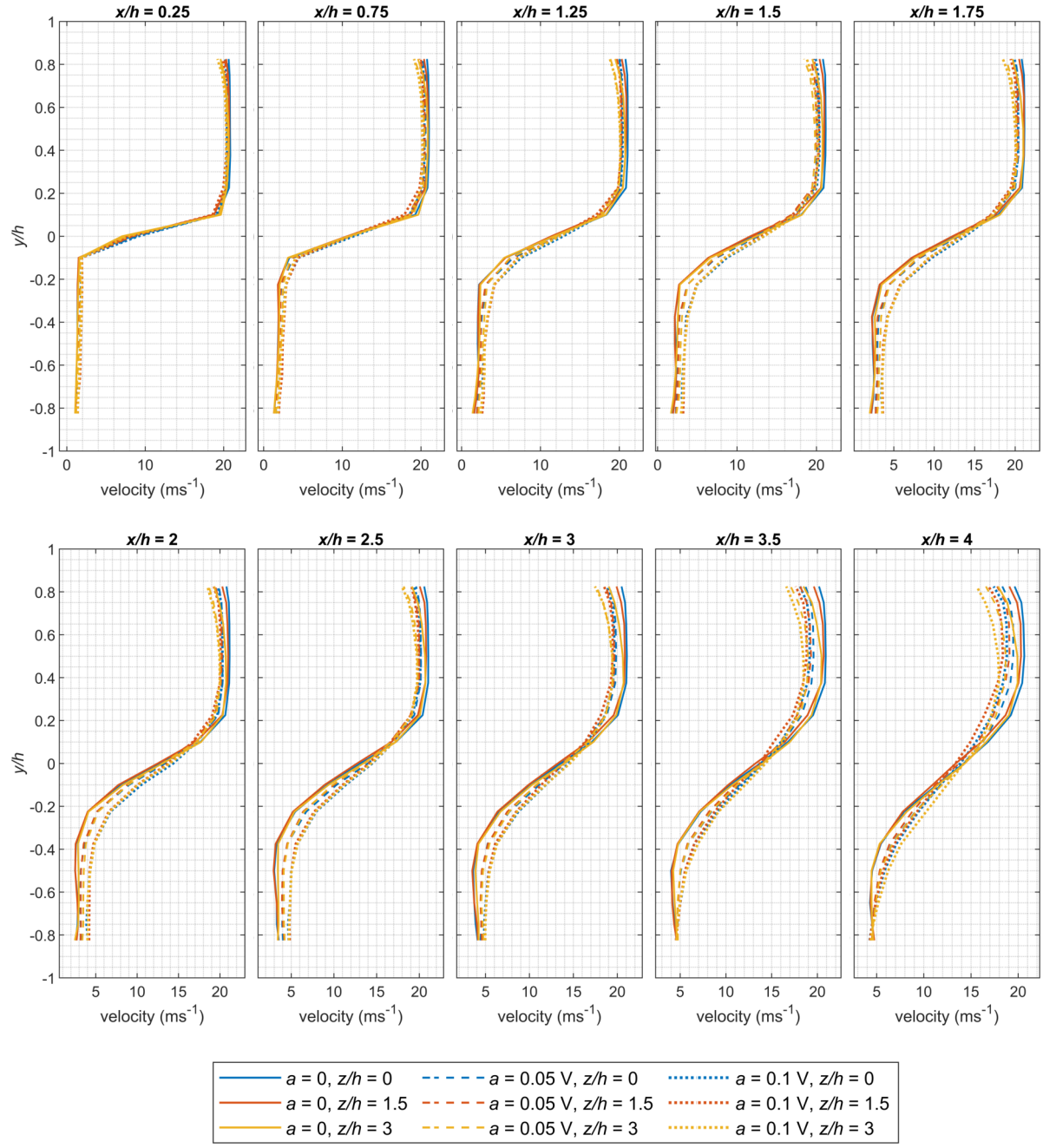


Figure 4.11: $20\,\mathrm{m\,s^{-1}}$ wall-normal mean velocity profiles at $z/h = 0$, 1.5, and 3, $a = 0$ (baseline), 0.05 V, and 0.1 V. $x/h = 0.25$ to $x/h = 4$

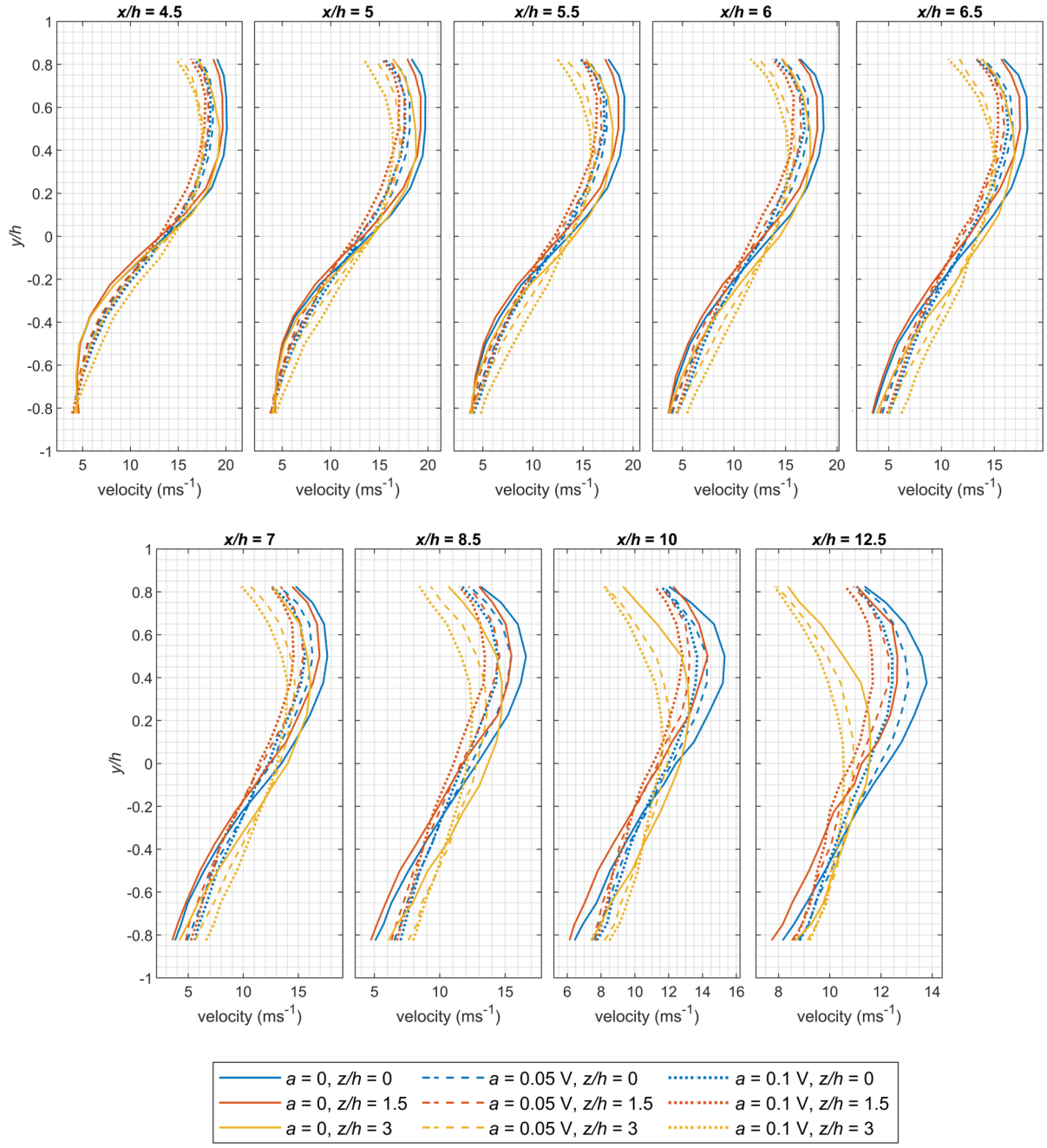


Figure 4.12: $20\,\mathrm{m\,s^{-1}}$ wall-normal mean velocity profiles at $z/h = 0$, 1.5, and 3, $a = 0$ (baseline), 0.05 V, and 0.1 V. $x/h = 4.5$ to $x/h = 12.5$

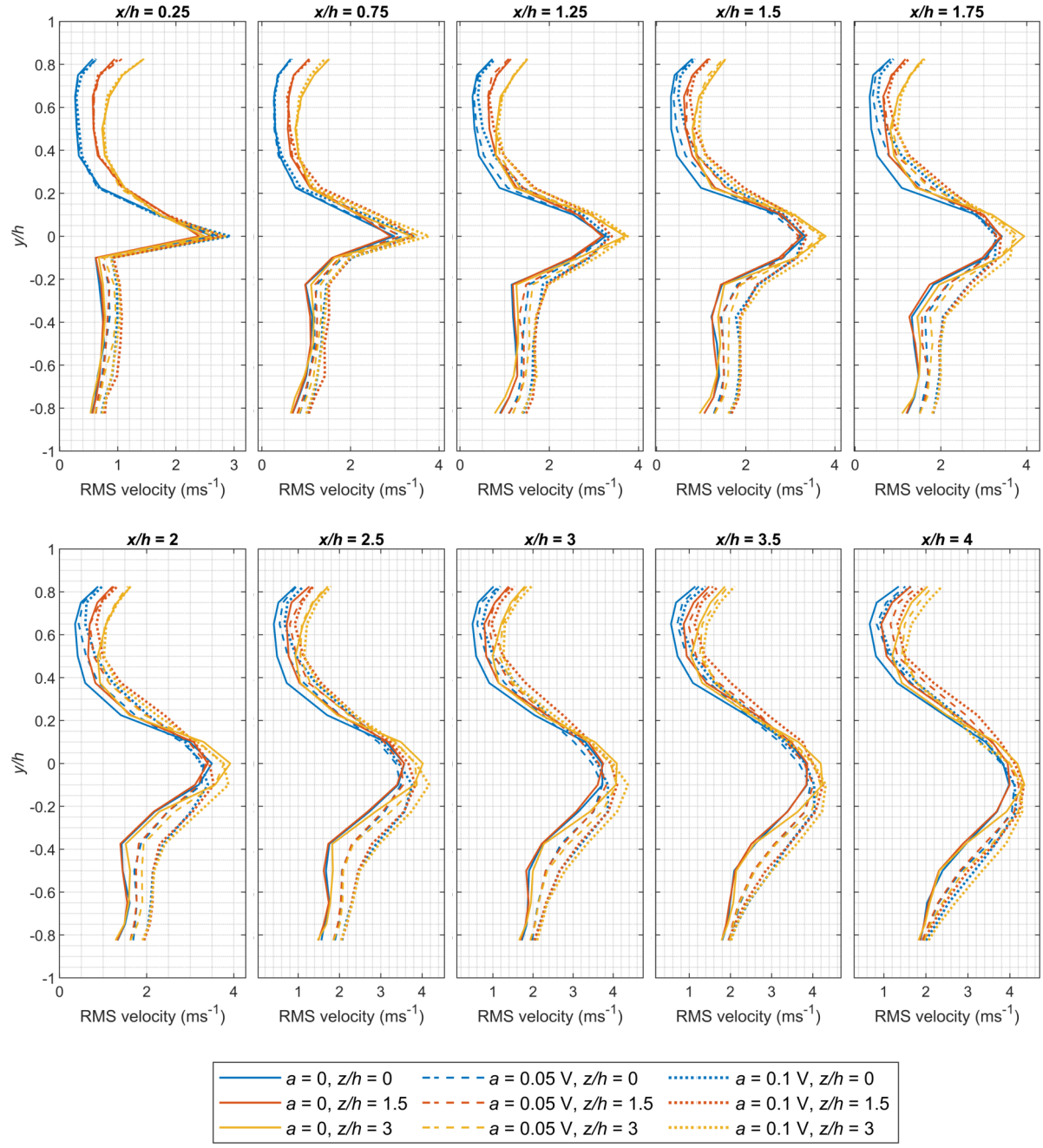


Figure 4.13: $20\,\mathrm{m\,s^{-1}}$ wall-normal RMS velocity profiles at $z/h = 0$, 1.5, and 3, $a = 0$ (baseline), 0.05 V, and 0.1 V. $x/h = 0.25$ to $x/h = 4$

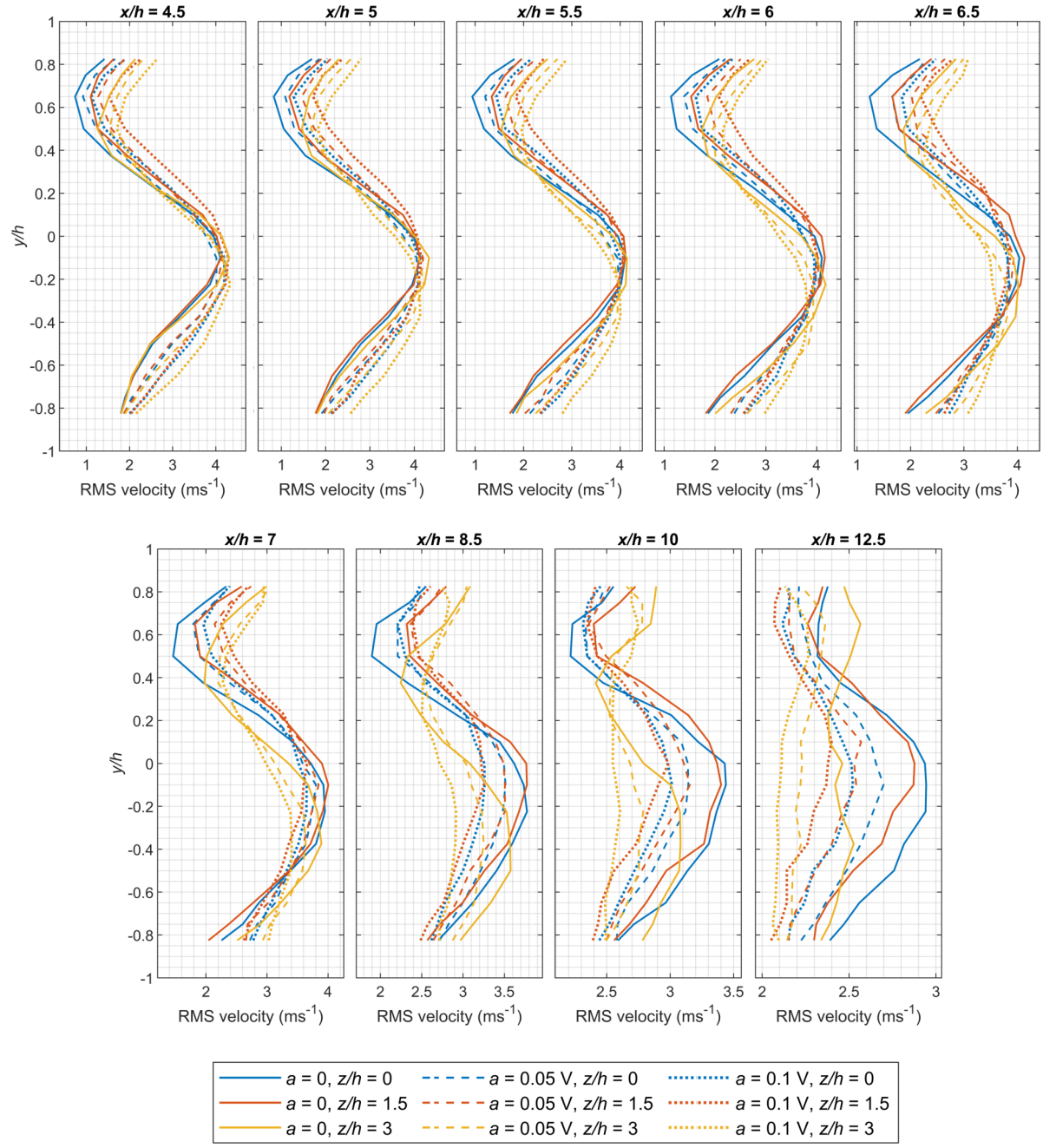


Figure 4.14: $20\,\mathrm{m\,s^{-1}}$ wall-normal RMS velocity profiles at $z/h = 0$, 1.5, and 3, $a = 0$ (baseline), 0.05 V, and 0.1 V. $x/h = 4.5$ to $x = 12.5$

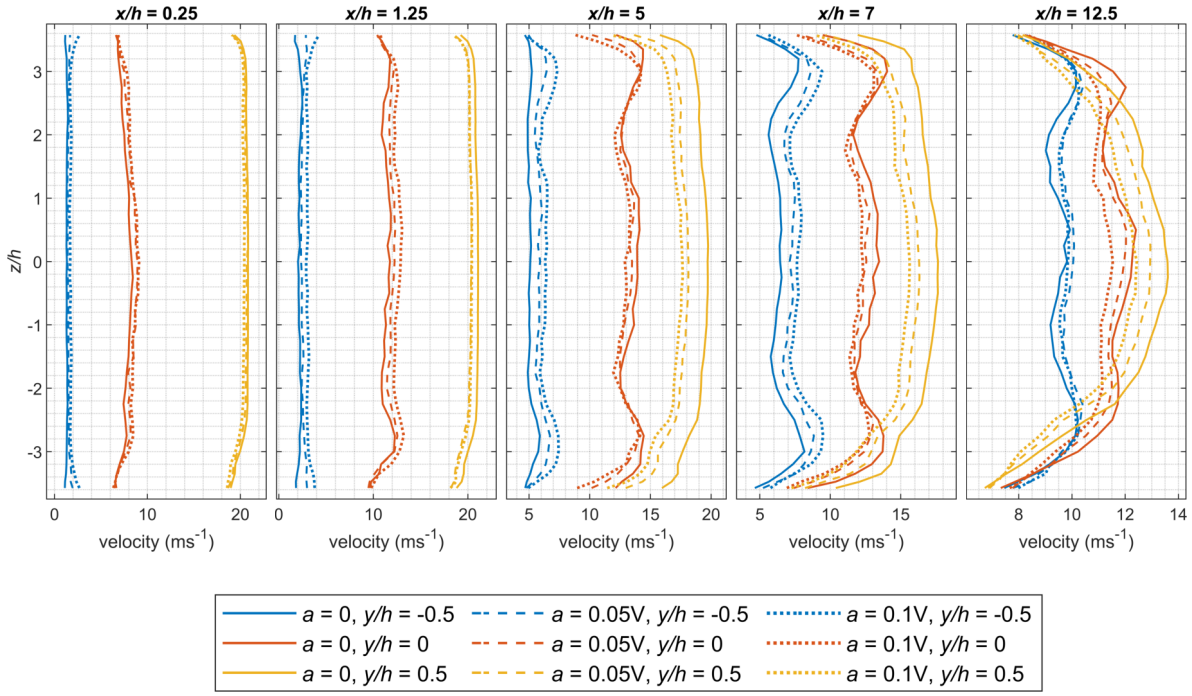


Figure 4.15: 20 ms^{-1} spanwise mean velocity profiles at y/h = -0.5, 0, and 0.5, $a = 0$ (baseline), 0.05 V, and 0.1 V, at several x locations

4.3.1 Effect of Actuation on Spatial Flow Uniformity

The standard metric for effectiveness of backwards facing step actuation is the reduction in reattachment length. However, given the current use of a backward-facing step geometry as representing the worst case of separation in a highly curved/diverging duct, a potentially more suitable metric would be the spatial uniformity of the flow downstream of the step. A spatial non-uniformity metric, NU, for the mean velocity is defined as the spatial standard deviation of the time-mean velocity at a given streamwise location. This metric was inspired by Blecich [7], who defined the flow non-uniformity as the unbiased standard deviation of velocities measured at the centres of a grid of separated heat exchanger channels, although in the current work a continuous formulation is more appropriate due to the non-uniform spacing of traverse measurement points. Two separate non-uniformity metrics are defined, the first, $NU_{\mathrm{y}}(x)$, evaluated only at the spanwise centre ($z = 0$), and the second, $NU_{\mathrm{yz}}(x)$, evaluated over the full cross-sectional area of the test section,

$$NU_{\mathrm{y}}(x) = \sqrt{\frac{1}{H}\int\left(\frac{\overline{u}(x,y,0) - \int \overline{u}(x,y,0)\,dy}{\int \overline{u}(x,y,0)\,dy}\right)^2 dy} \tag{4.3}$$

$$NU_{\mathrm{yz}}(x) = \sqrt{\frac{1}{H \times s} \iint \left(\frac{\overline{u}(x,y,z) - \iint \overline{u}(x,y,z)\, dy\, dz}{\iint \overline{u}(x,y,z)\, dy\, dz} \right)^2 dy\, dz} \tag{4.4}$$

where H is the test section height (y direction), s is the spanwise width, and $\overline{u}(x,y,z)$ is the time-mean streamwise velocity component. Approximations to NU_{y} and NU_{yz} are calculated numerically from the hot-wire measurements, shown in Figure 4.16.

It should be noted that, due to the inability of the single-wire probe to measure flow direction, the calculated non-uniformity values will underestimate the true values in the separated region, where there is reverse flow in the recirculation bubble. Actuation most effectively reduces non-uniformity between around $x/h = 2$ to $x/h = 10$. Upstream of $x/h = 2$ the scale of shear layer structures is small and so the effect of actuation is minimal, while downstream of $x/h = 10$ the flow is fairly developed regardless of actuation.

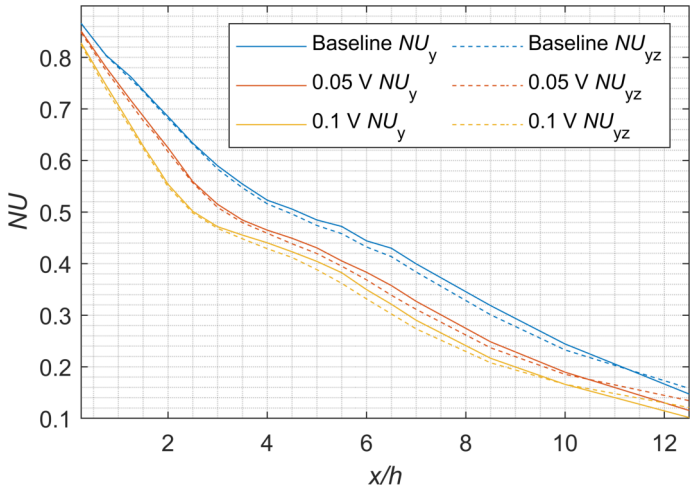


Figure 4.16: Velocity non-uniformity as a function of streamwise location

Blecich [7] investigated the effects of airflow non-uniformity on the performance of a fin-and-tube heat exchanger, the results of which are summarised in table 4.3. The deterioration of effectiveness (defined as the ratio of actual heat transfer to maximum possible heat transfer) was found to depended strongly on the orientation of fluid flow in the heat exchanger relative to the air flow non-uniformity, with airflow distributions that completely depleted the flow over entire tube circuits (A1, B1, C1) resulting in a greater loss in effectiveness than those with the airflow non-uniformity distributed along the tube paths (A2, B2, C2) for a similar value of NU. The results of Blecich [7] suggests that the reductions in NU

achieved by control in the current BFS flow might result in a relatively modest effectiveness increase of several percent in a similar heat exchanger flow.

Case	NU_{yz} **equivalent**	**Decrease in effectiveness**
A1	0.73	20-30%
A2	0.82	12-18%
C1	0.59	11-18%
C2	0.64	8-14%
B1	0.21	2-6%
B2	0.26	$< 3\%$

Table 4.3: Summary of results of Blecich [7]

While flow uniformity downstream of the step provides an alternative measure of control effectiveness to the reattachment length, and may be more useful in determining the benefit of control, it is not practical as a feedback measurement due to requiring multiple spatial velocity measurements. Despite this, the time-mean flow uniformity is at most a two-dimensional function of the inlet speed and forcing amplitude, and it has been demonstrated that there is an approximately linear relationship between wall pressure coefficient at $x/h = 5$ and reattachment length, therefore it seems reasonable to expect that a similar mapping between wall pressure coefficient and flow non-uniformity may exist.

Centre-span hot-wire measurements were taken across the test section height (y direction), at streamwise position $x/h = 5$ only, for inlet velocities $v_{in} = 20\,\mathrm{m\,s^{-1}}$, $25\,\mathrm{m\,s^{-1}}$, and $30\,\mathrm{m\,s^{-1}}$, and actuation amplitudes from $a = 0$ to $0.3\,\mathrm{V}$ in $0.05\,\mathrm{V}$ increments. Wall pressure coefficients were recorded concurrently with the hot-wire measurements, and measurements were recorded for $30\,\mathrm{s}$ per traverse point.

Figure 4.17 shows the measured velocity profiles for each of the inlet speeds and actuation amplitudes. The non-dimensional velocity profiles remain remarkably similar across all three inlet speeds, despite the differences in wall pressure distributions and estimated reattachment lengths. The calculated non-uniformity of the velocity profiles, plotted against actuation amplitude in Figure 4.18a, demonstrates that the maximum reduction in NU_y at $x/h = 5$ is slightly greater at higher inlet speeds, the converse of the relationship between inlet velocity and reattachment length. Figure 4.18 shows the wall pressure coefficient

at several of the tapping positions plotted against the calculated values of NU_{y}. Unlike estimated reattachment length, the values of NU_{y} at different inlet speeds do not collapse to a single line when plot against C_p, however the trend of NU_{y} against C_p is very approximately linear at constant inlet speed for wall pressure positions between $x/h = 5$ and $x/h = 7$.

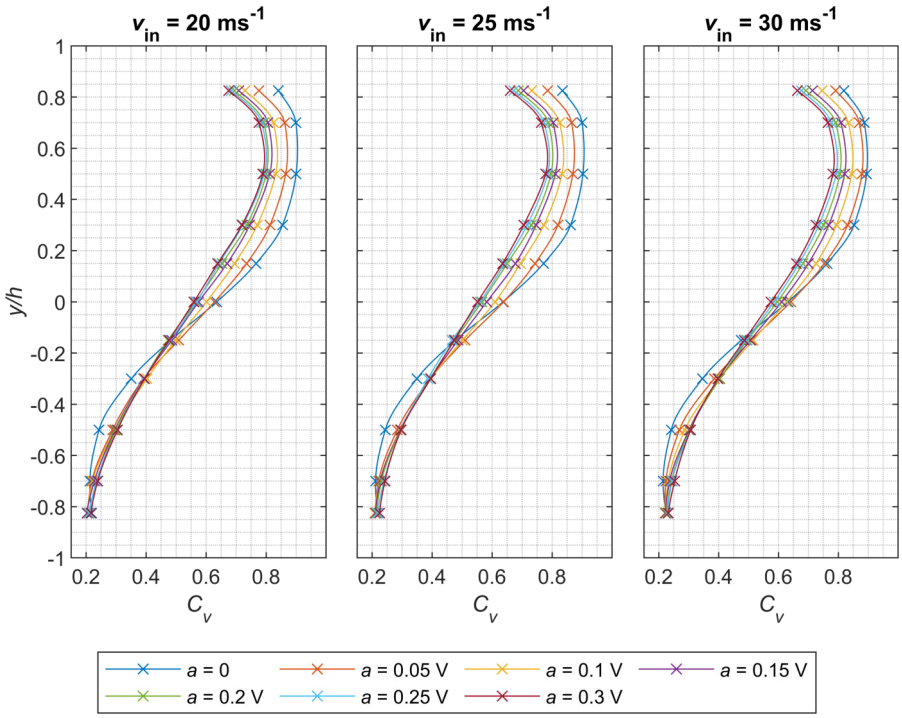
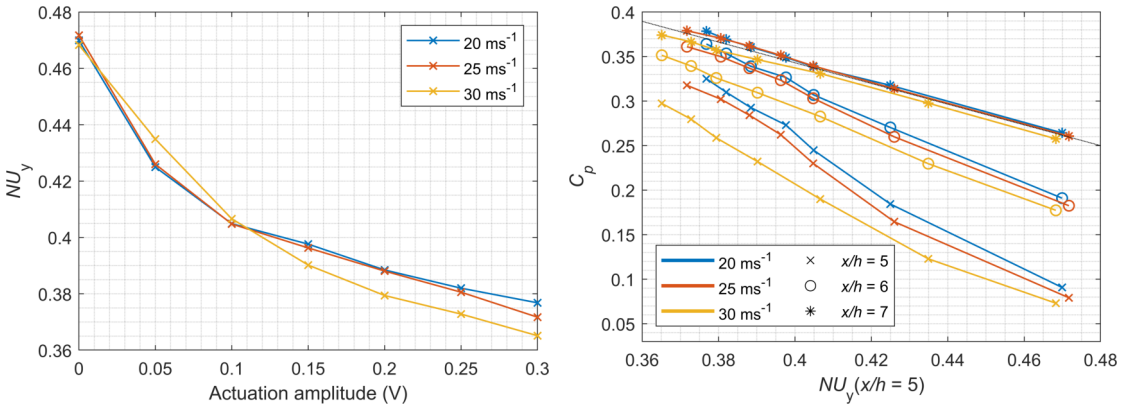


Figure 4.17: Centre span velocity profiles at $x/h = 5$



(a) NU_y at $x/h = 5$ vs actuation amplitude

(b) C_p as a function of NU_y at $x/h = 5$

Figure 4.18: NU_{y} at $x/h = 5$

4.4 Spanwise Non-uniform Actuation

So far the input voltage has been identical for all 6 of the loudspeaker drivers, however each driver has its own separate cavity and orifice, so it is possible to achieve a spanwise variation in forcing by varying the amplitude of the signal sent to each individual driver. It has already been established that the flow downstream of the step is non-uniform in the spanwise direction, owing to the finite width of the channel and side-wall effects, therefore it seems reasonable to propose that spanwise non-uniform actuation might be more optimal than uniformly distributed actuation.

Spanwise distributed actuation was previously investigated by Henning & King [114], who used an array of four internal oscillator type actuators across the span of the step edge, and four microphone arrays to estimate the local reattachment point behind each actuator slot from RMS pressure. However, there are several differences between the actuation strategy and aims in the current study to those of Henning & King [114]. Henning & King [114] demonstrated a strong local effect of distributed actuation on reattachment length, and constructed a MIMO controller designed to reject local disturbances in reattachment position, but did not investigate the effects of spanwise non-uniform actuation on the flow other than the reattachment point at four spanwise positions. There was also no investigation of secondary side-wall flow, although their tunnel aspect ratio was significantly larger than in the current work (20 vs 7.5) so the influence of side-wall effects on the rest of the flow were likely less significant.

Crucially, the opposite-side actuation used in the current study differs from the (more typical in the literature) oscillatory blowing/suction used by Henning & King [114]. The influence of the current actuation is expected to be less localised due to the radiating acoustic field with long wavelength compared to the orifice spacing and channel height/width. Despite this, it is not completely clear that the current actuation arrangement should be considered purely acoustic. The 'internal oscillator'/Helmholtz resonator style actuators undoubtedly induce a small local blowing/suction at the orifices, the strength of which will increase with actuation amplitude. It is hypothesized that a large local actuation amplitude could be used to target flow somewhat locally across the span, while the radiated acoustic excitation ensures a baseline of control effectiveness at all spanwise locations.

The drivers are grouped in three sets of two, each pair connected to a single amplifier, such that the actuation is symmetrical about $z = 0$. Preliminary experiments found that to achieve an equivalent effect, the sum of amplitudes of each signal needs to be approximately constant, so that the acoustic power remains similar.

Three spanwise non-uniform configurations of actuation amplitude, a_k, numbered from negative to positive z, were investigated:

Actuators	1 & 6	2 & 5	3 & 4
Orifice centres (z/h)	± 3.125	± 1.875	± 0.625
Config 1	a_1 & $a_6 = 0$	a_2 & $a_5 = 0$	a_3 & $a_4 = 0.3\,\mathrm{V}$
Config 2	a_1 & $a_6 = 0.3\,\mathrm{V}$	a_2 & $a_5 = 0$	a_3 & $a_4 = 0$
Config 3	a_1 & $a_6 = 0$	a_2 & $a_5 = 0.15\,\mathrm{V}$	a_3 & $a_4 = 0.15\,\mathrm{V}$

Table 4.4: Non-uniform actuation amplitudes. Actuators numbered across span from closest to side-wall at $z/h = -3.75$ to side-wall at $z/h = 3.75$

Configuration 1 was chosen to determine if concentrating actuation at the centre span was able to reduce the convexity of the downstream velocity distribution, by increasing shear layer spreading at the centre relative to the rest of the span. It was also hypothesized that the actuation may not be as effective on the secondary side-wall vortices as the (nominally 2D) centre flow, in which case concentrating forcing in the centre could achieve a greater effect for the same power input.

Configuration 2 was chosen to investigate if concentrating forcing at the side-walls has any effect on the streamwise secondary vortices, and if the non-uniformity due to the redistribution of momentum in the side-wall region might be mitigated by stronger actuation at the edges promoting the break up of the longitudinal vortices.

Configuration 3 was chosen after it was found that configuration 1 was effective at increasing shear layer spreading in the centre of the channel compared to spanwise uniform actuation, but made little difference to velocities away from the centre $\pm h$ slice of the channel. It was hoped that actuation from the four central orifices might have a similar effect to the using the centre two orifices only, but across a wider slice of the span.

Hot-wire traverses across the transverse y-z plane were taken at $x/h = 5$ and $x/h = 8.5$

downstream of the step, slightly upstream of reattachment and some way downstream of reattachment but before the flow has developed fully. Figures 4.19 and 4.20 show the spanwise mean and RMS velocity profiles at several y heights, for the traverses at $x/h = 5$ and $x/h = 8.5$ respectively.

The mean velocity profiles show that actuation using only the two centre transducers (configuration 1) does not significantly change the profile shape at heights below $y = 0$. However above $y = 0$ the mean velocity in the centre of the channel between $z/h = \pm 1$ is reduced compared to uniform forcing, with little difference to the velocity elsewhere. Two troughs in mean velocity (and corresponding peaks in RMS velocity) roughly in line with the centres of the actuation orifices are visible at $(x, y)/h = (5, 0.75)$, although by $x/h = 8.5$ these have merged into a single central trough.

In direct comparison to forcing only in the centre, actuation only from the edge transducers has no significant effect on the velocity profiles above $y = 0$ when compared to uniform amplitude forcing, but flattens out the spanwise velocity profiles for $y \leq 0$, reducing the magnitude of the peaks caused by the secondary longitudinal vortices and the velocity in the centre of the channel. The flattening of the peaks near the side-walls indicates that forcing does affect the secondary vortices, and suggests that stronger actuation may suppresses the secondary flow, or enhances its break-up compared to spanwise uniform actuation. Whilst this actuation configuration does appear to reduce the spanwise velocity non-uniformity, it has the opposite effect on the wall-normal (y-direction) uniformity, because the vertical spreading due to the secondary vortices is reduced.

Unlike the previous two configurations, configuration 3 was not particularly effective, having little effect on the spanwise velocity distribution compared to uniform actuation.

NU_{yz} is calculated at $x/h = 5$ and $x/h = 8.5$ for each of the spanwise forcing distributions, presented in Table 4.5. The overall non-uniformity at both x locations is the least for forcing by the centre two transducers (configuration 1), and the most for forcing only by the transducers at the edges (configuration 2). However, the effect of spanwise non-uniform actuation on overall velocity non-uniformity is small compared to difference made by actuation vs no actuation. Therefore, from this point all control is performed with spanwise-uniform amplitude.

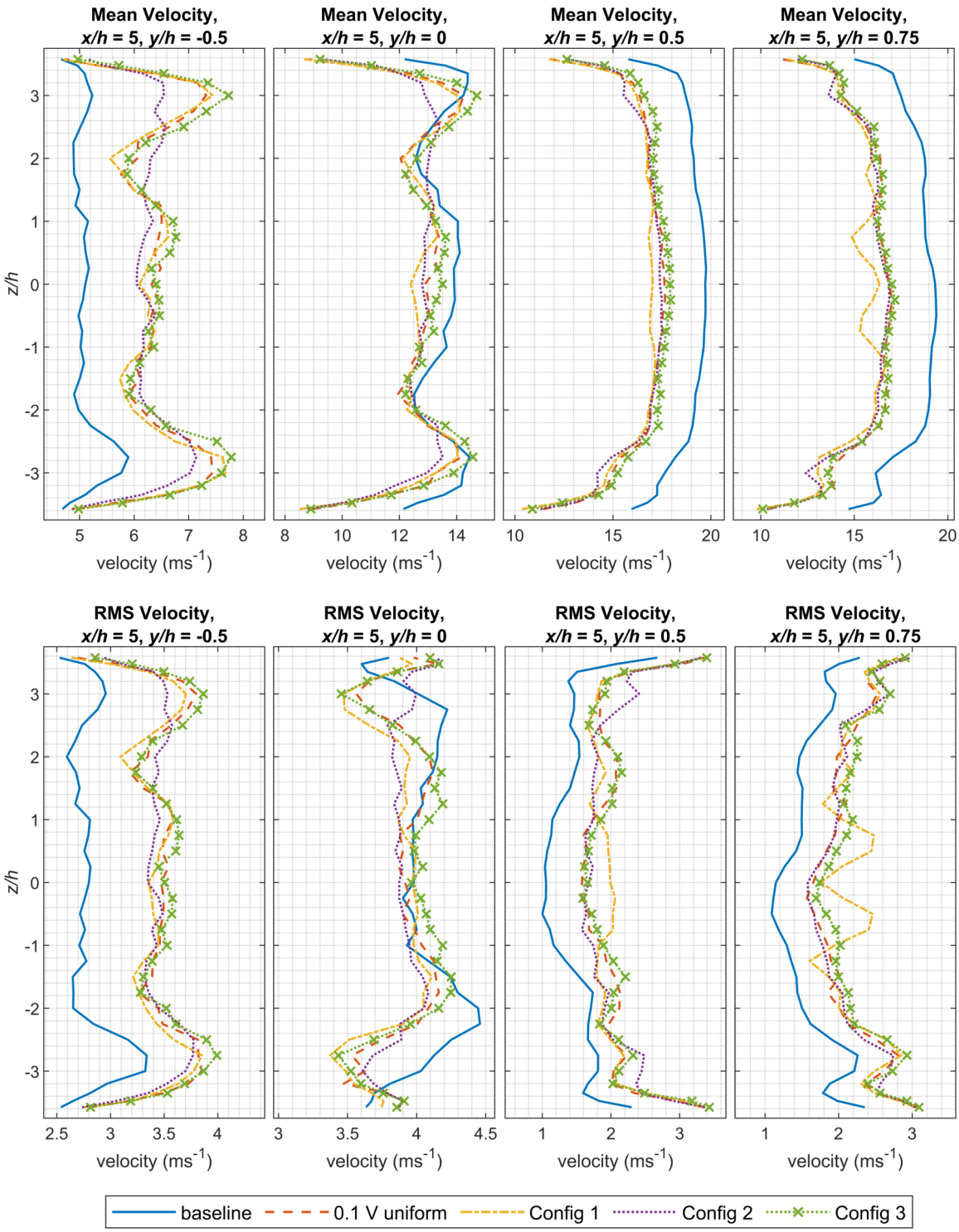


Figure 4.19: Spanwise velocity profiles at $x/h = 5$ for different spanwise actuation configurations

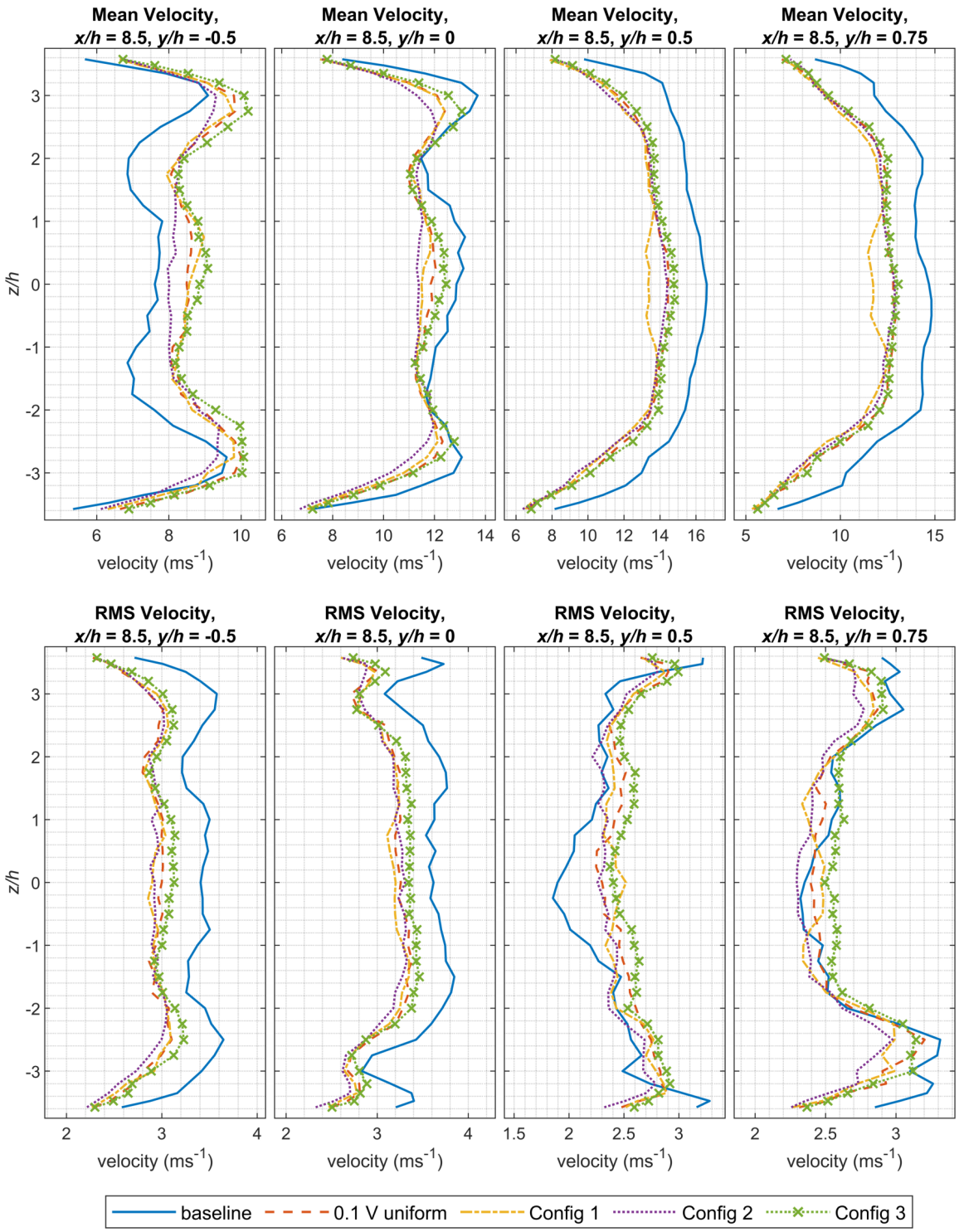


Figure 4.20: Spanwise velocity profiles at $x/h = 8.5$ for different spanwise actuation configurations

x/h	Non-uniformity (NU_{yz})				
	Baseline	**Uniform**	**Config 1**	**Config 2**	**Config 3**
5	0.4741	0.3883	0.3856	0.3900	0.3864
8.5	0.3008	0.2078	0.2001	0.2174	0.2069

Table 4.5: Non-uniformity metric for different spanwise actuation configurations

4.5 Conclusions

This chapter has dealt with the mean effects of opposite-side acoustic actuation on the backward-facing step flow. The effect of actuation on reattachment length was quantified by RMS wall pressure coefficients, and a linear correlation to the C_p value at $x/h = 5$ was demonstrated. The maximum reduction in reattachment length, of at least 24-28% (depending on flow speed), is similar to examples in the literature which employed periodic actuation at the step edge, and greater than those which used 'external' acoustic excitation. Hot-wire traverse measurements were used to examine the effects of actuation on shear layer spreading and the spatial non-uniformity of the flow behind the step. Actuation was shown to reasonably improve flow uniformity between around $x/h = 2$ and $x/h = 10$. The mean spanwise velocity profiles also demonstrate the presence of streamwise aligned vortices along the side-walls, which form due to the interaction between the separated shear layer and the oncoming side-wall boundary layer.

The mean/RMS wall pressure and hot-wire data are consistent with the explanation that acoustic forcing enhances momentum transfer in the separated shear layer, resulting in increased curvature and earlier reattachment. The effect of actuation on recirculation/reattachment length can be easily inferred from the mean and RMS wall pressure curves, which are shifted upstream by increasing actuation amplitude. The upstream shift of mean wall pressure distribution demonstrates that the dynamic pressure of the inlet flow is recovered sooner due to shortening of the recirculation bubble and increased streamline curvature. Similarly, the peak of the RMS wall pressure curve is indicative of the unsteady structures and turbulent eddies in the shear layer impinging on the wall, and has been shown to correlate to the reattachment position [168].

Although a maximum reduction in reattachment length was not yet reached at the amplitudes tested, the wall pressure curves demonatrate an asymptotic relationship between effectiveness and actuation amplitude. Given that unsteady actuation affects the flow by coupling to natural instabilities, it is expected that relative effectiveness diminishes with amplitude up to a maximum determined by the flow physics (e.g. size of coupled structures reaching a geometric maximum, the kinetic energy which can be redistributed by momentum transfer in the shear layer, etc.).

Three different spanwise actuation distributions were tested, with the aim of improving flow uniformity downstream of the step. Although spanwise distributed actuation is not completely novel, to the knowledge of the present author its effects on the spatial velocity distribution and the side-wall vortices have not previously been investigated. The opposite-side Helmholtz resonator type actuators are also somewhat unique, in that they appear to impart both spanwise localised and non-localised/radiating disturbances simultaneously. While distributed actuation does alter the spanwise velocity profiles, notably concentrating actuation near the side-walls successfully suppressed the secondary vortices, the improvements to overall flow non-uniformity compared to uniform actuation are minor.

Chapter 5

Flow Dynamics

5.1 Introduction

Following characterisation of the mean flow and effects of forcing, it is of interest to understand how the flow behaves dynamically. The main aims of this section are to better understand the roles of acoustic (i.e. resonance) and flow structure modes in the BFS flow, to investigate the mechanisms by which acoustic excitation interacts with flow structures, and to determine if there are any dynamics which should be targeted in a control scheme, or that pose limitations to the performance of a feedback controller. These aims are achieved by the following steps:

1. The unsteadiness in the baseline (unforced) flow is quantified, carried out by frequency analysis of unsteady wall pressure measurements and hot-wire point measurements at a range of positions on the centre plane of the test section, and several inlet speeds (Sections 5.2 and 5.3).

2. Acoustic resonances are identified and possible causes investigated by making minor geometric modifications to the test section (Section 5.2.1).

3. The effects of acoustic excitation are characterised by hot-wire frequency spectra at a number of point locations and inlet speeds (Section 5.4).

4. A more complete understanding of the vortex structures in the flow is gained by visualisation of the numerical BFS flow, and the extraction of dynamic modes (Section 5.5).

5. The spanwise distributions of frequency content are inspected, in the interest of identifying any side-wall effects or periodic structures which might be targeted to improve the spanwise uniformity or overall efficiency of control (Section 5.6).

5.2 Baseline Wall Pressure Measurements

Wall pressure measurements were taken using the HCX transducers at streamwise positions $x/h = 2$ to $x/h = 10$ downstream of the step with spacing $x/h = 0.5$, for inlet velocities 17.5, 20, 25, and 30 $\mathrm{m\,s^{-1}}$ (corresponding to Reynolds numbers based on step height $Re_h =$ 21800, 24900, 31000, and 37300, respectively). A total of 8 pressure transducers were used, 2 for upstream total and static pressure, and 6 for wall pressures, connected to the wall tappings via 20 mm lengths of 1.5 mm inner diameter flexible tubing such that attenuation from the tubing is minimised. The 17 wall pressure locations were measured in 3 sets of up to 6 concurrent measurements each for a measurement time 100 s at 4 kHz sample rate: wall tappings from $x/h = 2$ to $x/h = 4.5$, from $x/h = 5$ to $x/h = 7.5$, and from $x/h = 8$ to $x/h = 10$.

Although the transducers were connected to the tappings via the shortest possible tubes to reduce the attenuating effect, the coupling from thinner to larger diameter tube (Figure 3.5) and the volume of air contained in the larger diameter tube and transducer does affect the acoustic response of the measurement connections. The Helmholtz resonance frequency of the thinner tube (neck) and volume of air in the thicker tube/transducer (cavity) is estimated to be around 400 Hz, with some variation due to differences between individual adapters and the lengths of the larger diameter tubes. This resonance is confirmed by the presence of a peak in the wall pressure frequency content of inconsistent shape and exact frequency, depending on the transducer, at around 400 Hz, which can be seen in Figure 5.1. The wall pressure spectra are therefore not considered at frequencies above around 300 Hz.

Additionally, due to the relatively low roll-off frequency and resonances of the 1 m long tubes used to attenuate the acoustic pressure, the forced flow wall pressure measurements are unable to resolve frequencies in the range of the dominant flow structures clearly. Consequently, the frequency content of pressure measurements with acoustic excitation are

not presented, and the forced flow dynamics are investigated by hot-wire measurements in Section 5.4 instead.

Figures 5.1 and 5.2 show the power spectral density (PSD) of the wall pressures for the four velocities, plotted against frequency and Strouhal number based on step height, $St_h = fh/v_{\text{in}}$, respectively. The reasoning for repeating the plots on different axes is to aid in identifying and differentiating between acoustic and flow dynamic phenomena. Acoustic resonances are geometry dependent, hence present as peaks at constant frequency regardless of flow speed, while fluid dynamic phenomena are expected to have constant Strouhal number. Acoustic peaks are typically also sharp compared to flow phenomena peaks, due to the unsteadiness in the flow causing frequency spread, although there may also be some slight broadening of the acoustic peaks if flow structures lock on to or are induced by the acoustic resonance.

5.2.1 Identification of Acoustic Resonances

Two main acoustic resonances are identified from the pressure spectra in Figure 5.1: A strong, sharp, peak at 310 Hz, which is determined to be the half-wave resonance of the test section and upstream channel/bell mouth; and a peak at 21 Hz, corresponding to the Helmholtz resonance of the cavity and neck formed by the plenum and test section.

Both peaks are visible at all pressure tapping locations and do not shift with flow velocity, although the 21 Hz content does weaken with downstream distance. The cause of each of the resonances was inferred from the change in peak frequencies due to the geometric extension of the test section, outlined in the 'Effect of Extending Test Section' section below.

A weaker peak at approximately 155 Hz is also seen in the measurements closer to the step, the frequency of which appears to increase slightly with velocity. Despite the frequency shift, no evidence of a strong, persistent, coherent structure/motion at this frequency is found in the hot-wire measurements in section 5.3, although it does lie within the range of frequencies corresponding to vortex structures. While a clear explanation for this content is not proposed, it is concluded that this peak is most likely acoustic. It is possible that the slight increase in frequency with flow speed is caused by one or more weak resonance modes

being driven by flow structures. However, it is later seen (in Figure 5.5a) that lengthening of the test section does not appear to affect the frequency of the ∼155 Hz peak. A very broad peak at around 150 Hz is also identified in the pre-multiplied power spectra of the spanwise hot-wire traverse in the inlet channel $2.5h$ upstream of the step, shown in Figure 5.30a of Section 5.6. These observations suggest that the ∼155 Hz peak may be caused by a weak resonance mode of the plenum or bell-mouth.

Figure 5.3 shows the wall pressure PSDs at $x/h = 2$ downstream of the step, zoomed into the strong 310 Hz peak. A small but sharp dip near the peak frequency is seen at 306 Hz. Clearly this dip is acoustic and is not related to the measurement connections, as it is seen at all inlet velocities and for all tappings/transducers, and suggests a very narrow bandwidth attenuation at 306 Hz, for which there is not an obvious explanation. The possibility that the dip is caused by attenuation by the unforced actuation cavities is ruled out in section 5.2.1, where it is demonstrated that the attenuating effect of the unforced Helmholtz resonators does not affect the sharp dip. The very sharp peaks seen are due to electrical noise and/or the blade passing frequency of the blower, and are proportional to the inverter driver frequency.

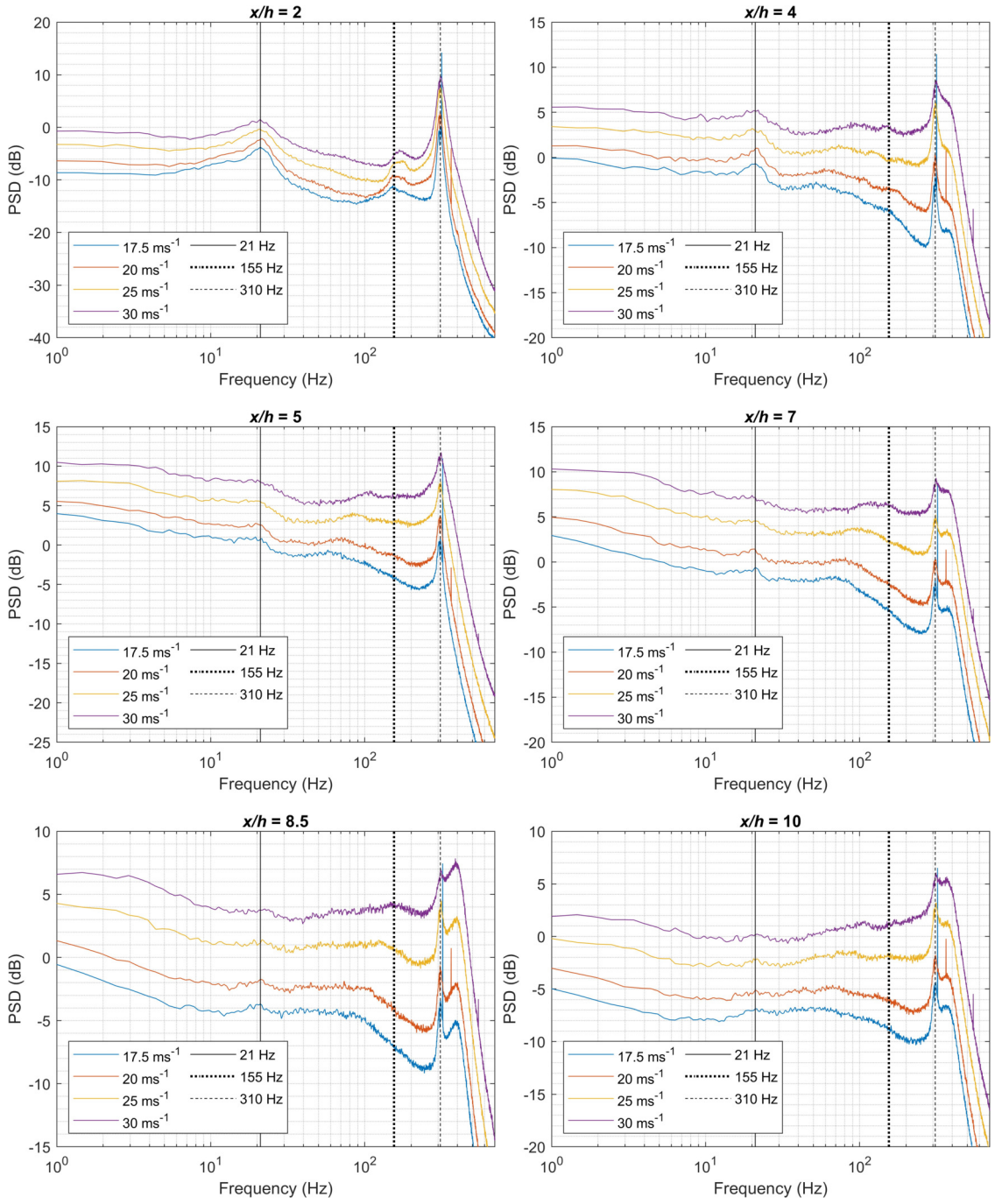


Figure 5.1: Baseline wall pressure PSDs plot against frequency in Hz (actuation cavities open)

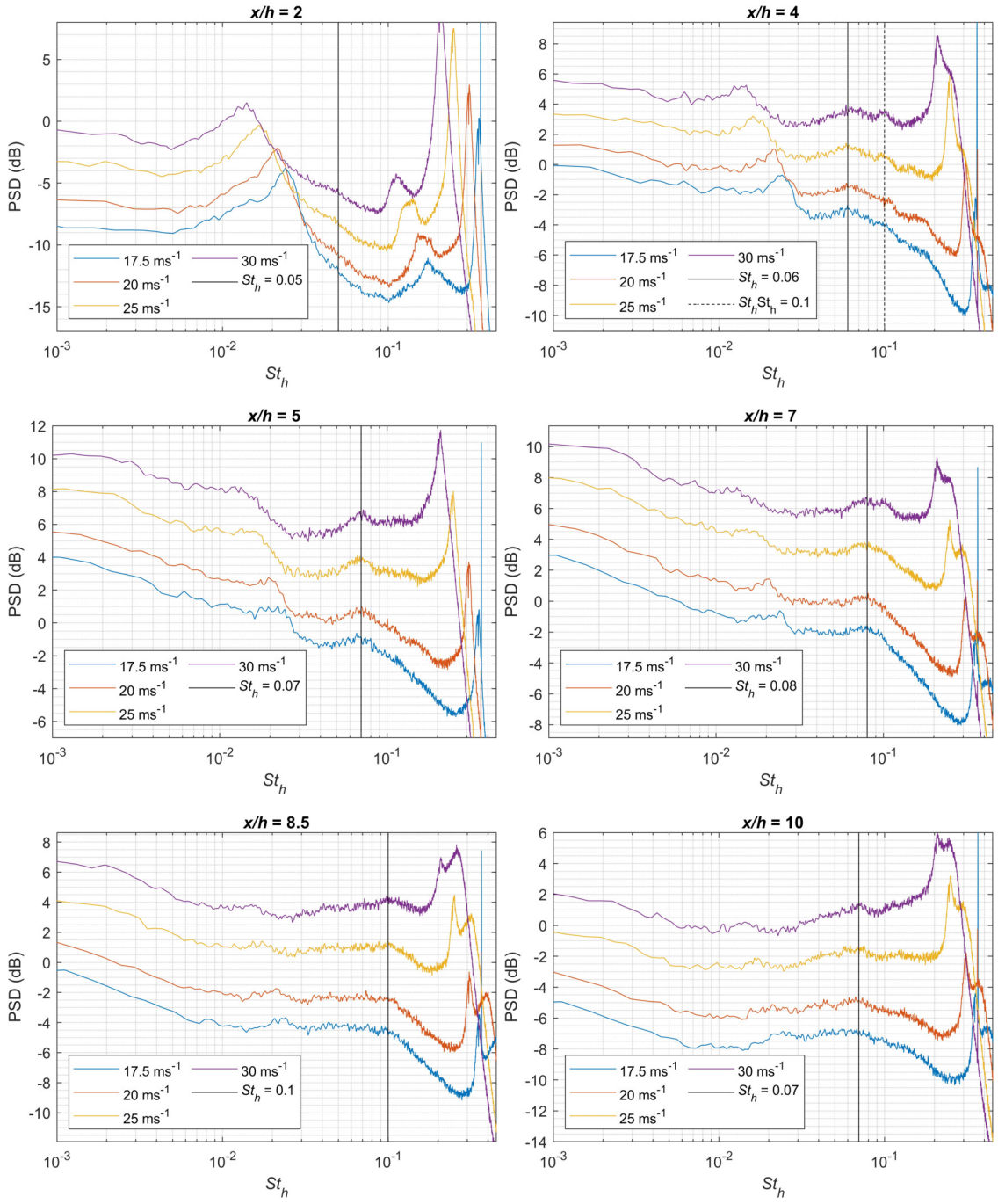


Figure 5.2: Baseline wall pressure PSDs plot against Strouhal number (actuation cavities open)

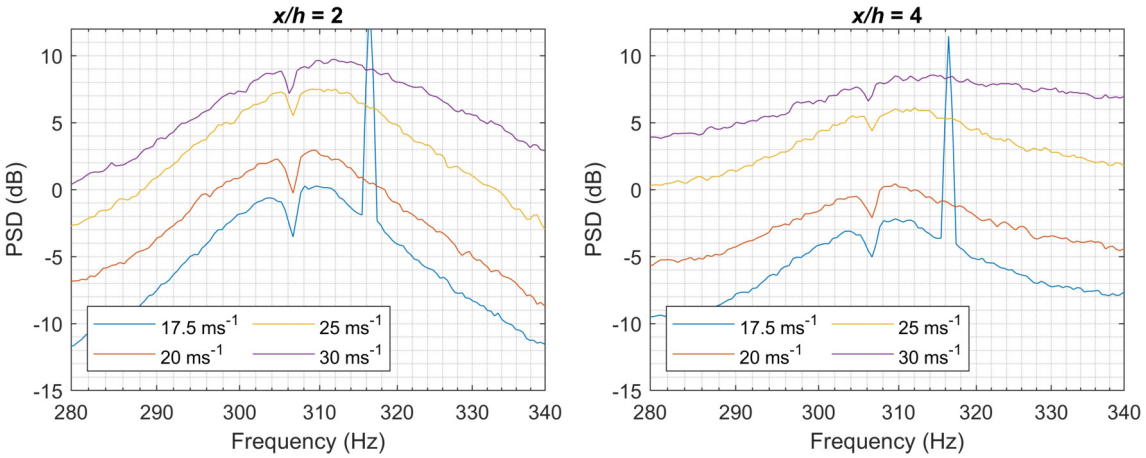


Figure 5.3: Wall Pressure PSDs at $x/h = 2$ and $x/h = 4$, actuation cavity orifices open. Zoomed in to 300 Hz peak

Effect of Actuation Cavities

The wall pressure measurements displayed so far were taken with the actuation cavity orifices open, which is the default configuration. However, it is of interest to determine if the cavities themselves have any effect on the flow. An unforced Helmholtz resonator mounted in the wall of a channel attenuates pressure fluctuations at its resonant frequency [170], although it is not trivial to accurately calculate the amount of attenuation analytically. To assess the amount of attenuation and possible effects of the unforced cavities on the flow, the orifices were sealed with tape and the baseline wall pressure measurements were repeated for the first 6 pressure tapping locations.

Figure 5.4 shows the comparison of the PSDs of wall pressures at $x/h = 2$ and $x/h = 4$ with and without the actuation orifices sealed. The effect of the cavities at all inlet velocities and locations is to reduce the magnitude of the strong peak around 300 Hz slightly, and also the magnitude of the bump at ~155 Hz where it is present. With the actuation orifices sealed, the strong peak is at 300 Hz, but increases to 310 Hz when the orifices are open. The 'true' dominant resonance frequency of the installation is 300 Hz, however the slight misalignment between this resonance and the narrow-band attenuation by the actuation cavities, which provide approximately 10 dB of attenuation at 295 Hz, results in the shift in apparent frequency of the resonance to 310 Hz. Sealing the actuation cavities does not appear to have any effect on the sharp dip at 306 Hz, other than the general attenuation of content in this frequency range, therefore it is concluded that the dip is not caused by

the cavities.

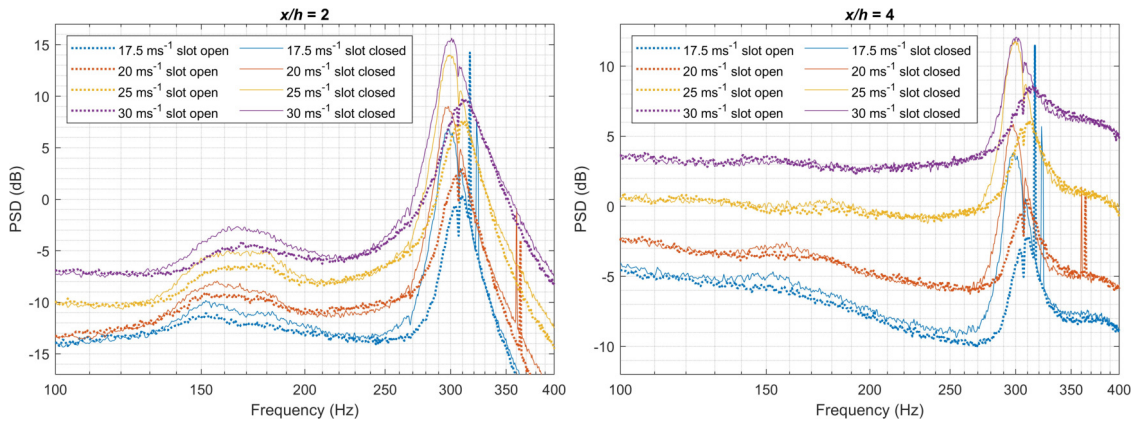


Figure 5.4: Wall Pressure PSDs cavity orifices open vs taped over

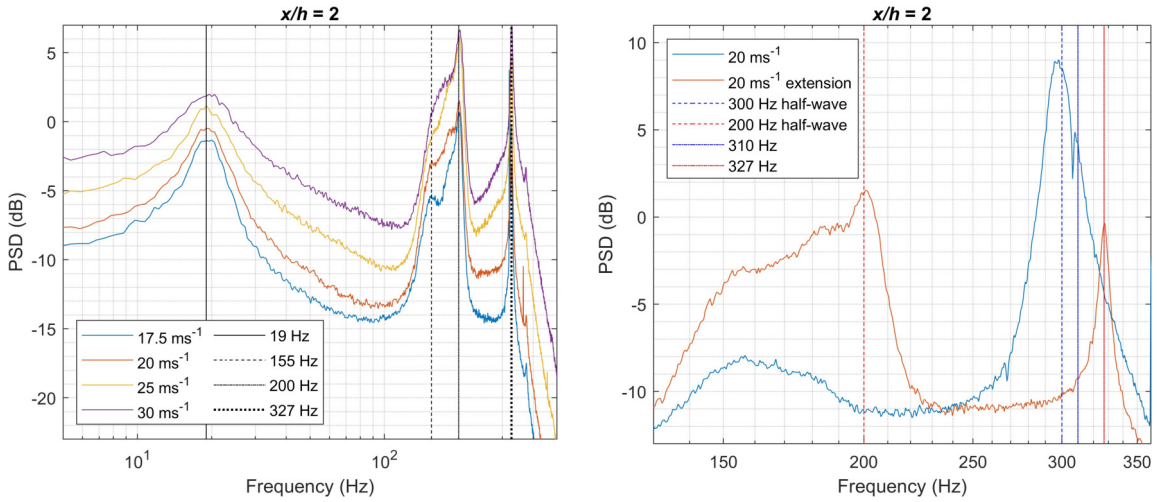
Effect of Extending Test Section

It was hypothesized that the two strong peaks at 21 Hz and 300 Hz are the Helmholtz resonance of the cavity-neck system formed by the plenum and test section, and the half-wave 'organ pipe' resonance of the test section and upstream channel/bell mouth, respectively. The half-wave resonance frequency of a channel with open ends on either side is given by $f = c/2L_c$, where c is the speed of sound and L_c is channel length. A frequency of 300 Hz at 30 °C therefore corresponds to an equivalent channel length of 0.582 m, close to the combined length of the test section and upstream channel/bell-mouth (170 mm bell-mouth and coupling section + 50 mm test section upstream of step + 300 mm test section downstream of step = 0.52 m not accounting for bell mouth curvature). Similarly, for this arrangement the Helmholtz resonance is estimated to be $f_H = 23.7$ Hz (based on an equivalent neck length 1/2 the wavelength of 300 Hz) which is remarkably close to 21 Hz.

To verify these hypotheses, a 0.2 m extension was added to the exit of the test section, to increase the wavelength of the acoustic resonances without significantly altering flow behaviour. The baseline wall pressure measurements were then repeated for the first 6 pressure tappings, with actuation orifices sealed. Increasing the channel length by 0.2 m would be expected to reduce the half-wave resonance frequency of the test section to $c/2L_c = 349/(2 \times (0.582 + 0.2)) = 223$ Hz, while repeating the calculation of Helmholtz resonance frequency, this time for an equivalent neck length $L_{eq} = 0.782$ m, gives $f_H = 20.5$ Hz, approximately 3 Hz lower than the estimate for the unextended test section.

Figures 5.5a and 5.5b show the $x/h = 2$ PSDs with the extension for all four inlet speeds, and a comparison of the PSD with/without the extension between 140 and 340 Hz, for only 20 $\mathrm{m\,s^{-1}}$ inlet speed. As before, the identifiable peaks in the spectra stay at constant frequencies regardless of inlet speed. However, the lower frequency peak has been shifted from 21 Hz to 19 Hz, and the high frequency peak appears to have split into two separate peaks at 200 Hz and 327 Hz. The reductions in frequency of the low and high frequency peaks from 21 to 19 Hz and 300 to 200 Hz, respectively, are approximately consistent with the estimations, therefore it is concluded that the hypotheses regarding the presence of a half-wave and Helmholtz resonance are likely correct.

It is less clear what might be the cause of the 327 Hz peak seen when the extension is in place. This peak does not correspond to a peak in the frequency content of the un-extended test section flow, nor does it match a harmonic frequency of the identified resonances. Regardless of the cause, the sharpness of the 327 Hz peak, and its invariance to flow speed indicate that it is acoustic. The extension does not appear to effect the frequency of the ~155 Hz content, which implies that it is not caused by a resonant mode of the test section, but may be a resonance of the upstream plenum.



(a) With 200 mm extension at multiple inlet speed, sealed actuation orificess

(b) With and without 200 mm extension at 20 $\mathrm{m\,s^{-1}}$, sealed actuation orifices

Figure 5.5: Effect of 200 mm extension on wall pressure frequency content

5.2.2 Identification of Flow Features

Figure 5.2 shows the pre-multiplied wall pressure power spectral density ($St_h\Phi$, where Φ is PSD) plotted against Strouhal number based on the step height, $St_h = fh/v_{\text{in}}$, for the same x locations as in Figure 5.1. Pre-multiplying the power spectra by the frequency unit scales it such that the area under the graph represents energy (the square of the quantity) when plot on a logarithmically scaled frequency axis, i.e. $\overline{u}^2 = \int \Phi(k)dk = \int k\,\Phi(k)d(\log(k))$. Peaks in the pre-multiplied spectra therefore correspond to the most energetic scales in the flow, even when plot as dB (i.e. $10\log_{10}(St_h\Phi)$), which is done for legibility.

Constant St_h peaks between $St_h = 0.06$ and $St_h = 0.1$ are identifiable from the plots in Figure 5.2, the number and frequency of which vary with x location. A clearer presentation of the evolution of frequency content peaks is presented in Figure 5.6, which shows the baseline wall pressure PSDs at all of the pressure tappings, between $St_h = 0.005$ and 0.2, for each inlet velocity. The PSD at each x location is offset by 2 dB compared to the previous location for legibility.

Figure 5.6 appears to show three distinct flow phenomena associated with peaks/corner frequencies, all in the range associated with the shedding/cross-flapping mode:

- A peak/corner frequency which increases in frequency with downstream location, indicated by the dotted magenta line, starting at $St_h \approx 0.04$ at $x/h = 2$ and reaching $St_h \approx 0.075$ around the reattachment location (The PSD of the tapping closest to reattachment, $x/h \approx 7$, is plotted in black in Figure 5.6). Downstream of the reattachment location, the gradient of the peak locus with downstream distance increases, reaching $St_h \approx 0.12$ at $x/h = 10$.

- A very broad bump/decrease in gradient seen around and downstream of reattachment, also increasing with streamwise position, from $St_h \approx 0.03$ near reattachment to $St_h \approx 0.06$ at $x/h = 10$, indicated by the magenta ellipses in Figure 5.6.

- A small peak at $St_h \approx 0.1$ which appears around the middle of the separated region, indicated by the dashed magenta line.

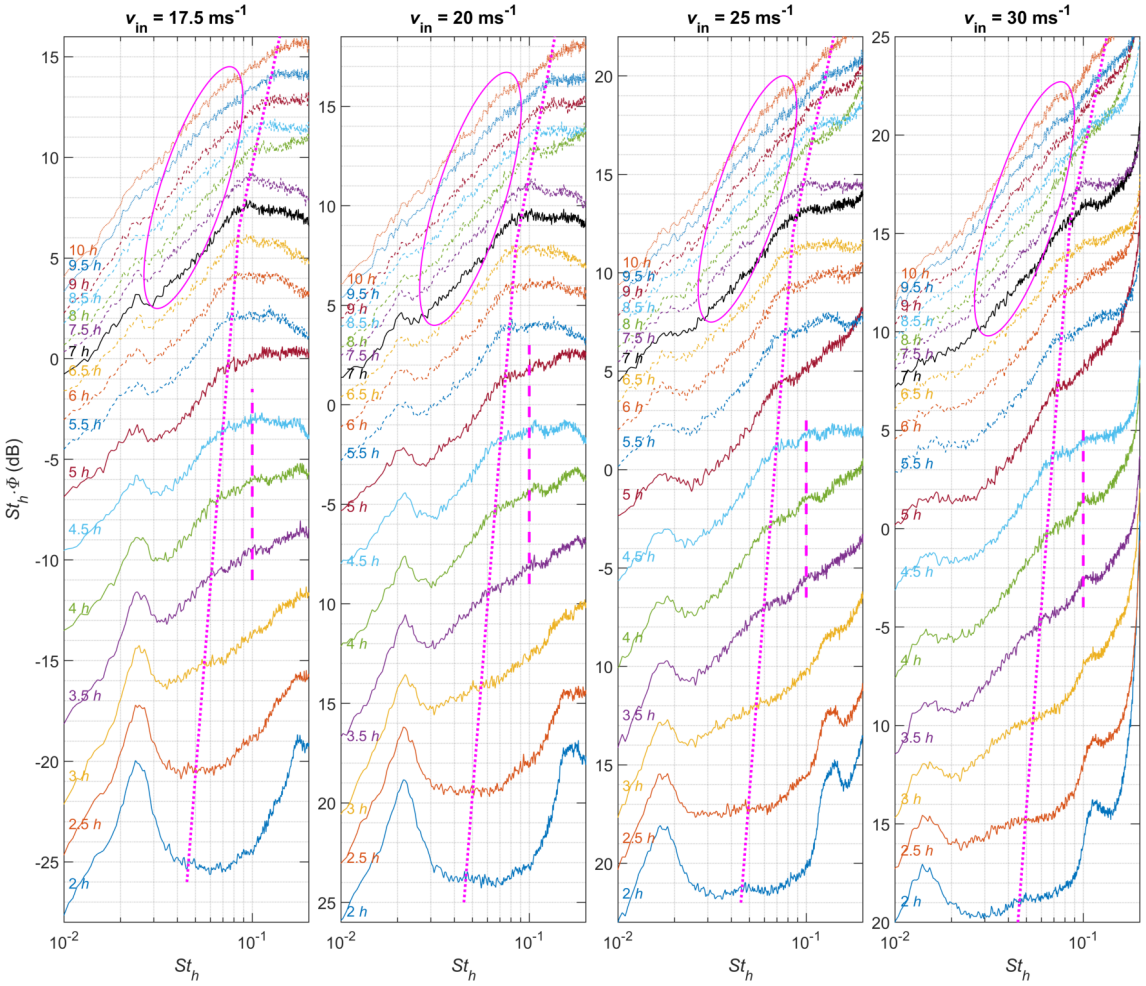


Figure 5.6: Streamwise evolution of baseline wall pressure PSD for each velocity (actuation cavities open). Measurement closest to estimated reattachment point in black. Each PSD offset by 2 dB compared to the previous location.

Based on the Strouhal numbers of the observed peaks/corner frequencies, it seems likely that all three relate to various scales of the shedding mode, although this is not conclusive from the data. Inside the separated region, the increase in frequency of the peak with streamwise position could be explained by the upstream travel of the structures that are 'torn' from the shear layer and re-ingested at the point of reattachment, which would be expected to start at the shedding mode frequency and amalgamate as they travel upstream in the recirculating flow. Downstream of reattachment, increasing peak frequency may be explained by the breaking up of larger coherent structures into a greater number of smaller eddies, although this does not appear to be supported by the hot-wire data, given in sections 5.3 and 5.6.

The wall pressure PSDs do not appear to show a clear constant St_h peak at low frequencies

($St_h = \mathcal{O}(0.01)$) where the flapping mode is expected. Given the Helmholtz resonance of the plenum and test section at 21 Hz, it seems likely that the longitudinal flapping mode has either locked on to this acoustic mode, or that is is undetectable due to its proximity to the large acoustic disturbance.

5.3 Baseline Hot-Wire Velocity Measurements

5.3.1 Identification of Coherent Modes

Hot-wire measurements were taken for a range of points on the centre plane of the test section at $20\,\mathrm{m\,s^{-1}}$ inlet speed, shown in Figure 5.7, for 1000 s per point. Initial points were chosen upstream of the step, near/in the shear layer, and along the lower wall around reattachment. Some additional points were then chosen near to those showing interesting frequency content in an attempt to better identify localised flow phenomena.

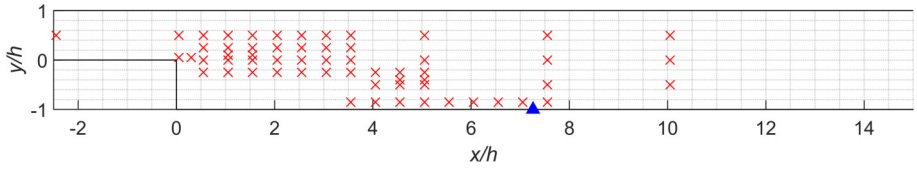


Figure 5.7: hot-wire measurement points at centre plane ($z = 0$). Estimated reattachment point at $v_{\mathrm{in}} = 20\,\mathrm{m\,s^{-1}}$ shown by blue triangle

Figure 5.8 shows the pre-multiplied power spectral densities ($St_h \cdot \Phi$, where Φ is the PSD) of the hot-wire measurements, grouped as measurements at constant y value, so that each plot shows the evolution of frequency content with distance downstream of the step.

Several flow phenomena can be inferred from peaks in the hot-wire PSDs, with reference to the expected modes reported in the literature:

1. The Helmholtz resonance of the plenum and test section, which is observed as a peak at 21 Hz ($St_h = 0.021$ at $v_{\mathrm{in}} = 20\,\mathrm{m\,s^{-1}}$), previously explained in Section 5.2.1. The 21 Hz content is seen strongly along the line $y/h = 0.5$ (Figure 5.8c) up to at least $x/h = 3.5$ downstream of separation, and to a lesser extent along $y/h = 0.25$ (Figure 5.8b) up to around $x/h \approx 2$. This peak is taken as evidence of longitudinal oscillation of the fluid in the upstream channel/test section, i.e. the 'neck' of the Helmholtz resonator.

2. Vortex roll-up/Kelvin-Helmholtz instability (the shear-layer mode), seen as a fairly broad/shallow peak at $(x, y)/h = (0.5, 0)$ with $St_h \approx 0.9$, ($f \approx 900\,\text{Hz}$, $St_\theta \approx 0.017$). Although the identified roll-up frequency is slightly higher than the typically agreed upon value of $St_\theta \approx 0.012$, it is still within the range reported in the literature, which spans at least from $St_\theta \approx 0.009$ to 0.025 [34, 35, 36, 37, 38, 39, 40, 41, 54, 42, 110]. The spread in reported St_θ may indicate that momentum thickness is not the appropriate length scale to characterise vortex roll-up. At the very least, it demonstrates the complex multi-scale nature of BFS flows.

3. The pairing/merging or shear layer vortices can be seen at y positions above the step (Figures 5.8a, 5.8b, and 5.8c) as a series of peaks which gradually decrease in frequency with distance downstream of the step. Figure 5.8a shows that between $(x, y)/h = (0.5, 0)$, which is assumed to be around where roll-up occurs, and $(x, y)/h = (1, 0)$, the peak frequency approximately halves, indicating that the first pairing happens almost immediately after vortex roll-up. This behaviour is later confirmed by CFD results in section 5.5. Subsequent merging occurs gradually with distance away from the step, reaching $St_h \approx 0.2$ (the 'step' mode) around half way through the reattachment region ($x/h = 3.5$).

4. The 'shedding' mode, seen as a peak or corner frequency between $St_h \approx 0.07$ and $St_h \approx 0.12$ ($f \approx 70\,\text{Hz}$ to $f \approx 120\,\text{Hz}$), at x locations downstream of $x/h = 5$. The apparent spread of the peak/corner frequency downstream of reattachment with y position suggests that the shedding mode may be multi-scale, rather than a single large coherent structure. This is consistent with the findings of Hu et al. [91], who extracted DMD modes capturing multiple scales of shedding from a numerical BFS simulation.

5. A weak peak/corner frequency at $St_h \approx 0.015$ ($f \approx 15\,\text{Hz}$,), identifiable at heights $y/h = -0.25$ and $y/h = -0.5$ (Figures 5.8d and 5.8e). This appears to be the dominant mode inside the recirculation bubble, which supports that it may be a 'flapping' mode of the shear layer. Dynamic mode decomposition of CFD data in section 5.5 confirms that the flapping mode has $St_h \approx 0.013$.

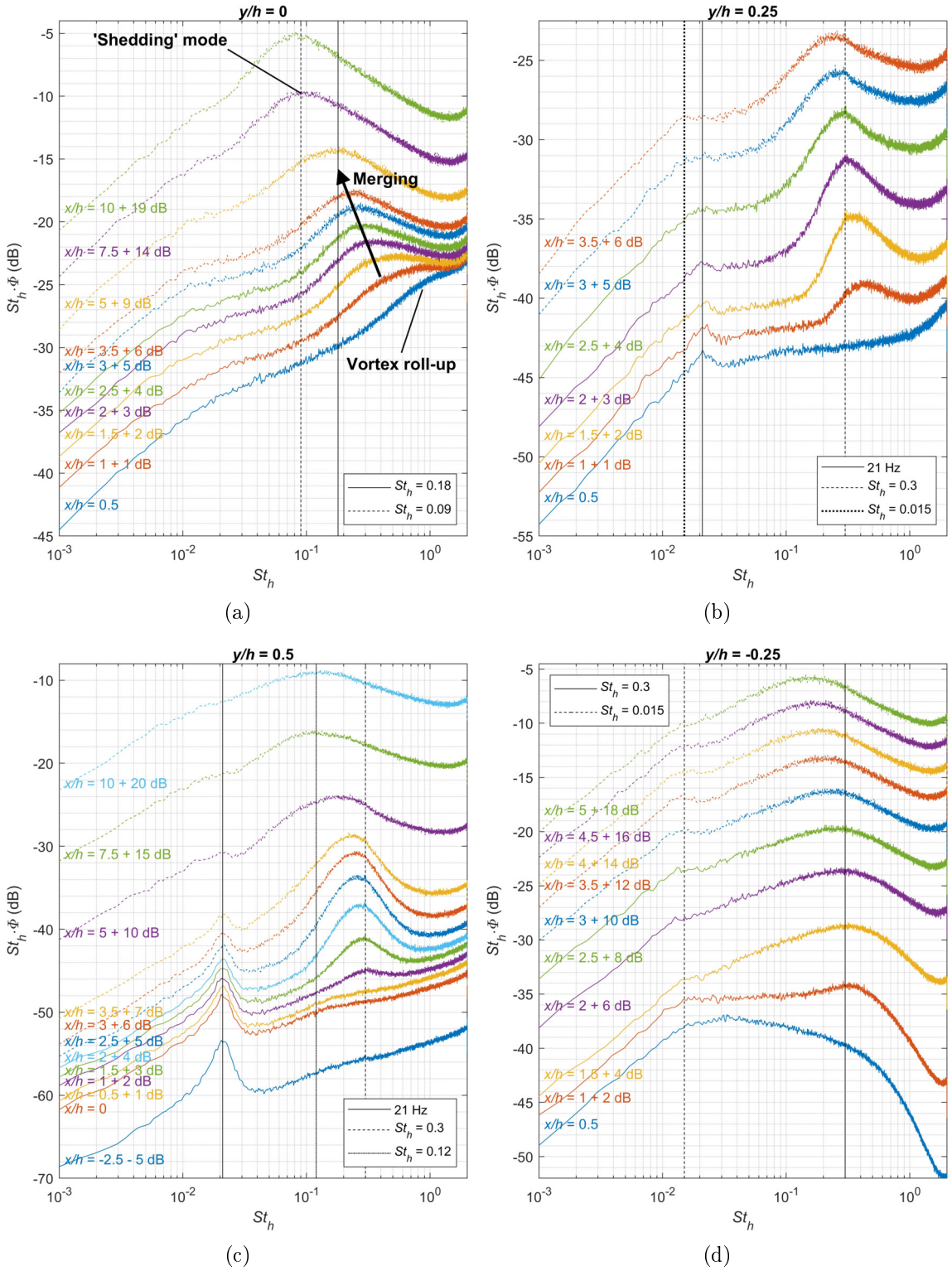
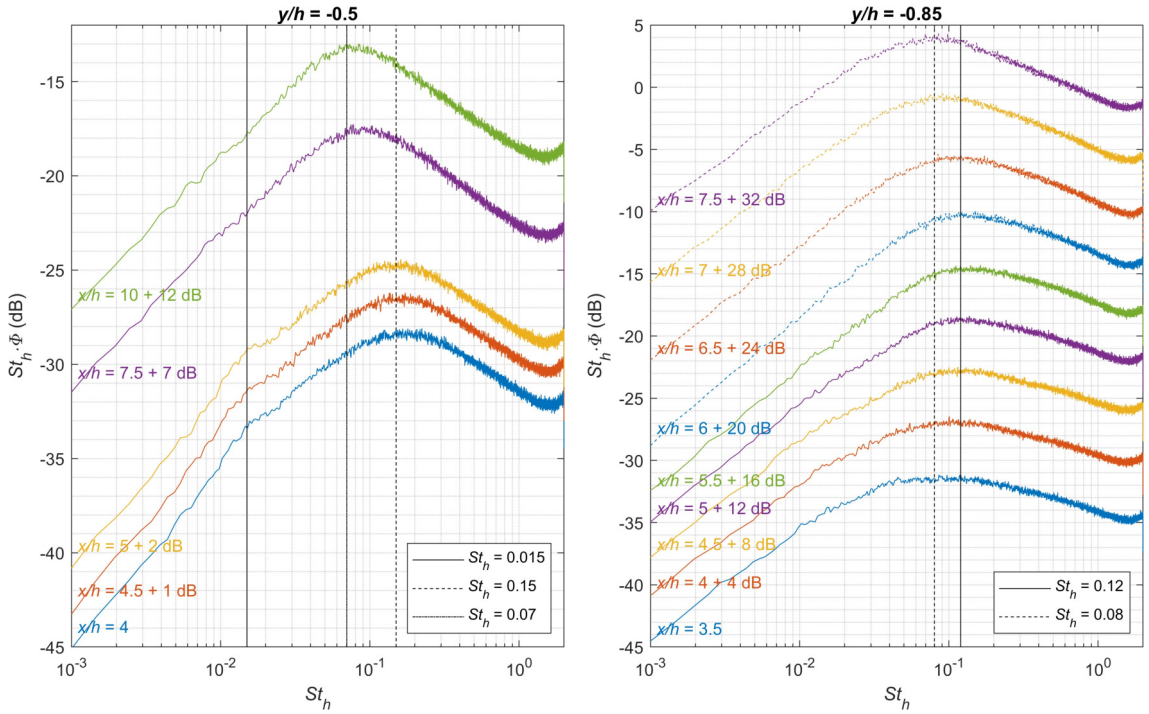


Figure 5.8: PSDs of hot-wire point measurements at $20\,\mathrm{m\,s^{-1}}$



(e) (f)

Figure 5.8: PSDs of hot-wire point measurements at $20\,\mathrm{m\,s^{-1}}$. PSD at each location offset for legibility by the amount indicated in the plot line labels.

The broadness and gradual decrease in frequency of the main vortex peak is indicative of the inconsistent frequency/phase of vortex roll-up and transport speed due to random unsteadiness [33, 40]. Winant and Browand [33] explain that as the shear layer spreads out downstream of separation, the shear layer vortices will also grow and slow down until eventually consecutive pairs of vortices make contact and merge into larger vortex structures able to conserve velocity enough that the subsequent vortex does not immediately catch up. If vortex roll-up were perfectly periodic and the flow free of random unsteadiness, pairing would be expected to occur at fixed positions and the passing of merged vortex structures seen at exact sub-harmonics of the roll-up frequency. However, inconsistent roll-up and/or transport speed leads to the occasional passing of merged structures across a large range of streamwise locations, with the likelihood of vortex amalgamation increasing with downstream distance. After ensemble averaging the frequency domain data, this inconsistent merging is seen as a gradual decrease in frequency of the main vortex peak with distance from the step.

The hot-wire measurements near to the lower wall at $y/h = -0.85$ (Figure 5.8f) do not show any strong peaks in frequency content, which can be explained by the influence of the proximity of the wall. Wall-tangential fluctuations are damped by viscous shear due to the no-slip condition, whereas wall-normal fluctuations are suppressed by the impermeability constraint at the solid wall.

Despite the lack of sharp peaks, the corner/roll-off frequencies of the $y/h = -0.85$ PSDs are consistent with the shedding mode, indicating that the majority of content near the wall is captured by this and larger scales. The hot-wire spectra do not appear to show any evidence of flow phenomena corresponding to the ∼155 Hz content seen in the wall pressure spectra at x locations closer to the step, which supports that this is not a flow structure mode of the unforced backward-facing step flow.

It was hypothesized from the lack of identifiable flapping mode peak in the wall pressure spectra (Figures 5.6 and 5.2) that the flapping mode may have locked on to the Helmholtz resonance at 21 Hz. However, the identification of the flapping peak/mode at $St_h = 0.015$ confirms that this is not the case.

Roll-up/Shear-layer mode

Although the broad peak at $(x, y)/h = (0.5, 0)$ with $St_\mathrm{h} \approx 0.9$ ($St_\theta \approx 0.017$) is consistent with the expected shear layer mode frequency and location, it is difficult to make definite conclusions from only a single point measurement appearing to capture the roll-up phenomena. Furthermore, while the hot-wire point measurement spectra in Figure 5.8 are high fidelity owing to the long measurement time, the sample rate of 4 kHz limits the maximum frequency that can identified, and the broad peak at $St_\mathrm{h} \approx 0.9$ (corresponding to around 900 Hz) is close to this limit.

A closer look at the roll-up phenomenon can be provided by the 10 s-per-point hot-wire traverse data previously used for the mean flow characterisation, which were measured at a sample rate of 10 kHz and for a greater number of locations around where roll-up is expected to occur. The reduction in data quality due to the shorter measurement time was overcome by using Welch's method with a window length of 500 samples to calculate the power spectral density, and ensemble averaging the PSDs across the span of the test section between $z/h = \pm 1$, over which the frequency content was found to be fairly invariant. PSDs

calculated with such a short window length do not resolve low frequency content; however, only frequencies above the large scale merged vortex frequency (around $St_h \approx 0.3$) are currently of interest.

Figure 5.9 shows the spanwise ensemble averaged pre-multiplied power spectra of the hot-wire traverse measurements some way upstream and downstream of the expected roll-up location along lines of constant y value (or close to constant y value, given slightly different traverse points upstream and downstream of the step). These spectra show a high frequency peak at $St_h \approx 1.6$ ($St_\theta \approx 0.03$) which develops somewhere between the most upstream measurement plane at $x/h = -2.5$ and in line with the step at $x/h = 0$. The peak frequency then decreases with streamwise distance from the step, although at different rates depending on the y position of the measurements, until reaching the large scale vortex frequency, $St_h \approx 0.3$-0.4.

It seems unlikely that the $St_h \approx 1.6$ peak seen at the step is the roll-up phenomenon, given that it is over twice the typically stated frequency and outside the range reported in literature, $St_\theta \approx 0.009$ to 0.025 [34, 35, 36, 37, 38, 39, 40, 41, 54, 42, 110], and that this dominant frequency is only found close the the step, before vortex roll-up is expected to have occurred. Figure 5.9 illustrates that the apparent roll-up frequency depends on the measurement location, even by several millimetres, which might account for some of the spread in reported values of St_θ. For example, taking the streamwise position $x/h = 0.75$ and wall-normal positions $y/h = 0$, $y/h = 0.1$, and $y/h = 0.225$, one might conclude that the shear-layer mode frequency were $St_h \approx 0.9$, $St_h \approx 1.1$, or $St_h \approx 0.7$ ($St_\theta \approx 0.017$, 0.02, or 0.013), respectively.

In addition to the measurement location, there is also some uncertainty as to whether the roll-up can be characterised by the momentum thickness at separation alone. θ was initially identified as the characteristic scale of shear-layer roll-up in an isolated plane mixing layer, with $St_\theta \approx 0.012$ [38, 171], and it was later concluded by Hasan [39, 40] that the same relationship holds for BFS flows. Despite this, the influence of the lower wall/reattachment marks a significant difference between BFS and free shear-layer flows. Entrainment or re-ingestion of flow into in the recirculation bubble and the upstream propagation of frequency content may be responsible for some of the spread in shear-layer mode Strouhal numbers for different BFS geometries in literature.

Without flow visualisation it is difficult to say at what point a vortex has formed, but the spread of peak frequencies and relatively rapid decrease with streamwise distance suggests that the roll-up period/phase is fairly inconsistent, and that the rolled-up vortices do not persist far before amalgamating into larger scale vortices.

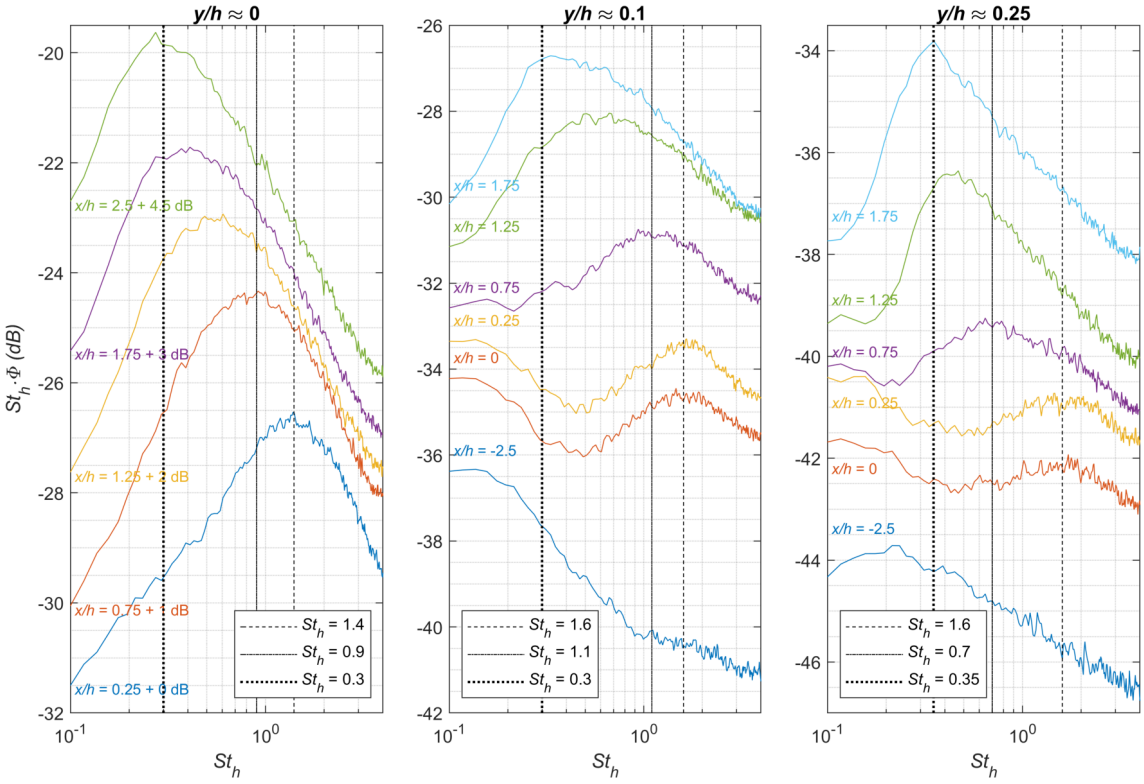


Figure 5.9: Pre-multiplied power spectra of hot-wire measurements around expected roll-up location

Effect of Inlet Velocity

Hot-wire measurements were then repeated for inlet speeds $25\,\mathrm{m\,s^{-1}}$ and $30\,\mathrm{m\,s^{-1}}$ at several of the locations showing the strongest frequency dynamics: $(x, y)/h = (-2.5, 0.5)$, $(2.5, 0.5)$, $(1.5, 0.25)$, $(3, 0.25)$, and $(5, -0.5)$.

Figures 5.10a shows the pre-multiplied PSDs at locations $(x, y)/h = (-2.5, 0.5)$ and $(2.5, 0.5)$ plotted against frequency in Hz, while Figures 5.10b, 5.10c, and 5.10d show the pre-multiplied PSDs at all of the locations against Strouhal number based on step height. The hot-wire PSDs at multiple inlet speeds are consistent with the conclusions made from the $20\,\mathrm{m\,s^{-1}}$ hot-wire data and wall pressure measurements. Figure 5.10a demonstrates that neither the 21 Hz peak (the Helmholtz resonance), or a smaller, sharper, peak at

300 Hz (the half-wave resonance) change frequency with velocity, confirming that these are acoustic and not fluid dynamic phenomena. Conversely, Figures 5.10b to 5.10d show that the $St_h = 0.2$ to 0.3 and $St_h = 0.013$ peaks stay at constant Strouhal number, which supports the hypotheses that these peaks are due to vortex structures and the flapping, respectively.

Unfortunately, neither the momentum thickness of the boundary layer at separation, nor the hot-wire frequency spectrum close to the step edge were measured at inlet speeds other than $20\,\mathrm{m\,s^{-1}}$, therefore it is not possible to make any conclusions regarding the effects of inlet velocity on the roll-up (shear-layer) mode. Despite this, the good agreement of the frequency spectra at the point locations measured, and the general agreement of wall pressure spectra, demonstrate that the flow dynamics, as a function of St_h, are not significantly affected by flow speed.

As discussed in the previous section, it is not clear from single velocity measurements if there is any coupling of flow structures to the acoustic resonances of the rig. However, if this were true then some influence of the acoustic resonance on either the frequency of a particular flow structure, or the strength and periodicity of the flow structure closest to the resonance frequency, would be expected. In either case, the Strouhal number of the vortex peak at a fixed position would be expected to vary with velocity, which it does not for the measurement locations in Figure 5.10. While it is a known phenomenon that flow structures can couple to acoustic tones [42, 48, 172], and this is the mechanism by which the acoustic control in the current study operates, it is concluded that the amplitude of the unforced test section resonance is not sufficient to affect the vortex structures significantly.

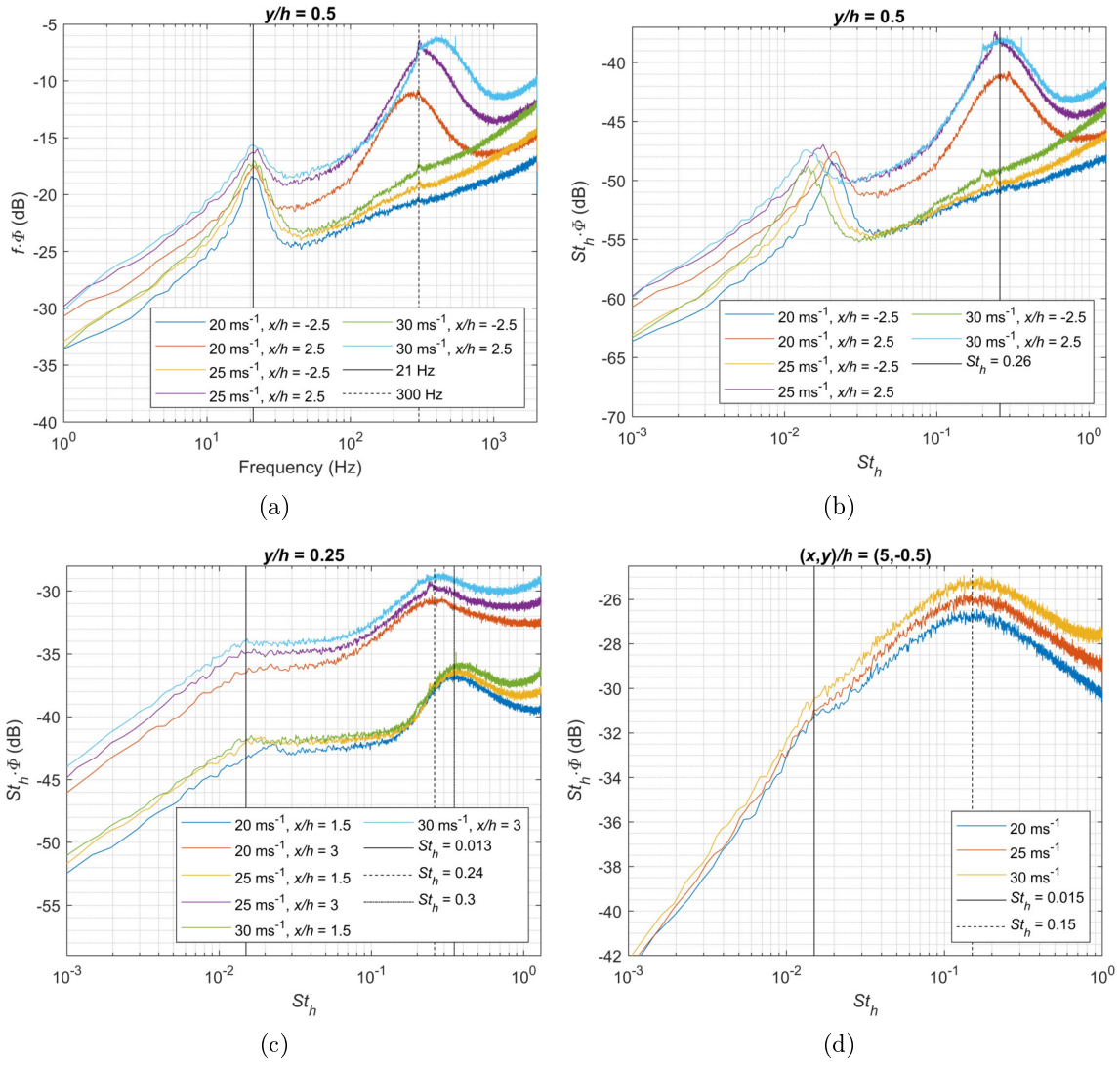


Figure 5.10: hot-wire spectra at multiple inlet velocities

5.3.2 Very Low Speed Flow

In an attempt to investigate the effects of turbulence on the backwards facing step flow, an inlet speed of approximately $1\,\mathrm{m\,s^{-1}}$ ($Re_h = 1200$) was achieved by venting a significant proportion of the air from the blower, just upstream of the inlet to the plenum. This is a low enough Reynolds number that the flow should be in the laminar regime [9], therefore some insight into the effects of turbulence may be gained by comparing the power spectra at this low flow rate with those at the higher speeds.

Several hot-wire point measurements were taken, again for 1000 s per point, along $y/h = 0.25$ from $x/h = 0.5$ to $x/h = 5$, and along $y/h = 0.5$ from $x/h = -2.5$ to $x/h = 1$, with

the intention of capturing vortex formation and evolution, shown in Figure 5.11. As with the higher inlet speeds, there is a strong peak attributed to the Helmholtz resonance of the plenum and test section, although the resonance is now at 23.5 Hz instead of 21 Hz, due to the venting of the flow from the blower.

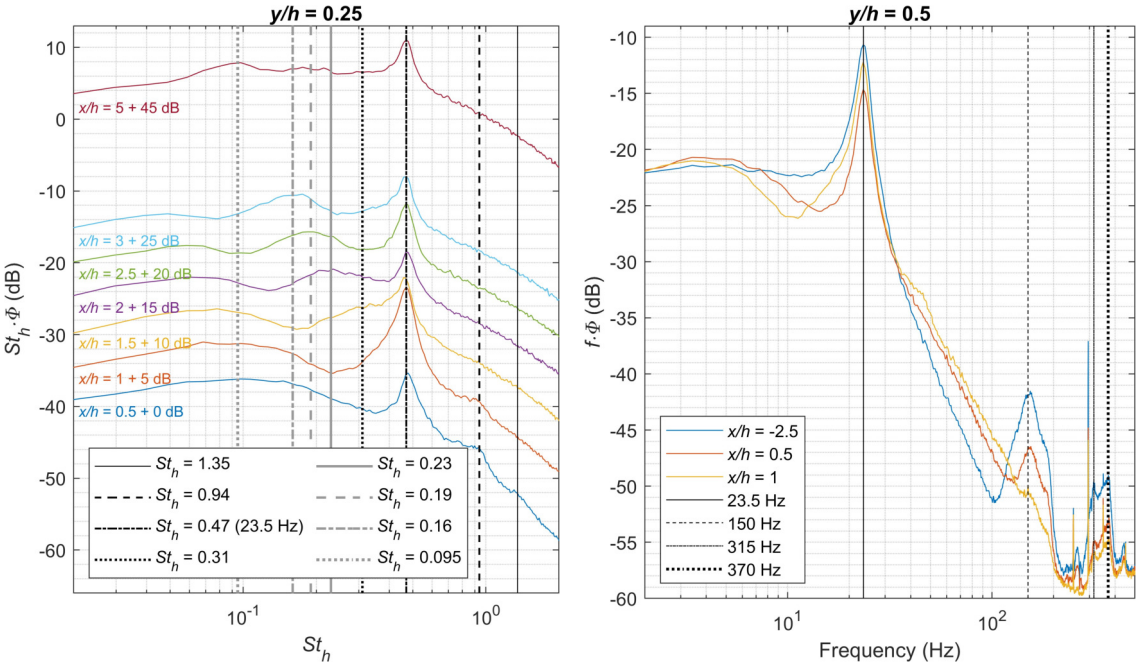
Vortex peaks with similar behaviour as in the faster flows are seen along $y/h = 0.25$. At the two measurement locations closest to the step, shallow peaks are seen at $St_h \approx 0.94$, which most likely correspond to the dominant shear layer roll-up frequency ($St_h \approx 0.8$ at $20\,\mathrm{m\,s^{-1}}$). A smaller, just detectable, peak is also visible at $St_h \approx 1.35$ in the measurement closest to the step, which may be a less dominant roll-up frequency. It should be noted that the roll-up frequencies $St_h \approx 0.94$ and $St_h \approx 1.35$ are approximate harmonics of the Helmholtz resonance ($St_h = 0.47$). Furthermore, the $St_h = 0.47$ peak at $(x, y)/h = (1, 0.25)$ is significantly stronger than at the other measured locations, which is evidence that the first merged vortex mode and the acoustic tone have locked-on.

Just as for the higher flow speeds, a gradual decrease in the frequency of the apparent vortex peaks is seen with downstream distance, from approximately $St_h = 0.47$ at $x/h = 1$ to $St_h = 0.08$ at $x/h = 5$, indicating vortex amalgamation. Interestingly, although the decrease in peak frequency initially appears smooth, all of the identified peaks happen to be at or close to the sub-harmonics of the $St_h = 0.94$ roll-up frequency. This may indicate that vortex merging is much more regular than at higher speeds, or it may be a false correlation drawn due to the broadness of the vortex peaks.

Figure 5.11b shows the three measured $1\,\mathrm{m\,s^{-1}}$ point PSDs along $y/h = 0.5$, for a wider frequency range than the $y/h = 0.25$ PSDs. These point data do not appear to capture any flow structures, but clearly show the 23.5 Hz Helmholtz resonance, along with ~150 Hz and ~300 Hz peaks which are strongest in the channel upstream of the step, consistent with the previously identified acoustic resonances. Unfortunately the PSD resolution at low frequencies is not sufficient to identify a flapping mode in the $1\,\mathrm{m\,s^{-1}}$ flow, $St_h = 0.013$ corresponds to a frequency of 0.65 Hz.

While the low speed measurements provide an interesting example of acoustic-flow structure lock-on, interpretation of the effects of turbulence is complicated by the acoustic coupling. The similarity of the identified roll-up and vortex merging behaviour between the $1\,\mathrm{m\,s^{-1}}$ flow and at higher speeds does however suggest that they are fundamentally

'laminar' phenomena.



(a) Along $y/h = 0.25$. Plot offset indicated in line labels

(b) Along $y/h = 0.5$

Figure 5.11: $1\,\mathrm{m\,s^{-1}}$ inlet speed pre-multiplied hot-wire spectra

5.4 Hot-wire Velocity Measurements under Acoustic Forcing

As for the baseline flow hot-wire spectrum measurements, a range of point locations was measured at $20\,\mathrm{m\,s^{-1}}$ inlet speed with forcing, before measuring only a subset of those points where interesting dynamics are seen at other inlet speeds. Measurements at $20\,\mathrm{m\,s^{-1}}$ and actuation amplitude $a = 0.05\,\mathrm{V}$ were taken for point locations $(x, y)/h = (2.5, 0.5)$, $(1.5, 0.25)$, $(3, 0.25)$, for $1000\,\mathrm{s}$ each, chosen as the query points for the baseline flow which captured the strongest frequency dynamics. A traverse of 9 streamwise locations between $x/h = -2.5$ and $x/h = 5$ along the line $y/h = 0.5$ was also taken to better understand the effect of acoustic actuation on vortex formation and evolution. The hot-wire measurements with forcing were then repeated at inlet speeds 17.5, 25, and $30\,\mathrm{m\,s^{-1}}$ for only $(x, y)/h = (2.5, 0.5)$, where the strongest dynamics were observed.

Figure 5.12 shows baseline pre-multiplied hot-wire velocity PSDs compared to actuation

at the four initial measurement points. The acoustic actuation increases the frequency content slightly for all frequencies above about 0.1 Hz at location $(x, y)/h = (1.5, 0.5)$, and increases content moderately across the entire spectrum for the remaining three locations, confirming that the actuation enhances broadband unsteadiness in the shear layer rather than only causing a narrow band velocity perturbation.

The merged vortex peak observed in the baseline flow, whose frequency gradually decreased from $St_h \approx 0.4$ near the step to $St_h \approx 0.2$ (the step mode) midway through the separated region, is replaced by two distinct peaks around the actuation frequency and half the actuation frequency in the forced flow. The content around the actuation frequency consists of a very sharp spike at exactly the actuation frequency ($f_c = 300$ Hz), emerging from a weaker and broader, but still well defined, peak at around 307 Hz. No sharp spike is seen in the peak at half the actuation frequency, although one is observed at the first harmonic of the actuation frequency ($2f_c = 600$ Hz) for the measurement locations downstream of $x/h = 0.5$ along $y/h = 0.25$ (Figure 5.12) and $y/h = 0.5$ (Figure 5.13), also emerging from a much smaller broad peak.

Both of the spikes at f_c and $2f_c$ seem suspiciously sharp for fluid phenomena, which may suggest they are due to electrical noise from the actuation signal. However, the $2f_c$ spike is not found in the frequency spectra of the hot-wire measurements upstream of $x/h = 1$ along $y/h = 0.5$, or at the measurement in the recirculation bubble at $(x, y)/h = (5, -0.5)$, which would be expected if it were due to electrical interference. Similarly, although not pictured, the f_c spike is not seen at some measurement locations near the corner below the step. Based on this, it is concluded that the sharp spikes are plausibly evidence of non-vortex fluid motion directly coupled to the actuation and its first harmonic, most likely the longitudinal acoustic modes of the test section, and/or a vertical flapping-type oscillation. The broader peaks near the actuation frequency and its harmonic/sub-harmonic demonstrate the coupling of acoustic actuation to flow structures. Although broader peaks are characteristic of flow structures/vortices, for which inconsistent spacing results in frequency spread, the flow structure peaks in the forced flow are considerably narrower bandwidth than those in the baseline flow, indicating that the lock-on of structures to actuation enhances periodicity/consistency.

Figure 5.13 shows the forced pre-multiplied hot-wire PSDs at the points along the line $y/h = 0.5$. As for the mean velocity field, acoustic actuation does not appear to influence the character of the flow upstream of the step, except for the sharp spike attributed to the driven acoustic mode. By $x/h = 1$ downstream of the step, the strong peak at $\sim$307 Hz has developed, which reaches its strongest relative to the broadband spectrum around $x/h = 2$, before gradually decaying until it is almost completely gone by $x/h = 5$. The peak at half the actuation frequency is not present at $x/h = 1$, but has begun to develop by $x/h = 1.5$ and reaches maximum sharpness around $x/h = 2.5$, flattening out considerably by $x/h = 5$. Similarly, the small broad peak at the base of the $2f_c$ spike is not present in the more upstream and most downstream measurement locations, but visible from $y/h = 1.5$ to $y/h = 3.5$.

Unlike in the baseline flow, where the frequency of the merged-vortex peak gradually decreases with downstream distance, the forced flow PSDs do not show transitional peaks between the forcing tone and its sub-harmonic, which is consistent with the expectation that vortex pairing occurs regularly due to enhanced periodicity. The persistence of the $\sim$307 Hz content reasonably far downstream of where the corresponding to sub-harmonic structures develops suggests that the vortices may not fully amalgamate, instead travelling as a packet but retaining some of their original motion. A very slight mound/corner frequency is apparent at $x/h = 3.5$ and 5, with centre at approximately 70 Hz ($St_h \approx 0.07$), the location and frequency of which are consistent with the shedding/cross-flapping mode. A broad shedding peak is also found further downstream, with frequency $St_h \approx 0.08$-0.1, shown in Figure 5.14. While acoustic excitation increases the broadband unsteadiness at low frequencies, it does not affect the sharpness of the Helmholtz resonance at 21 Hz, indicating that there is no interaction between this acoustic mode and the steady amplitude actuation.

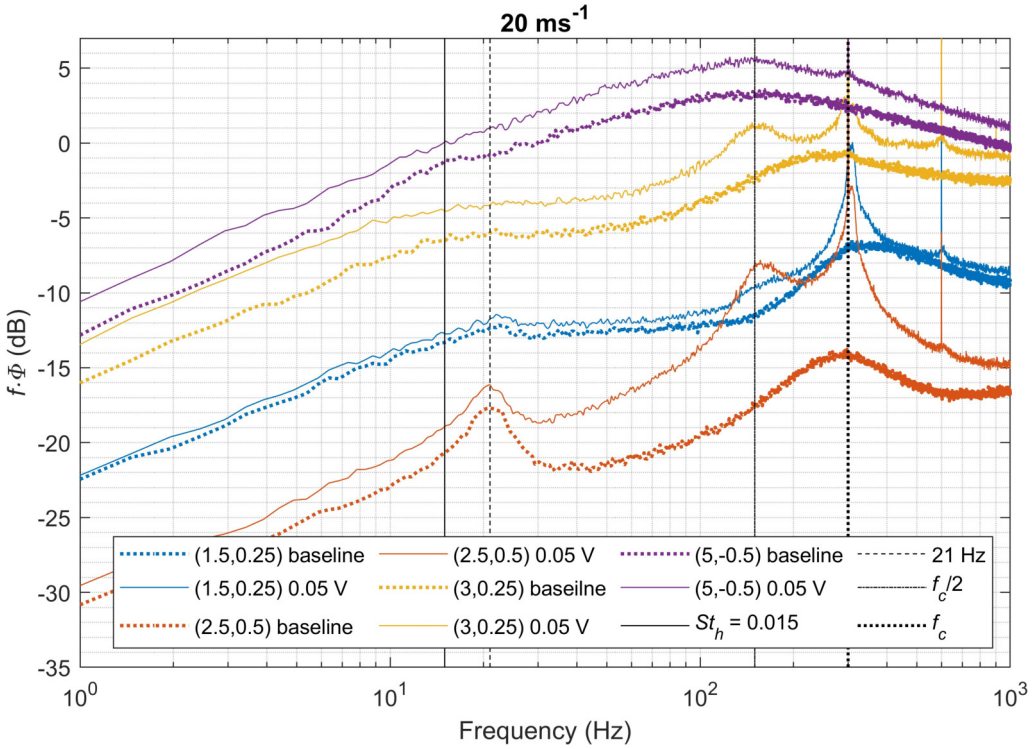


Figure 5.12: Effect of acoustic actuation on pre-multiplied hot-wire PSD at several query points

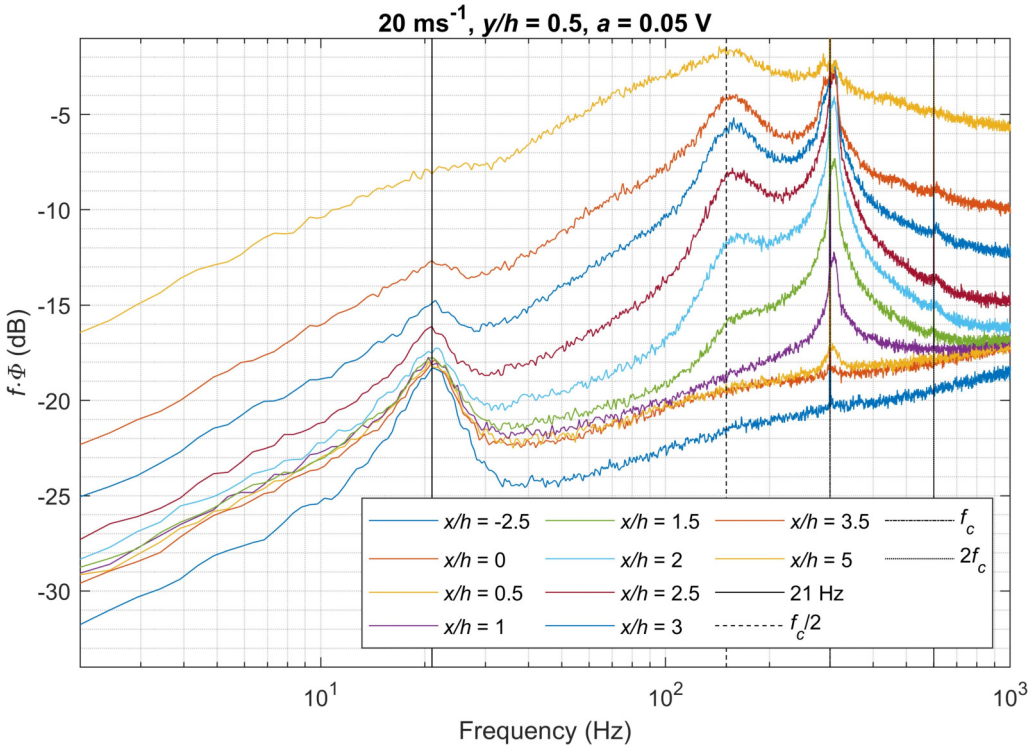


Figure 5.13: Pre-multiplied hot-wire PSD along $y/h = 0.5$ at $v_{in} = 20\,\mathrm{m\,s^{-1}}$ with acoustic forcing

The results of Marrot et al. [42, 109, 48], who investigated the effects of external acoustic excitation on a backward-facing step flow over a range of frequencies, indicate that acoustic excitation couples to the flow structure, or mode, closest to the excitation frequency. This was also seen in the experiments with $1\,\mathrm{m\,s^{-1}}$ inlet speed in section 5.3.2, where the peaks in frequency content suggest that the large merged vortices locked-on to the Helmholtz resonance of the rig (f_H), which also appeared to have the effect of locking-on the smaller scale (most likely the shear layer mode) vortices to the $2f_\mathrm{H}$ and $3f_\mathrm{H}$ harmonics. Given that the 300 Hz forcing tone lies within the range of vortex merging in the baseline flow (∼200 Hz to ∼400 Hz), and the 600 Hz harmonic is reasonably close to the frequency of the vortex roll-up mode (∼900 Hz), it seems most likely that the structures locked-on to the first harmonic of the forcing tone, the forcing tone, and its sub-harmonic are the roll-up mode, the scale of vortices preceding the step mode, and the step mode, respectively.

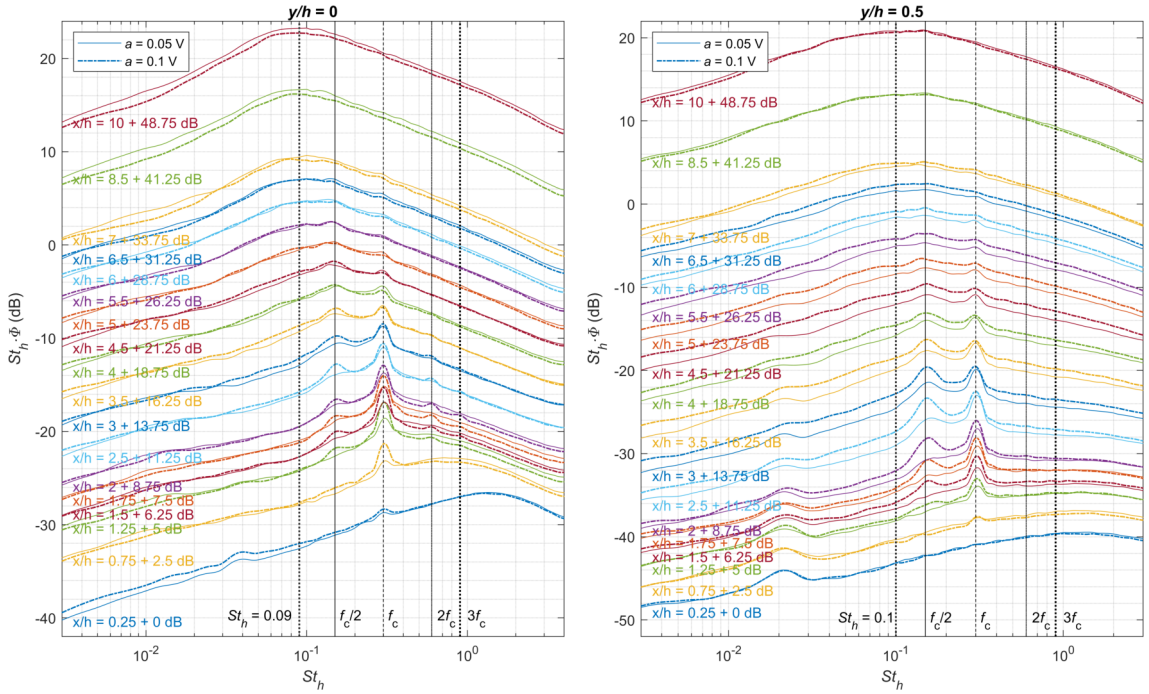
5.4.1 Effect of Excitation Volume

Figure 5.14 shows the pre-multiplied spectra along $y/h = 0$ and $y/h = 0.5$ from $x/h = 0.25$ to $x/h = 10$, calculated from the $20\,\mathrm{m\,s^{-1}}$ hot-wire traverse data with forcing amplitudes $a = 0.05\,\mathrm{V}$ and $a = 0.1\,\mathrm{V}$, averaged across the span between $z/h = \pm 3.2$. The sharp spikes at f_c and $2f_\mathrm{c}$ have been removed, and the spectra smoothed to aid legibility.

The forcing tone and harmonic/sub-harmonic peaks are initially stronger/sharper for the higher amplitude excitation, and the sub-harmonic peak appears to both develop, and decay, slightly further upstream than for the lower excitation amplitude. The strength and positions at which the sub-harmonic peak is seen are consistent with the expectation that stronger forcing promotes the formation of the step mode scale of vortices and enhances their strength and periodicity, which will then lead to enhanced shear layer spreading and earlier reattachment.

Higher amplitude actuation also enhances the strength/sharpness of the small peak at the $2f_\mathrm{c}$ harmonic, and an additional small peak at the $3f_\mathrm{c}$ harmonic is apparent along $y = 0$ for $a = 0.1\,\mathrm{V}$, suggesting an secondary/alternative roll-up mode. However, it is interesting that these peaks only become visible at streamwise positions somewhere downstream of the forcing tone peak, and around or downstream of the sub-harmonic peak, when it is believed that they correspond to the initial vortex roll-up. This may be due to the measurement

locations, given that the initial roll-up vortices are small. It is also not surprising that the forcing tone peak is identifiable upstream of roll-up, as the excitation is almost certainly forcing non-vortex motions of the shear layer in addition to the vortex modes.



(a) $y = 0$ (b) $y/h = 0.5$

Figure 5.14: Comparison of pre-multiplied hot-wire spectra with $a = 0.05\,\mathrm{V}$ and $a = 0.1\,\mathrm{V}$ amplitude excitation. PSD at each x location offset by $0.25(x - x_1)/h$, where $x_1/h = 0.25$ (the most upstream measurement location)

5.4.2 Effect of Inlet Speed

The power spectra of the hot-wire measurements at $(x, y)/h = (2.5, 0.5)$ for the four inlet velocities from 17.5 to $30\,\mathrm{m\,s^{-1}}$ are shown in Figure 5.15. As for $v_{\mathrm{in}} = 20\,\mathrm{m\,s^{-1}}$, forcing causes there to be distinct vortex peaks at roughly the forcing frequency and sub-harmonic for all the velocities, although the strength of the sub-harmonic peak reduces as inlet speed increases, and is barely present at $v_{\mathrm{in}} = 30\,\mathrm{m\,s^{-1}}$.

Zoomed-in views of the PSDs around the forcing and sub-harmonic frequencies are displayed in Figure 5.16. The flow structure peak frequencies increase slightly with flow speed, the reason for which is not understood. Broadening of the vortex peaks is expected due to slight differences in the transport speed of individual vortices, but it seems odd that the flow structures would *almost* lock-on to the excitation tone, which implies that the

formation of the large vortices occurs at constantly changing phase relative to actuation. In addition to the peak at slightly above f_c, a smaller local bump in content is found at a frequency slightly below f_c at 25 and $30\,\mathrm{m\,s^{-1}}$, which decreases slightly with flow speed. A similar bump is seen at several of the streamwise locations along $y/h = 0.5$ at $20\,\mathrm{m\,s^{-1}}$ in Figure 5.13. Interestingly, the peak/bump on either side of the f_c spike appear to be symmetrically spaced, as if they are the side bands of an AM signal. Furthermore, the spacing is consistent with the identified flapping mode frequency, $St_h \approx 0.01$. It is therefore hypothesized that the lower frequency bump, and at least some of the contribution to the higher frequency peak, may be due to the modulation of the directly coupled velocity at f_c by the flapping of the shear layer.

The decay of the sub-harmonic peak with inlet velocity, seen in Figures 5.15 and 5.16b, is consistent with the argument that acoustic forcing couples to the flow structures closest to the excitation frequency. The actuation frequency, $f_c = 300\,\mathrm{Hz}$, corresponds to $St_h = 0.34$, 0.3, 0.24, and 0.20 at $v_{in} = 17.5$, 20, 25, and $30\,\mathrm{m\,s^{-1}}$, respectively, which lies somewhere between the natural step mode frequency ($St_h \approx 0.18$) and the preceding scale of vortices which merge to form the step mode vortices. At 17.5 and $20\,\mathrm{m\,s^{-1}}$, the sub-harmonic of excitation lines up with the natural step mode frequency, which is fed by the pairing of the locked-on vortices, so a strong response is seen. At $25\,\mathrm{m\,s^{-1}}$, the presence of the sub-harmonic peak indicates that the actuation is still coupled to the preceding scale of vortices, but the step mode has been driven away from its natural frequency (now $St_h \approx 0.12$), and so is weaker. At $30\,\mathrm{m\,s^{-1}}$, the excitation frequency lines up with the natural step mode frequency, and is assumed to couple to this mode. There is only a very slight bump in content at the sub-harmonic of f_c, as larger scale structures do not form until further downstream (i.e. the shedding mode). The roll-off of the $30\,\mathrm{m\,s^{-1}}$ PSD above the forcing peak is also significantly less steep than at lower speeds, potentially indicative of less consistent vortices preceding the step mode, and suggesting in this case that the smaller scale modes may not lock-on to forcing harmonics.

A more thorough investigation of the lock-on phenomena and the relationship between flow speed (hence natural mode frequencies) and acoustic excitation frequency requires a great deal more data than is presented here, and is left for future work.

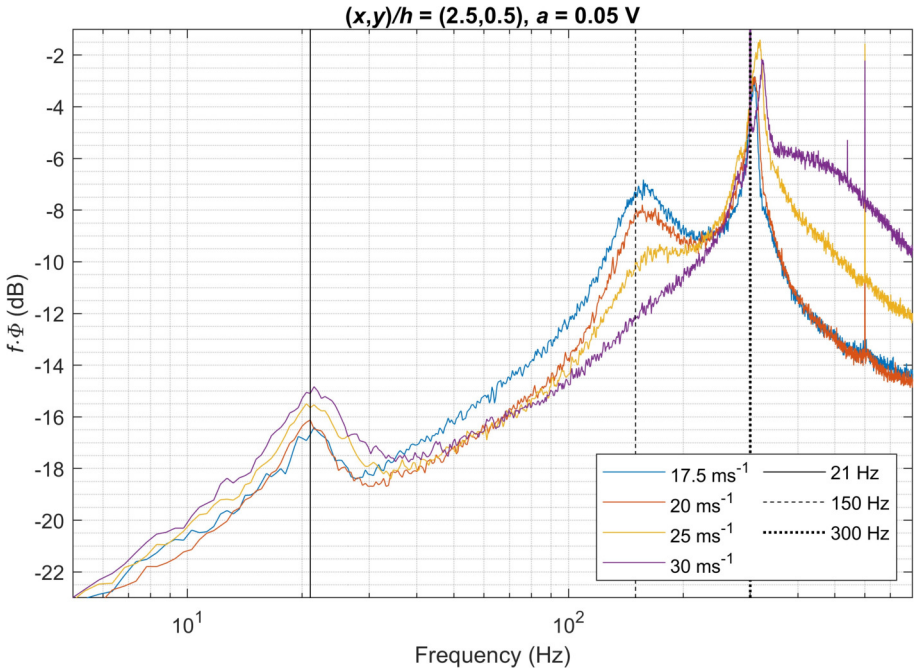
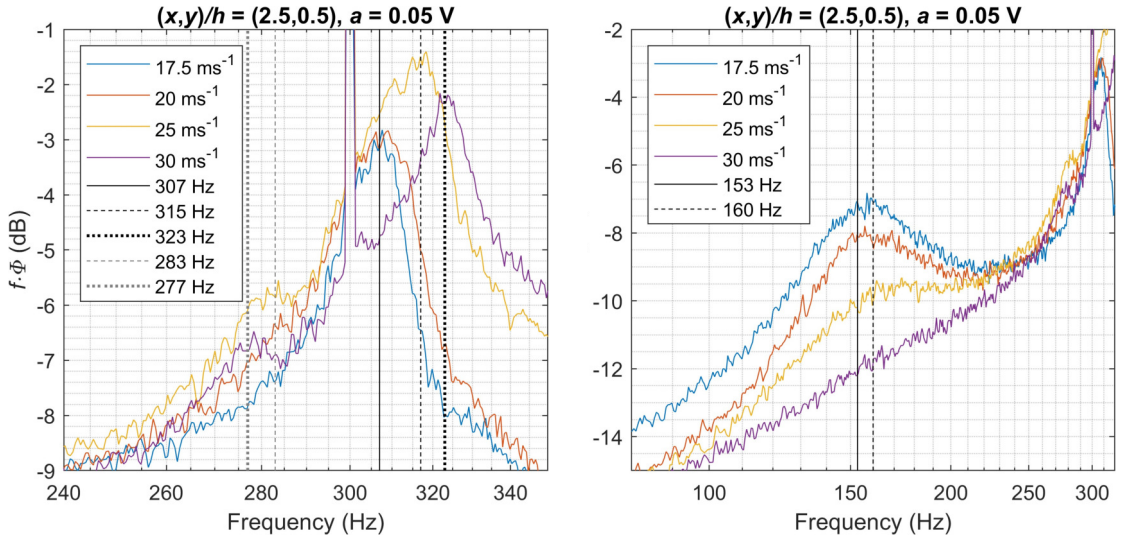


Figure 5.15: Effect of acoustic actuation on hot-wire velocity spectrum at multiple velocities



(a) Main peak

(b) Sub-harmonic peak

Figure 5.16: Effect of acoustic actuation on hot-wire velocity spectrum at multiple velocities, zoomed in peaks at forcing frequency and first sub-harmonic

5.5 Laminar CFD Analysis

5.5.1 Roll-Up and First Merging

Figures 5.17 and 5.18 display zoomed in views of the shear layer shortly after separation at several consecutive time steps, for the baseline and forced flows respectively. In both cases, vortex roll-up almost immediately followed by pairing can be clearly seen. In the baseline flow, roll-up occurs at around $x/h = 1$, at a frequency $St_h \approx 0.8$ ($St_\theta \approx 0.015$), followed by pairing at around $x/h = 1.75$ to 2. In the forced flow, roll-up occurs at around $x/h = 0.75$ at twice the actuation frequency ($St_\theta = 0.011$), followed by pairing at around $x/h = 1.25$.

The observation that vortex roll-up occurs at twice the forcing frequency is consistent with the hot wire data presented above, and with the studies of Marrot et al. [42, 109, 48], who demonstrated that external acoustic excitation at approximately half the natural roll-up frequency introduced peaks in the velocity frequency spectrum at both the excitation frequency and its first harmonic at $(x, y)/h = (0.7, 0.08)$. This indicates the same behaviour as is currently observed: that the acoustic excitation couples to the first merged vortex mode, and roll-up locks on to its harmonic. This is an important point to make, as the vast majority of studies of the effects of periodic excitation on backward-facing step and similar flows employed either a method of excitation, or a range of excitation frequencies, for which the shear layer (roll-up) mode locked-on directly to the excitation tone [70, 41, 54, 55, 110, 45, 111, 53, 130].

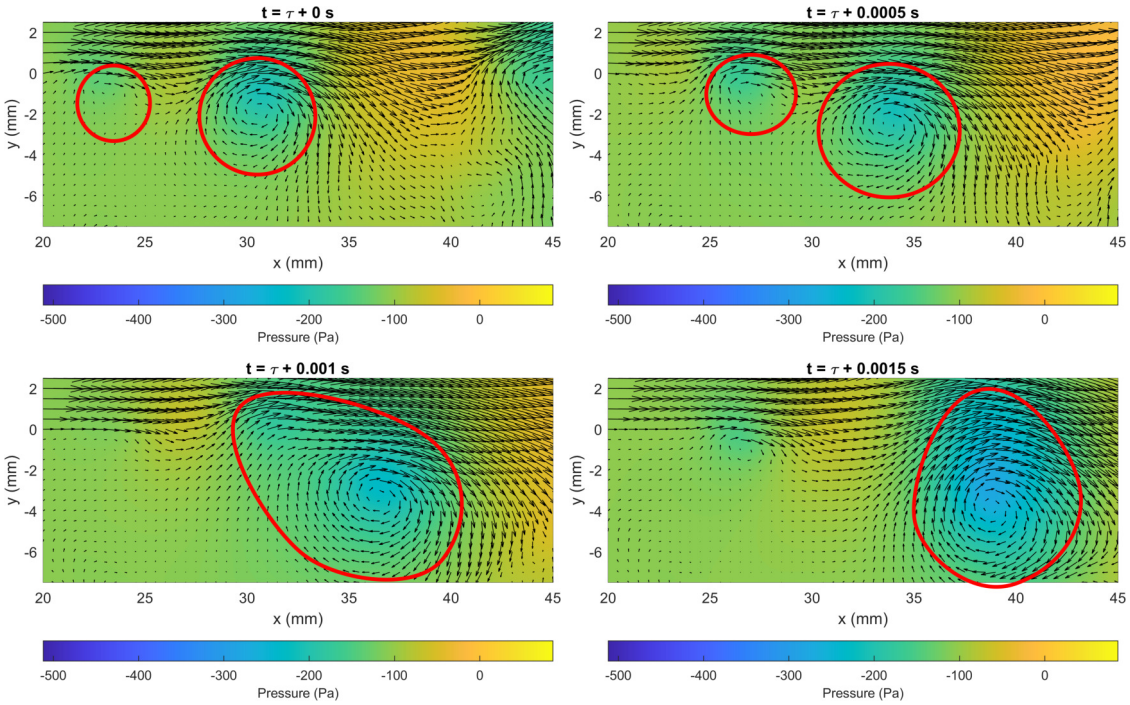


Figure 5.17: Baseline CFD vortex roll-up and merging

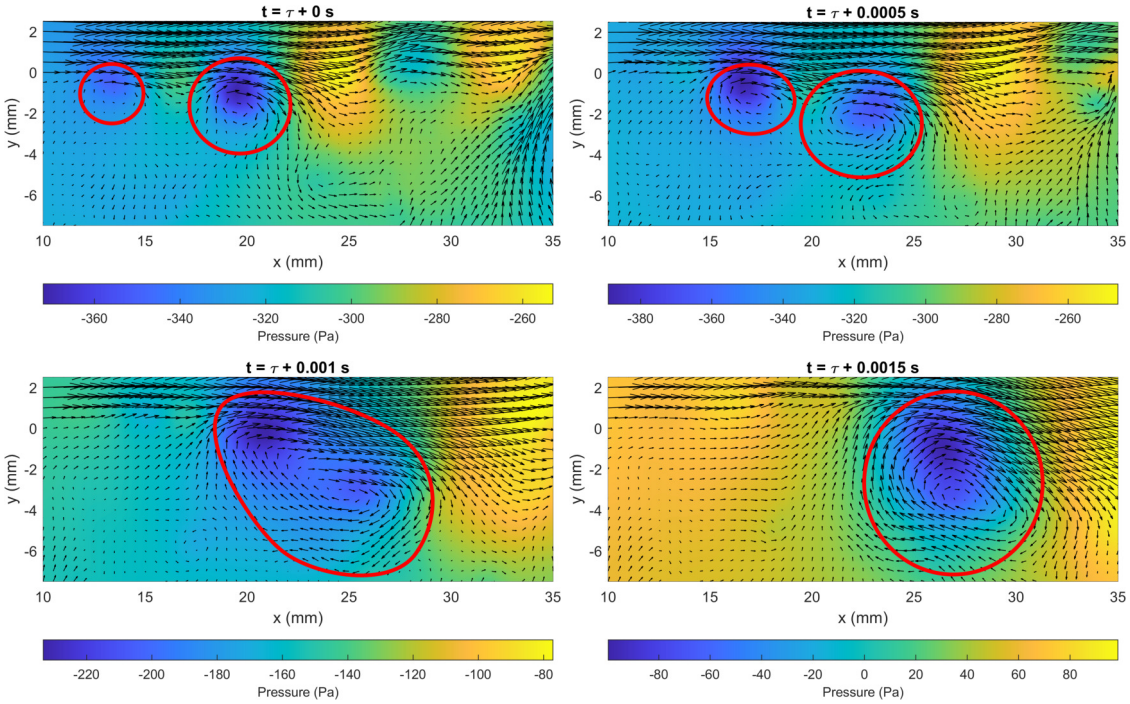


Figure 5.18: Actuated CFD vortex roll-up and merging

5.5.2 'Step mode' Vortex

Figure 5.19 illustrates a pairing of two consecutive shear layer vortices in the unactuated flow. The subsequent vortex catches up with its preceding vortex slightly further than half way through the reattachment region, and a larger, stronger, vortex of the order of the step height in diameter is formed. The large vortices maintain their size until around the reattachment location, where the vortices appear to partially break up, with a section of the fluid closest to the wall propagating upstream into the recirculation bubble, and the remaining fluid continuing to travel downstream, before eventually dissipating. The large vortices of the order of the step height are identified as the 'step mode', with St_h very approximately equal to 0.2 in the baseline flow, and $St_h = 0.15$ $(f_c/2)$ in the forced case, compared to the value of $St_h \approx 0.18$ identified by Hasan [39, 40]. The location and size of the step mode vortices are consistent with the findings of Hudy at al. [93] and Wee at al. [90] that the largest structure in the shear layer grows in place about half way through the separated region before shedding and propagating downstream.

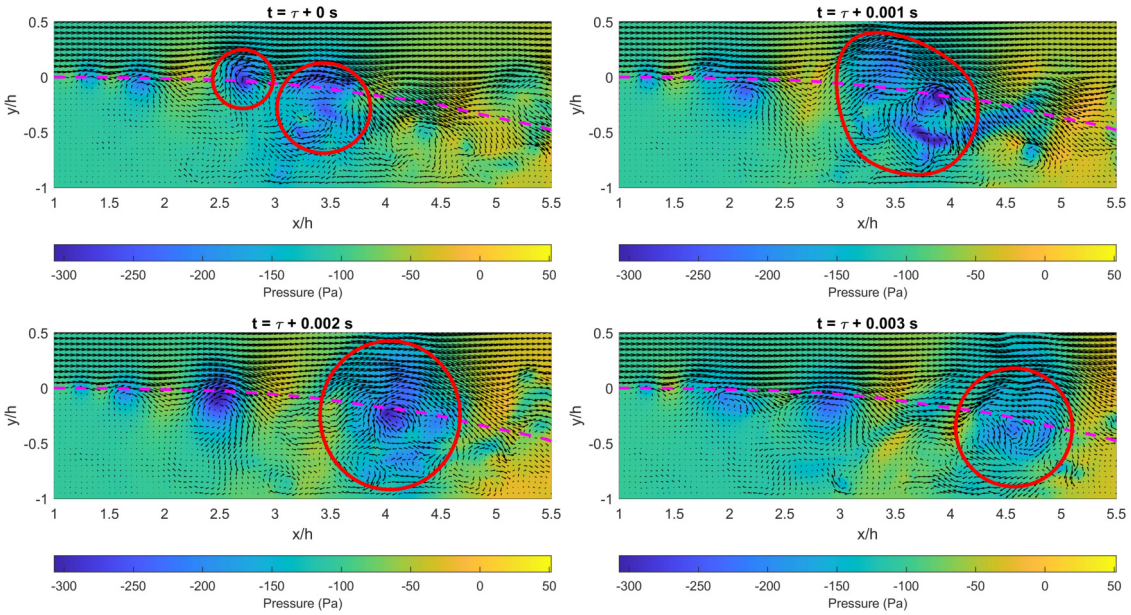


Figure 5.19: Baseline CFD vortex merging.

5.5.3 Modal Decomposition

Proper Orthogonal Decomposition

Proper orthogonal decomposition (POD) was performed on the mean subtracted CFD centre plane snapshots of the baseline and forced flows, for pressure coefficient and 2D velocity coefficients separately, and the combination of pressures and velocities. Figure 5.20 shows the cumulative variance (sum of POD eigenvalues) captured by the POD modes for both the baseline and steady actuation simulations. It is worth noting that the total variance captured in the case where POD is applied to stacked pressure and velocity measurements is related to but not directly a measure of energy due to the inconsistent units (the square of velocity is proportional to energy while pressure is linearly proportional). Fewer modes are needed to capture the variance in the pressure field than the velocity field, especially so for the actuation case, where the majority of pressure field variance is captured by the first POD mode, which accounts for most or all of the large pressure fluctuations due to actuation. Conversely, the forced velocity field requires only slightly fewer modes than the baseline flow to capture the same proportion of total variance, indicating that the direct effect of actuation does not dominate the velocity field. From this point forward only modal decompositions of the stacked pressure and velocity coefficient fields, C_p and C_v, are considered, so that the calculated modes represent both the velocity and pressure perturbations of coherent structures.

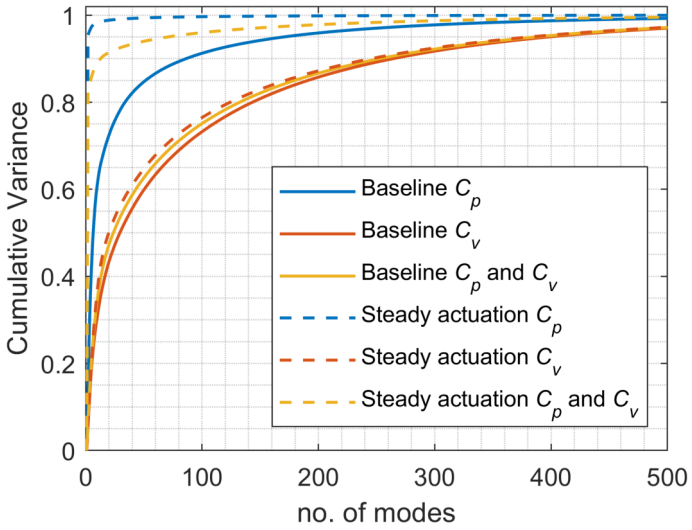


Figure 5.20: Cumulative POD mode variance

As discussed earlier in Section 2.6.1, the POD modes optimally represent the data for any number of truncated modes in terms of variance, therefore lower order modes tend to represent the largest structures in a flow field, and capturing the smallest structures requires that higher order modes with relatively small contributions to overall variance are kept. Additionally, including multiple variables with different relations to system energy (e.g. velocities and pressures) complicates the choice of truncation value, as the POD eigenvalues/mode variance can no longer be taken as simple a measure of energy, and it is not necessarily clear how to apply an appropriate energy criteria to the truncation.

As an alternative to a variance criterion, the number of POD modes required to capture the flow dynamics is determined by comparing the frequency content of the POD projected flow to the full dimension data at several reference points. Figure 5.21 shows the pressure power spectrum of the data projected onto the truncated POD modes for several truncation values, for baseline and steady actuation cases. The reference locations are chosen to be in the shear layer somewhere between where vortex roll-up and the first pairing occur, at $(x, y)/h = (1.5, 0)$, slightly downstream around where the second vortex pairing begins, at $(x, y)/h = (3, 0)$, and on the wall in the reattachment region, at $(x, y)/h = (5, -1)$. Although comparing the reconstructed power spectrum is not a precise method for determining the number of POD modes that should be kept, particularly in the current case where the summation of spectra is reasonably noisy, it provides a useful guideline. In comparison, an energetic criterion would be significantly more ambiguous in terms of how many modes are needed to capture the frequency dynamics of interest. The spectra in figure 5.21 indicate that the dominant flow dynamics, namely vortex roll-up, subsequent merging, and lower frequency motions (e.g. flapping), are sufficiently captured by about 150 POD modes for the baseline flow, and 50 modes for the forced flow. Removing the higher order modes effectively low-pass filters the data, demonstrated by the roll-off of the POD projected frequency content at higher frequencies.

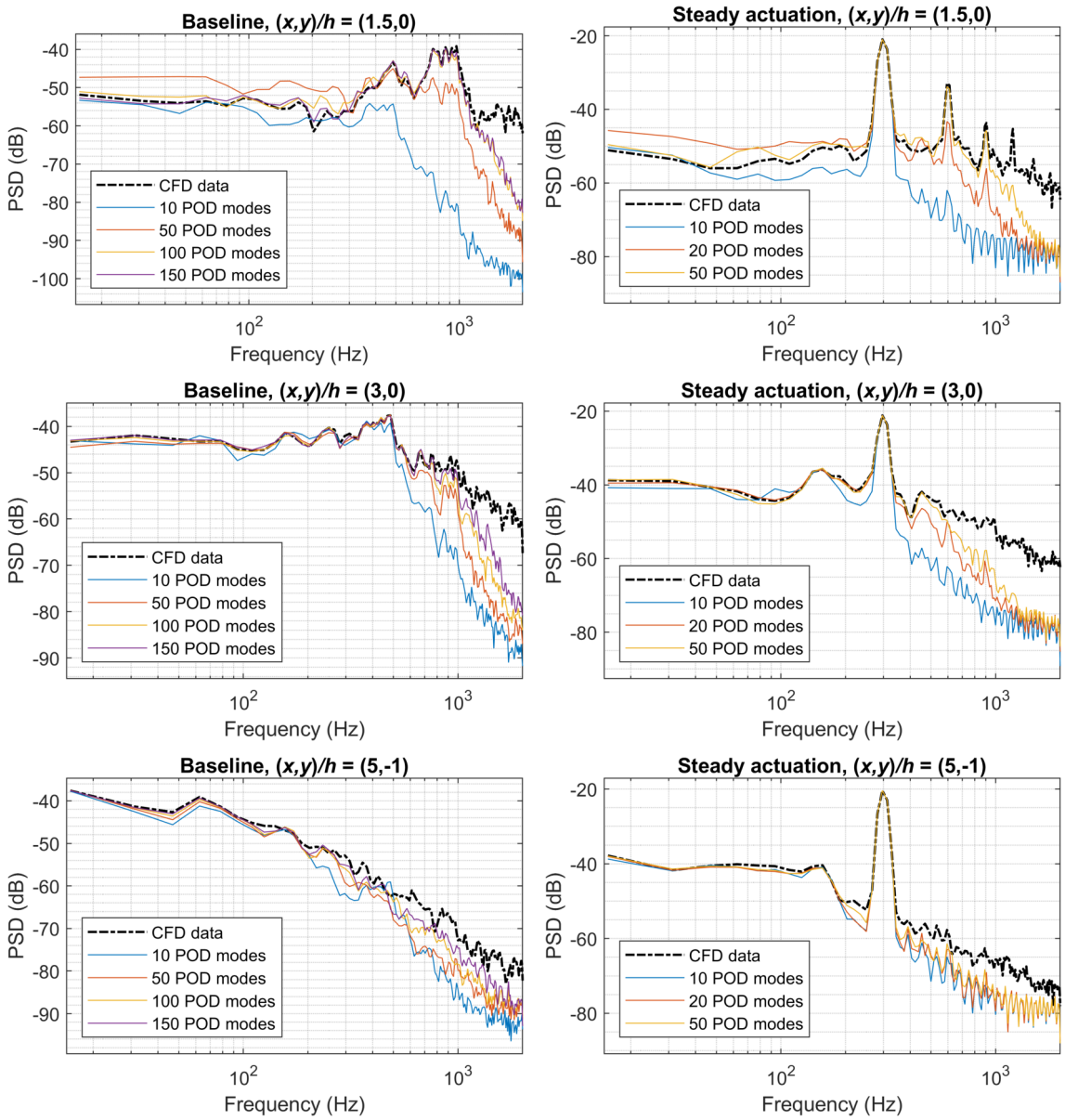


Figure 5.21: Frequency content of truncated POD reconstruction

Figures 5.23 and 5.23 show the leading 10 POD modes for the baseline and forced flows, respectively. Pressure and velocity magnitude labels are omitted for conciseness as the POD modes represent flow structures/shapes but not the absolute magnitude of each mode in the total flow field, which is determined by the combination of the shape modes and their coefficients. The POD modes clearly identify coherent vortex structures, which for the baseline flow decrease in scale with mode order, while for the actuated flow several of the modes capture multiple scales, and the leading modes are those corresponding to the shear layer vortices at the actuation frequency rather than the largest structures.

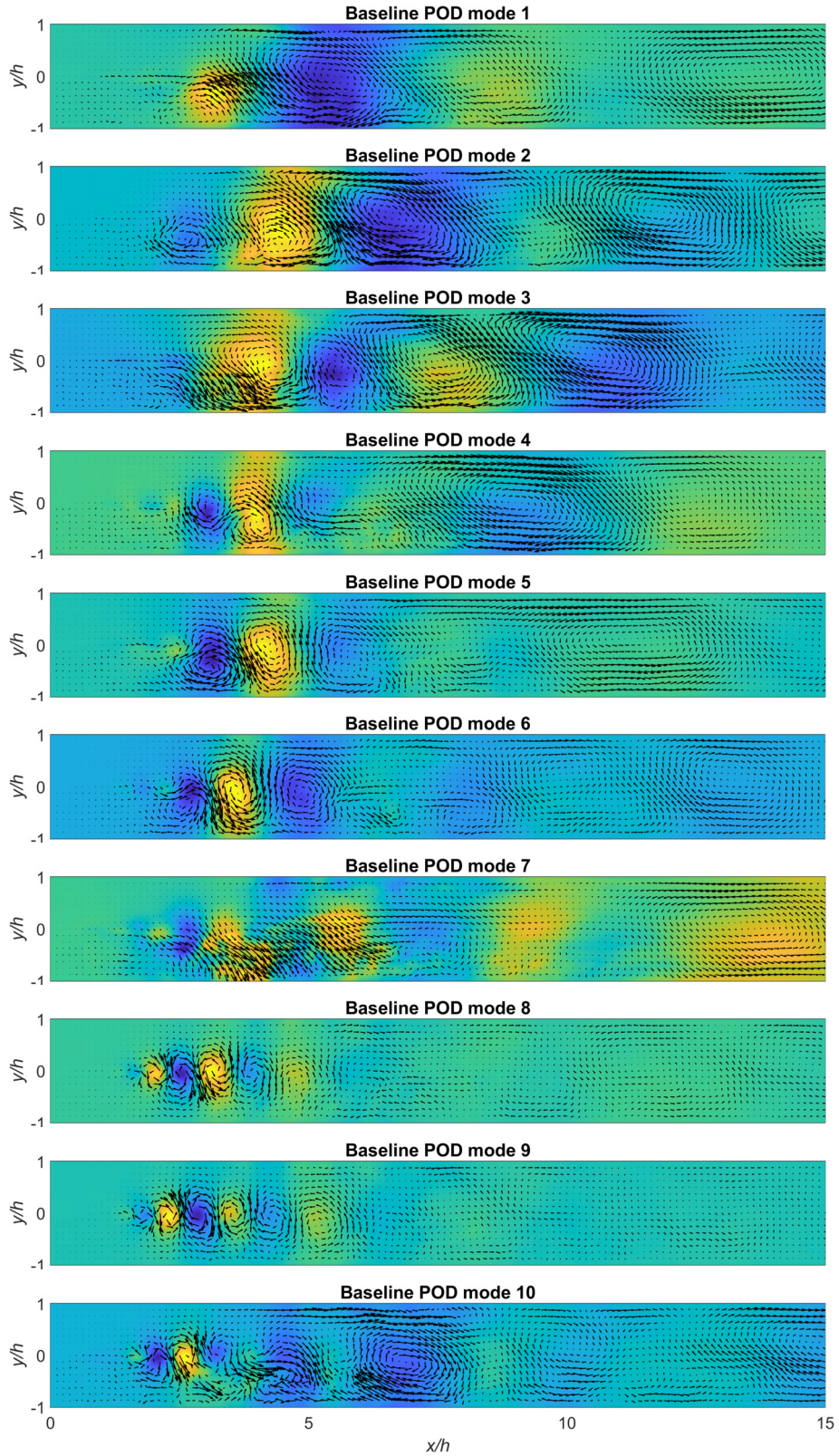


Figure 5.22: First 10 Baseline POD modes. Colour levels show pressure, arrows show velocity direction and magnitude

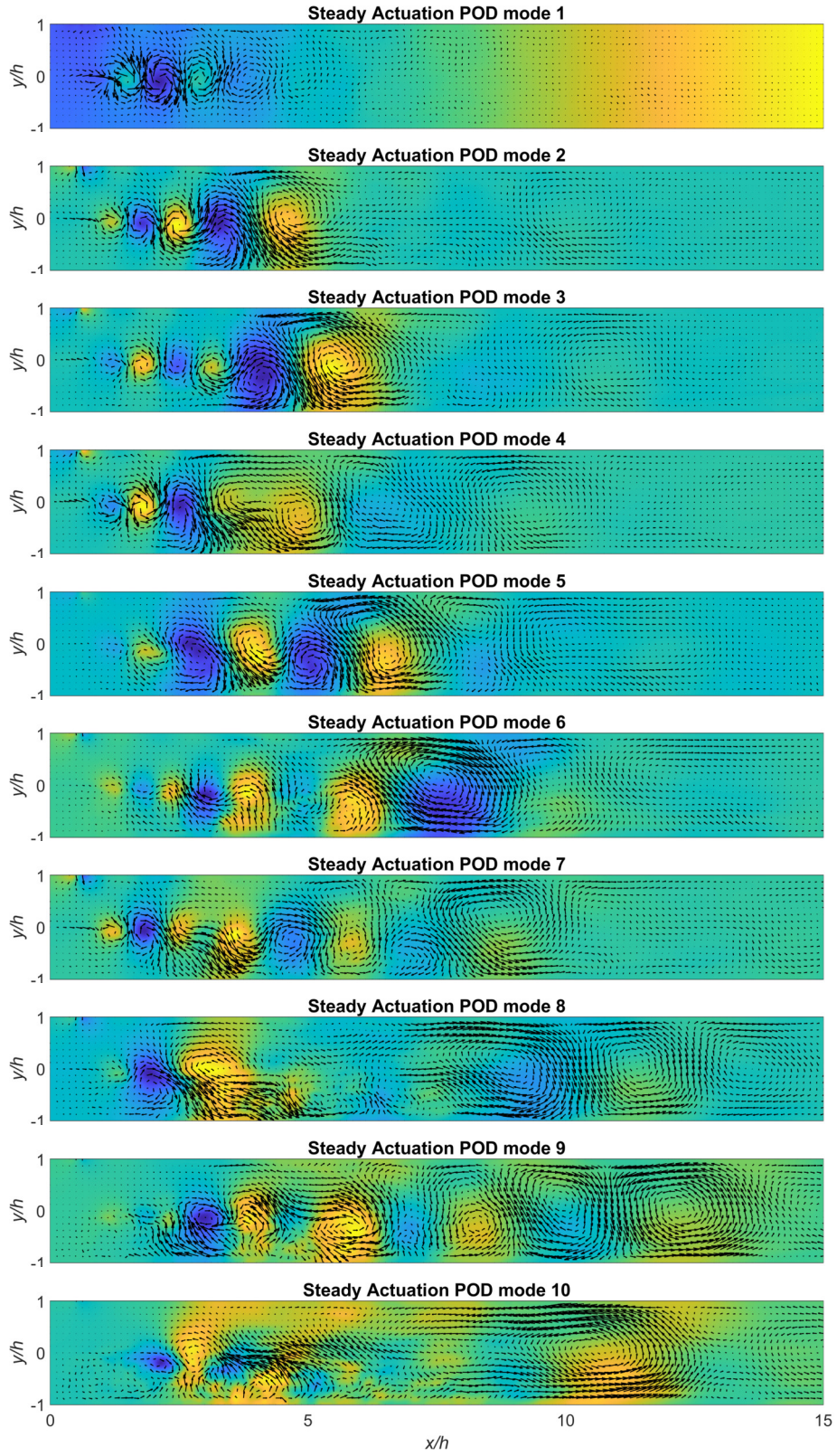


Figure 5.23: First 10 Steady Actuation POD modes Colour levels show pressure, arrows show velocity direction and magnitude

Dynamic Mode Decomposition

Dynamic mode decomposition (DMD) was performed on the baseline and forced CFD data, using the truncation values determined from the POD frequency spectra.

In the interest of identifying shear layer modes, the POD modes were calculated with respect to the weighting, $\mathbf{W}$, shown in Figure 5.24. The calculated POD modes used for dimensionality reduction in the DMD are therefore optimal in the energetic sense defined through $\mathbf{W}$, as detailed in Section 2.6.1. Applying this weighting effectively biases the DMD modes towards capturing the flow structures which contribute most to the energy in the shear layer and separation region.

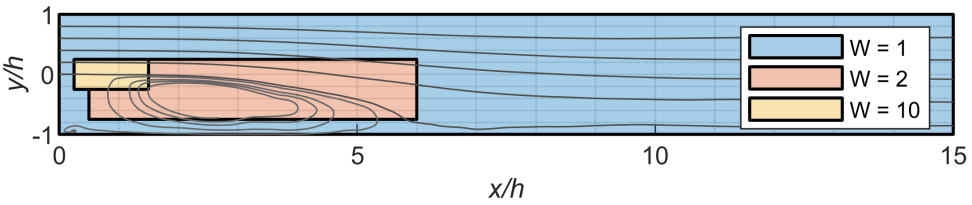


Figure 5.24: Weighting, $\mathbf{W}$, used for DMD. Superimposed on mean streamlines of baseline CFD solution

Unlike POD modes, DMD modes are not ordered. Tissot et al. [173] proposed ranking the DMD modes by contribution to variance of the reconstructed flow over a given time horizon. Similarly, the Sparsity-promoting DMD of Jovanović et al. [150] returns a sparse set of mode amplitudes that optimally represent the variance of the data snapshots for a given sparsity. Despite being widely used, neither of these methods are particularly well suited to the analysis of the current problem, in which the inconsistent nature/phase shifting of vortex roll-up and pairing, especially in the unforced flow, results in modes of dynamical interest having fast decaying eigenvalues. As a result, the DMD reconstructed flow field deviates significantly from the data for even short time horizons, and the methods of Tissot et al. [173] and Jovanović et al. [150], which implicitly assume that the DMD modes and eigenvalues provide a satisfactory reconstruction of the data, tend to select modes with low decay rates rather than those of interest.

Figure 5.25 shows the (positive frequency) DMD eigenvalues, plotted as fractional change in mode amplitude over one period, $e^{\sigma/f}$, against frequency, f. This fractional decay can be thought of as the persistence of the corresponding DMD mode, and the modes dominating

a particular frequency range selected based on the magnitude of fractional decay. The identified modes are displayed in figure 5.26 and 5.27. As for the POD modes, pressure and velocity magnitude labels are omitted for conciseness and because the contribution from each mode is determined through the corresponding coefficient. Each of the dominant DMD mode frequencies extracted from the CFD agrees remarkably well with the modes identified from experimental hot-wire measurements in Section 5.3.1.

The baseline flow DMD identifies several roll-up modes of similar scales at frequencies from around $St_h \approx 0.6$ to $St_h \approx 0.93$ ($St_\theta \approx 0.012$ to $St_\theta \approx 0.017$), followed by a cascade of modes of gradually larger scales and lower frequencies. The range of St_θ identified as shear layer roll-up is consistent with the literature, albeit slightly higher than the typical value of $St_\theta \approx 0.012$ [39, 40].

The dominant shear layer roll-up mode and subsequent paired vortex modes have frequencies of $St_h = 0.927$, and its approximate sub-harmonics, $St_h = 0.459$ and $St_h = 0.223$ respectively, demonstrating that there are at least two strong pairing events, each halving the vortex passing frequency. Modes at $St_h = 0.064$ and $St_h = 0.013$ are also identified as being dominant in their frequency ranges, corresponding to the shedding/cross-flapping mode [35, 92, 87, 88, 89, 90, 55, 91, 99], and the longitudinal flapping mode [95, 96, 97, 89, 55, 98, 99, 100]. The largest vortex structures in the separation region, i.e. the 'step' mode, form after two successive pairings starting from the shear layer mode, corresponding to modes with frequencies from around $St_h \approx 0.15$ to $St_h \approx 0.23$.

DMD on the forced flow identifies modes at the forcing frequencies and its harmonics/sub-harmonics, consistent with the understanding that the vortices lock-on to the actuation tone. In addition to the vortex roll-up mode at double the actuation frequency, a mode at three times the actuation is also extracted by the DMD, although with faster decay. This mode is consistent with the small peak seen in the forced hot-wire spectra (Figure 5.14), confirming that there is an additional roll-up mode at $3f_c$. This mode/peak imply that there are sometimes three vortices rolled-up per actuation period which merge into the vortices seen at the actuation frequency. The comparatively slow decay of the DMD eigenvalue at the forcing frequency indicates that the strong vortex train locks-on to the actuation with little phase drift, again consistent with the conclusions made from the hot-wire data in Section 5.4.

The cross-flapping and longitudinal flapping modes are identified at $St_h = 0.054$, and $St_h = 0.011$, respectively. That the frequency of the shedding/cross-flapping mode has decreased slightly to remain approximately 1/3 of the step mode frequency suggests that there may be a harmonic relationship between the modes.

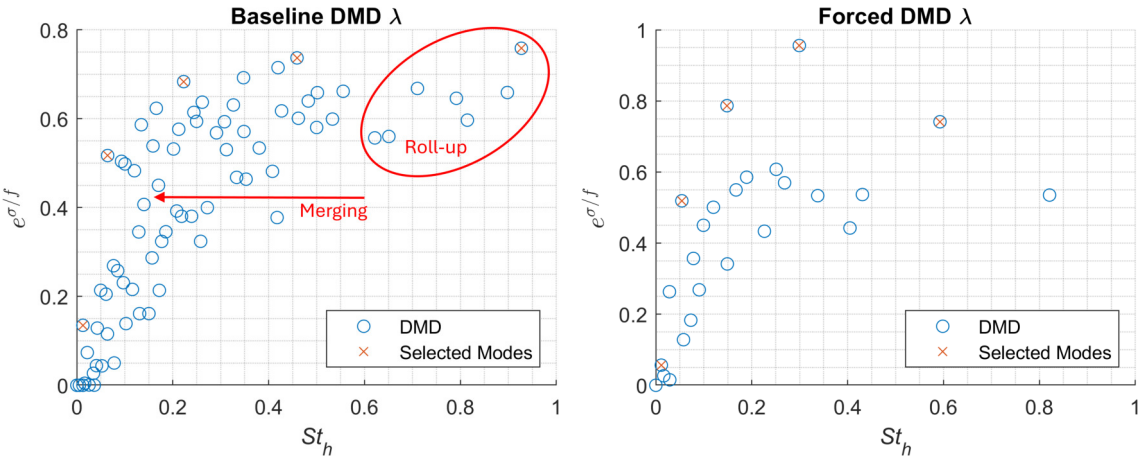


Figure 5.25: DMD eigenvalues of baseline and forced flows

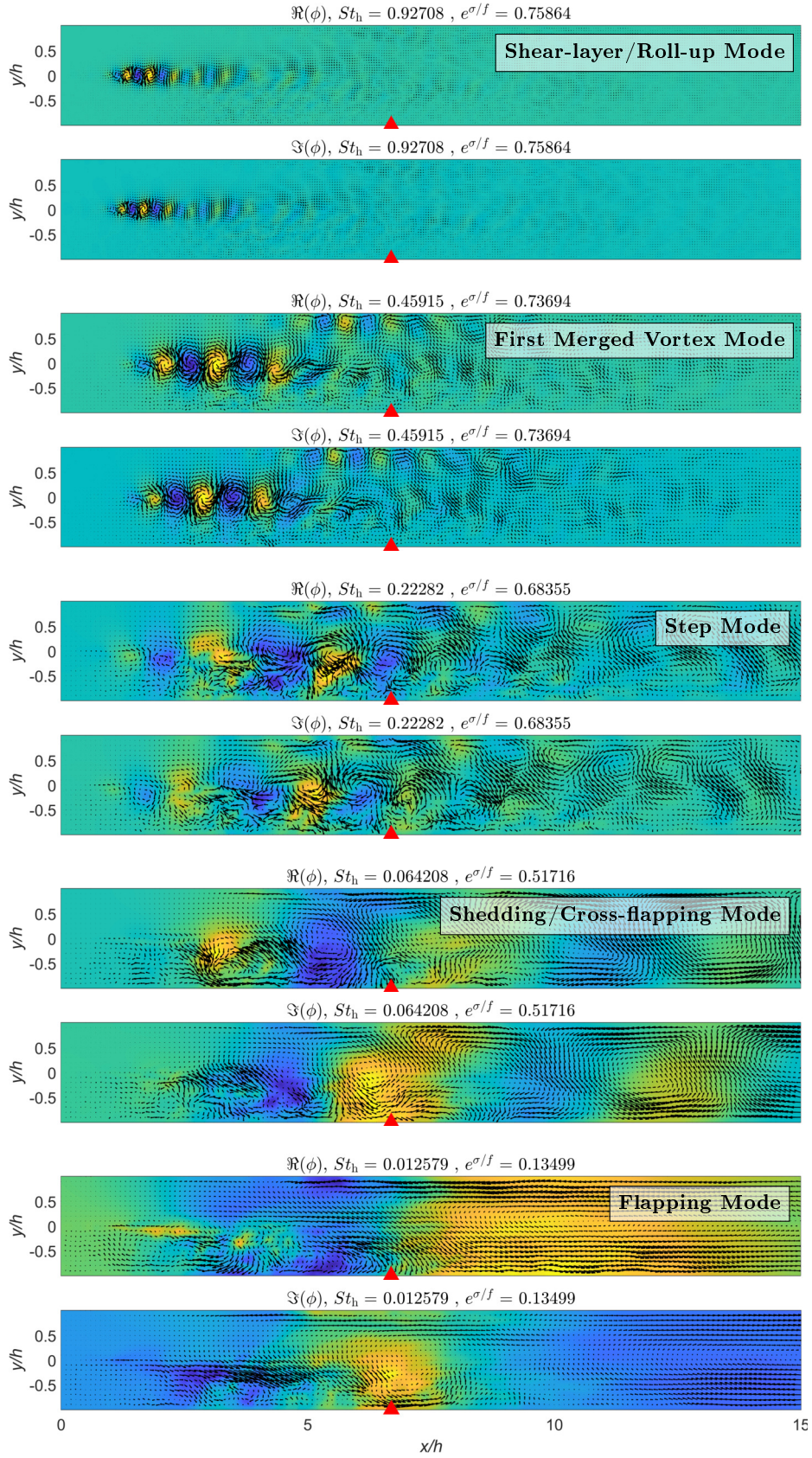


Figure 5.26: Baseline DMD modes. Colour levels show pressure, arrows show velocity direction and magnitude. Red triangle indicates mean reattachment point

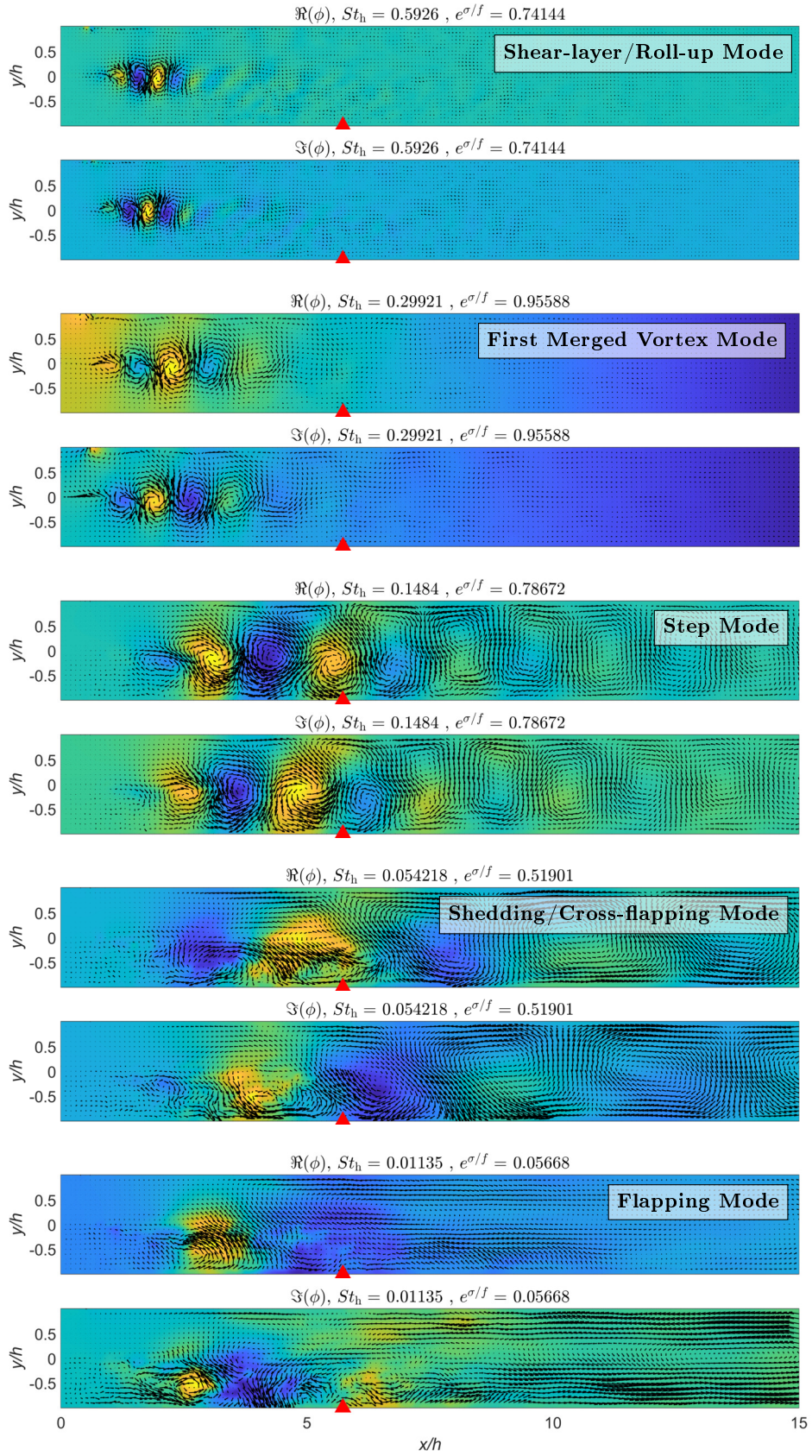


Figure 5.27: Steady actuation DMD modes. Colour levels show pressure, arrows show velocity direction and magnitude. Red triangle indicates mean reattachment point

Flapping Mode

Slightly more attention is given to the extracted 'flapping' mode than the shear layer vortex modes. The flapping motion is both the least clearly visualised from the DMD modes plotted in figures 5.26 and 5.27, and the least well understood in literature [94]. Despite having been studied for several decades, there is still no consensus or definite conclusion on what causes flapping.

While the flapping mode is successfully extracted by dynamic mode decomposition, as a data-based method that does not take account of flow physics, it is unlikely that any meaningful conclusions can be made about the cause of flapping from DMD modes. Regardless, it is still informative from the perspective of understanding the character of the flow to visualise the flapping motion.

Figures 5.28 and 5.29 show contour plots of the sum of u-velocity component of the mean flow and the DMD flapping mode, and the calculated wall shear stress of the mean flow plus flapping mode, respectively, at several phases for the baseline flow. Where the flapping motion is not obvious from the velocity vectors of the real and imaginary parts of the DMD mode, the u-velocity contours in figure 5.28 depict a clear vertical flapping of the shear layer/'jet' flow, accompanied by an elongation and shrinking of the recirculation bubble. Similarly, the wall shear stress profiles in figure 5.29 show that the streamwise position at which the wall shear stress crosses the x axis drifts back and forth by approximately 2 step heights between the maximum and minimum positions. This is of the order of the variation in x_r typically observed in the literature [95, 98, 99]. It is interesting though, that the distribution does not smoothly elongate and contract throughout the cycle, instead displaying an oscillating peak/trough around the mean reattachment location and a significant variation in the magnitude of wall shear stress downstream of reattachment. The oscillating peak/trough is similar to the trace left by a passing vortex, and appears to demonstrate the impingement point moving downstream by the shear layer 'breaking away', followed by a re-establishment of the further upstream impingement.

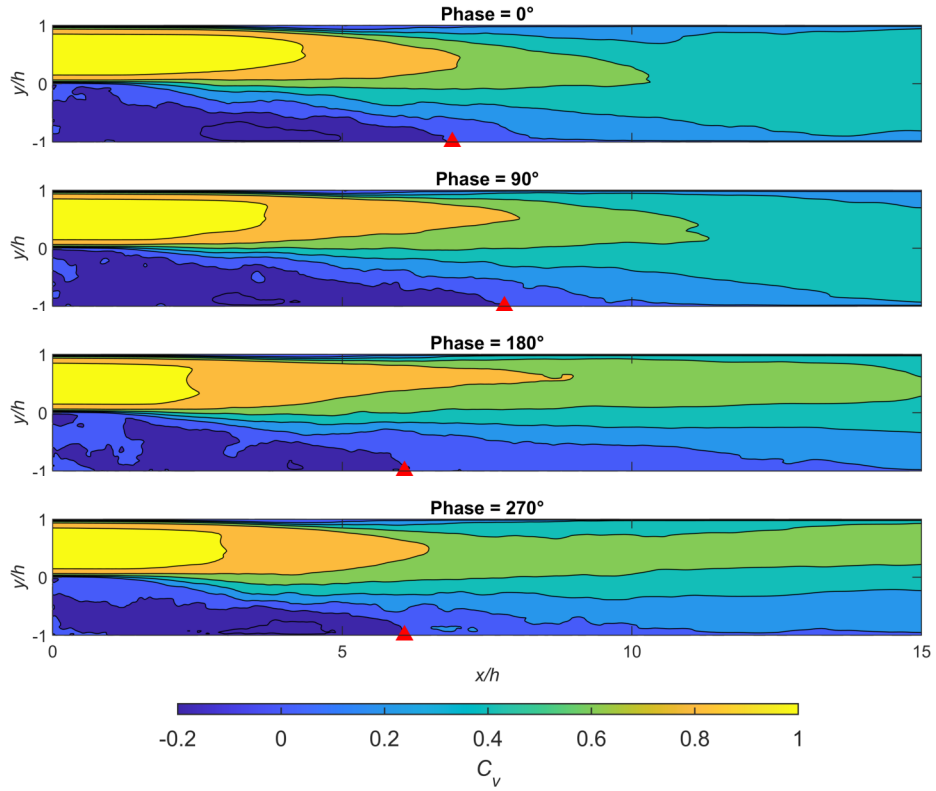


Figure 5.28: u-velocity contours of baseline flow DMD flapping mode + mean. Red triangle indicates instantaneous reattachment point based on wall shear stress.

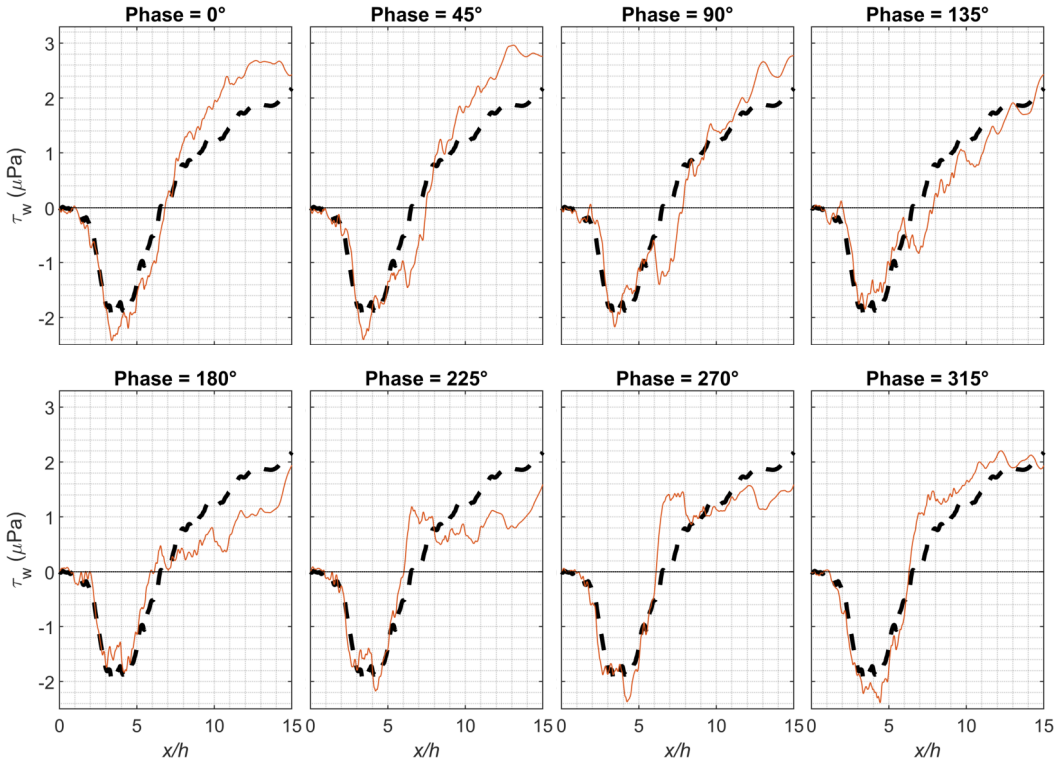


Figure 5.29: Wall shear stress of baseline flow DMD flapping mode + mean. Mean shown by black dashed line, instantaneous wall shear stress shown in red.

5.6 Spanwise Frequency Content

Having identified frequency dynamics along the centre channel, it is of interest to understand the spanwise distribution of flow structures. It has already been determined from the mean flow that the interaction between the separated shear layer and side wall boundary layers causes the formation of streamwise aligned secondary vortices along the side-walls. The secondary flow has a significant effect on the spanwise distribution of the mean velocity field, however it is yet to be seen if the side-wall vortices exhibit any shedding behaviour which might be targeted by control, or how they interact with the spanwise flow structures. Frequency analysis is performed on the 10 s-per-point hot-wire traverse data previously used for the mean characterisation of the baseline and actuated flows. Although the quality of the calculated spectra is significantly less that that of the longer point measurements, the content associated with the strongest dynamics can still be identified from the pre-multiplied spectra, and the full-traverse measurements demonstrate the spatial distribution of the dominant flow structures.

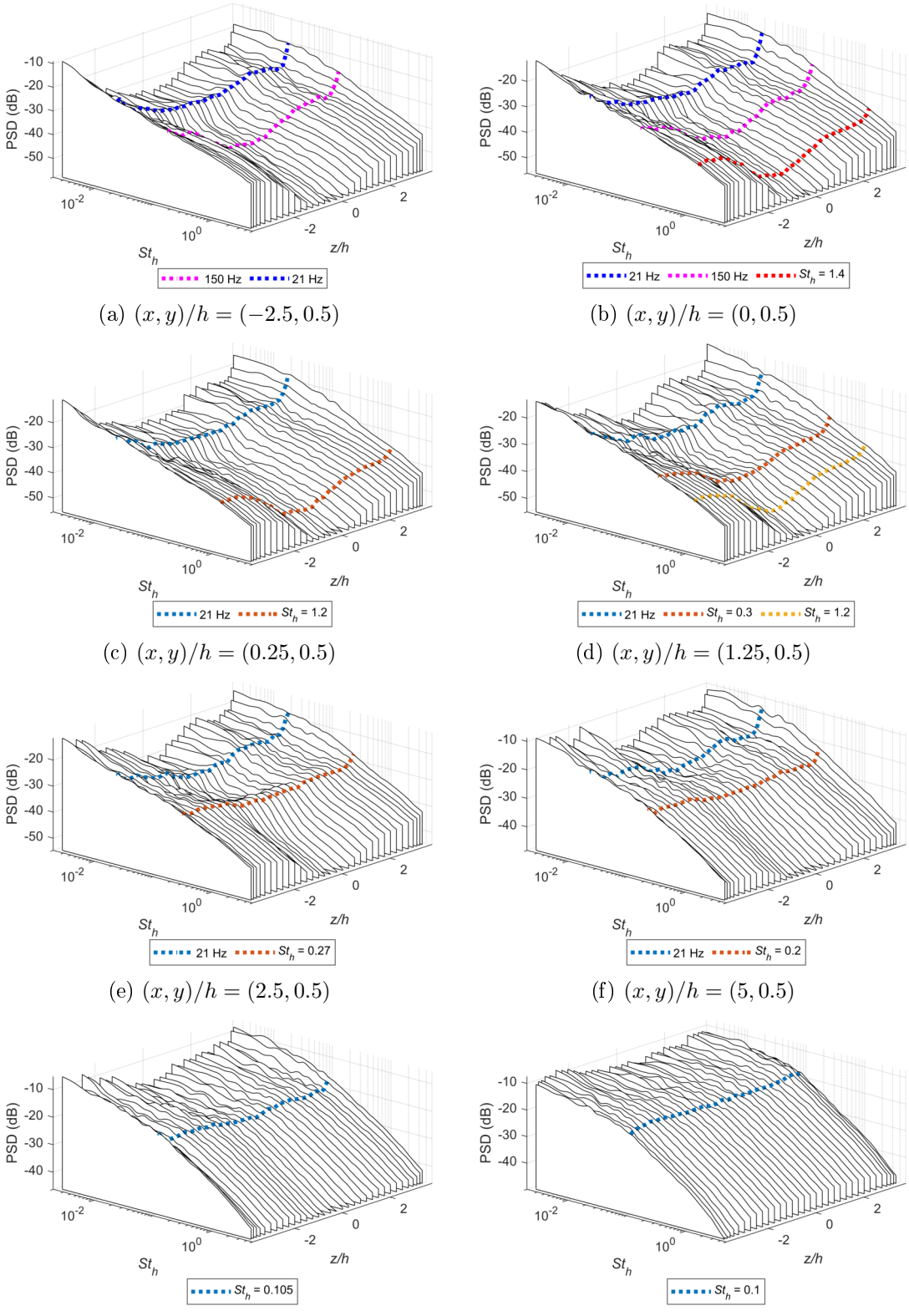
5.6.1 Baseline Flow

Figures 5.30, 5.31, and 5.32 show the smoothed hot-wire PSDs across the span of the channel at various streamwise and wall-normal locations. The PSDs were calculated using Welch's method with window length 4000 samples, which provides sufficient fidelity to identify approximate frequencies of the dominant peaks after smoothing, but not for the identification of smaller local peaks or those at low frequencies (e.g. the flapping mode).
The spanwise PSD plots along $y/h = 0.5$ (Figure 5.30) show significant spanwise variation of broadband frequency content upstream of the step and over the separated region (figures 5.30a to 5.30f), with a trough in the centre of the channel between around $z/h = -1.25$ and $z/h = 1.25$, and increase in content near the side walls for all frequencies. The spanwise variation diminishes from somewhere around reattachment (Figure 5.30g), until the frequency content is almost uniform across the channel by $(x, y)/h = (12.5, 0.5)$, with only slight variation near the side walls (Figure 5.30h). These spanwise distributions are consistent with the RMS velocity plots shown in Figures 4.7 and 4.8, and the broadband nature of the variation indicates that the increased variance away from the centre, assumed to be

largely due to the bell-mouth, is unlikely to be from periodic coherent structures/motions. Immediately after separation along $y = 0$ (Figure 5.31), the frequency content below around $St_h \approx 0.1$ is greater in the centre and just off the side walls at around $z/h \approx \pm 3$, relative to the 1/4 and 3/4 span. However by $x/h = 5$ these low frequency spanwise peaks have mostly flattened out. It is noted that the low frequency unsteadiness close to the step is greater near the lower side of the test section at $z/h \approx -3$, compared to $z/h \approx 3$, due to the disturbance caused by the total pressure probe in the upstream channel, positioned at approximately $(x, y, z)/h = (-4.5, 0.5, -3.5)$, $0.25h$ away from the side-wall. Close to the lower wall along $y/h = -0.825$ (Figure 5.32), a spanwise distribution similar to that along $y = 0$, with slight troughs in broadband content around 1/4 of the span from the centre, and ridges around the 3/4 span, is seen near the reattachment point at $(x, y)/h = (7, -0.825)$, but not inside the recirculation bubble or further downstream. This spanwise distribution seems consistent with the redistribution of fluid in the shear layer by the streamwise side-wall vortices, from around $z/h \approx \pm 1.75$ to $z/h \approx \pm 3$.

The 21 Hz Helmholtz resonance and identified vortex/flow-structure peak are indicated by dotted lines joining the crests in figures 5.30, 5.31, and 5.32. While the sharpness of the peaks is reduced by the higher broadband content away from the centre, the vortex peak frequency does not appear to vary significantly across the span, with the exception of very close to the side-walls at (x, y) locations in/near the shear layer where the peaks are washed-out by the high broadband content and cannot be identified.

Despite the overall spanwise variation in frequency content, all of the identifiable peaks are observed across the entire span, indicating that there are unlikely to be any unidentified time-periodic motions or shedding-type behaviours associated with the side-walls or the longitudinal secondary vortices. This does not, however, mean that the identified structures/modes are not spatially periodic. A number of studies have observed that the shedding and flapping modes are three dimensional with spatially periodic phase in the spanwise direction [92, 101, 99]. Unfortunately this cannot be investigated by single wire hot-wire measurements.



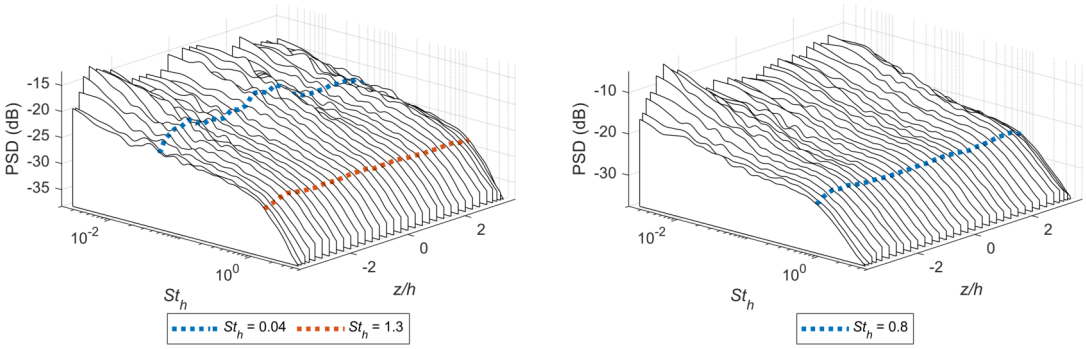
(a) $(x, y)/h = (-2.5, 0.5)$ (b) $(x, y)/h = (0, 0.5)$

(c) $(x, y)/h = (0.25, 0.5)$ (d) $(x, y)/h = (1.25, 0.5)$

(e) $(x, y)/h = (2.5, 0.5)$ (f) $(x, y)/h = (5, 0.5)$

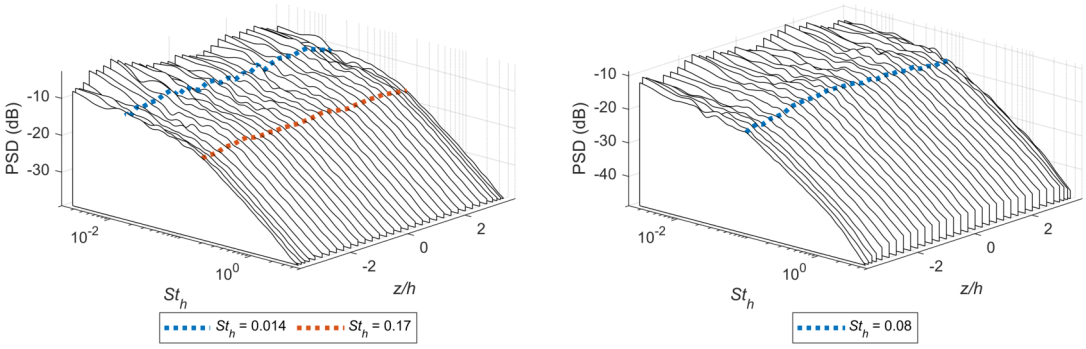
(g) $(x, y)/h = (7, 0.5)$ (h) $(x, y)/h = (12.5, 0.5)$

Figure 5.30: Spanwise PSD distribution at $y/h = 0.5$ and several streamwise locations



(a) $(x, y)/h = (0.25, 0)$

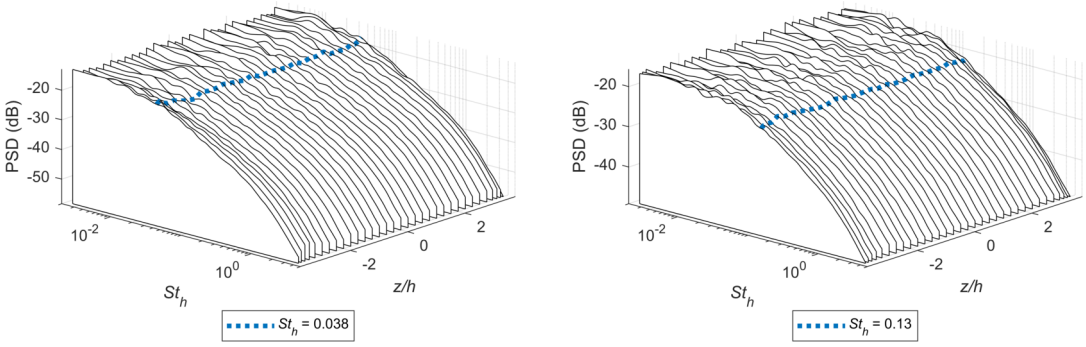
(b) $(x, y)/h = (0.75, 0)$



(c) $(x, y)/h = (5, 0)$

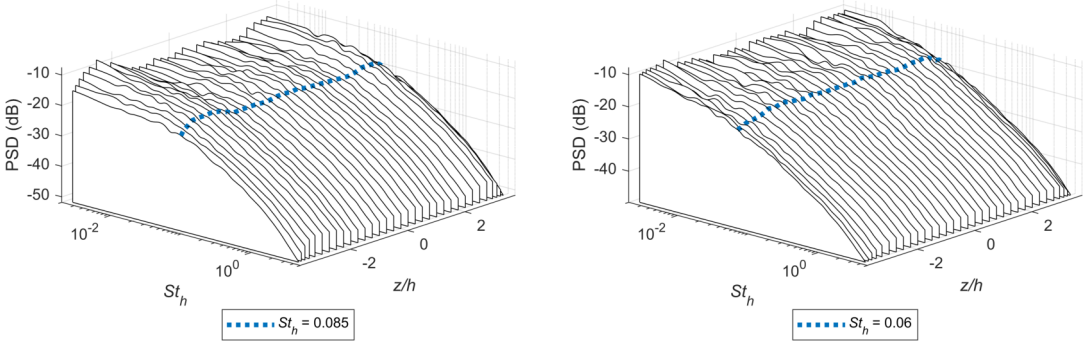
(d) $(x, y)/h = (12.5, 0)$

Figure 5.31: Spanwise PSD distribution at $y = 0$ and several streamwise locations



(a) $(x, y)/h = (2.5, -0.825)$

(b) $(x, y)/h = (5, -0.825)$



(c) $(x, y)/h = (7, -0.825)$

(d) $(x, y)/h = (12.5, -0.825)$

Figure 5.32: Spanwise PSD distribution at $y/h = -0.825$ and several streamwise locations

5.6.2 Forced Flow

Unlike the baseline flow frequency spectra, the shear layer vortex peaks in the forced flow are locked on to the actuation tone and its harmonics/sub-harmonics, so there is no uncertainty related to the identification of shear layer vortex peak frequencies. However, it is still of interest to investigate the spanwise effects of the acoustic excitation. As seen previously, the $f_c = 300\,\text{Hz}$ spike in the hot-wire measurements is too sharp to be due to passing vortices/flow-structures, however this spike appears to emerge from a broader peak at its base. The sharpness of the f_c spike indicates a strong periodic motion perfectly locked-on to the actuation frequency, which is concluded to be the direct coupling of the actuation to the flow, likely a combination of periodic snaking of the oncoming 'jet'/shear layer and a streamwise aligned 'acoustic' perturbation due to forcing of the test section resonance.

The motivation for this analysis is to understand the effect of acoustic forcing on the mechanism of shear-layer spreading and reattachment, which is believed to be vortex driven. Therefore, the sharp spike due to direct coupling of the flow to the acoustic excitation, along with the harmonic at double the forcing frequency are removed by excluding the frequency bins $\pm 5\,\text{Hz}$ around f_c and $2f_c$, followed by smoothing of the spectra.

An example of this is given in figure 5.33, which shows the un-smoothed PSD at $(x, y, z)/h = (1.75, 0.5, 0)$ compared to the smoothed spectrum with the sharp spikes at f_c and $2f_c$ removed. The example demonstrates that although the 'directly coupled' spikes are removed, weaker, broader, peaks are identifiable around the forcing frequency and its harmonic. These broader peaks are attributed primarily to the passing vortex structures, although they undoubtedly include contributions from non-periodic and non-vortex-structure unsteadiness which interacts with the directly-coupled motion (e.g. modulation of the directly coupled velocity perturbation by the low frequency flapping mode, suggested in section 5.4). Removal of the sharp spike also aids in the visualisation of the data, allowing the PSDs to be viewed as a waterfall plot across the span, where the sharp spike at f_c otherwise obscures the content at lower frequencies.

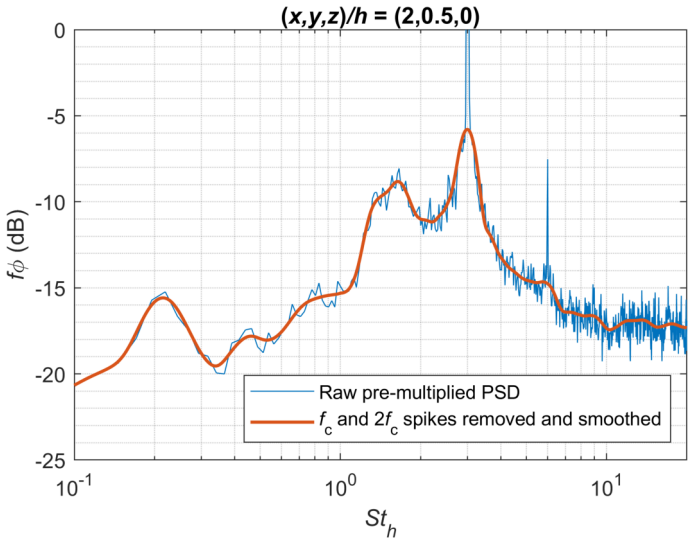
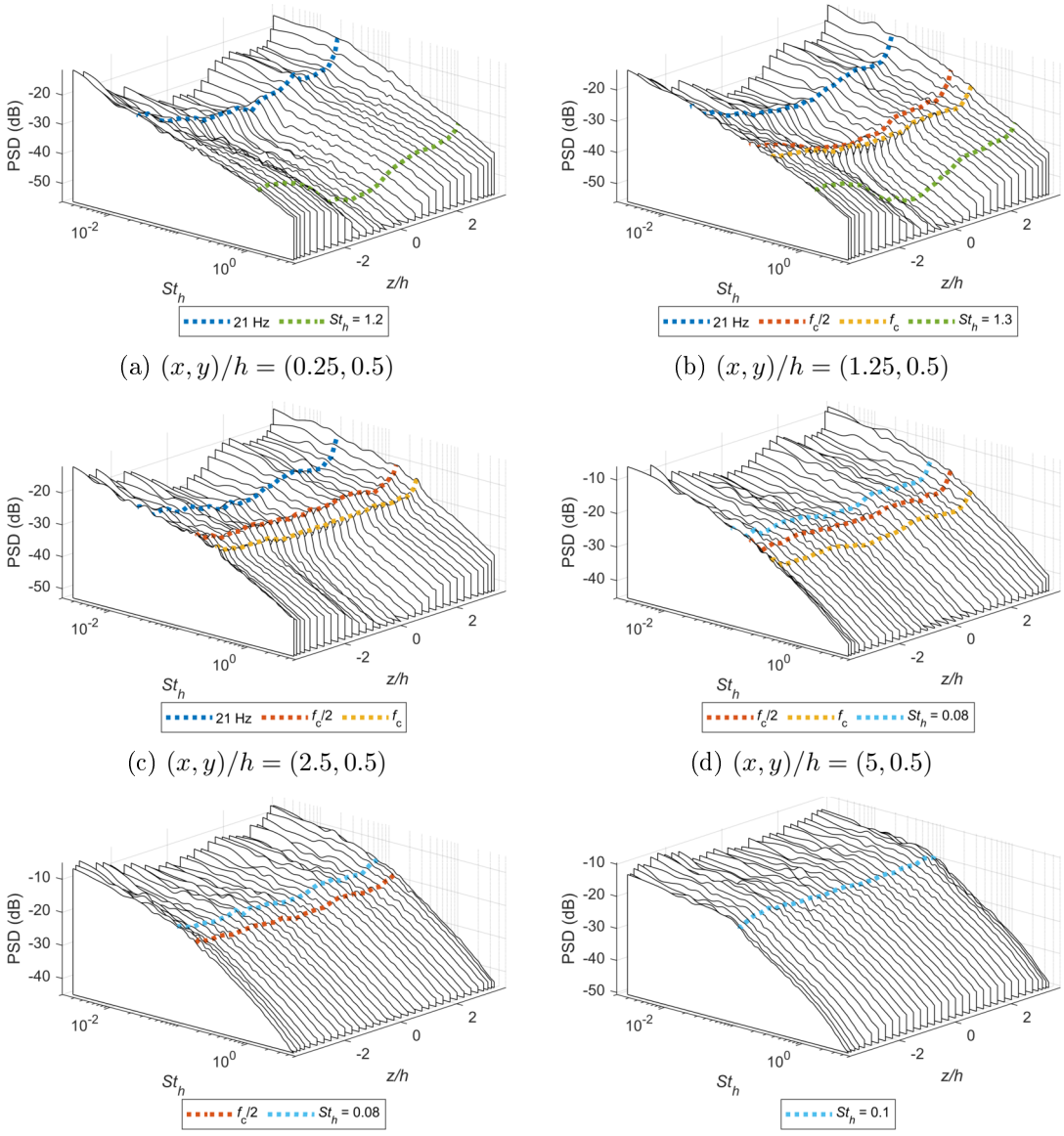


Figure 5.33: Comparison of smoothed and un-smoothed pre-multiplied hot-wire PSD with actuation

Figures 5.34, 5.35, and 5.36 show the spanwise distributions of hot-wire spectra of the forced flows for several x locations along $y/h = 0.5$, $y = 0$, and $y/h = -0.825$, respectively. These plots do not demonstrate any unexpected behaviour. As for the baseline flow, the peaks in frequency content are more visible in the centre of the channel due to the larger broadband content near the side walls, however the forced vortex peak at f_c and the merging peak at $f_c/2$ are strong enough that they can be seen across the full span at the majority of locations where they are identifiable. An exception to the relative spanwise uniformity of the forcing peak is observed at $(x, y)/h = (0.25, 0)$ (figure 5.35a), where the f_c peak is significantly stronger in the centre of the channel, between around $z/h = \pm 1$. Considering that this peak is seen so close to the step, is it suggested that it is due to a motion other than vortex passage (e.g. shear layer 'wiggling' or the interaction of unsteadiness with the driven acoustic mode). This is consistent with the later peaks at the forcing tone being spanwise-uniform in magnitude, as would be expected due to a plane vortex.

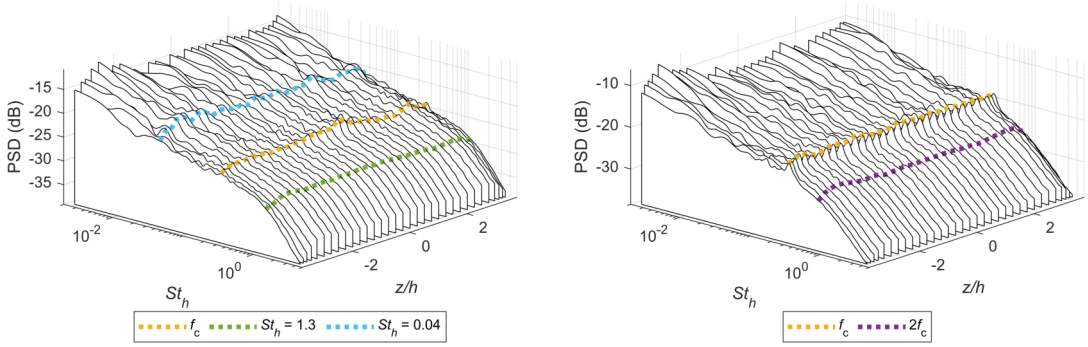


(a) $(x, y)/h = (0.25, 0.5)$ (b) $(x, y)/h = (1.25, 0.5)$

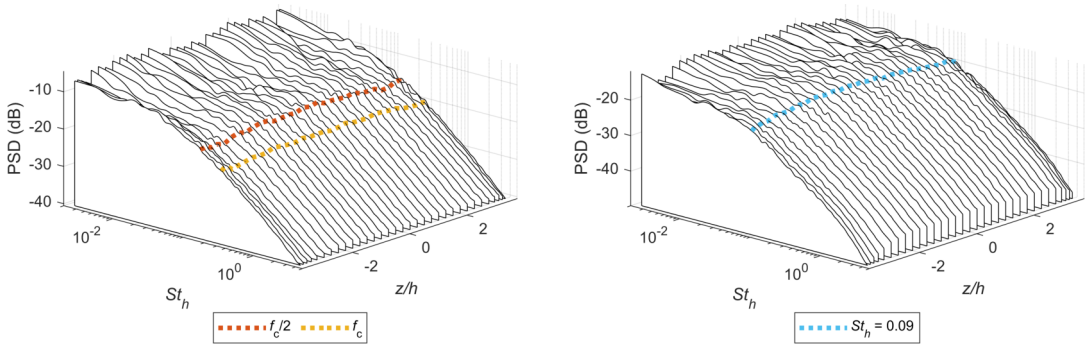
(c) $(x, y)/h = (2.5, 0.5)$ (d) $(x, y)/h = (5, 0.5)$

(e) $(x, y)/h = (7, 0.5)$ (f) $(x, y)/h = (12.5, 0.5)$

Figure 5.34: Spanwise PSD distribution at $y/h = 0.5$ and several streamwise locations

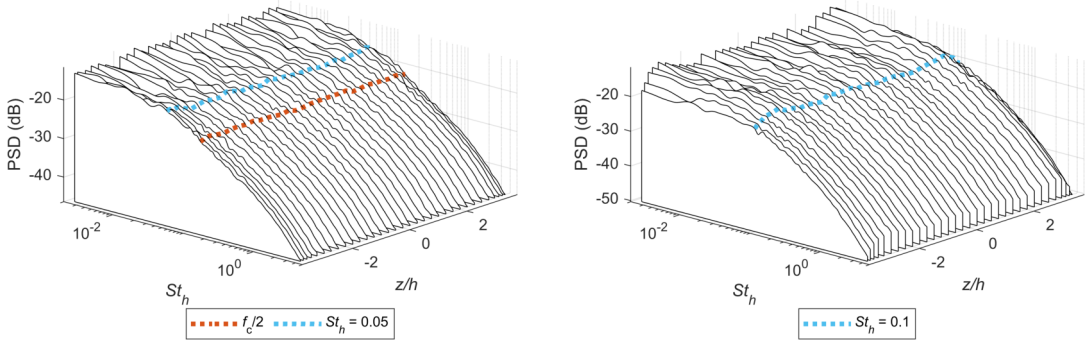


(a) $(x, y)/h = (0.25, 0)$ (b) $(x, y)/h = (0.75, 0)$

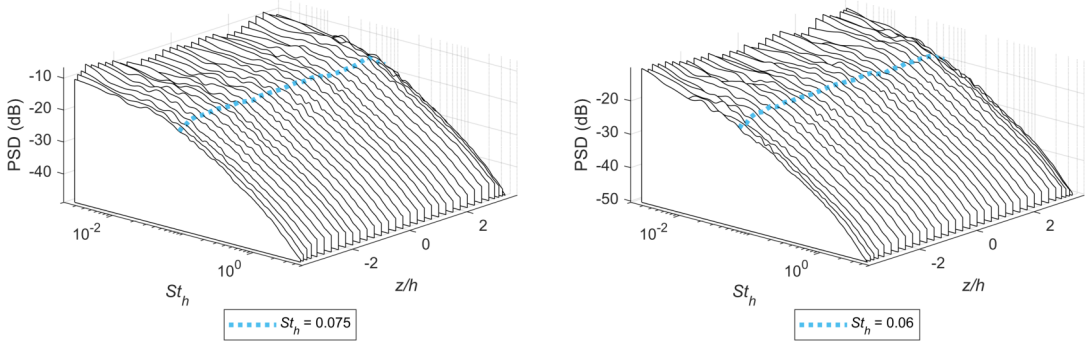


(c) $(x, y)/h = (5, 0)$ (d) $(x, y)/h = (12.5, 0)$

Figure 5.35: Spanwise PSD distribution at $y = 0$ and several streamwise locations



(a) $(x, y)/h = (2.5, -0.825)$ (b) $(x, y)/h = (5, -0.825)$



(c) $(x, y)/h = (7, -0.825)$ (d) $(x, y)/h = (12.5, -0.825)$

Figure 5.36: Spanwise PSD distribution at $y/h = -0.825$ and several streamwise locations

5.7 Conclusion

The dynamic behaviour of both the unforced and acoustically excited backward-facing step flows have been investigated by inspecting the frequency content of wall pressure and hot-wire measurements at a range of positions and operating conditions.

The two main acoustic modes of the rig were characterised by modifying the test section length, and concluded to be the first longitudinal 'organ pipe' resonance at 300 Hz, and the Helmholtz resonance of the cavity-neck system formed from the plenum and test section at $f_H = 21\,\text{Hz}$.

Each of the natural spanwise vortex/coherent modes commonly cited in literature were identified from peaks in the hot-wire frequency spectra of the baseline flow:

- The 'shear layer mode', or roll-up mode, located approximately $x/h = 0.75$-1 from the step edge with $St_\theta \approx 0.017$.
- Vortex amalgamation in the shear layer, reaching the scale associated with the 'step mode', $St_h \approx 0.2$, around half way through the separated region.
- The 'shedding mode', associated with the vortical structures which break away from the shear layer at reattachment and propagate downstream, with $St_h \approx 0.07$-0.12.
- The 'flapping mode' of the recirculation bubble/shear layer, at $St_h \approx 0.015$

Separately, dynamic mode decomposition was used to extract and visualise the dominant modes from the numerical simulations. The DMD mode frequencies agree remarkably well with the peaks in the hot-wire spectra, and confirm that each of the identified peaks corresponds to the expected dynamic structure/motion.

The mechanism by which acoustic excitation modifies the flow was investigated by frequency analysis of hot-wire point measurements, and inspection of the forced CFD DMD modes. Unlike the more typical periodic blowing/suction from the step edge, which is widely reported to directly force vortex roll-up at the actuation frequency [41, 54, 110, 45, 111], the opposite-side acoustic actuation used in the current work is demonstrated to couple to the vortex scale between the shear layer (roll-up) and step modes at $v_{\text{in}} =$

$20\,\mathrm{m\,s^{-1}}$, and vortex roll-up locks-on to the harmonics of the excitation tone at $2f_c$ and $3f_c$. The step mode vortices were also found to occur consistently at the sub-harmonic of the excitation tone. These findings consolidate those of Marrot et al. [42, 109, 48], who presented hot-wire spectra indicating that external acoustic excitation couples to the dominant mode closest in frequency to the excitation rather than exclusively to the shear layer mode.

A brief examination of the influence of excitation amplitude demonstrated that actuation enhances the strength and periodicity of the shear layer vortices/coherent structures, and appears to promote the pairing of vortices into larger scale structures at slightly more upstream locations. All of the evidence presented is consistent with the general consensus in literature, that periodic actuation causes larger, stronger, shear layer vortices which enhance momentum transfer and hence shear layer spreading/curvature, resulting in earlier reattachment [41, 54, 110, 45, 111, 47].

Finally, the spanwise distribution of frequency content is investigated. While there are some variations in broadband content, notably increased unsteadiness near the side-walls in the upstream channel and 'jet' flow until some way downstream of separation, there is little spanwise variation in the peak frequencies associated with the dominant vortex/coherent modes. Additionally, no evidence of as-yet unidentified time-periodic coherent modes resulting from the side-wall flow is observed.

Chapter 6

Closed-loop Control

6.1 Introduction

In Chapter 4 it was shown that steady amplitude acoustic actuation is effective at reducing the mean reattachment length and velocity non-uniformity of the flow downstream of the backward-facing step. Some understanding of how acoustic excitation interacts with the natural acoustic modes and flow structures was gained in Chapter 5, by analysis of the frequency content of wall pressure and hot-wire measurements. While open-loop control is effective, it is not robust to variations in steady-state effectiveness with ambient conditions or due to static flow disturbance and is unable to reject dynamic disturbances, for example those that may be produced by the passage of fan blades upstream of a heat exchanger duct inlet.

This chapter demonstrates closed-loop control of the wall pressure coefficient in the reattachment zone behind the BFS, as a proxy for reattachment length, by amplitude modulation of the acoustic excitation. In Section 6.2 the empirical input-output behaviour of the BFS flow is measured at 16 individual operating points (inlet velocity and actuation amplitude), and linear transfer functions are fit to the input-output dynamics. Two feedback controllers are then designed and validated, a proportional integral (PI) controller in Section 6.3, and a linear quadratic Gaussian regulator (LQG) controller in Section 6.4. The PI controller is designed to achieve the highest possible consistent bandwidth across operating conditions given a maximum sensitivity transfer function magnitude of $|S| \lesssim 2$

[174]. This is achieved by designing PI gains for each of the identified operating points, and 'scheduling' between them by linear interpolation based on the current operating point. The LQG controller is designed with a slightly different aim: to attenuate the disturbance due to the 21 Hz Helmholtz resonance, in addition to tracking a reference and rejecting low frequency disturbances. Robustness is achieved across operating conditions despite the large variation in plant gain by running 16 individual controllers in parallel, one for each identified operating point, and interpolating the control action based on the current operating conditions. This approach is justified by Bacic et al. [175], and ensures that closed-loop behaviour remains reasonably consistent despite the unknown dynamics between the identified points.

Although a number of studies have demonstrated model-based closed-loop control of backward-facing step and similar separated flows [108, 114, 57, 151, 153, 152, 48], they all essentially lead to low bandwidth pure (or predominantly) integral control. In this work an LQG controller is designed to be able to reject a disturbance mode that is roughly the same order of magnitude as the open-loop response time ($St_h \approx 0.014$-0.024).

6.2 Model Identification of Backward-facing Step Dynamics

6.2.1 Empirical Transfer Function Estimates

The input-output behaviour of a linear system can be determined experimentally by calculating its empirical transfer function estimate (ETFE),

$$\hat{G}(i\omega) = \frac{\Phi_{yu}(i\omega)}{\Phi_{uu}(i\omega)} \tag{6.1}$$

where $\Phi_{yu}(i\omega)$ and $\Phi_{uu}(i\omega)$ are the cross-spectral density of output and input, and the power spectral density of the input, respectively.

For a system with significant measurement noise (or in the case of the BFS, uncontrollable flow unsteadiness) the simplest way to determine the ETFE is to perform a sweep of pure sinusoid tones at discrete frequencies f_m as input, then calculate the magnitude and phase of the ETFE at each frequency by

$$|\hat{G}(f_\mathrm{m})| = \frac{|Y(f_\mathrm{m})|}{|U(f_\mathrm{m})|} = \frac{|Y(f_\mathrm{m})|}{B/2} \tag{6.2}$$

and

$$\angle\hat{G}(f_\mathrm{m}) = \angle Y(f_\mathrm{m}) - \angle U(f_\mathrm{m}) \tag{6.3}$$

where $U(f_\mathrm{m})$ and $Y(f_\mathrm{m})$ are the Fourier transforms of the input and output evaluated at f_m respectively, and B is the peak-to-peak amplitude of the sinusoid input.

6.2.2 Wall Pressure ETFEs

It is already known that the mean wall pressure coefficient is a non-linear function of both velocity and excitation voltage. Therefore, at the very least, the magnitude of the plant gain changes with operating conditions even if the dynamics are constant when scaled by the DC gain. System identification is performed at several different velocities and steady input amplitudes to assess the extent to which plant dynamics vary with operating conditions.

ETFEs are calculated for the wall pressures measured at $x/h = 2$, 3, 4, 5, 6, and 7, at inlet velocities $v_\mathrm{in} = 17.5$, 20, 25, and $30\,\mathrm{m\,s^{-1}}$, and mean actuation amplitudes $u_\mathrm{m} = 0.05$, 0.1, 0.15, and 0.2 V. The local dynamics were identified for each operating point by applying a sinusoidal perturbation of amplitude 0.05 V to the steady input, so that the modulation signal is $u = u_\mathrm{m} + 0.05\sin(2\pi f_\mathrm{m} t)$. 50 individual frequencies f_m were chosen from 2 to 150 Hz, measured for 50 s per frequency which was found to be just long enough to average out measurement noise (flow unsteadiness) and give an acceptable ETFE. Identification above 150 Hz was not attempted due to aliasing of the modulation signal by the 300 Hz carrier tone.

Figures 6.1 to 6.6 show the calculated ETFEs for all operating conditions and pressure tapping locations. It is clear from the plots that both the shape and magnitude of the ETFEs change with inlet speed, actuation velocity, and location. However, all exhibit the same two notable features:

1. a narrow peak/bump at around 21 Hz, attributed to the Helmholtz resonance of the test section/plenum

2. a much broader peak centred at approximately 60 Hz, believed to be primarily due to the under damped 2nd order transfer function of the 1 m long tubes connecting the wall tappings to the transducers, rather than a physical flow behaviour

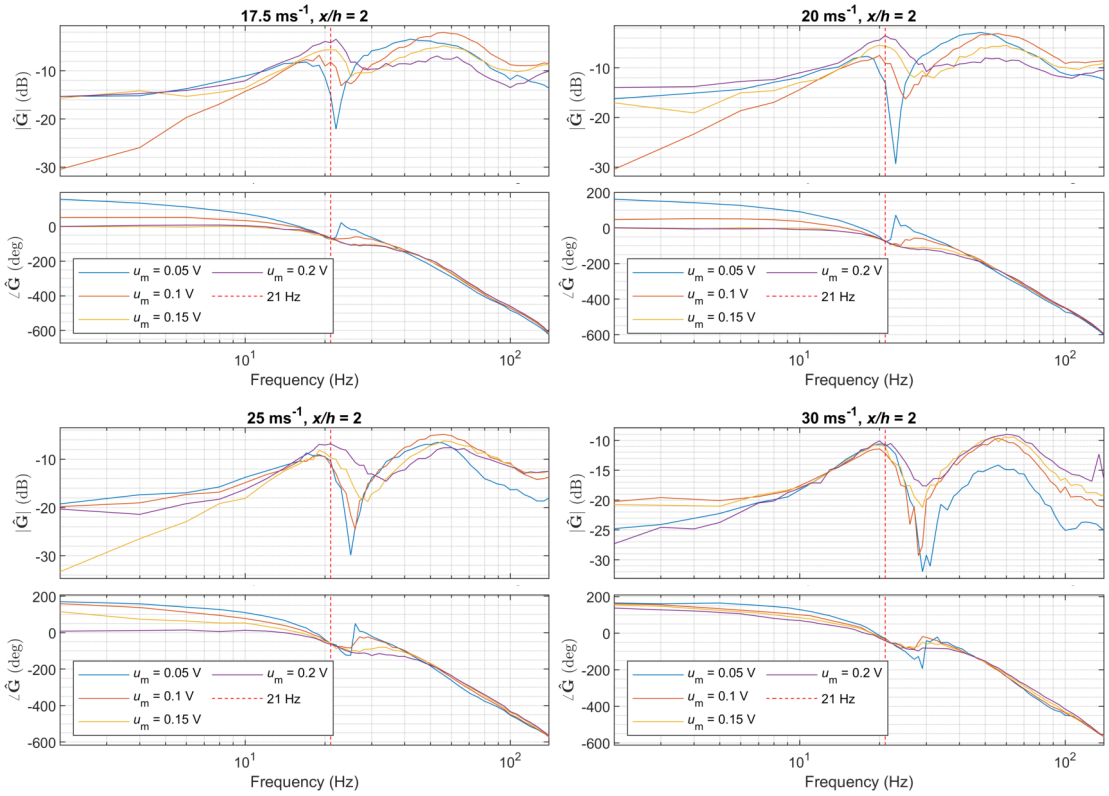


Figure 6.1: ETFEs at $x/h = 2$

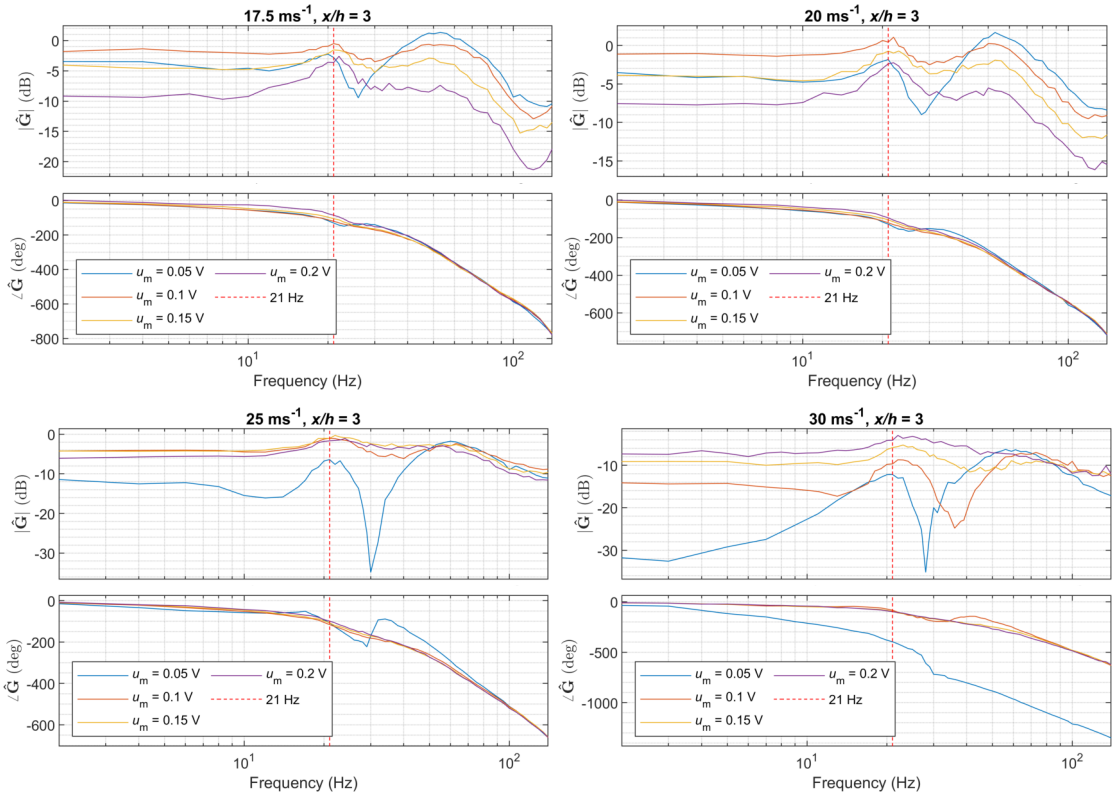


Figure 6.2: ETFEs at $x/h = 3$

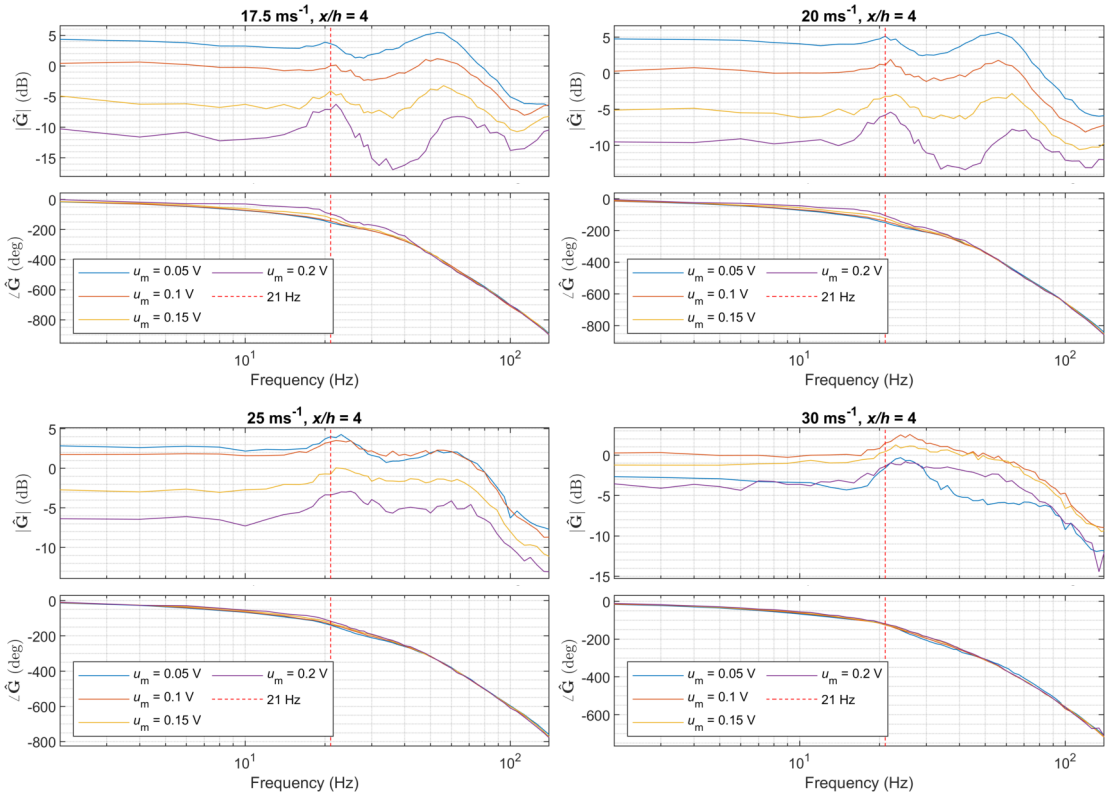


Figure 6.3: ETFEs at $x/h = 4$

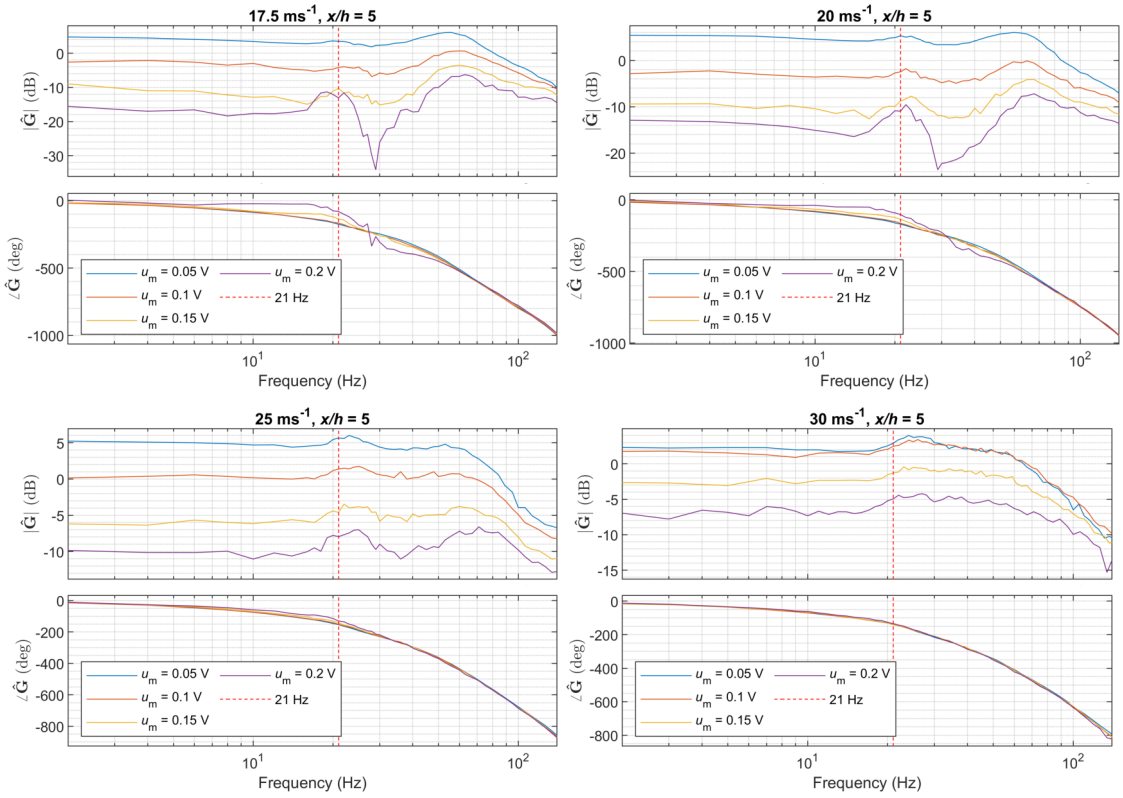


Figure 6.4: ETFEs at $x/h = 5$

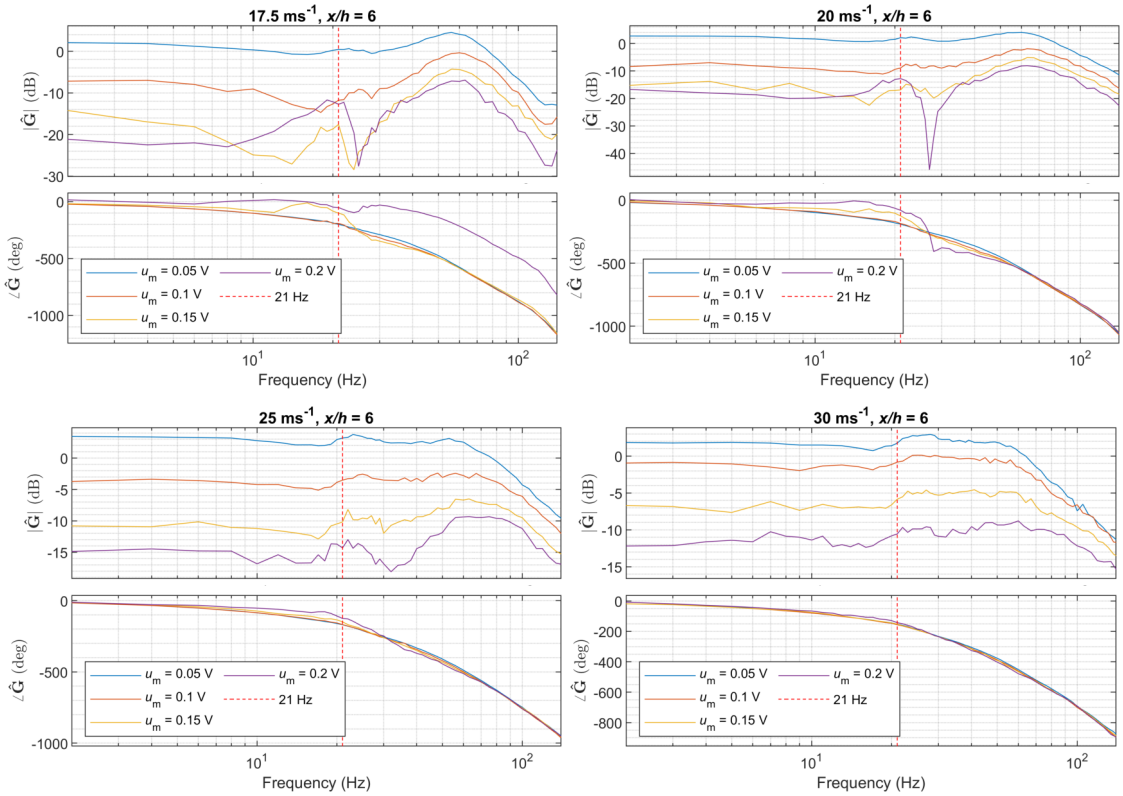


Figure 6.5: ETFEs at $x/h = 6$

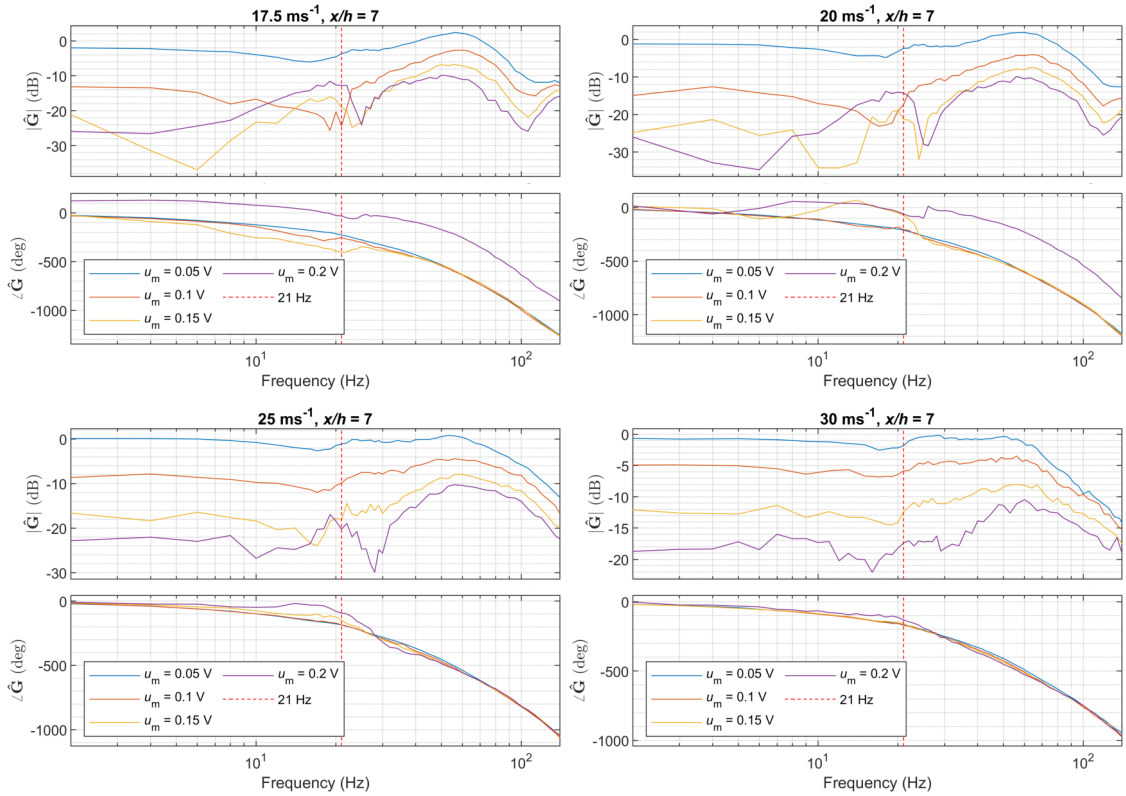


Figure 6.6: ETFEs at $x/h = 7$

Flow Physics Implications of Wall Pressure Transfer Functions

Despite the reasonably uncomplicated shapes of the transfer functions, the input-output behaviour is somewhat complicated conceptually. The carrier tone couples to both the large scale shear layer vortices, the strength/size of which is affected by the input amplitude (and potentially the distance from the step for the vortices to develop), and to the half-wave acoustic mode of the test section. The AM excitation is then demodulated (i.e. the reattachment position responds to the low frequency modulation signal and not the higher frequency carrier tone) in the shear layer by momentum transfer, vortex amalgamation, or both, and the effects of the demodulated perturbation interact with both the shear layer position and the acoustics of the test section and measurement tubes.

The ETFEs at the most upstream locations when the steady actuation amplitude is low (Figures 6.1 to 6.3), and also at the most downstream locations when the steady amplitude is high (Figures 6.4 to 6.6), show a slightly lower DC gain relative to the 21 Hz peak and a sharp dip on the high frequency side of the peak. The phase curves of these ETFEs also

demonstrate a step corresponding to the sharp dip, while the ETFEs without the dip have a phase curve resembling that of a pure delay (i.e. the measured phase matches that of a model with no dynamics other than an input/output delay).

It is inferred, from the operating conditions and the previous characterisation of mean actuation effectiveness, that this sharp dip in the ETFE is indicative of the wall pressure location being outside of the reattachment zone. The magnitude response at these locations implies that outside of the shear layer there is a relatively strongly response at the 21 Hz Helmholtz resonance and the ∼60 Hz resonance of the measurement tubes compared to other frequencies. Conversely, the shear layer has a much more even response up to the roll-off of the measurement tubes. Considering the tapping locations downstream of or near the end of the reattachment region (Figures 6.4, 6.5, and 6.6), the phase curves show reduced delay at frequencies around the 21 Hz peak, consistent with the perturbation being acoustic outside of the shear layer.

6.2.3 Hot-Wire ETFEs

Compared to pressure transducers, hot-wire probes are expensive, fragile, require frequent calibration, and need to be regularly replaced if used in an environment where fouling is a concern [176]. Additionally, wall pressure tappings are non invasive. Despite this, it was hypothesized that using a hot-wire velocity measurement placed in or near the shear layer as feedback might better capturing dynamics of interest, and give the shortest possible measurement delay. The choice of probe/measurement will have some effect on the dynamics which are captured, particularly for acoustic resonances where a large pressure disturbance is accompanied by a comparatively small velocity disturbance. However, given that the ETFEs are between the amplitude modulation signal as input and the demodulated flow response as output (i.e. a convective disturbance) the choice of probe is not expected to have a significant effect over the frequency range of interest.

ETFEs were calculated for hot-wire measurements at locations $(x, y, z)/h = (1.5, 0.25, 0)$ and $(2.5, 0.5, 0)$ for operating conditions $20\,\mathrm{m\,s^{-1}}$ inlet velocity and $u = 0.03 + 0.02\sin(2\pi f_\mathrm{m} t)$, shown in Figure 6.7. Measurements were taken for 40 modulation frequencies from $f_\mathrm{m} = 1$ to 100 Hz, for 100 s per frequency, which was found to be long enough to average out the flow noise for the $(2.5, 0.5, 0)$ ETFE, but not the $(1.5, 0.25, 0)$

ETFE, where the response to actuation was significantly weaker at most frequencies.

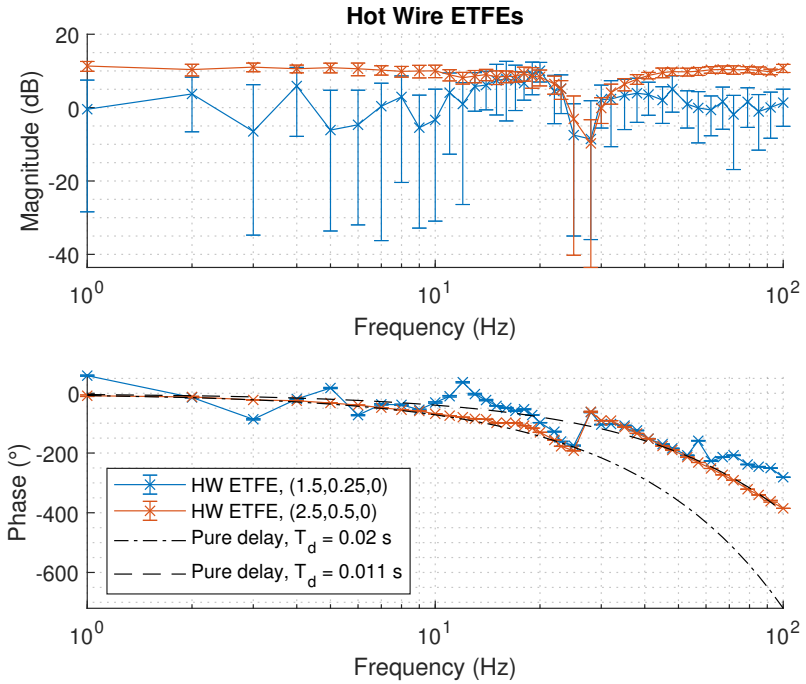


Figure 6.7: Hot-wire velocity ETFEs. Error bars show one standard deviation

Despite the strong 21 Hz peak in the baseline velocity spectrum at location $(x, y, z)/h = (2.5, 0.5, 0)$, the hot-wire amplitude response is almost completely flat except for a trough at around 25-28 Hz and accompanying phase shift. The phase of the $(x, y, z)/h = (2.5, 0.5, 0)$ hot-wire ETFE is roughly equivalent to a pure time delay of $T_\mathrm{d} = 0.02\,\mathrm{s}$ up to the step, and $T_\mathrm{d} = 0.011\,\mathrm{s}$ at higher frequencies. This shift in apparent delay, and the corresponding magnitude trough, suggests that there may be a transition between the mode of shear-layer demodulation. Previous studies have identified that shear layer can demodulate AM excitation either by the amalgamation of vortices [51], or vortex strength/size affecting momentum transfer [45, 53]. However, to the knowledge of the present author no studies have investigated the interaction of AM excitation with low frequency flapping or acoustic modes, which are certainly of importance in the current case, either because the modes were not present (e.g. studies conducted on free jets/shear-layers) or because the focus was on shear layer vortices.

Fitting a pure delay to the phase curves of the wall pressure ETFEs at $x/h = 5$ gives an equivalent delay of around $0.022\,\mathrm{s}$ at $v_\mathrm{in} = 20\,\mathrm{m\,s^{-1}}$. Accounting for the time it takes sound to travel through the 1 m measurement tube, approximately 0.003 s, the physical

delay/transport time for frequency content below about 25 Hz is similar between the wall pressure at $x/h = 5$ and the velocity at $(x, y, z)/h = (2.5, 0.5, 0)$, despite the pressure tapping being $2.5h$ downstream of the hot-wire probe. Based on this, it is not clear that there are any benefits to using a hot-wire probe for feedback which would outweigh the practical limitations in real world conditions.

6.2.4 Choice of Feedback Measurement

Having decided on using a wall-pressure measurement as feedback, the question remains as to which tapping should be used. To ease the design of the gain scheduled controller, it is clear from Figures 6.1 to 6.6 that the most smoothly varying transfer functions were with output at $x/h = 4$ and 5. Although it is not necessary to relate reattachment length to the feedback variable, it is conceptually convenient if there is a linear (or at least low order) relationship between the the C_p measurement used for feedback and reattachment length as the most obvious metric for control effectiveness. It was demonstrated in Section 4.2 that mean wall pressure coefficient at $x/h = 5$ is approximately linear with the reattachment length estimated from the maximum in the RMS wall pressure distribution, therefore this seems the most appropriate measurement to use as feedback.

However, there is not a clear definition for instantaneous reattachment length in turbulent/unsteady flows, where any given snapshot of the flow consists of multiple vortical structures and random eddies. Nevertheless, tracking a steady-state value of C_p will guarantee a steady-state reattachment length, and low frequency unsteadiness in the C_p measurement will relate to either fluctuations of the reattachment position or other large scale structures/motions, both of which are desirable to suppress.

The use of multiple wall pressure measurements as feedback was considered, with the aim being to reduce the effect of smaller scale unsteadiness and improve the signal to noise ratio of the controllable dynamics. Preliminary controller designs, however, suggested that there was no significant reduction in uncontrollable noise fed through to the control action, while the controller complexity was increased considerably. Further work might include a sensor fusion approach to feedback, or skipping between the wall pressure tapping used such that the variation of input-output dynamics is minimised, but both approaches were beyond the scope of the current work.

6.2.5 High Order Plant Model fits

9^{th} order discrete transfer function models ($f_s = 4\,\text{kHz}$) with no delay were fitted to all 16 of the ETFEs, shown in Figure 6.8. There was found to be no improvement in fit across identified frequencies from increasing the model order or specifying an input delay. These model fits are later used for the design of a gain scheduling PI controller, in section 6.3.

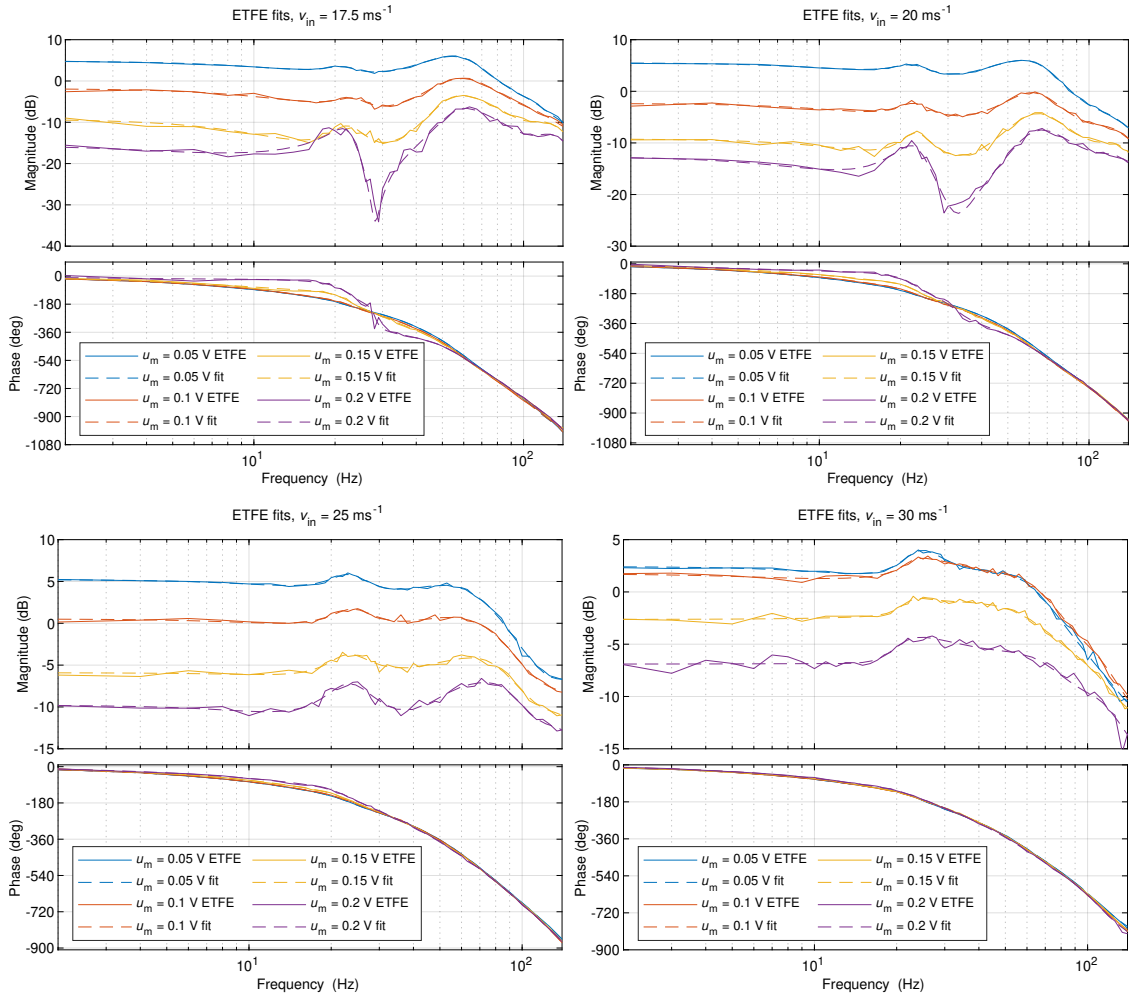


Figure 6.8: 9^{th} order model fits to identified ETFEs

The equations of the transfer function, $G(i, j)$ at each of the identified operating points are given in Appendix A.1.

6.2.6 Low Order State Space Model Fits

While the 9^{th} order transfer functions provide a good fitted to the ETFEs, a lower model order/complexity is preferable for model based controllers, like the LQG. Prioritising low

model order is of even greater importance for the parallel-interpolating LQG controller designed in section 6.4, where multiple controllers are run in parallel on an FPGA with a limited number of gates.

Third order state space models with input delays were fit to the ETFEs at all 16 of the identified operating points, with the aim of fitting the low frequency gain and magnitude/shape of the 21 Hz peak, shown in Figure 6.9. No attempt was made to fit the second broader peak, as compactness of the models is prioritised, and the achievable bandwidth is below even the initial peak due to the relatively long transport/measurement delay.

For the few cases where a 3$^{\text{rd}}$ order model struggles to fit both the DC/low frequency gain and the magnitude/shape of the 21 Hz peak, accurately modelling the peak magnitude was prioritised. The reason for doing so is that the difference in low frequency gain between model and experiment can be accounted for by an integral term, while the 21 Hz peak is above the maximum integral bandwidth, and accuracy of the model is more important in this region if the intention of the controller is to suppress content due to the Helmholtz resonance.

The phase of the ETFEs at operating conditions where the wall tapping at $x/h = 5$ is within the reattachment region can be modelled well by a pure input delay. Those downstream of or close to the end of the reattachment zone have less phase delay up to the Helmholtz resonance frequency, followed by a steep decrease in phase across the frequencies of the magnitude peak, then roughly match the phase of a pure delay at higher frequencies, which the third order models struggle to fit. In these cases the phase curve is only fitted up to the Helmholtz resonance frequency, above which the models are not expected to capture any dynamics.

Embedding an input delay in a state space model results in one extra state for each time-step of delay, therefore in the interest of model order the input delays are replaced by a second order Padé approximation, which models the delay as non-minimum phase zeros and brings the total number of states to 5. The second order Padé delay is only able to fit the model phase up to around 25-30 Hz, which is deemed sufficient as the models are not fitted to the ETFEs at frequencies above the 21 Hz peak.

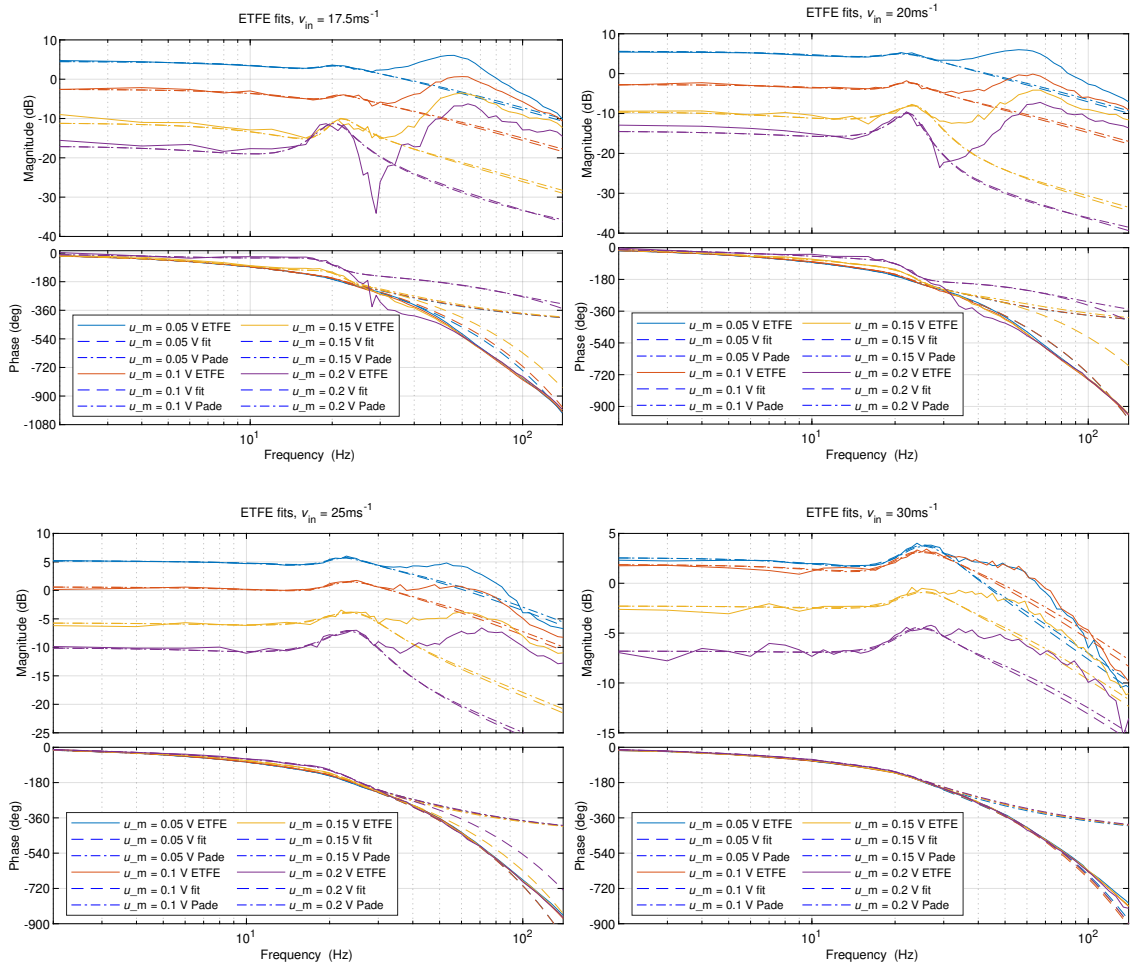


Figure 6.9: 3rd order model fits to identified ETFEs

The state space models of each identified plant are summarised in Appendix A.2.

Effects of Operating Conditions on Poles and Zeros

Figure 6.10 shows the variation with inlet velocity of poles and zeros of each of the 3rd order models (without Padé approximated delays), at each steady state input voltage. While the poles and zeros appear to occupy similar regions of the complex plane for all operating conditions, there does not appear to be an obvious functional relationship between operating conditions and pole-zero positions, which rules out the identification of a parametrised non-linear model. It is possible that smooth functions of pole and zero values in terms of input speed and steady state amplitude could be found with a much denser grid of identified operating points, however this is experimentally unfeasible given the time taken to conduct the ETFE measurements.

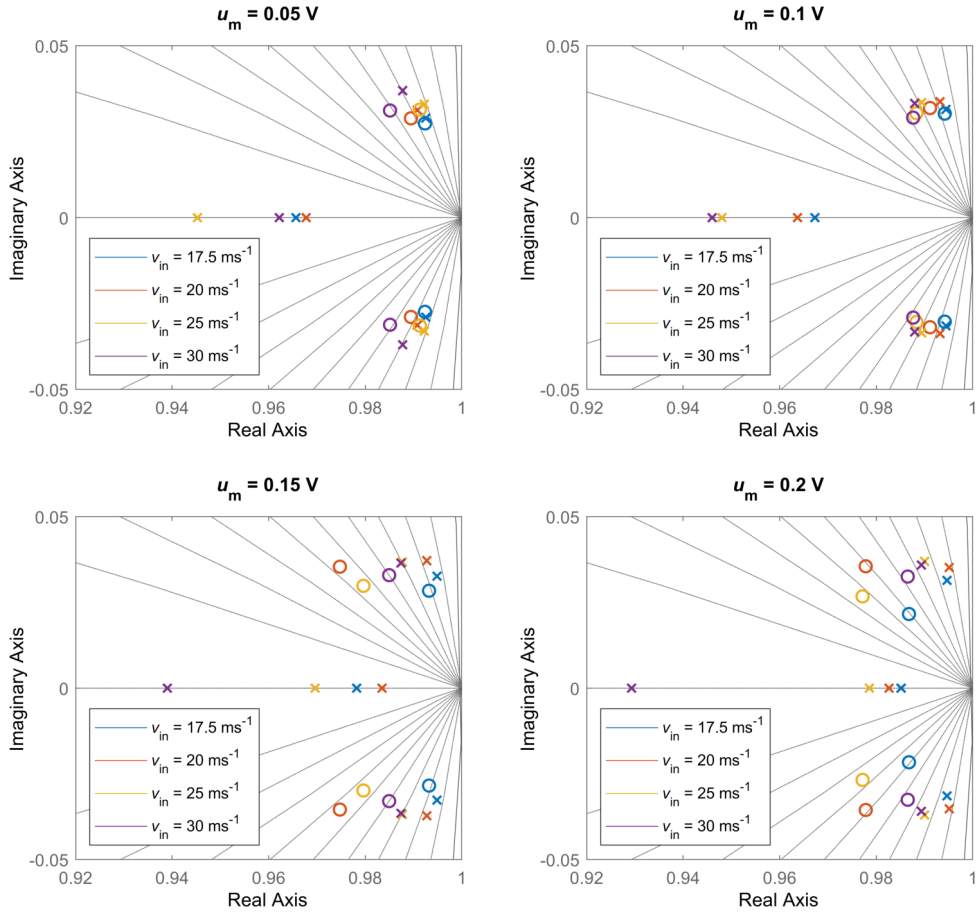


Figure 6.10: Pole-zero plots of 3rd order transfer function fits for all velocities at each mean input voltage

6.2.7 Static Mapping

Having identified the dynamics of the wall pressures across various operating conditions, the final piece of a full plant model is the steady state mapping from input amplitude to wall C_p. Without this mapping, the DC gain of the transfer functions gives only an approximation to the gradient of this curve, but not the steady value of C_p achieved by the steady input.

A static mapping of mean wall C_p at $x/h = 5$ as a function of inlet velocity and actuation amplitude is constructed by smooth 2D interpolation of the measured values ($C_{p,\text{map}}$). Figure 6.11 shows the measured C_p against input amplitude for all of the measured velocities and the interpolated curves.

An inverse mapping of input amplitude u as a function of inlet velocity and mean C_p was also constructed in a similar manner (referred to as u_{map}), the only difference being

that the steady actuation input was interpolated onto a grid of C_p values rather than the other way around. This mapping is limited to between $C_p = 0.1$ and 0.28, as values outside this range are not necessarily achievable for all velocities given limits on actuation amplitude. The inverse mapping will be used as the open-loop controller, and also as a coordinate transform from requested C_p to the input amplitude operating point used for gain scheduling and interpolation of control action.

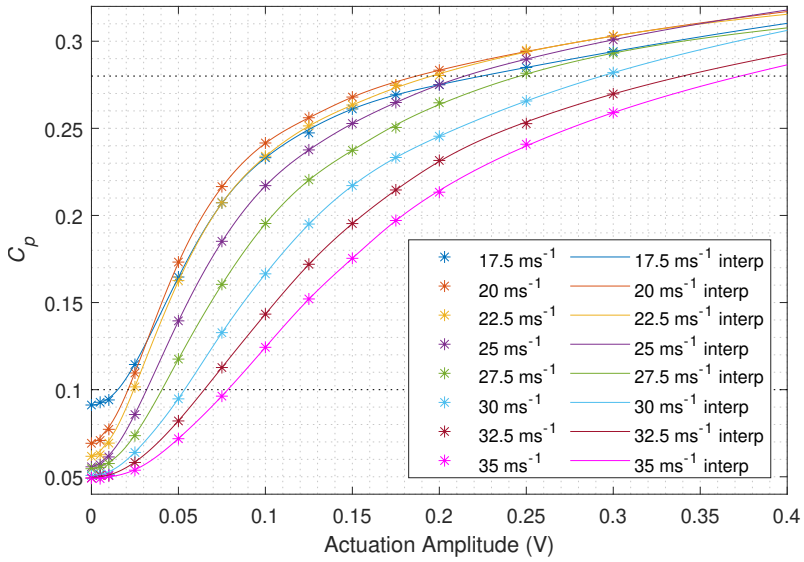


Figure 6.11: C_p at $x/h = 5$ vs actuation amplitude

Non-linearity of Static Response with Modulation

Figure 6.12 shows the difference between the mean value of C_p with amplitude modulation, calculated from the ETFE frequency sweeps, and the C_p value with steady amplitude (i.e. the static mapping, shown in Figure 6.11) at the same mean voltage input, for all four inlet speeds at which dynamics are identified. It was implicitly assumed when identifying the linearised plant dynamics and the static (mean) input-output mapping that the AM response of the C_p value, and by extension the reattachment length, is a perturbation around a fixed mean value which is independent of modulation frequency.

Figure 6.12 shows that while there is a small deviation from the static mapping for all modulation frequencies, in general the mean C_p value increases with modulation frequency. This trend is not surprising, given that excitation by multiple sub-/harmonics at once has been shown to target multiple scales of vortex structure/pairing, and lead to more effective

control [177, 178, 49]. Despite the AM frequency non-linearity, the error between the AM C_p value and the steady amplitude mean is less than 5% of the achievable C_p span for modulation frequencies up to $f_{\mathrm{m}} \approx 20\,\mathrm{Hz}$, which is small enough to be easily accounted for by an integral term in the feedback controller without any noticeable effect on performance.

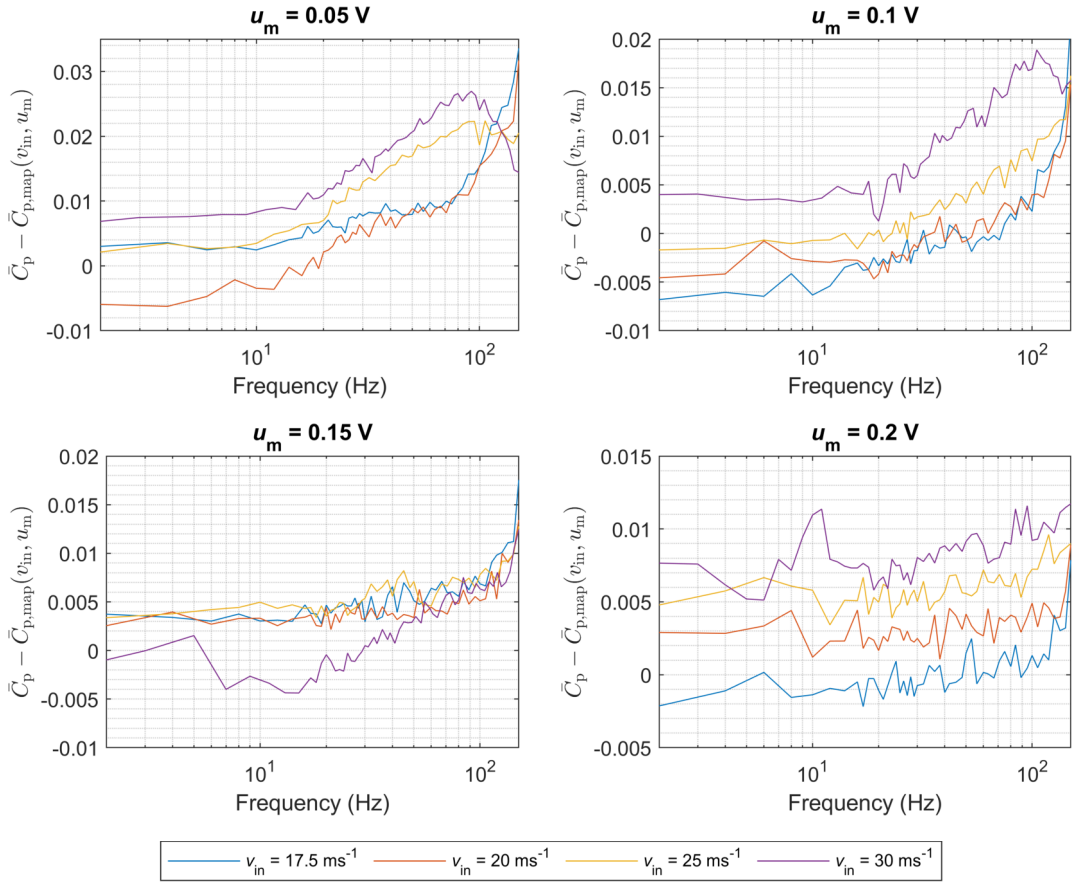


Figure 6.12: Difference between mean C_p with amplitude modulated input voltage and steady amplitude input

6.3 PI Controller

As a first attempt, a classical proportional-integral controller (PI) is designed to ensure accurate tracking of a requested wall pressure coefficient with acceptable bandwidth and rejection of low frequency noise. A challenge in the control of fluid systems is the broadband noise introduced by turbulence and large but uncontrollable unsteadiness. The resulting low signal-to-noise ratio ultimately limits the achievable performance. Unlike the classical control assumption that noise amplitudes are small at lower frequencies, here there is no clear separation between signal and noise bandwidths. Since derivative action amplifies

the noise with its gain increasing proportionally to frequency, heavy filtering would be required. For the purposes of PID design the differential gain has therefore been set to $k_\mathrm{d} = 0$, and the controller is PI only. Arguably the proportional gain may not be entirely helpful either, as it will feed through noise due to primarily uncontrollable flow unsteadiness at all frequencies, however the term is included in the controllers as a means to achieve a higher closed loop bandwidth than an integral-only feedback law.

Given that the open-loop plant gain varies significantly with inlet velocity and steady voltage input, any controller with fixed gains will result in inconsistent bandwidth and stability depending on the current operating conditions. To address this, gain scheduling is implemented such that the gains are selected based on the current velocity and steady state actuation required to achieve the requested C_p (determined using the steady-state mapping explained in Section 6.2.7). Gain scheduling does not guarantee the performance of the controller away from identified operating points, nor does it assure general guarantees of stability, but it is generally accepted as good means to control a smoothly varying plant like the current problem [179]. This also allows the bandwidth to be similar regardless of operating point, whereas guaranteeing stability at all conditions when using fixed gains would necessitate limiting the gains based on the operating point with the highest plant gain, resulting in lower bandwidth at all other points.

It is necessary to filter the C_p measurement prior to the PI controller to remove the acoustic tone, which requires about $-60\,\mathrm{dB}$ attenuation at $300\,\mathrm{Hz}$. It is also beneficial to filter above about $30\,\mathrm{Hz}$, as flow dynamics cannot be separated from the measurement tube response at higher frequencies, and the phase has either passed or is approaching $-360°$. The lowest order filter that meets these requirements is a 4^{th} order low-pass filter with cut-off frequency $40\,\mathrm{Hz}$. PI gains for each of the 16 identified operating points are designed with the filter in series with the plant models to account for the additional phase lag from the filter.

Figure 6.13 shows the block diagram of the gain-scheduling PI controller.

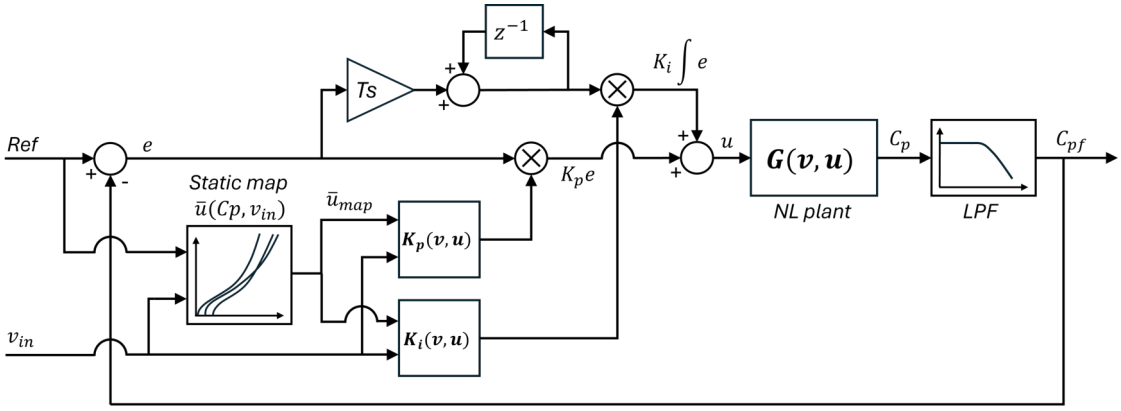


Figure 6.13: Simplified block diagram of closed loop gain-sheduling PI controller

The PI gains are tuned with the aim of achieving the highest possible closed-loop bandwidth consistently across the operating range. It is possible to set a relatively high $-3\,\text{dB}$ frequency of the closed loop response (around 10-20 Hz depending on operating point), however the phase lag is very large at these frequencies, exceeding $-180°$, and a corresponding large magnitude peak is observed in the sensitivity transfer function, given by

$$S(s) = \frac{1}{1 + C(s)G(s)} \tag{6.4}$$

The sensitivity function tells us two things: First, it is the closed loop transfer function from an output disturbance to the measured output, and second, it indicates the relative effect of errors in plant dynamics on the overall system. A perfect controller would have infinite bandwidth and sensitivity well below 0 dB across all frequencies, but this is not possible in practice. Instead the controllers are tuned with the following aims:

1. Peak sensitivity magnitude, $|S(s)|$, to be kept below some threshold. This requirement effectively sets the maximum amplification of output noise, and also the level of deviation of the actual closed loop response from designed in the case where dynamics are imperfectly modelled or unknown

2. Peaks in $|S(s)|$ should ideally not coincide with frequency ranges in which plant dynamics vary significantly with small changes in conditions.

3. Peaks in $|S(s)|$ should be kept away from frequency ranges in which amplification of natural content might be unfavourable, in this case it is intended to attenuate rather

than strengthen the 21 Hz Helmholtz resonance.

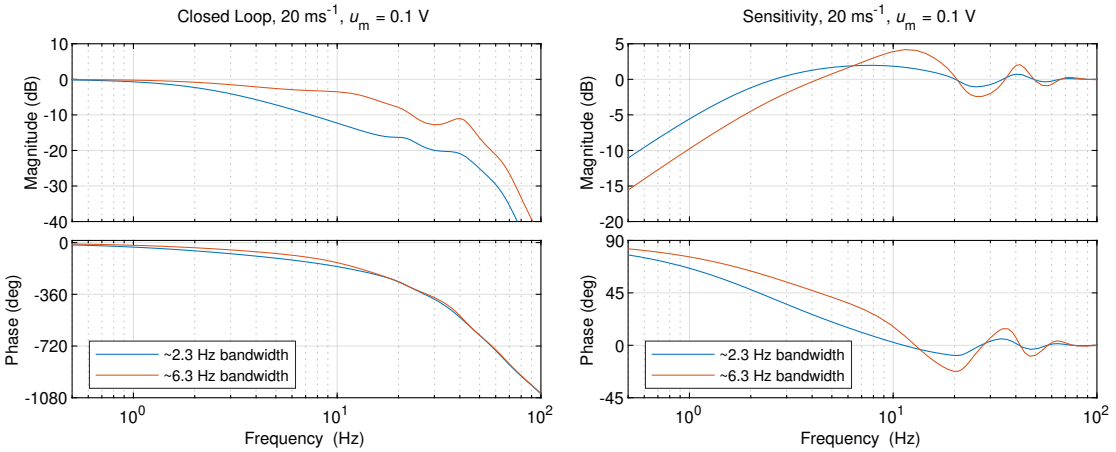
4. Highest possible -3 dB bandwidth given the previous three requirements

Unfortunately, the large variation of plant gain with inlet velocity and steady actuation voltage at all frequencies up to roll-off effectively rules out achieving requirement 2, increasing the importance of choosing an appropriate maximum $|S(s)|$.

6.3.1 Gain Tuning

Proportional and integral gains were tuned for each of the 16 identified 9^{th} order models, such that the closed-loop bandwidth of the controller remains approximately constant at all of the identified operating points. The gain-scheduling map was then constructed by a 2D linear interpolation of the tuned gains at each point. Two separate tunings were considered, the first with bandwidth just above 6 Hz but peak sensitivity exceeding 4 dB, and the second with bandwidth just above 2 Hz while sensitivity was limited to not exceed 2 dB at any of the operating points. Figure 6.14 shows a comparison of the two tunings at $v_{\text{in}} = 20\,\text{m}\,\text{s}^{-1}$ and $u_{\text{m}} = 0.1\,\text{V}$ (Design point 1). Apart from the obviously desirable higher bandwidth, the 6 Hz tuning has lower sensitivity at low frequencies, and peak sensitivity at a higher frequency than the 2 Hz tuning (11.5 Hz vs 8 Hz respectively). The gain and phase margins of the two tunings are:

Tuning	**Gain Margin** (dB)	**Phase Margin** (°)
6 Hz	8.48 @ 12.8 Hz	73.9 @ 3.17 Hz
2 Hz	14.9 @ 11.2 Hz	76.6 @ 1.75 Hz



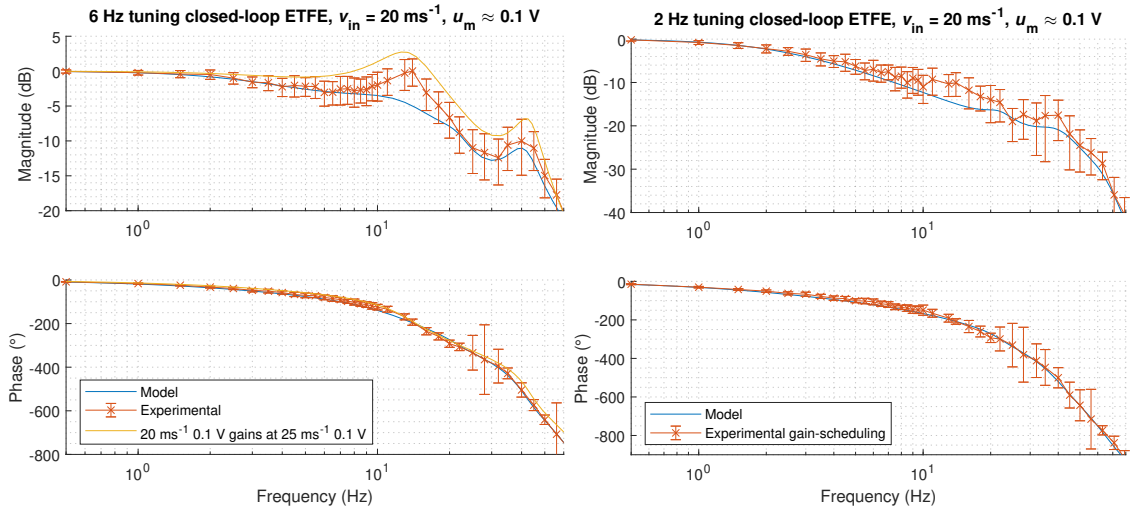
(a) Closed-loop transfer function (b) Sensitivity transfer function

Figure 6.14: Comparison between high and low bandwidth PI tuning at $20\,\mathrm{m\,s^{-1}}$, $0.1\,\mathrm{V}$

Both sensitivity transfer functions also exhibit a trough from around 21 Hz to 35 Hz, which should provide some attenuation of the Helmholtz resonance even though there is only partial overlap. Despite the 2 Hz tuned sensitivity function first crossing over 0 dB at a lower frequency (2.6 Hz vs 4.28 Hz), this cross-over point is above the closed-loop -3 dB bandwidth for the lower tuning, but within the bandwidth for the higher tuning. This indicates that the bandwidth of the 2 Hz tuned controller should be relatively unaffected by inaccuracies in the model/expected plant gain compared to actual plant gain, while the experimental bandwidth of the 6 Hz tuning may be affected significantly, resulting in unpredictable controller performance.

Figures 6.15a and 6.15b show the experimental closed loop transfer functions for the 6 Hz and 2 Hz tuned controllers at the $20\,\mathrm{m\,s^{-1}}$ 0.1 V operating point, respectively. The 6 Hz tuned experimental transfer function follows the model well up to around 6.5 Hz, after which there is an unmodelled peak with maximum magnitude approximately 0 dB at 14 Hz, effectively raising the bandwidth to around 16 Hz. This is consistent with the conclusions made from the sensitivity transfer function, and additionally illustrates that the experimental actuation effectiveness, hence the plant gain at any given operating point $(v_{\mathrm{in}}, u_{\mathrm{m}})$, varies over long time periods. To further demonstrate this point, the transfer function achieved by using the gains designed for the $20\,\mathrm{m\,s^{-1}}$ 0.1 V model on the $25\,\mathrm{m\,s^{-1}}$ 0.1 V model is also plot in Figure 6.15a, and exhibits a peak of a similar shape to the experimental $20\,\mathrm{m\,s^{-1}}$ transfer function, but with slightly higher magnitude. This confirms that

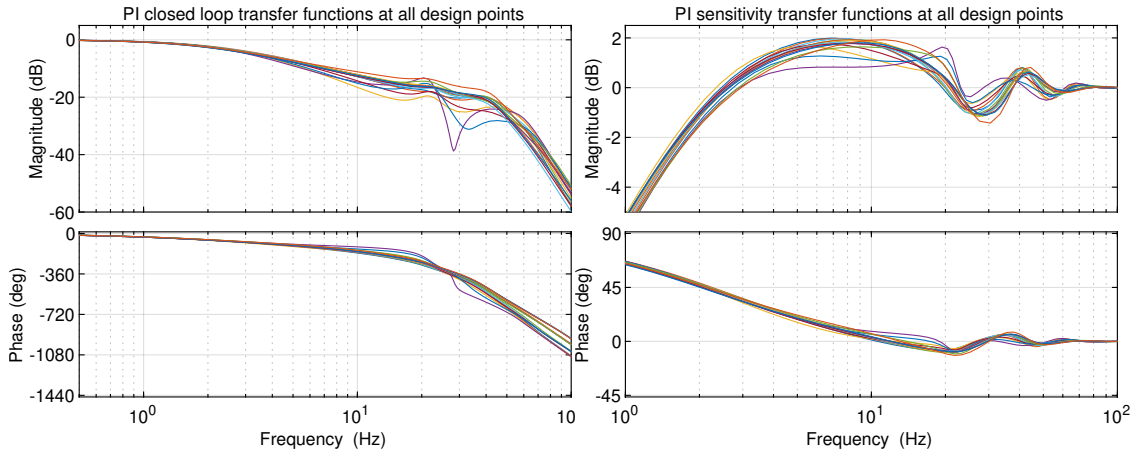
the difference between the intended closed-loop response and experimental response can be caused by a small change in plant gain from the expected value, and the experimental transfer function is within the bounds set by adjacent identified operating points. Conversely, the magnitude of the 2 Hz tuned experimental closed-loop transfer function has only a slight bump from around 10 Hz to 22 Hz, and very little deviation from the model until well over the bandwidth frequency. From this point on the maximum sensitivity magnitude criteria is set as $|S| < 2$, and the slower 2 Hz tuning is used for all of the remaining experiments.



(a) ∼6 Hz bandwidth controller (b) ∼2 Hz bandwidth controller

Figure 6.15: Model vs experimental closed-loop transfer function at $v_{\text{in}} = 20\,\text{m}\,\text{s}^{-1}$, $C_{p,\text{ref}} = 0.24$ ($u_{\text{m}} \approx 0.1\,\text{V}$). Input signal $u = u_{\text{m}} + 0.03\sin(2\pi f_{\text{m}} t)$ V with f_{m} from 0.5 to 100 Hz, measured for 100 s per frequency. Error bars show 1 standard deviation

Having decided on an appropriate controller tuning, PI gains were tuned for the remaining identified models, such that the sensitivity magnitude $|S|$ does not exceed 2, and the closed loop bandwidth is approximately constant at each design point (between 2.2 Hz ($St_h = 0.0015$-0.0025) and 2.4 Hz ($St_h = 0.0016$-0.0027)). The minimum gain and phase margins of the 16 systems are 5.23 dB and 75.4°, respectively. Figure 6.16 shows the closed-loop and sensitivity transfer functions for all 16 design points.



(a) Closed-loop transfer functions (b) Sensitivity transfer functions

Figure 6.16: PI controller tunings for all 16 design points

6.3.2 Gain Scheduling

The gain schedule mapping was then implemented in the FPGA code via lookup table by linearly interpolating the designed gains onto a 64 by 64 point grid of inlet velocity and steady actuation voltage, then scaling and rounding the gains so that they could be represented as an 8-bit integer, shown in Figure 6.17. The scheduling could equally have been achieved by directly linearly interpolating between the four design points bounding the operating conditions in the FPGA code, however given the relatively small steps in gains and the uncertainty of the system this is unlikely to make a significant difference. For operating points outside of the design space, v_{in} and u_{map} are limited to the maximum/minimum design value, i.e, the nearest point on the gain map to the current operating conditions. Given that the plant gain should vary smoothly with operating conditions, linear interpolation will not be optimal, however the exact dynamics between identified points are unknown (DC gain could be estimated from the static mapping, but not dynamics). There is therefore no guaranteed benefit to scheduling over some smooth function which would still be a guess between the tuned points.

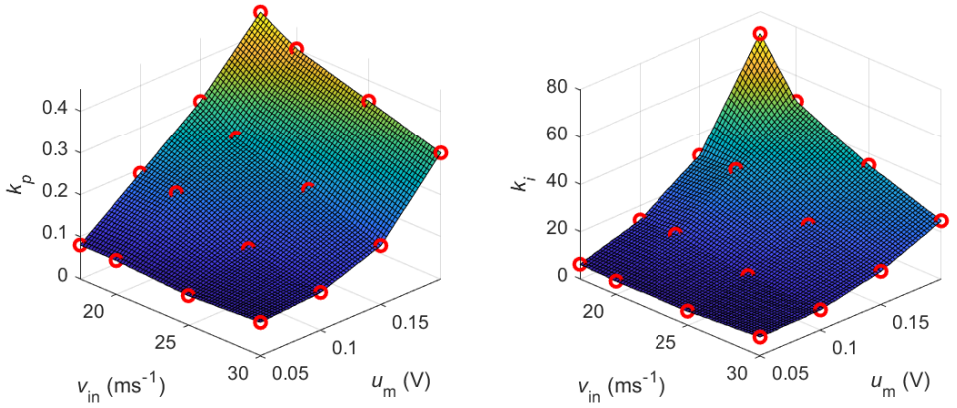


Figure 6.17: Linearly interpolated gain schedule

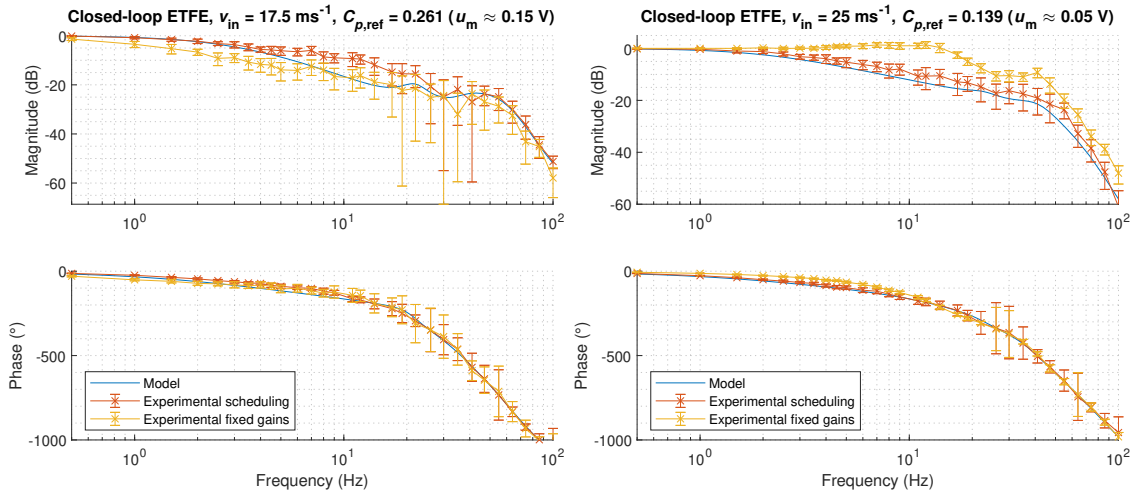
6.3.3 Validation of Gain Scheduling

The effectiveness of gain scheduling compared to using fixed PI gains is demonstrated by experimental closed-loop transfer functions at several representative operating points. Two additional design points, and two off-design points requiring gain interpolation were chosen:

	Design point 1	Design point 2	Design point 3	Off-design point 1	Off-design point 2
v_{in} (m s^{-1})	20	17.5	25	27.5	18.5
$C_{p,\text{ref}}$ ($\sim u_{\text{m}}$ (V))	0.24 (0.1)	0.261 (0.15)	0.139 (0.05)	0.22 (0.125)	0.27

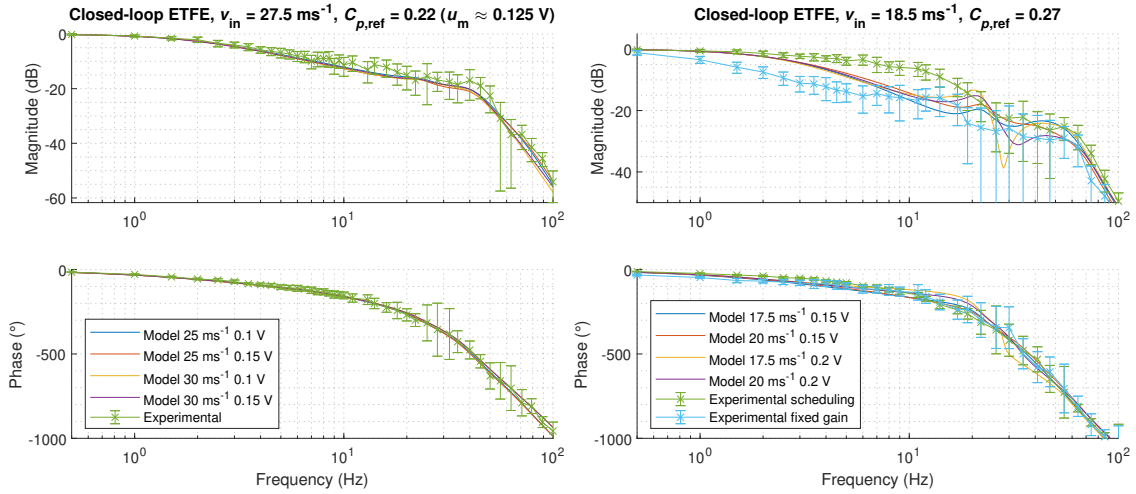
The two additional design points were chosen based on having lower plant gain (hence higher PI gains) and higher plant gain (hence lower PI gains) than the reference point of $v_{\text{in}} = 20\,\text{m s}^{-1}$ $u_{\text{m}} = 0.1\,\text{V}$, respectively. The first of the two off-design points was chosen to be in a range where the plant transfer function gain/shape is expected to vary fairly predictably/linearly. The second was chosen to be in a range where the wall pressure location used for feedback is close to the boundary of the reattachment zone, where the plant transfer function is expected to be relatively unpredictable and almost certainly not vary linearly between the identified operating points.

Figures 6.18 and 6.19 show the experimental closed-loop transfer functions using both scheduled gains and fixed gains calculated for the $v_{\text{in}} = 20\,\text{m s}^{-1}$ $u_{\text{m}} = 0.1\,\text{V}$ model.



(a) Design point 2 (b) Design point 3

Figure 6.18: Experimental closed loop PI transfer functions at design points



(a) Off-design point 1 (b) Off-design point 2

Figure 6.19: Experimental closed loop PI transfer functions at off-design points

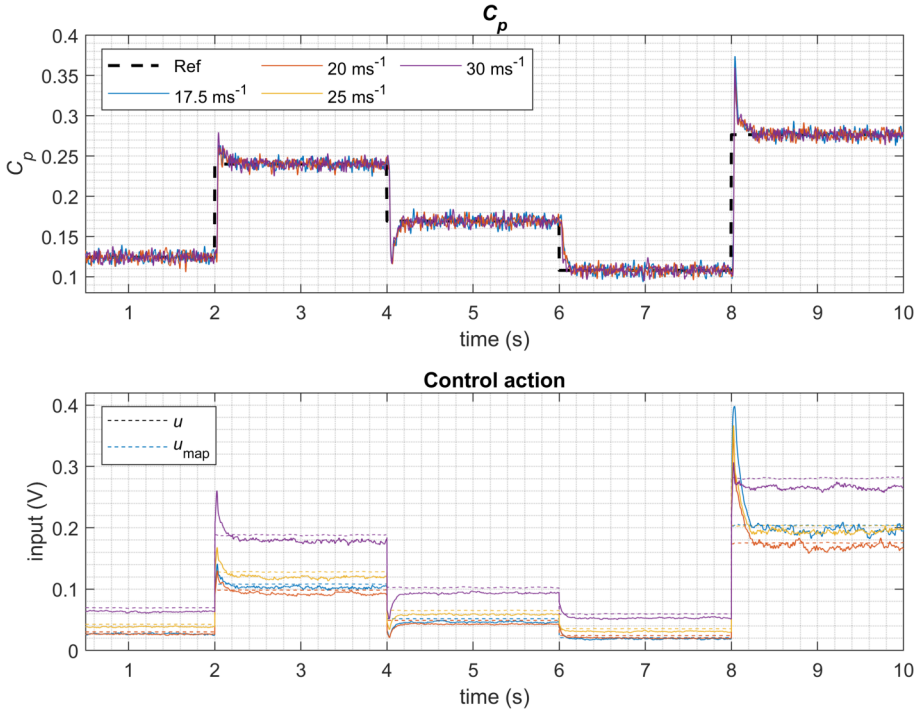
The experimental transfer functions are consistent with expectations. At the two design points, the scheduled controller ensures that the experimental magnitude is close to the model, albeit with noticeable deviation corresponding with the broad peak in the sensitivity transfer function. Contrary to this, the fixed gains are either too small or two large when used at a point they were not tuned at, therefore the achieved $-3\,\mathrm{dB}$ bandwidth is lower than intended at design point 2 ($< 1\,\mathrm{Hz}$) and higher than intended at design point 3 ($\sim$17 Hz).

The experimental transfer function at off-design point 1 almost perfectly matches the

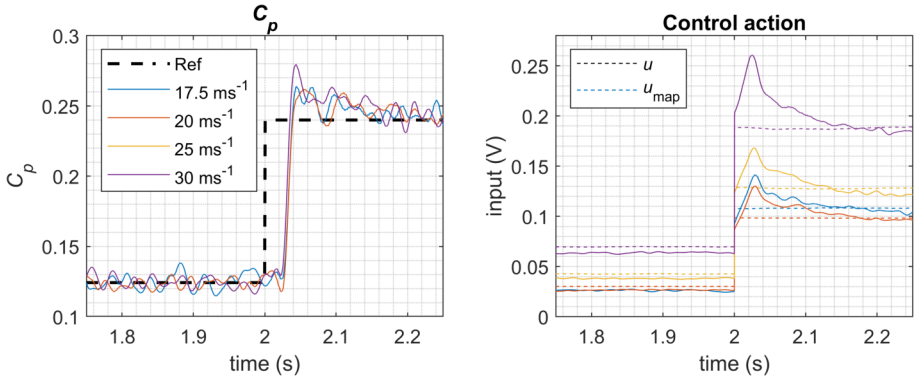
model transfer function, confirming that linear interpolation of the gains is valid in regions where the plant transfer function varies predictably. In direct comparison to this, the experimental transfer function of the gain-scheduled controller at off-design point 2 shows significantly larger magnitude than the tuned controller models from around 2 to 17 Hz, having -3 dB bandwidth about 4.5 Hz. This confirms that linear interpolation of the gains is not an ideal approach where the plant gain varies non-linearly with operating conditions. Nevertheless, the fixed-gains closed-loop transfer function at this point has significantly lower bandwidth than desired (< 1 Hz), and gain scheduling is clearly appropriate for systems exhibiting the behaviour seen, even if the current implementation is not optimal.

6.3.4 Step Responses

Although the closed-loop transfer functions provide all the information necessary to characterise the behaviour of a linear system, this is not the case for the current backward-facing step flow, where the transfer functions are linearised around the current operating point and give only the behaviour of the system to small perturbations. It is therefore necessary to further verify that the controller gives a satisfactory step response to large changes in requested C_p. The step response of the controller was tested by requesting a series of 5 $C_{p,\mathrm{ref}}$ values between 0.1 and 0.28, which should be achievable across the full range of inlet velocities, for 2 s per value. The response to this reference signal was then measured for 100 repeats and ensemble averaged, for each of the four identified velocities, $v_{\mathrm{in}} = 17.5$, 20, 25, and 30 m s^{-1}. Figure 6.20 shows the filtered ensemble averaged step responses and corresponding actuation amplitude u.



(a) Full response



(b) Zoomed in to step at $t = 2\,\mathrm{s}$

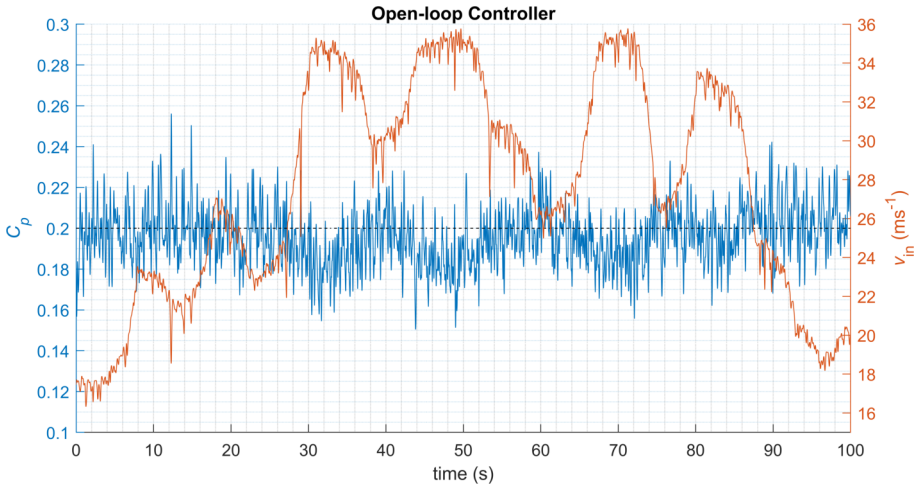
Figure 6.20: Ensemble averaged experimental step responses of gain scheduled PI controller

The experimental step-response time is between 0.2-0.3 s, with over/undershoot depending on C_p values either side of the step, irrespective of velocity. A response time of 0.3 s corresponds to non-dimensional time fraction $tv_{\mathrm{in}}/h \approx 263$, 300, 375, and 450 at 17.5, 20, 25, and 30 $\mathrm{m\,s^{-1}}$, respectively. The rise/fall times are also shorter than expected from the closed-loop bandwidth, suggesting that the effective experimental bandwidth is around 3-5 Hz. This may be explained by the implementation of gain scheduling, where the gains change based on the static mapping as soon as the reference changes, immediately causing a drop or rise in the control action before the system states have changed. The slight offset

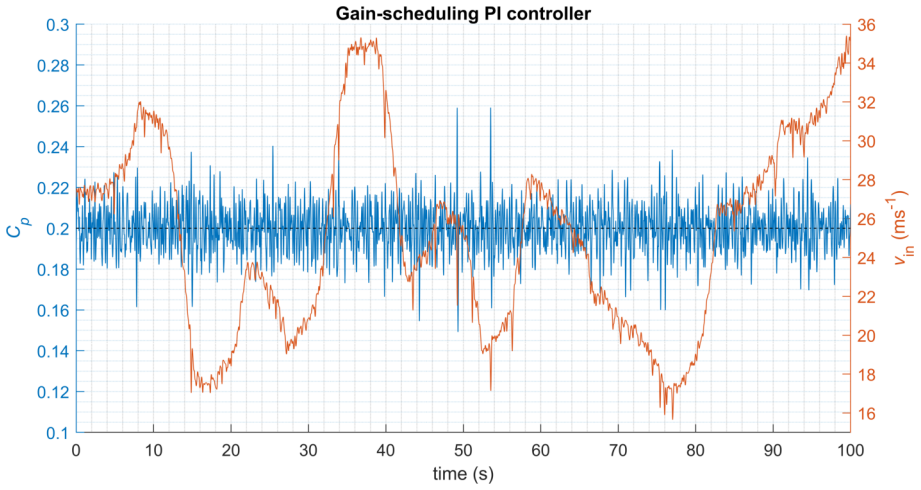
between the actual steady input amplitude and u_{map} demonstrates the slight day-to-day drift of actuation effectiveness.

6.3.5 Inlet Velocity Disturbance Rejection

The ability of the PI controller to track a constant C_p reference despite varying inlet velocity was tested by manually adjusting the blower speed for a time of 100 s while requesting $C_{p,\text{ref}} = 0.2$, shown in Figure 6.21b. The rig was not set up to automate tracking a velocity set point, therefore it was not possible to ensemble average these measurements. Instead, the estimated velocity based on upstream pressures and measured wall C_p were filtered using a 4^{th} order zero-phase filter with cut-off frequency 5 Hz to remove high frequency content. Even with strong filtering, the wall C_p measurement is still relatively noisy due to the large magnitude broadband unsteadiness in the BFS flow. Despite the unsteadiness it can clearly be seen that the PI controller rejects the slow variation due to the drifting inlet speed, compared to open-loop actuation using only the static mapping to set input amplitude without feedback, shown in Figure 6.21a, where velocity variation causes a corresponding drift of the C_p value from the reference. Given the low rate of change of blower speed, the operating point and gain-schedule are not important factors for controller performance when subject to quasi-steady inlet velocity disturbances, as the integral term guarantees zero-steady state error, and the bandwidth of the controller is well above that of the blower.



(a) Open-loop controller



(b) PI controller

Figure 6.21: Inlet velocity disturbance rejection of open-loop and PI controllers

6.3.6 Output Disturbance Rejection

From the perspective of the controller, all flow unsteadiness can be considered output noise. Therefore, the output disturbance rejection can be determined by comparison of the frequency spectra of the wall C_p measurement with open-loop actuation and PI control. Open-loop actuation and the PI controllers with fixed and scheduled gains were run with requested $C_{p,\text{ref}} = 0.2$ and 0.25, for 5 repeats of 100 s long measurements. Frequency spectra were then calculated for each repeat, using Welch's method with window length 4000 samples, before ensemble averaging across repeats, shown in Figure 6.22. These plots show that the PI controller behaves as expected based on the model sensitivity transfer functions. The controller reduces wall pressure content relative to open-loop actuation

below about 3 Hz, after which there is an increase in content in line with the broad peak in sensitivity, followed by a reduction at around 30 Hz and an increase around 45 Hz, matching the oscillatory behaviour seen in the sensitivity functions. At higher frequencies, the sensitivity tends to 0 dB and the long measurement tubes attenuate measured pressures so little effect is seen from around 60 Hz until the acoustic actuation peak, where amplitude modulation introduces side bands around the 300 Hz tone. As predicted, the first trough in the sensitivity function does cause the PI controller to slightly attenuate the 21 Hz Helmholtz resonance bump, by up to around 1 dB depending on inlet velocity and input amplitude.

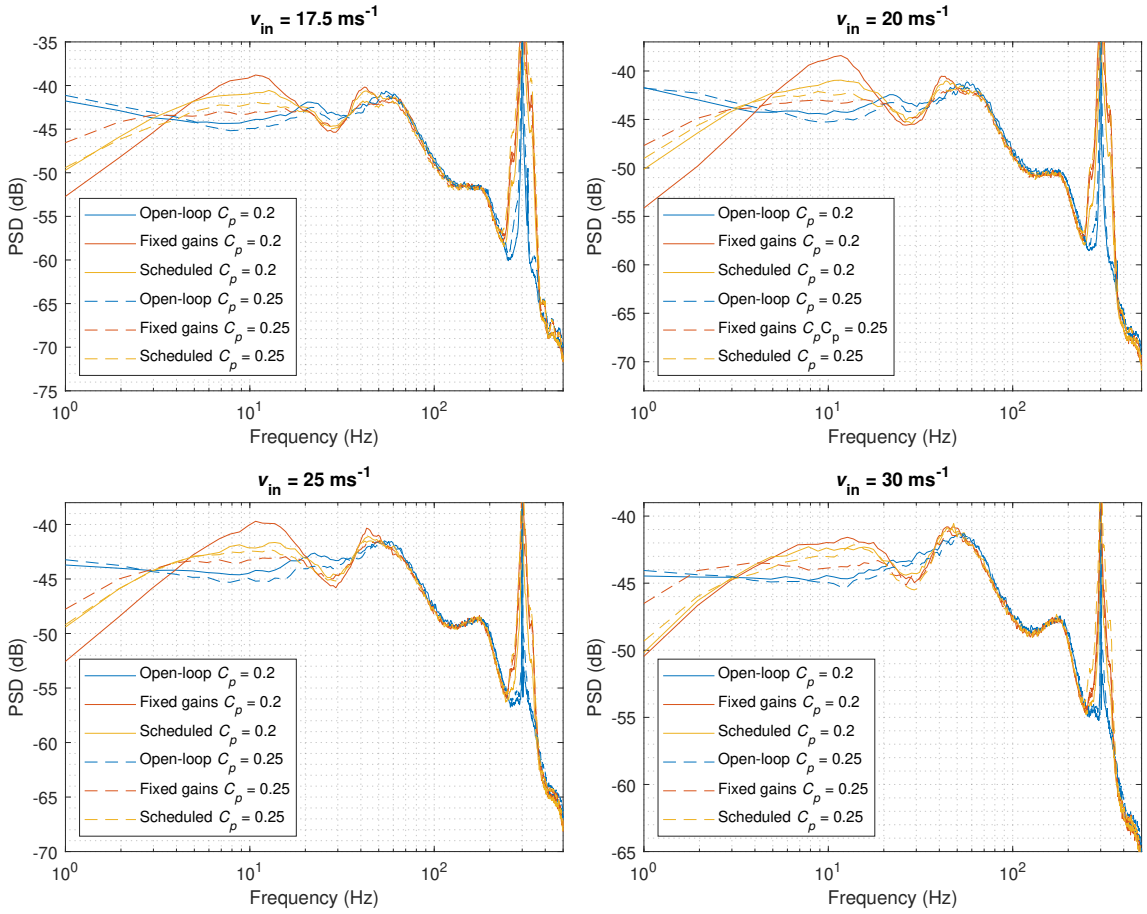


Figure 6.22: Effect of PI controller on C_p frequency content

The gain-scheduling PI controller has been shown to effectively track a requested wall pressure coefficient measured at $x/h = 5$, as well as rejecting inlet velocity disturbances and suppressing low frequency content, but influence on velocity fluctuations is yet to be demonstrated. Figure 6.23 shows the frequency spectra of hot-wire velocity measurements

at $(x, y, z)/h = (3, 0.5, 0)$ taken concurrently with the wall pressure measurements shown in Figure 6.22. This location was chosen based on where the frequency peaks due to shear-layer vortices and the Helmholtz resonance are strongest, and should be enough downstream of the step that the large scale shear layer vortices have formed and the amplitude input has (at least partially) been demodulated.

The PI controller increases the magnitude of velocity fluctuations at frequencies below the 21 Hz bump for all velocities, which is not consistent with slightly attenuation of the wall pressure at frequencies below $\sim$ 2-3 Hz. This discrepancy may indicate that using wall pressure as feedback is unsuitable for stabilising velocity fluctuations, although it is possible that low frequency velocity fluctuations closer to the pressure measurement are reduced. The PI controller does however slightly attenuate the 21 Hz peak by less than 1 dB at 17.5 m s^{-1} and 20 m s^{-1}, but has very little effect on 21 Hz content at higher velocities.

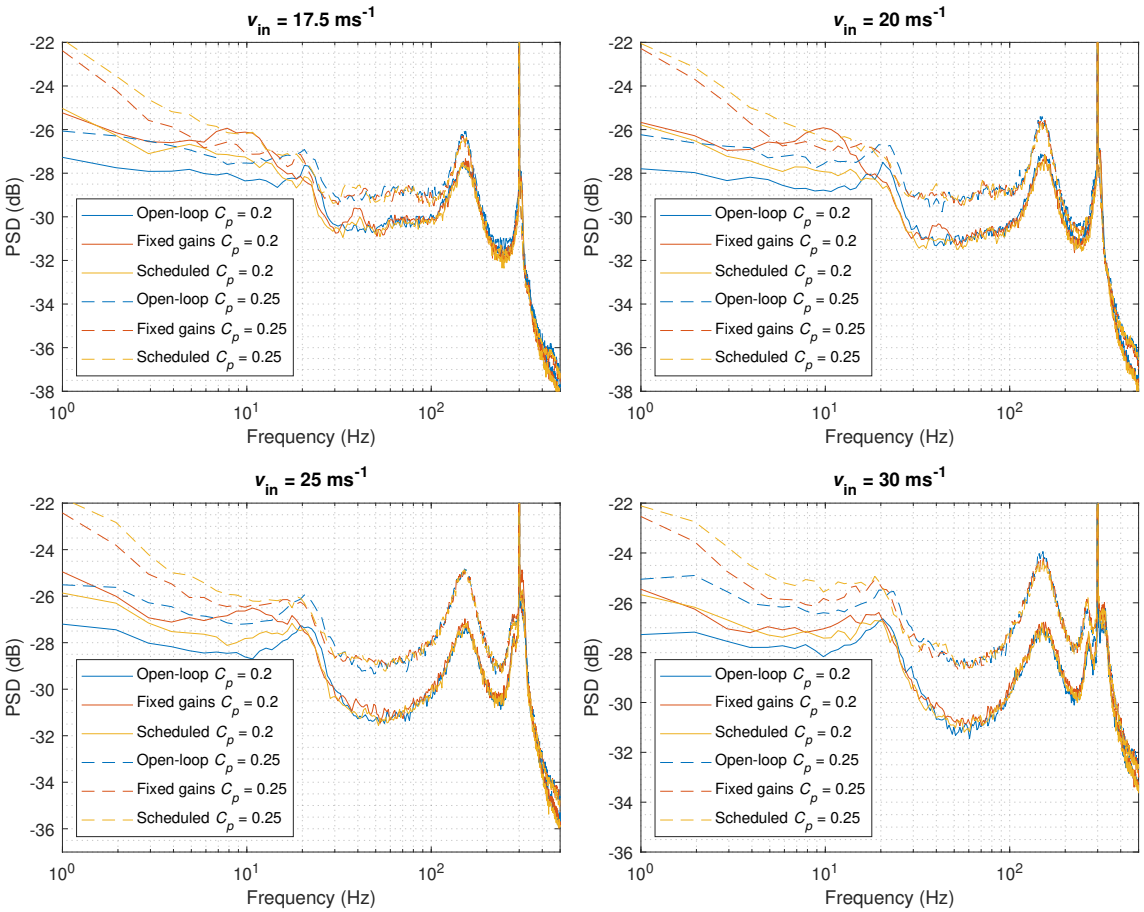


Figure 6.23: Effect of PI controller on velocity frequency content

6.4 Interpolating LQG Controller

6.4.1 Introduction

Although the PI controller successfully tracks a C_p reference, its inconsistent behaviour away from design points due to plant gain uncertainty and non-optimal interpolation of tuned gains is not ideal. The influence of the PI controller on velocity content also leaves something to be desired. The controller is able to attenuate velocity fluctuations due to the Helmholtz resonance of the plenum-test-section system slightly at $(x, y, z)/h = (3, 0.5, 0)$, but increases low frequency fluctuations.

The obvious next question is whether a model based controller can overcome the limitations of long delay time and varying system dynamics. Large phase delay prevents the PI controller from achieving a high closed-loop bandwidth while remaining robust, however bandwidth is not necessarily a priority. Heat exchanger duct flows are unlikely to benefit from a very fast response time, instead it is of much greater interest to suppress low frequency and harmonic disturbances which may interact unfavourably with HEX flow and downstream components. In the following section, a linear quadratic regulator is designed to achieve both satisfactory response time and attenuate the Helmholtz resonance.

6.4.2 Non-linear control by interpolation of control action

It is necessary to extend the LQG method (detailed in Section 2.5.3) to account for the varying plant gain as operating point changes. The possibility of using scheduled LQR gains [179] was considered, however the additional requirement of a time varying Kalman filter (KF) complicates this. Given that the transfer functions of the plant have only been identified at a limited number of operating points, the behaviour between these point is undefined, and there is no guarantee that an interpolation of plant dynamics would be valid, assuming that the state space models can be interpolated at all without unpredictable results. A constantly changing plant model would also impact the stability of the controller, although LQR and KF gains could at least be calculated over a fine grid of operating conditions in advance to avoid the computational cost of real-time calculation. To overcome these problems, an alternative approach is proposed in which a separate LQG

controller is designed for each of 16 of the identified plant models, and all are run in parallel. The control action u is then interpolated based on the current operating point, (v_{in}, u_0), according to

$$\begin{aligned} u_k = (1-\lambda_{u_0})((1-\lambda_{v_{\text{in}}})\mathbf{u}_k(i,j) + \lambda_{v_{\text{in}}}\mathbf{u}_k(i+1,j)) \\ +\lambda_{u_0}((1-\lambda_{v_{\text{in}}})\mathbf{u}_k(i,j+1) + \lambda_{v_{\text{in}}}\mathbf{u}_k(i+1,j+1)) \end{aligned} \tag{6.5}$$

where $\mathbf{u}_k(i,j)$ is control action of the LQG controller designed at the operating point $(\mathbf{v}_{\text{in}}(i), \mathbf{u}_0(j))$, λ_v and λ_u are the interpolation fractions

$$\lambda_{v_{\text{in}}} = \begin{cases} \frac{v_{\text{in}} - \mathbf{v}_{\text{in}}(i)}{\mathbf{v}_{\text{in}}(i+1) - \mathbf{v}_{\text{in}}(i)}, & \mathbf{v}_{\text{in}}(i) < v_{\text{in}} < \mathbf{v}_{\text{in}}(i+1) \\ 1, & v_{\text{in}} \geq \max(\mathbf{v}_{\text{in}}) \\ 0, & v_{\text{in}} \leq \min(\mathbf{v}_{\text{in}}) \end{cases} \tag{6.6}$$

$$\lambda_{u_0} = \begin{cases} \frac{u_0 - \mathbf{u}_0(j)}{\mathbf{u}_0(j+1) - \mathbf{u}_0(j)}, & \mathbf{u}_0(j) < u_0 < \mathbf{u}_0(j+1) \\ 1, & u_0 \geq \max(\mathbf{u}_0) \\ 0, & u_0 \leq \min(\mathbf{u}_0) \end{cases} \tag{6.7}$$

and i and j are the indices of design point velocity and voltage amplitude such that the current operating conditions lie between $\mathbf{v}_{\text{in}}(i) \leq v_{\text{in}} \leq \mathbf{v}_{\text{in}}(i+1)$, and $\mathbf{u}_0(i) \leq u_0 \leq \mathbf{u}_0(i+1)$. In the case that one or both of the inlet velocity or steady voltage amplitude lie outside of the range of identified operating conditions, then the control action is held at that of the closest point within the identified range (nearest neighbour).

The value of u_0 is set as the steady input amplitude to achieve the reference value of C_p based on the predetermined static mapping, $u_0 = u_{\text{map}}(C_{\text{p0}}, v_{\text{in}})$, demonstrated in Figure 6.11, to avoid negative impacts on the step response that might arise from using a heavily filtered or moving-window average of the experimental control action. The parallel controller interpolation approach used is justified by Bacic et. al. [175], who demonstrate that interpolation between state feedback controllers is an efficient means for implementing a non-linear terminal control law in the context of model predictive control.

Figure 6.24 shows the top-level block diagram of the interpolating LQG controller. The controller consists of the 16 independent LQG controllers, each outputting its own control

action request $u_{i,j}$, followed by a 2D linear interpolation of the outputs. It was observed that the behaviour of the BFS varies slightly day-to-day, presumably due to atmospheric conditions, therefore using u_{map} as the operating point for interpolation is equivalent to assuming that the dynamics can be considered a function of C_p rather than input voltage. However, given that the ETFE measurements at all 16 identified operating points and the static mapping take multiple days to measure, there will almost always be some small error between the controller models and the real system. All 16 controllers share a common integral term, as the measured C_p output is used and not the Kalman filter estimates. The addition of a low-pass filter on the measured C_p value prior to feedback was necessary to remove the remaining $f_c = 300\,\text{Hz}$ acoustic pressure tone and other higher frequency content not modelled by the third-order transfer functions from the signal. The same 4^{th} order filter as for the PI control was used, with cut-off frequency 40 Hz.

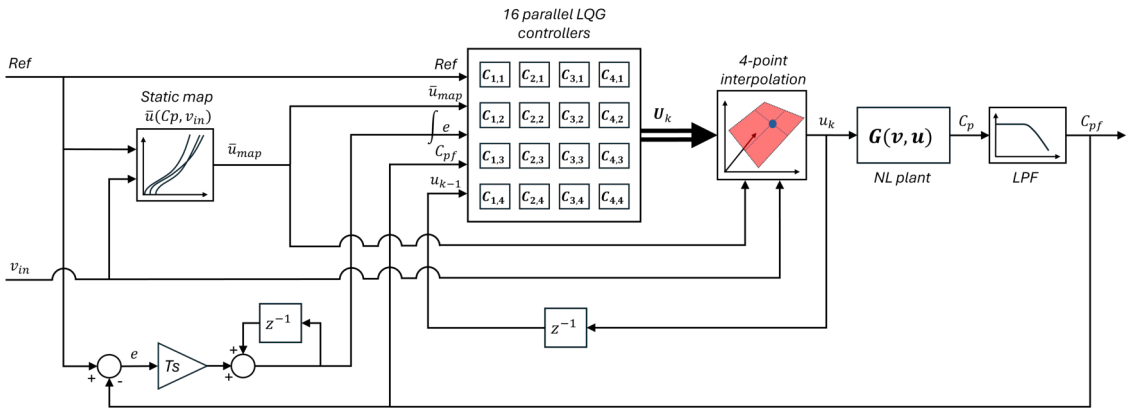


Figure 6.24: Simplified block diagram of closed loop interpolating LQG controller

6.4.3 Adjusting the LQT for static non-linearity

The linear quadratic tracking gain in equation 2.14 is valid for a linear plant, however the current model uses an interpolation between linearisations of the plant around the current operating point. Therefore, the feed-forward gain on the reference to achieve zero steady state error calculated based on the DC gain of the linearisation at the current operating point will not give the correct reference gain for the non-linear system.

If the inverse static mapping between mean input u_0 and pressure coefficient C_{p0} is denoted $u_{\text{map}}(C_{p0}, v_{\text{in}})$, then the required steady-state input to achieve a reference value r at a given inlet velocity is $u_{\text{map}}(r, v_{\text{in}})$. The LQG gain therefore requires a corrective feed-forward

gain, $\mathbf{K}_0$, such that

$$u_0 = \mathbf{K}_0(r) - \mathbf{K}_{LQR}\hat{\mathbf{x}}_0 = u_{\text{map}}(r, v_{\text{in}}) \tag{6.8}$$

where u_0 is the steady-state input, and $\hat{\mathbf{x}}_0$ are the steady-state Kalman filter state estimates. Substituting the steady-state input and output $u_0 = u_{\text{map}}(r, v_{\text{in}})$ and $y_0 = r$ into equation 2.16 gives the Kalman filter estimated states,

$$\hat{\mathbf{x}}_0 = (\mathbf{I} - \mathbf{A} + \mathbf{K}_{\text{f}}\mathbf{C})^{-1}\mathbf{B}u_{\text{map}}(r, v_{\text{in}}) + (\mathbf{I} - \mathbf{A} + \mathbf{K}_{\text{f}}\mathbf{C})^{-1}\mathbf{K}_{\text{f}}r \tag{6.9}$$

and finally, the closed-loop input adjusted to achieve zero steady state error becomes:

$$u_k = (\mathbf{I} - \mathbf{K}_{LQR}(\mathbf{I} - \mathbf{A} + \mathbf{K}_{\text{f}}\mathbf{C})^{-1}\mathbf{B})u_{\text{map}}(r, v_{\text{in}}) + \mathbf{K}_{LQR}(\mathbf{I} - \mathbf{A} + \mathbf{K}_{\text{f}}\mathbf{C})^{-1}\mathbf{K}_{\text{f}}r - \mathbf{K}_{LQR}\hat{\mathbf{x}}_k \tag{6.10}$$

In reality, the static mapping, $u_{\text{map}}(C_{p0}, v_{\text{in}})$, and linear interpolation between LQG models do not fully capture the non-linearities of the experimental response, and so the integral term is necessary to achieve true zero steady-state tracking error. Nevertheless, accounting for the static non-linearity in the feed-forward part of the gain will ensure the best possible step response time and minimum overshoot.

6.4.4 LQG Tuning

Despite individual robustness guarantees of the LQR and Kalman filter, there is no guarantee of robustness of the combined controller [180]. To recover LQR robustness, the LQR and Kalman filter are designed using the loop transfer recovery (LTR) method of Doyle and Stein [180]. If the plants are minimum phase or have long time delay, the LTR procedure does not guarantee robustness recovery, but it is still effective tool to obtain a useful degree of robustness [181, 182].

As for the PI control design, the sensitivity transfer function is the main consideration for the tuning of the LQG, however this time there are two aims:

1. As before, limit the maximum magnitude of the sensitivity transfer function, $|S|$, to not exceed 2 dB.

2. Additionally, the knowledge of model dynamics should be used to target content

around 21 Hz to attempt to suppress the Helmholtz resonance, therefore the magnitude of $|S|$ over this range should be as low as possible.

Aim 2 is achieved by costing only the first two model states and the integrator in the LQR design. The first two states are responsible for the 21 Hz bump in the plant transfer functions, and including the third state was found to be detrimental to this aim.

Figure 6.25 shows the open-loop, closed-loop, and sensitivity transfer functions of the 16 tuned LQR and LQG controllers. A 4^{th} order low-pass filter with the same parameters as in the PI controller is used to remove high frequency content from the feedback measurement. The filter dynamics are embedded in the each of the Kalman filters, resulting in a total of 9 states per controller (3 model + 2 Padé delay + 4 low-pass filter).

Due to the large delays it is not possible to exactly recover the LQR behaviour with the LQG system, and the LQG has reasonably lower bandwidth and higher sensitivity magnitude. Tuning down the LQR to allow for approximate loop-transfer recovery results in a controller with bandwidth so low as to be functionally useless, therefore the LQG transfer functions are the focus of the tuning and the response of the stand-alone LQR controllers are not considered.

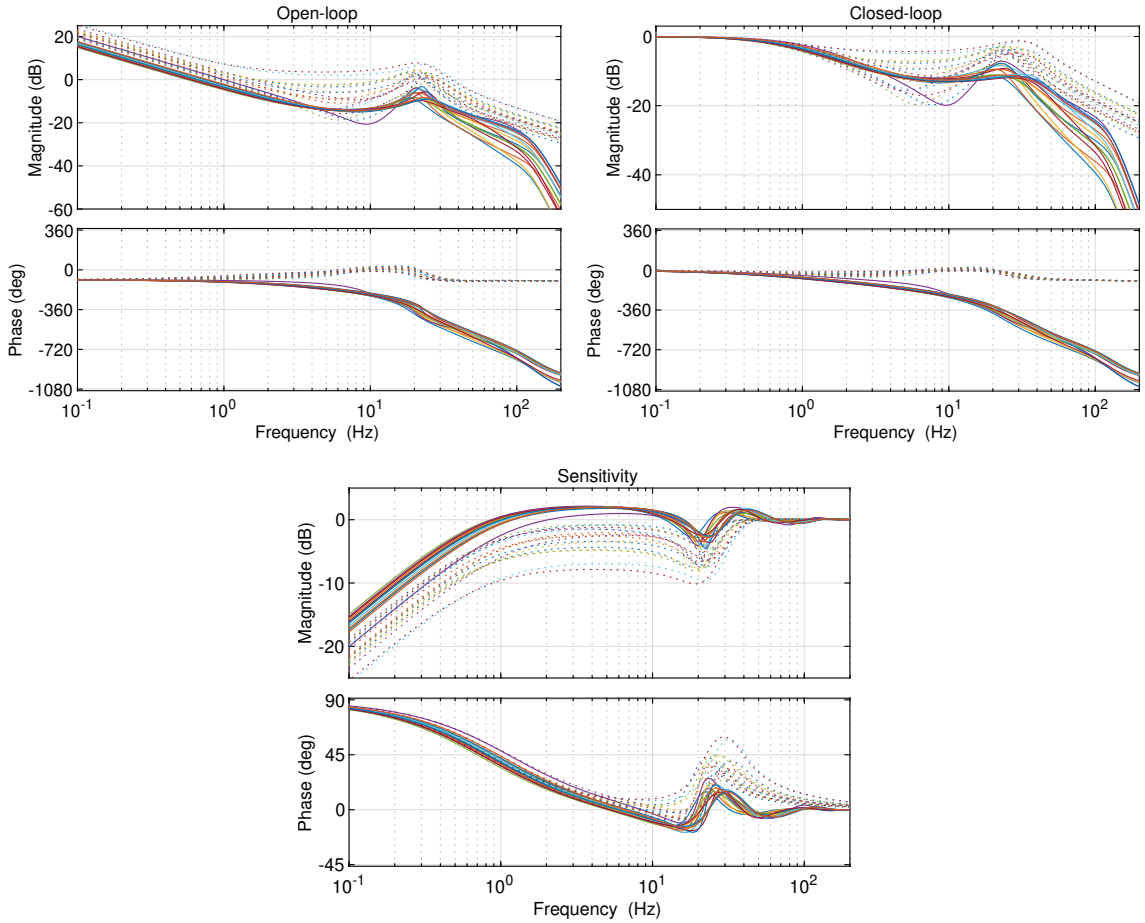


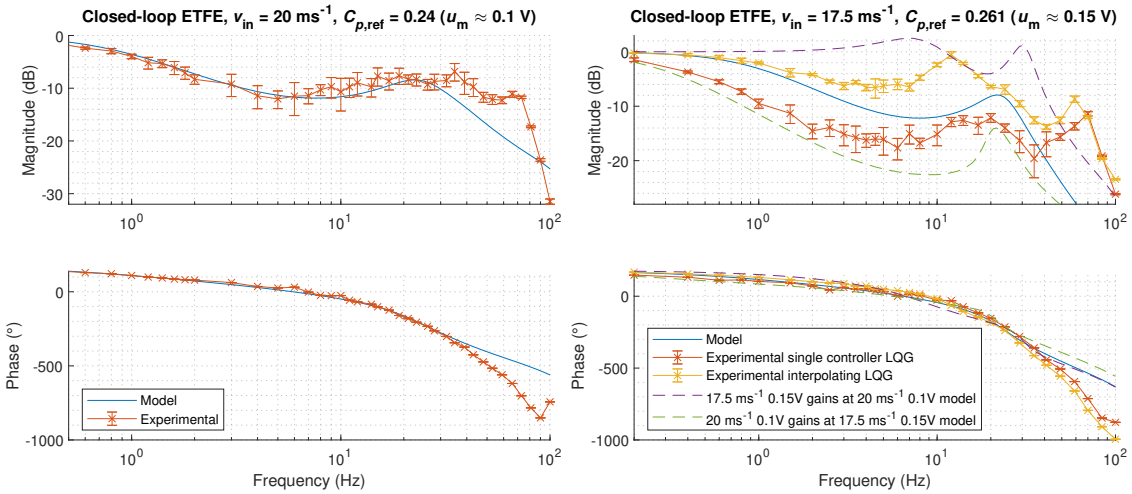
Figure 6.25: LQG low-pass filter augmented controller tunings for all 16 design points. Dotted lines = LQR, solid lines = LQG

A closed loop bandwidth of approximately 0.8 Hz ($St_h \approx 5.3 \times 10^{-4}$ to 9.1×10^{-4}) was achieved across the design points, with maximum and minimum $|S|$ at the targeted peak frequency -2.44 dB and -4.57 dB, respectively [2].

[2] It is possible to achieve a much greater attenuation of the 21 Hz bump, however Bode's sensitivity integral, which states that the integral of the log of the sensitivity function magnitude is always equal to a constant value (zero in the case of a stable system) [183], poses a significant constraint on the controller design. Although the aim is to attenuate content at a particular frequency of interest, dropping the magnitude of the sensitivity transfer function, $|S|$, in this region increases the magnitude of $|S|$ at frequencies on either side of the attenuated region, leading to the amplification of output noise at these frequencies. One would ideally be able to choose the frequency range over which the increase in $|S|$ is observed, so that the amplified frequencies are well above the controller bandwidth and could be ignored, but this is not possible for real systems hence the limiting of maximum $|S|$ to not exceed 2 dB, to avoid excessive amplification of content at frequencies above and below the Helmholtz resonance. Although this behaviour may not be preferred, a clear example of when it may be perfectly acceptable is a case where flow unsteadiness forces a narrow band structural resonance, and there are no mechanical consequences of large magnitude pressure/velocity fluctuations at other nearby frequencies.

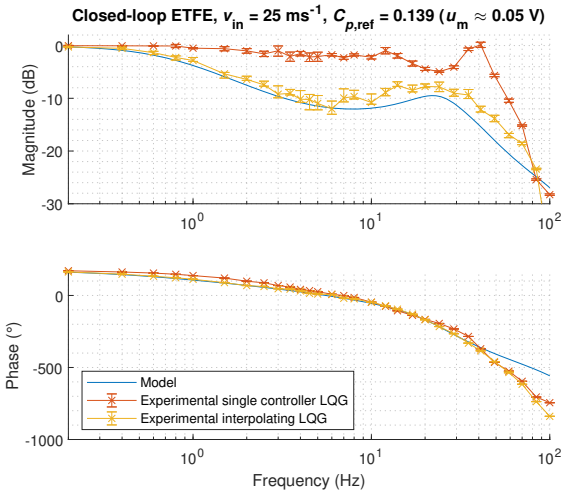
6.4.5 Experimental Closed-Loop Transfer Functions

Experimental closed-loop transfer functions were measured for the same operating points as for the PI controller, for both the interpolating LQG controller and the single model controller designed for the $20\,\mathrm{m\,s^{-1}}$ 0.1 V operating point (design point 1), shown in Figures 6.26 and 6.27. The experimental closed-loop transfer functions demonstrate that the interpolating controller is behaving as designed, achieving approximately the designed $-3\,\mathrm{dB}$ bandwidth of $\sim$0.8 Hz at all of the tested operating points, including the off-design points. While the fits of the model and experimental transfer functions are good at design points 1 ($20\,\mathrm{m\,s^{-1}}$, 0.1 V), design point 3 ($25\,\mathrm{m\,s^{-1}}$,0.05 V), and off-design point 1 ($27.5\,\mathrm{m\,s^{-1}}$, 0.125 V), there is some deviation at design point 2 ($17.5\,\mathrm{m\,s^{-1}}$, 0.15 V) and off-design point 2 ($18.5\,\mathrm{m\,s^{-1}}$ $C_{p,\mathrm{ref}} = 0.27$) for frequencies above $\sim$1 Hz, notably peaks at around 12 Hz and 50-60 Hz, the latter of which is due to to the unmodelled dynamics above the Helmholtz resonance frequency. The 12 Hz peak (corresponding to $St_h = 0.0137$ at $v_{\mathrm{in}} = 17.5\,\mathrm{m\,s^{-1}}$ and $St_h = 0.013$ at $v_{\mathrm{in}} = 18.5\,\mathrm{m\,s^{-1}}$) is potentially interesting from a flow physics perspective, as this is around the frequency at which the flapping mode was identified. However, it is also possible that the peak could be explained by slight discrepancies between modelled and actual plant dynamics. Similarly to the fixed-gain PI controller, the single model LQG bandwidth is either higher or lower than designed depending on the operating point.



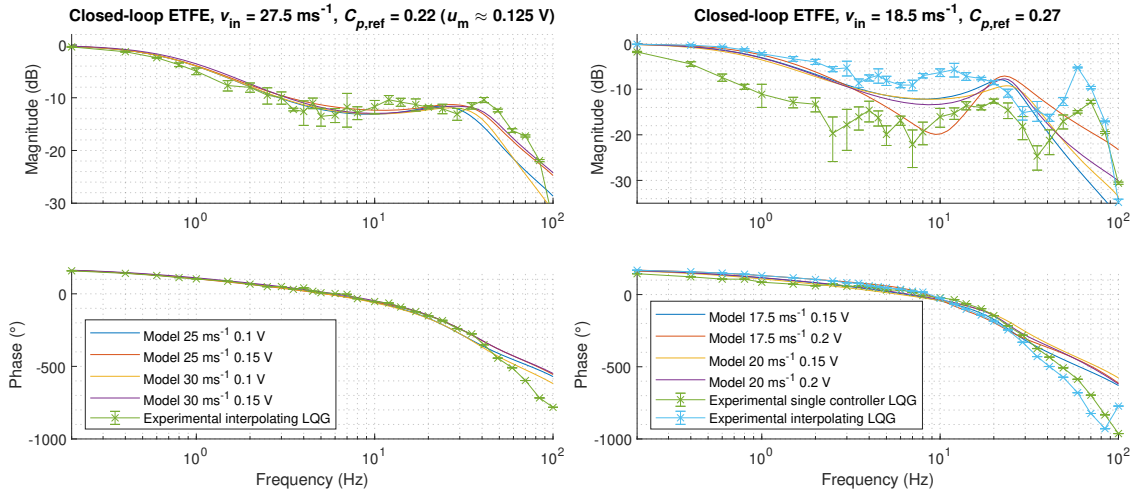
(a) Design point 1

(b) Design point 2



(c) Design point 3

Figure 6.26: Experimental closed loop LQG transfer functions at design points

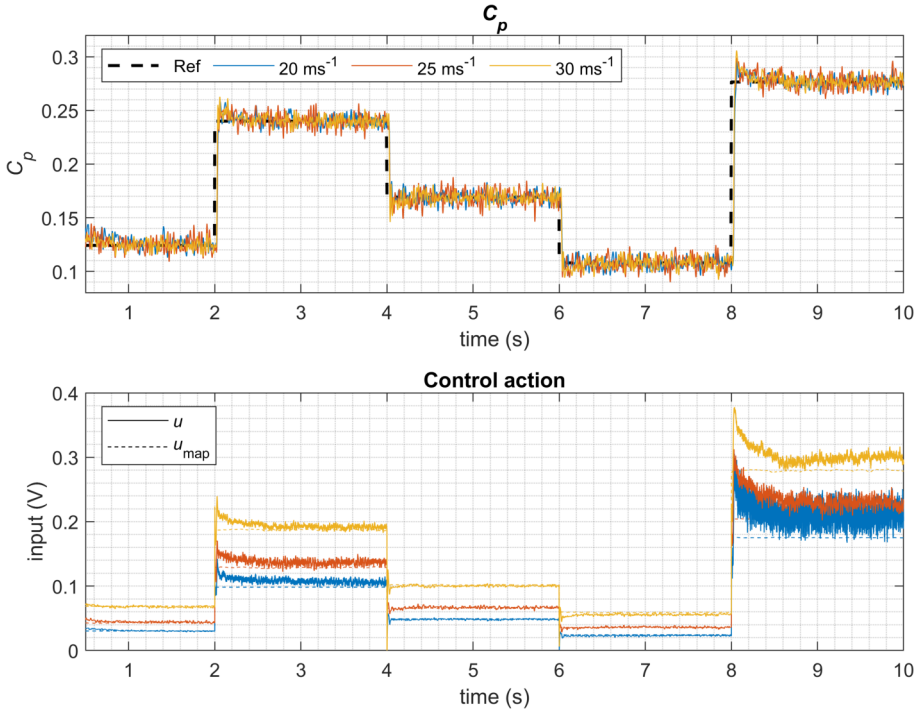


(a) Off-design point 1 (b) Off-design point 2

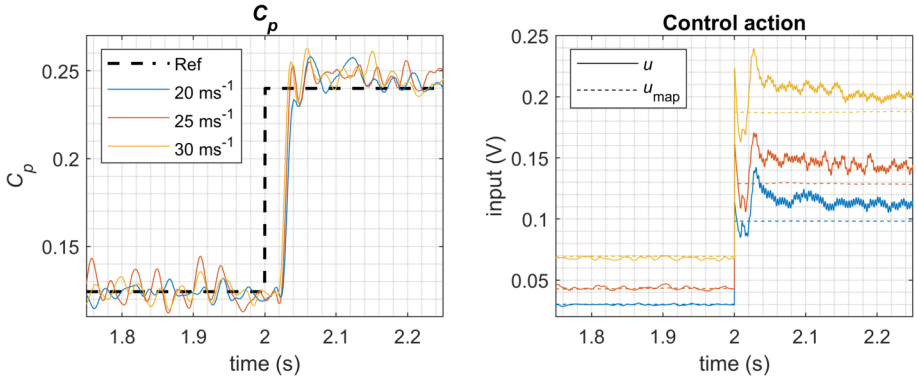
Figure 6.27: Experimental closed loop LQG transfer functions at off-design points

6.4.6 Step Response

The interpolating LQG controller was tested on the same step requests as the PI controller, at inlet velocities $v_{\text{in}} = 20$, 25, and $30\,\text{m}\,\text{s}^{-1}$, shown in Figure 6.28. The LQG controllers achieve a response time effectively as fast as open-loop actuation ($\sim$0.04 s) and with significantly less over/undershoot than the PI controller, although it takes around 0.6 s for the control-action to completely settle. This is guaranteed by the feed-forward gains on the reference and u_{map} terms, which cause an immediate response and consequently avoid large integrator wind-up despite the low LQG bandwidth. It is interesting that the initial (effectively open-loop) response to a step input appears to depend only slightly on inlet speed. The non-dimensional step response times, tv_{in}/h, are approximately 35, 40, and 45, at $v_{\text{in}} = 20$, 25, and $30\,\text{m}\,\text{s}^{-1}$, respectively, when the acoustic transport delay of the measurement tube ($1\,\text{m}/c \approx 0.003\,\text{s}$) is subtracted from the step time. This observation somewhat complicates the comparison of controller bandwidth between studies, as it suggests that the open-loop response time may not scale linearly with velocity. Given that the shear layer response is achieved via momentum transfer by the large scale vortices locked-on to the carrier tone and it's harmonics/sub-harmonics, it is possible that the step response time scales with actuation carrier frequency (which is held constant) rather than flow speed. Although unsurprising, it should also be noted that the step response time is also slightly longer for larger steps in requested C_p.



(a) Full response



(b) Zoomed in to step at $t = 2\,\mathrm{s}$

Figure 6.28: Ensemble averaged filtered experimental step responses of LQG controller

6.4.7 Inlet Velocity Disturbance Rejection

The same inlet velocity disturbance experiment as for the PI controller was run with the interpolating LQG controller. Figure 6.29 shows the inlet velocity and wall C_p filtered by a 4^{th} order zero-phase filter with cut-off frequency 5 Hz.

Similarly to the PI controller, it can be seen that the controller keeps the quasi-steady C_p constant at the reference value of 0.2, however, even after filtering, the variance of the C_p measurement is slightly larger than for the PI controller. This is not a surprising result given that the controllers were tuned with different goals, resulting in different bandwidths

and noise attenuation/amplification. The LQG controller was tuned to attenuate content around 21 Hz at the cost of amplifying other frequency ranges, while the PI controller was designed for maximum closed-loop bandwidth given a maximum sensitivity magnitude.

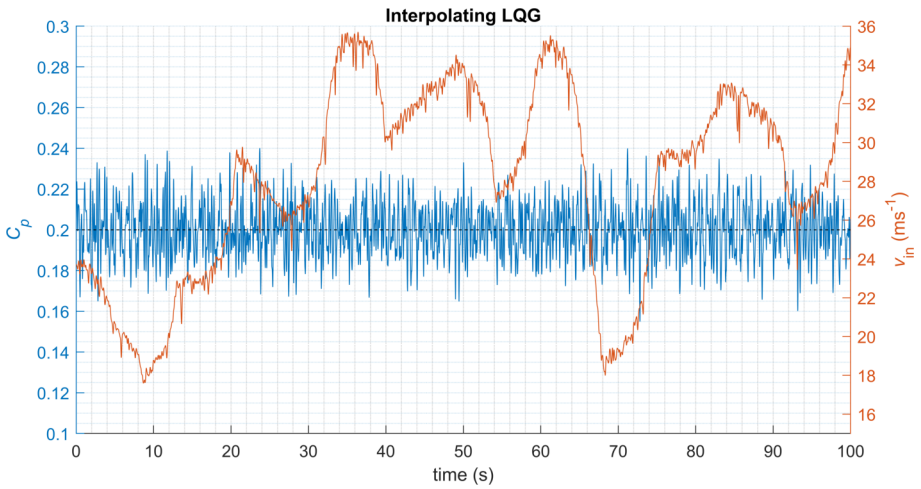


Figure 6.29: Interpolating LQG controller velocity disturbance

6.4.8 Output Disturbance Rejection

Figures 6.30 and 6.31 show the frequency spectra of wall C_p and hot-wire measured velocity at $(x, y, z)/h = (3, 0.5, 0)$ relative to the centre of the step edge, respectively, for open-loop, single model, and interpolating LQG controllers with requested $C_{p,\text{ref}} = 0.2$ and 0.25. As for the PI controller, the C_p spectra are consistent with the sensitivity transfer functions. Depending on the operating point, the interpolating LQG controller attenuates the 21 Hz bump by between 2.4 dB and about 5.4 dB compared to open-loop steady amplitude actuation, summarised in Table 6.1.

Since each of the individual controllers was tuned based on the maximum value of $|S|$ and not the minimum, this slight inconsistency is expected. The single model controller also behave much the same as the fixed-gain PI controller, having inconsistent attenuation/amplification as operating point varies. This is however a good illustration of how the controller can be tuned to attenuate the target frequency more aggressively if the maximum sensitivity magnitude requirement is eased.

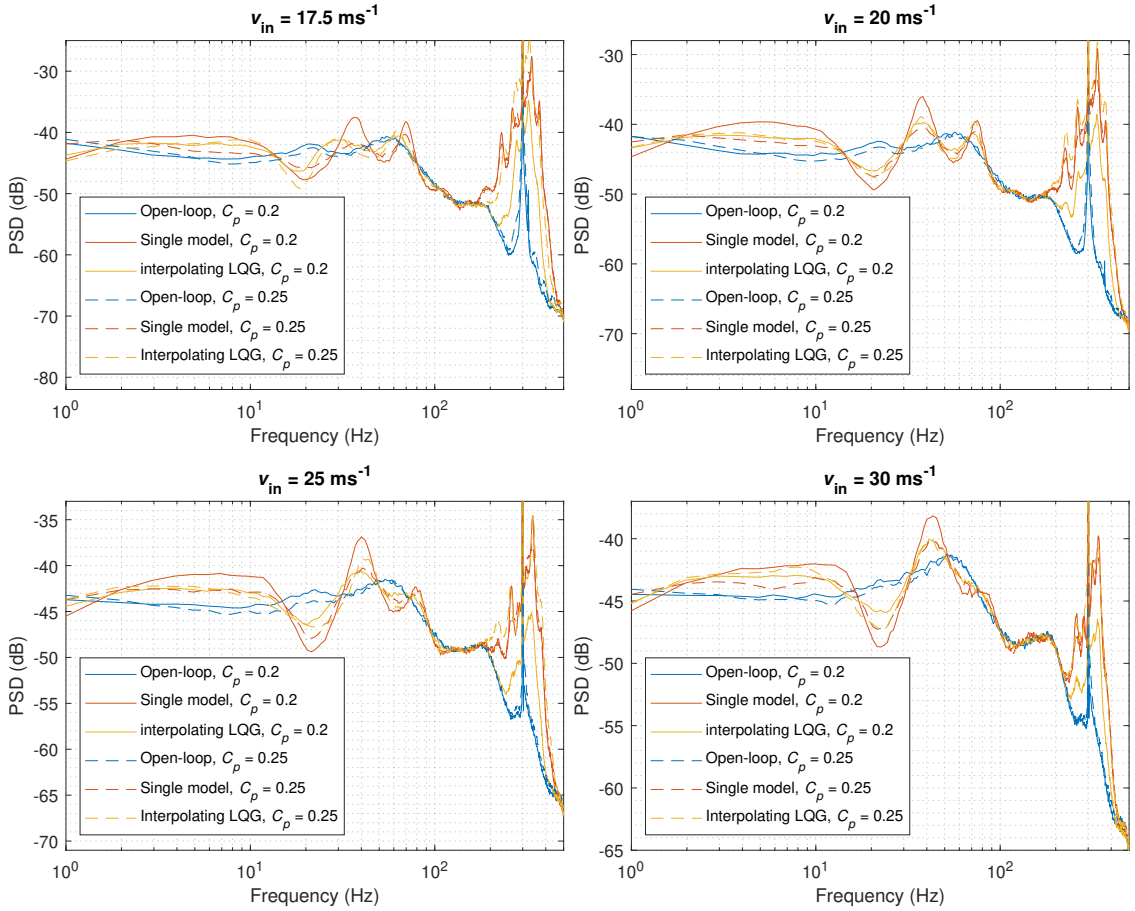


Figure 6.30: Effect of LQG controller on C_p frequency content

	Controller	
Operating point	**Single model**	**Interpolating**
$v_{\text{in}} = 17.5\,\text{m}\,\text{s}^{-1}$, $C_{p,\text{ref}} = 0.2$	5.71 dB	3.58 dB
$v_{\text{in}} = 17.5\,\text{m}\,\text{s}^{-1}$, $C_{p,\text{ref}} = 0.25$	3.24 dB	4.29 dB
$v_{\text{in}} = 20\,\text{m}\,\text{s}^{-1}$, $C_{p,\text{ref}} = 0.2$	6.70 dB	4.18 dB
$v_{\text{in}} = 20\,\text{m}\,\text{s}^{-1}$, $C_{p,\text{ref}} = 0.25$	3.94 dB	3.80 dB
$v_{\text{in}} = 25\,\text{m}\,\text{s}^{-1}$, $C_{p,\text{ref}} = 0.2$	6.50 dB	3.19 dB
$v_{\text{in}} = 25\,\text{m}\,\text{s}^{-1}$, $C_{p,\text{ref}} = 0.25$	3.92 dB	2.87 dB
$v_{\text{in}} = 30\,\text{m}\,\text{s}^{-1}$, $C_{p,\text{ref}} = 0.2$	5.41 dB	2.46 dB
$v_{\text{in}} = 30\,\text{m}\,\text{s}^{-1}$, $C_{p,\text{ref}} = 0.25$	2.85 dB	2.80 dB

Table 6.1: LQG controller 21 Hz bump pressure attenuation compared to open-loop

The hot-wire velocity spectra shown in Figure 6.31 demonstrate that the LQG controller has a significant effect on the shear layer flow compared to open-loop actuation at a constant amplitude. Like the PI controllers, the LQG controllers increase the content at low frequencies, however the LQG has a much more noticeable effect on the spectrum at frequencies well above the bandwidth of the controller. The success of the LQG controller in suppressing velocity content due to the Helmholtz resonance is dependent on operating point, and is more effective at lower inlet speeds and higher $C_{p,\mathrm{ref}}$. Attenuation at 21 Hz varies from about 0.4 dB to 1.3 dB, summarised in Table 6.2.

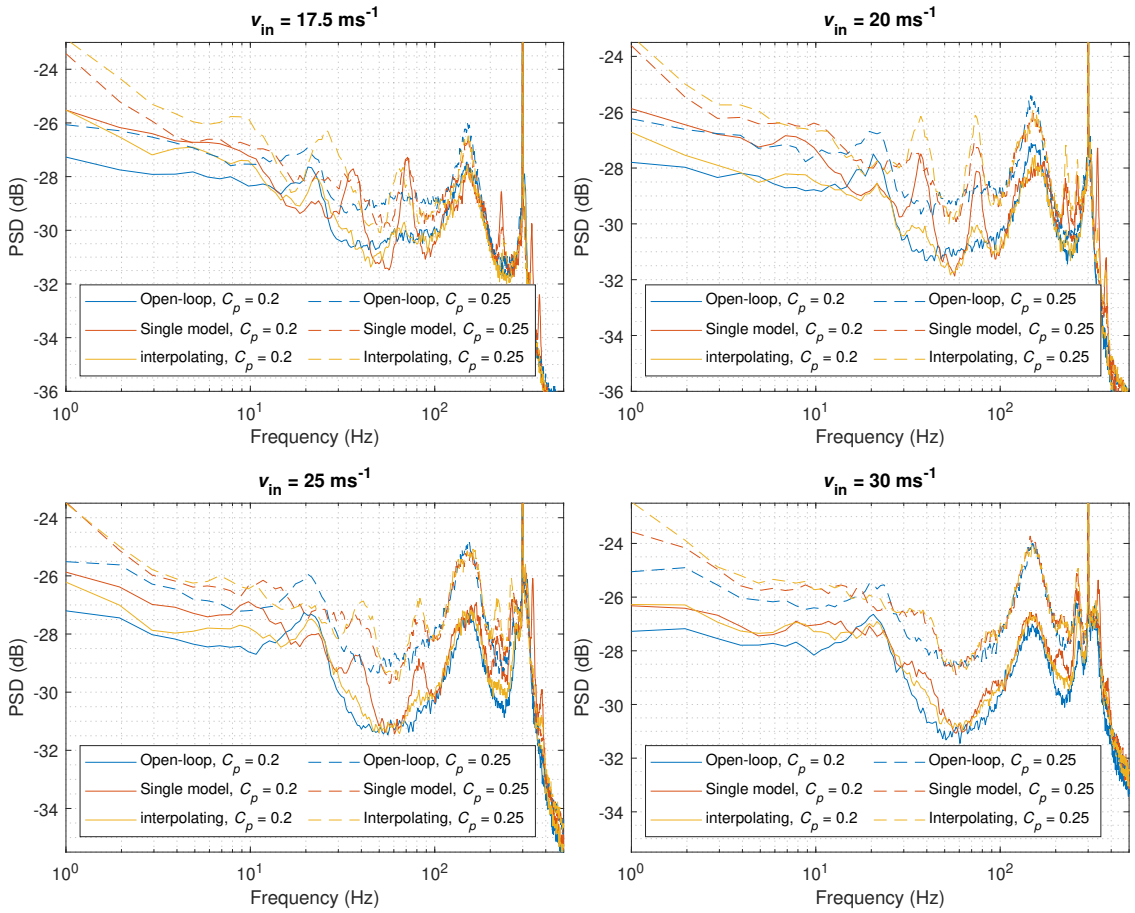


Figure 6.31: Effect of LQG controller on velocity frequency content at $(x, y, z)/h = (3, 0.5, 0)$

	Controller	
Operating point	**Single model**	**Interpolating**
$v_{\text{in}} = 17.5\,\text{m s}^{-1}$, $C_{p,\text{ref}} = 0.2$	1.46 dB	0.94 dB
$v_{\text{in}} = 17.5\,\text{m s}^{-1}$, $C_{p,\text{ref}} = 0.25$	1.32 dB	0.64 dB
$v_{\text{in}} = 20\,\text{m s}^{-1}$, $C_{p,\text{ref}} = 0.2$	1.22 dB	1.27 dB
$v_{\text{in}} = 20\,\text{m s}^{-1}$, $C_{p,\text{ref}} = 0.25$	1.29 dB	1.34 dB
$v_{\text{in}} = 25\,\text{m s}^{-1}$, $C_{p,\text{ref}} = 0.2$	0.94 dB	0.52 dB
$v_{\text{in}} = 25\,\text{m s}^{-1}$, $C_{p,\text{ref}} = 0.25$	1.54 dB	1.05 dB
$v_{\text{in}} = 30\,\text{m s}^{-1}$, $C_{p,\text{ref}} = 0.2$	0.62 dB	0.47 dB
$v_{\text{in}} = 30\,\text{m s}^{-1}$, $C_{p,\text{ref}} = 0.25$	0.90 dB	0.43 dB

Table 6.2: LQG controller 21 Hz bump velocity attenuation compared to open-loop

At frequencies above the Helmholtz resonance, the controller causes alternating amplification/attenuation of velocity content. This behaviour is partially seen in the modelled sensitivity transfer functions, where there are a slight peak and trough after the targeted attenuation, however the experimental data shows two peak-trough pairs before the 150 Hz vortex peak. This discrepancy can be explained by the phase lag in the real system which the 3$^{\text{rd}}$ order models do not fit beyond the 21 Hz bump. The lag causes the feedback from higher frequency fluctuations to be delayed by in excess of half a period, acting constructively when in phase with the output disturbance and destructively when out of phase. Above the 150 Hz peak, the direct influence of the acoustic actuation can be seen as peaks at the carrier tone and side-band frequencies matching the lower frequency peak-trough pairs.

Figure 6.32 shows the frequency spectra of the input signals (modulation signal), which demonstrate up to two clear peaks above the target frequency (and one just below), after which the content rolls-off. There are also sharp peaks at the 300 Hz carrier frequency, indicating that the tone is not fully attenuated by the low-pass filter, although this should not significantly affect control as after modulation it will result in content at 600 Hz and a DC offset, neither of which are within the actuation cavity bandwidth. It is interesting that the input signals do not have strong peaks around 21 Hz, as it was expected that the

controller would be attenuating the targeted bump by responding with an opposite-phase signal, instead the strongest tone in the input is at around double the targeted frequency.

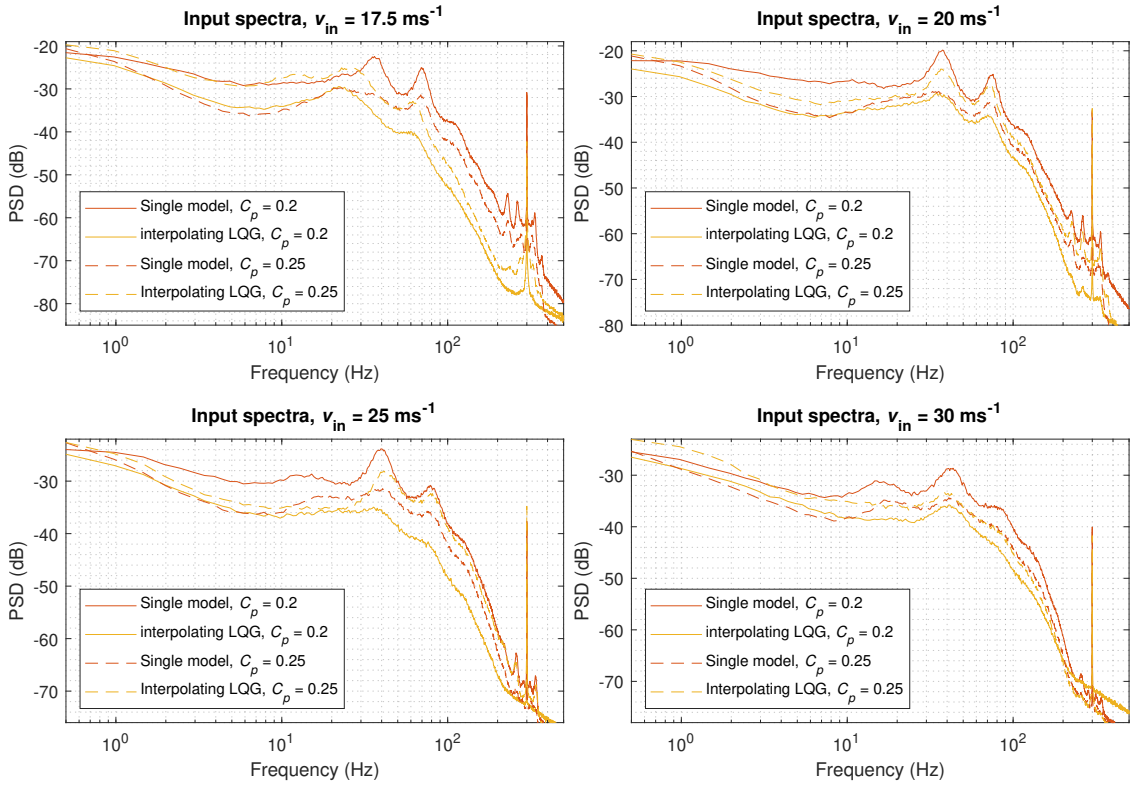


Figure 6.32: Frequency spectra of input signals

6.5 Conclusions and Discussion

In this chapter, two separate closed-loop controllers were designed and implemented to achieve steady state tracking of reattachment length (by proxy of wall C_p at $x/h = 5$) and disturbance rejection: a gain-scheduling Proportional Integral (PI) controller; and a novel interpolating Linear Quadratic Gaussian (LQG) controller. Experimental transfer function estimates (ETFEs) were first calculated for the input-output behaviour across a total of 16 inlet velocities and actuation amplitudes (4 of each), and transfer function/state-space models were fitted to each of the ETFEs. While the dominant features of the ETFEs were similar across all operating points, notably a bump corresponding to the 21 Hz Helmholtz resonance, a simple linear parameter-varying representation of the plant non-linearities with operating conditions could not be identified.

The PI controller was designed using a gain-scheduling approach to account for the plant non-linearity. The gains were tuned to achieve a closed-loop $-3\,\mathrm{dB}$ bandwidth of about $2.3\,\mathrm{Hz}$ ($St_h = 0.0026$-0.0015 at 17.5-$30\,\mathrm{m\,s^{-1}}$), which was limited by the long time-delay and the uncertainty of plant gain between the identified operating points. A closed-loop step response time of approximately $0.3\,\mathrm{s}$ was achieved, corresponding to $tv_{\mathrm{in}}/h \approx 260$ to 450 at inlet speeds 17.5 to $30\,\mathrm{m\,s^{-1}}$. The PI controller successfully attenuates low frequency wall pressure content compared to open-loop actuation, along with slightly attenuating the $21\,\mathrm{Hz}$ Helmholtz resonance bump.

The LQG controller was intended to improve on the robustness and disturbance rejection of the PI controller. A novel approach of running 16 LQG controllers in parallel, one for each of the identified operating points, and interpolating the control action based on the current inlet speed and steady state C_p was used to account for the plant non-linearity. Experimental closed-loop transfer functions demonstrate that the interpolating-LQG controller improves robustness across operating conditions when compared to a single-model controller.

The LQG controller suffers from the same limitations relating to large delay and plant uncertainty as the PI controller. However, a different approach was taken to tuning the LQG. Where the PI controller was tuned based on bandwidth, the LQG controller was designed to suppress the disturbance due to the $21\,\mathrm{Hz}$ Helmholtz resonance, at the cost of slightly amplifying content at frequencies above and below the $21\,\mathrm{Hz}$ peak. The Helmholtz resonance is used as a convenient physical analogy to a general periodic disturbance. Although the amplification of unsteadiness is not desirable, an example of where it may be acceptable is when flow unsteadiness forces a structural resonance which can be avoided by shifting the unsteadiness to other frequencies. There may also be applications in combustor flows, where couplings between flame unsteadiness, chamber acoustics, and vortex structures can be significant.

The closed-loop bandwidth of the LQG controller was approximately $0.8\,\mathrm{Hz}$ ($St_h \approx 5.3 \times 10^{-4}$ to 9.1×10^{-4}), however, the use of a feed-forward term ensured that the output reached almost the requested value in the open-loop step-response time ($\sim 0.04\,\mathrm{s}$ or $tv_{\mathrm{in}}/h \approx$ 35-45). The interpolating LQR successfully suppressed the $21\,\mathrm{Hz}$ peak in

both wall pressure and hot-wire velocity measurements, although the effectiveness of suppressing velocity content depended on the operating point, achieving from around 0.4 dB attenuation at the worst to 1.3 dB at the best.

Previous similar studies have achieved response times from $tv_{\text{in}}/h \approx 15.5$ to 8×10^3 [108, 114, 151, 153], compared to which the currently achieved step response times/closed-loop bandwidths are unremarkable. Despite this, it is not clear that non-dimensional step response time can be meaningfully compared between experiments, particularly those using different actuators. For example, Morioka & Honami [108] also used a PI controller with a wall pressure measurement in the reattachment zone as feedback, but with actuation by vortex generating jets at the step edge. They achieved a step response time of $tv_{\text{in}}/h \approx 25$ at $Re_h = 2.7 \times 10^4$, significantly faster than the step response time of the PI controller in the current work, $tv_{\text{in}}/h \approx 300$ at $Re_h \approx 2.6 \times 10^4$, despite the similar controller and Reynolds number. Considering that the open-loop step response times of the current arrangement are approximately $tv_{\text{in}}/h \approx 35$, 40, and 45, at $v_{\text{in}} = 20$, 25, and $30\,\text{m}\,\text{s}^{-1}$, respectively, and given the amount of unsteadiness in the feedback measurement, a closed-loop bandwidth an order of magnitude larger than the open-loop step response seems reasonable.
In addition to the complication of comparing controllers where different actuation strategies are used, that the open-loop strep response times observed in the current work do not increase proportionally to inlet velocity calls into question the suitability of non-dimensional response time, tv_{in}/h. However, it is possible that the step response time of acoustic actuation also depends on the excitation frequency.

Chapter 7

Summary and Conclusions

7.1 Summary of Work

This thesis has investigated the dynamics and control of a high expansion ratio backward-facing step (BFS) flow with acoustic actuation from the side opposite to the step. Emphasis was placed on the mechanisms of flow modification by acoustic excitation and the implementation of closed-loop control. A combined experimental and numerical approach was taken to characterise the mean effects of the actuation and to identify dynamically important modes with which the acoustic excitation interacts. Following the detailed characterisation of the flow dynamics and the influence of open-loop forcing, two alternative closed-loop control schemes were developed and compared: a gain-scheduling PI controller; and an interpolating LQG controller, which used a novel multi-model interpolation approach to account for plant non-linearities.

An experimental rig was developed, consisting of a centrifugal blower, large plenum and bell-mouth designed to condition the flow, and a backward-facing step test section of expansion ratio 2 and aspect ratio 7.5. The test section was instrumented by an array of wall pressure tappings and a hot-wire probe positionable by motorised traverse. A range of Reynolds numbers based on inlet velocity and step height from $Re_h = 21000$ to 42000 was achievable by varying the blower speed, and lower Re_h could be reached by venting a portion of the flow from the blower. Opposite-side acoustic actuation was provided by an array of six Helmholtz resonator type actuators, each driven by an individual loudspeaker,

allowing distributed actuation strategies to be investigated. Complementary CFD simulations were also carried out to provide visualisation of flow structures and to support the interpretation of experimental measurements.

The static and unsteady characteristics of the baseline and actuated BFS flows were examined over a range of inlet velocities and actuation amplitudes. Acoustic excitation at 300 Hz, the first longitudinal resonance of the test section, was found to reduce the mean reattachment length by at least 24-28% across a range of Reynolds numbers from $Re_h = 21000$ to 42000 (reattachment length was not estimated at the maximum actuation amplitude due to sensor constraints, although was predicted to be around or just above 30%). This reduction is comparable to results obtained in the literature using local periodic actuation at the step edge, and exceeds those which used 'external' acoustic excitation. Hot-wire traverses revealed that forcing enhanced shear-layer spreading and improved velocity uniformity in the recovery region. A quantitative measure of flow uniformity, based on the spatial standard deviation of the mean streamwise velocity, was introduced to relate actuation effectiveness to practical heat-exchanger applications. The influence of spanwise distributed actuation was investigated in the interest of improving flow uniformity downstream of the step. While distributed actuation was successful in altering the mean velocity distribution, particularly in suppressing the secondary side-wall vortices, the overall improvements on spanwise uniform actuation were minimal.

The dominant coherent modes of the backward-facing step flow were identified by frequency analysis of the wall pressure and hot-wire velocity data, namely: the shear-layer/roll-up/Kelvin-Helmholtz instability mode, with $St_\theta \approx 0.017$; the step mode, with $St_h \approx 0.2$; the shedding mode, with $St_h \approx 0.07$-0.12; and the flapping mode, with $St_h \approx 0.015$. Dynamic Mode Decomposition (DMD) of the CFD data confirmed the correspondence between the identified dominant frequencies and the coherent modes reported in literature. Acoustic forcing was shown to couple to the vortex scale closest to the actuation frequency, the intermediate vortex scale between the shear-layer and step modes (at $v_{\text{in}} = 20\,\text{m}\,\text{s}^{-1}$), concurring with the findings of Marrot et al. [42, 109, 48]. Vortex roll-up and the step mode were also found to lock on to the harmonics and the sub-harmonic of the excitation tone, respectively. This coupling promoted the early formation and strengthening of

large scale coherent vortices, thereby enhancing momentum transfer and shear layer spreading/curvature, and reducing the extent of the separated region.

Finally, the problem of closed-loop control of the backward-facing step flow was tackled. The input-output dynamics of the system were characterised by wall pressure empirical transfer function estimates (ETFEs), measured at 16 individual operating points (inlet velocity and steady actuation amplitude). The non-linearities of the plant with operating conditions presented as variations in the DC gain and the shape of the transfer function around a bump at $\sim$21 Hz, corresponding to the Helmholtz resonance of the installation. These non-linearities were explained as a consequence of the shear-layer/reattachment position. The wall pressure coefficient at $x/h = 5$ was chosen as the feedback measurement based on its linear relationship with the estimated reattachment length and the similarity of the ETFE shapes across operating conditions. Low-order state-space models and higher order transfer function models were then fitted to each of the 16 ETFEs.

Following the system identification, two closed-loop controllers were designed and implemented: a Proportional Integral (PI) controller, and a Linear Quadratic Gaussian (LQG) controller. The aims for both controllers were generally the same: to track a requested value of wall pressure coefficient and reject disturbances/unsteadiness. However, different approaches were taken for each. The PI controller was designed to achieve the highest bandwidth across the identified operating range given noise/uncertainty constraints, and gain scheduling was used to account for the system non-linearities. The LQG controller was designed to specifically target the $\sim$21 Hz Helmholtz resonance content, despite the achievable closed-loop bandwidth being an order of magnitude less than the resonance due to the large phase delay. By costing the model states related to the Helmholtz resonance bump, the associated content was attenuated (around 2.4-4.3 dB for pressure content and 0.5-1.3 dB for velocity content) at the cost of slightly amplifying unsteadiness at other frequencies. Despite the simplicity of the low order plant models, a parameter varying model to account for the non-linearities with operating condition could not be identified. Instead, a novel parallel-interpolating strategy was used, in which 16 individual LQG controllers, one for each of the identified operating points, were run in parallel and the control action interpolated based on the current inlet speed and requested C_p.

7.2 Conclusions

1. Opposite-side acoustic actuation can achieve substantial control authority over separated BFS flows, and is similarly effective in terms of reattachment length reduction to (the more commonly studied) periodic excitation at the step edge. However, the required excitation level necessitates that acoustic resonances of the actuator and installation be exploited. The maximum demonstrated reattachment length reduction was approximately 28% at $v_{\text{in}} = 20\,\text{m}\,\text{s}^{-1}$, although the maximum achievable reduction slightly exceeds this. Opposite-side acoustic actuation may provide a practical alternative to forcing near/at the separation line, for flows where packaging/installation constraints make it difficult to install or service actuators on the separated side, particularly for duct flows with strong longitudinal resonance modes at similar frequencies to the natural vortex modes.

2. Acoustic forcing modifies vortex dynamics by the locking-on of coherent vortex modes to the excitation tone and its harmonics/sub-harmonics, and enhancing vortex strength/consistency. The mechanism differs from more frequently studied forcing at of near the separating edge, in that acoustic actuation couples with the scale of coherent mode with natural frequency closest to the excitation frequency, whereas excitation at the step edge has been shown to directly force vortex roll-up (i.e. couple to the smallest scale of coherent vortices) [41, 54, 110, 45, 111]. This phenomenon has previously been observed by Marrot et al. [42, 109, 48], but was not thoroughly discussed, and has been further examined and clarified in the present work.

3. Opposite-side acoustic excitation improved transverse (y-z) plane spatial velocity uniformity significantly compared to baseline, between $x/h \approx 2$ and $x/h \approx 10$. The effectiveness of several spanwise distributed actuation strategies on the spatial uniformity of the flow was also investigated. While distributed actuation had some influence on the spanwise velocity distribution (in particular, concentrated forcing near the side-walls suppressed the effects of the streamwise aligned secondary vortices), there was minimal sensitivity to the precise actuation distribution in terms of the uniformity metric.

4. Closed-loop control strategies using a wall-pressure measurement in the reattachment zone as feedback can provide robustness in actively controlled reattaching shear-layer flows. However, controller performance is hindered by the lack of separation between uncontrollable unsteadiness (i.e. noise) and controllable bulk motion (i.e. disturbance) bandwidths, and by the uncertainty in plant dynamics relating to variation with operating conditions. The maximum possible bandwidth is also limited by the input-output delay, which is a combination of the mechanism of demodulation and the transport time of the shear-layer, and the measurement delay due to the long tubes connecting the pressure transducers to the wall tappings.

   For separated flows with a dominant periodic disturbance close to or above the open-loop bandwidth of the system (e.g. the Helmholtz resonance of the plenum and test section in the current work), a model-based controller with knowledge of the disturbance dynamics can be used to attenuate the disturbance, at the cost of amplifying unsteadiness at frequencies above and below the disturbance. Although not ideal, this may be an acceptable trade-off in cases where a periodic disturbance forces a natural flow instability or structural resonance, and 'moving' the disturbance to other frequencies is preferable.

7.3 Recommendations for Future Work

i. Direct calculation of reattachment length from experimental measurements. In the current work, reattachment length was estimated from RMS wall pressures according to the observations of Mabey [168]: that the peak RMS pressure occurs slightly upstream of reattachment. However, the accuracy of this method is unknown, and saturation of the pressure transducers by the acoustic pressure at higher volumes prevented quantification of the maximum reattachment length reduction. Accurate determination of reattachment position, e.g. from split film probe or PIV measurements, could be used to validate the estimations and assess the maximum achievable reattachment length reduction by opposite-side acoustic actuation.

ii. Detailed investigation of vortex-excitation lock-on at different actuation frequencies/flow speeds. While the data presented here show a reasonably clear picture of

the interaction of acoustic excitation with the formation and evolution of coherent vortex structures, further work is needed to understand the effects of varying excitation frequency (relative to natural flow frequencies) fully. The current work has to some extent confirmed the findings of Marrot et al. [48], who presented data which indicated that acoustic actuation coupled to the vortex scale closest to the excitation frequency. However, the current work investigated only one actuation frequency and flow velocity in detail ($v_{\text{in}} = 20\,\text{m}\,\text{s}^{-1}$, $f_c = 300\,\text{Hz}$). The behaviour of vortex lock-on in transitional frequency regimes where the coupling shifts from one mode to the mode of preceding or following scale is also of academic interest.

Previous studies have demonstrated that harmonic (multi-frequency) excitation can have some influence on vortex pairing in circular jets and plane mixing layers [177, 178, 49]. Therefore, it seems plausible that excitation designed to target multiple scales at once may be beneficial in terms of promoting early pairing and enhancing vortex strength, in reattaching jet/shear-layer flows.

iii. Full flow visualisation. Experimental (ideally time-resolved) flow visualisation would be beneficial for differentiating between vortex structures and other motions driven by actuation, and to confirm the conclusions made from single wire measurements.

CFD simulations were used for this purpose in the present work. However, despite being a surprisingly good fit to the experimental data, a number of approximations were made in the numerical setup, including the lack of turbulence treatment in the laminar solver, lack of simulated side-wall effects, and approximate inlet and actuation boundary conditions. Addressing the resulting inaccuracies would considerably increase the computational cost and run time of simulations, and the quantitative agreement of experimental and numerical results would still be unlikely. PIV, on the other hand, could be used to generate a great deal of experimental data over multiple operating conditions and actuation frequencies in a relatively short amount of time.

iv. Multiple feedback measurements for closed-loop control. A sensor fusion approach using multiple feedback measurements could be used to design a more effective controller by averaging out the pressure traces of small scale flow structures/turbulence and increasing the signal-to-noise ratio of the large scale motions which control is

targeting. Preliminary controller designs however suggested that the potential benefits of this approach are outweighed by increased complexity. Alternatively, a SISO controller with changing feedback location could be designed, where the wall tapping used for feedback changes based on reattachment length, so that its position relative to the shear layer remains fairly constant and hence dynamics remain similar. Scheduling the feedback measurement this way might allow for more compact and robust controllers.

v. Integration and assessment of opposite-side acoustic actuation within realistic heat-exchanger duct geometries. The canonical backward-facing step geometry exhibits abrupt flow separation at the step edge, whereas the separation line in an aggressive but smooth duct may shift with operating condition or dynamically due to some instability. Furthermore, the BFS flow studied in this thesis was open and unconstricted (i.e. no blockage or separated channels), which allowed the flow to reattach and continue to develop downstream. Inserting a heat exchanger, particularly if the AIP were upstream of the reattachment point, would significantly alter the flow due to blockage effects and prevention of mixing by the HEX channels. Opposite-side acoustic actuation may be well suited to internal flows with variable separation point and the excitation frequency can be chosen to couple to various scales of vortex/coherent mode, although maximum effectiveness necessitates exploiting the acoustic resonances of the duct.

Appendix A

Identified Transfer Function and State Space Models

A.1 Transfer Function Model Fits

The equations of the 9^{th} order identified transfer functions, $G(i,j)$, at each of the operating points $(v_{\text{in}}(i), u_{\text{m}}(j))$, shown in Figure 6.8, are given by:

$$G(1,1) = \frac{0.04225z^{-1} - 0.3481z^{-2} + 1.257z^{-3} - 2.597z^{-4} + 3.358z^{-5} - 2.783z^{-6} + 1.444z^{-7} - 0.4285z^{-8} + 0.05573z^{-9}}{1 - 8.727z^{-1} + 33.89z^{-2} - 76.86z^{-3} + 112.2z^{-4} - 109.3z^{-5} + 71.1z^{-6} - 29.76z^{-7} + 7.277z^{-8} - 0.7918z^{-9}}$$

$$G(1,2) = \frac{0.03368z^{-1} - 0.2771z^{-2} + 0.9987z^{-3} - 2.06z^{-4} + 2.659z^{-5} - 2.2z^{-6} + 1.139z^{-7} - 0.3374z^{-8} + 0.04379z^{-9}}{1 - 8.712z^{-1} + 33.78z^{-2} - 76.49z^{-3} + 111.5z^{-4} - 108.5z^{-5} + 70.48z^{-6} - 29.47z^{-7} + 7.199z^{-8} - 0.7826z^{-9}}$$

$$G(1,3) = \frac{0.01981z^{-1} - 0.1629z^{-2} + 0.5869z^{-3} - 1.21z^{-4} + 1.561z^{-5} - 1.291z^{-6} + 0.668z^{-7} - 0.1978z^{-8} + 0.02564z^{-9}}{1 - 8.735z^{-1} + 33.96z^{-2} - 77.15z^{-3} + 112.8z^{-4} - 110.2z^{-5} + 71.86z^{-6} - 30.17z^{-7} + 7.402z^{-8} - 0.8084z^{-9}}$$

$$G(1,4) = \frac{0.01258z^{-1} - 0.1028z^{-2} + 0.3681z^{-3} - 0.7545z^{-4} + 0.9677z^{-5} - 0.7954z^{-6} + 0.4091z^{-7} - 0.1204z^{-8} + 0.01552z^{-9}}{1 - 8.742z^{-1} + 34.02z^{-2} - 77.37z^{-3} + 113.3z^{-4} - 110.8z^{-5} + 72.39z^{-6} - 30.45z^{-7} + 7.487z^{-8} - 0.8195z^{-9}}$$

$$G(2,1) = \frac{0.04116z^{-1} - 0.3422z^{-2} + 1.247z^{-3} - 2.599z^{-4} + 3.391z^{-5} - 2.836z^{-6} + 1.484z^{-7} - 0.4445z^{-8} + 0.05833z^{-9}}{1 - 8.693z^{-1} + 33.63z^{-2} - 76.02z^{-3} + 110.6z^{-4} - 107.4z^{-5} + 69.68z^{-6} - 29.09z^{-7} + 7.096z^{-8} - 0.7703z^{-9}}$$

$$G(2,2) = \frac{0.03422z^{-1} - 0.2833z^{-2} + 1.027z^{-3} - 2.132z^{-4} + 2.77z^{-5} - 2.306z^{-6} + 1.201z^{-7} - 0.358z^{-8} + 0.04675z^{-9}}{1 - 8.666z^{-1} + 33.42z^{-2} - 75.3z^{-3} + 109.2z^{-4} - 105.7z^{-5} + 68.34z^{-6} - 28.44z^{-7} + 6.912z^{-8} - 0.7477z^{-9}}$$

$$G(2,3) = \frac{0.0197z^{-1} - 0.1632z^{-2} + 0.5924z^{-3} - 1.23z^{-4} + 1.599z^{-5} - 1.332z^{-6} + 0.6946z^{-7} - 0.2072z^{-8} + 0.02707z^{-9}}{1 - 8.683z^{-1} + 33.56z^{-2} - 75.79z^{-3} + 110.2z^{-4} - 107z^{-5} + 69.35z^{-6} - 28.94z^{-7} + 7.058z^{-8} - 0.7662z^{-9}}$$

$$G(2,4) = \frac{0.01647z^{-1} - 0.1358z^{-2} + 0.4903z^{-3} - 1.013z^{-4} + 1.31z^{-5} - 1.086z^{-6} + 0.5628z^{-7} - 0.167z^{-8} + 0.02169z^{-9}}{1 - 8.659z^{-1} + 33.38z^{-2} - 75.17z^{-3} + 109z^{-4} - 105.6z^{-5} + 68.28z^{-6} - 28.43z^{-7} + 6.92z^{-8} - 0.7497z^{-9}}$$

$$G(3,1) = \frac{0.08153z^{-1} - 0.6764z^{-2} + 2.459z^{-3} - 5.12z^{-4} + 6.675z^{-5} - 5.579z^{-6} + 2.92z^{-7} - 0.8748z^{-8} + 0.1149z^{-9}}{1 - 8.551z^{-1} + 32.55z^{-2} - 72.42z^{-3} + 103.8z^{-4} - 99.29z^{-5} + 63.47z^{-6} - 26.13z^{-7} + 6.289z^{-8} - 0.674z^{-9}}$$

$$G(3,2) = \frac{0.03796z^{-1} - 0.3165z^{-2} + 1.156z^{-3} - 2.418z^{-4} + 3.166z^{-5} - 2.657z^{-6} + 1.396z^{-7} - 0.4197z^{-8} + 0.05529z^{-9}}{1 - 8.613z^{-1} + 33.02z^{-2} - 74z^{-3} + 106.8z^{-4} - 102.9z^{-5} + 66.24z^{-6} - 27.46z^{-7} + 6.652z^{-8} - 0.7176z^{-9}}$$

$$G(3,3) = \frac{0.02608z^{-1} - 0.2175z^{-2} + 0.7949z^{-3} - 1.663z^{-4} + 2.178z^{-5} - 1.828z^{-6} + 0.9606z^{-7} - 0.2889z^{-8} + 0.03807z^{-9}}{1 - 8.6z^{-1} + 32.93z^{-2} - 73.68z^{-3} + 106.2z^{-4} - 102.2z^{-5} + 65.68z^{-6} - 27.19z^{-7} + 6.578z^{-8} - 0.7086z^{-9}}$$

$$G(3,4) = \frac{0.01337z^{-1} - 0.1122z^{-2} + 0.4124z^{-3} - 0.8677z^{-4} + 1.143z^{-5} - 0.9641z^{-6} + 0.5091z^{-7} - 0.1538z^{-8} + 0.02036z^{-9}}{1 - 8.638z^{-1} + 33.22z^{-2} - 74.69z^{-3} + 108.2z^{-4} - 104.6z^{-5} + 67.6z^{-6} - 28.14z^{-7} + 6.846z^{-8} - 0.7418z^{-9}}$$

$$G(4,1) = \frac{-0.006235z^{-1} + 0.03382z^{-2} - 0.0567z^{-3} - 0.02227z^{-4} + 0.2146z^{-5} - 0.3365z^{-6} + 0.2592z^{-7} - 0.1028z^{-8} + 0.01682z^{-9}}{1 - 8.175z^{-1} + 29.66z^{-2} - 62.67z^{-3} + 84.95z^{-4} - 76.58z^{-5} + 45.89z^{-6} - 17.61z^{-7} + 3.928z^{-8} - 0.3874z^{-9}}$$

$$G(4,2) = \frac{-0.03722z^{-1} + 0.3067z^{-2} - 1.107z^{-3} + 2.286z^{-4} - 2.954z^{-5} + 2.445z^{-6} - 1.266z^{-7} + 0.3751z^{-8} - 0.04866z^{-9}}{1 - 8.709z^{-1} + 33.74z^{-2} - 76.35z^{-3} + 111.2z^{-4} - 108z^{-5} + 70.08z^{-6} - 29.25z^{-7} + 7.132z^{-8} - 0.7736z^{-9}}$$

$$G(4,3) = \frac{0.1463z^{-1} - 1.223z^{-2} + 4.478z^{-3} - 9.39z^{-4} + 12.33z^{-5} - 10.38z^{-6} + 5.468z^{-7} - 1.649z^{-8} + 0.218z^{-9}}{1 - 7.895z^{-1} + 27.53z^{-2} - 55.56z^{-3} + 71.4z^{-4} - 60.41z^{-5} + 33.52z^{-6} - 11.69z^{-7} + 2.303z^{-8} - 0.192z^{-9}}$$

$$G(4,4) = \frac{-0.02319z^{-1} + 0.1833z^{-2} - 0.6331z^{-3} + 1.249z^{-4} - 1.537z^{-5} + 1.209z^{-6} - 0.5935z^{-7} + 0.166z^{-8} - 0.02026z^{-9}}{1 - 8.44z^{-1} + 31.67z^{-2} - 69.36z^{-3} + 97.68z^{-4} - 91.73z^{-5} + 57.44z^{-6} - 23.13z^{-7} + 5.431z^{-8} - 0.5669z^{-9}} \tag{A.1}$$

A.2 State Space Model Fits

The equations of the identified state space model fits shown in Figure 6.9 (without Padé delay approximation), $x_{k+1}^{i,j} = \mathbf{A}_{i,j}x_k^{i,j} + \mathbf{B}_{i,j}u_{k-Id_{i,j}}$, $y_k = \mathbf{C}_{i,j}x_k^{i,j}$, at each of the operating points $(v_{\text{in}}(i), u_{\text{m}}(j))$, are summarised below:

$$\mathbf{A}_{1,1} = \begin{bmatrix} 0.9925 & 0.03125 & -3.3\times10^{-6} \\ -0.02687 & 0.9925 & 0.008726 \\ -2.325\times10^{-6} & 1.774\times10^{-7} & 0.9656 \end{bmatrix} \quad \mathbf{A}_{1,2} = \begin{bmatrix} 0.9944 & 0.03125 & -4.803\times10^{-6} \\ -0.0317 & 0.9944 & 0.01113 \\ -7.043\times10^{-6} & -4.271\times10^{-6} & 0.9673 \end{bmatrix}$$

$$\mathbf{A}_{1,3} = \begin{bmatrix} 0.9949 & 0.03125 & 8.277\times10^{-7} \\ -0.03407 & 0.9949 & 0.01439 \\ 4.603\times10^{-7} & -2.173\times10^{-6} & 0.9782 \end{bmatrix} \quad \mathbf{A}_{1,4} = \begin{bmatrix} 0.9947 & 0.03125 & -5.397\times10^{-6} \\ -0.03154 & 0.9947 & 0.01569 \\ -9.373\times10^{-6} & 5.709\times10^{-6} & 0.9851 \end{bmatrix}$$

$$\mathbf{A}_{1,1} = \begin{bmatrix} 0.9908 & 0.03125 & -2.005\times10^{-8} \\ -0.03137 & 0.9908 & 0.01283 \\ -2.664\times10^{-7} & -4.462\times10^{-7} & 0.9678 \end{bmatrix} \quad \mathbf{A}_{1,2} = \begin{bmatrix} 0.9932 & 0.03125 & 3.935\times10^{-8} \\ -0.03639 & 0.9932 & 0.01601 \\ -4.107\times10^{-8} & -8.106\times10^{-8} & 0.9637 \end{bmatrix}$$

$$\mathbf{A}_{1,3} = \begin{bmatrix} 0.9927 & 0.03127 & -5.294\times10^{-5} \\ -0.0443 & 0.9928 & 0.02375 \\ -2.003\times10^{-5} & 1.597\times10^{-5} & 0.9835 \end{bmatrix} \quad \mathbf{A}_{1,4} = \begin{bmatrix} 0.9951 & 0.03125 & -3.085\times10^{-6} \\ -0.03968 & 0.9951 & 0.02325 \\ -2.947\times10^{-6} & 1.992\times10^{-6} & 0.9827 \end{bmatrix}$$

$$\mathbf{A}_{1,1} = \begin{bmatrix} 0.9923 & 0.03125 & 7.611\times10^{-9} \\ -0.03485 & 0.9923 & 0.01088 \\ -2.012\times10^{-9} & -1.126\times10^{-8} & 0.9452 \end{bmatrix} \quad \mathbf{A}_{1,2} = \begin{bmatrix} 0.9894 & 0.03125 & 5.714\times10^{-7} \\ -0.03593 & 0.9894 & 0.01151 \\ 1.76\times10^{-7} & -5.051\times10^{-7} & 0.948 \end{bmatrix}$$

$$\mathbf{A}_{1,3} = \begin{bmatrix} 0.9877 & 0.03127 & -4.418\times10^{-5} \\ -0.04351 & 0.9877 & 0.03174 \\ -3.343\times10^{-5} & 5.028\times10^{-5} & 0.9697 \end{bmatrix} \quad \mathbf{A}_{1,4} = \begin{bmatrix} 0.99 & 0.03125 & -2.782\times10^{-5} \\ -0.04387 & 0.99 & 0.02003 \\ -2.209\times10^{-5} & 1.545\times10^{-5} & 0.9786 \end{bmatrix}$$

$$\mathbf{A}_{1,1} = \begin{bmatrix} 0.9878 & 0.03125 & -1.938\times10^{-6} \\ -0.04379 & 0.9878 & 0.0182 \\ -1.232\times10^{-6} & 2.004\times10^{-6} & 0.9622 \end{bmatrix} \quad \mathbf{A}_{1,2} = \begin{bmatrix} 0.988 & 0.03124 & 2.586\times10^{-6} \\ -0.03541 & 0.988 & 0.02639 \\ 4.245\times10^{-6} & -4.278\times10^{-5} & 0.946 \end{bmatrix}$$

$$\mathbf{A}_{1,3} = \begin{bmatrix} 0.9874 & 0.03124 & 8.317\times10^{-6} \\ -0.04261 & 0.9874 & 0.01742 \\ 2.312\times10^{-6} & -5.62\times10^{-6} & 0.939 \end{bmatrix} \quad \mathbf{A}_{1,4} = \begin{bmatrix} 0.9893 & 0.03125 & -7.707\times10^{-6} \\ -0.04126 & 0.9893 & 0.01876 \\ -2.431\times10^{-6} & 8.409\times10^{-6} & 0.9293 \end{bmatrix}$$

(A.2)

$$
\begin{aligned}
\mathbf{B}_{1,1} &= \begin{bmatrix} 1.225 \times 10^{-6} \\ -4.455 \times 10^{-7} \\ -4.45 \times 10^{-7} \end{bmatrix} & \mathbf{B}_{1,2} &= \begin{bmatrix} 5.108 \times 10^{-7} \\ -2.379 \times 10^{-7} \\ -2.38 \times 10^{-7} \end{bmatrix} & \mathbf{B}_{1,3} &= \begin{bmatrix} 6.262 \times 10^{-7} \\ 6.735 \times 10^{-8} \\ 6.74 \times 10^{-8} \end{bmatrix} & \mathbf{B}_{1,4} &= \begin{bmatrix} -1.873 \times 10^{-6} \\ 2.037 \times 10^{-6} \\ 2.04 \times 10^{-6} \end{bmatrix} \\
\mathbf{B}_{2,1} &= \begin{bmatrix} 4.647 \times 10^{-7} \\ -2.532 \times 10^{-7} \\ -2.53 \times 10^{-7} \end{bmatrix} & \mathbf{B}_{2,2} &= \begin{bmatrix} 1.381 \times 10^{-8} \\ -1.036 \times 10^{-8} \\ -1.04 \times 10^{-8} \end{bmatrix} & \mathbf{B}_{2,3} &= \begin{bmatrix} 1.481 \times 10^{-5} \\ 1.608 \times 10^{-5} \\ 1.61 \times 10^{-5} \end{bmatrix} & \mathbf{B}_{2,4} &= \begin{bmatrix} -3.32 \times 10^{-6} \\ -4.803 \times 10^{-6} \\ -4.8 \times 10^{-6} \end{bmatrix} \\
\mathbf{B}_{3,1} &= \begin{bmatrix} 1.083 \times 10^{-8} \\ -4.623 \times 10^{-9} \\ -4.62 \times 10^{-9} \end{bmatrix} & \mathbf{B}_{3,2} &= \begin{bmatrix} 4.229 \times 10^{-7} \\ 3.261 \times 10^{-8} \\ 3.26 \times 10^{-8} \end{bmatrix} & \mathbf{B}_{3,3} &= \begin{bmatrix} -1.756 \times 10^{-6} \\ -2.424 \times 10^{-6} \\ -2.42 \times 10^{-6} \end{bmatrix} & \mathbf{B}_{3,4} &= \begin{bmatrix} -9.007 \times 10^{-6} \\ 1.809 \times 10^{-5} \\ 1.81 \times 10^{-5} \end{bmatrix} \\
\mathbf{B}_{4,1} &= \begin{bmatrix} -2.919 \times 10^{-7} \\ -6.795 \times 10^{-8} \\ -6.79 \times 10^{-8} \end{bmatrix} & \mathbf{B}_{4,2} &= \begin{bmatrix} 2.844 \times 10^{-5} \\ 1.632 \times 10^{-6} \\ 1.63 \times 10^{-6} \end{bmatrix} & \mathbf{B}_{4,3} &= \begin{bmatrix} 9.793 \times 10^{-7} \\ 1.535 \times 10^{-6} \\ 1.54 \times 10^{-6} \end{bmatrix} & \mathbf{B}_{4,4} &= \begin{bmatrix} -4.942 \times 10^{-6} \\ 1.273 \times 10^{-6} \\ 1.27 \times 10^{-6} \end{bmatrix}
\end{aligned}
\tag{A.3}
$$

$$
\begin{aligned}
\mathbf{C}_{1,1} &= \begin{bmatrix} -0.082\,58 \\ 0.008\,543 \\ 0.008\,54 \end{bmatrix}^T & \mathbf{C}_{1,2} &= \begin{bmatrix} -0.022\,63 \\ 0.004\,617 \\ 0.004\,62 \end{bmatrix}^T & \mathbf{C}_{1,3} &= \begin{bmatrix} -0.034\,94 \\ 0.014\,18 \\ 0.0142 \end{bmatrix}^T & \mathbf{C}_{1,4} &= \begin{bmatrix} -0.024\,76 \\ 0.026\,72 \\ 0.0267 \end{bmatrix}^T \\
\mathbf{C}_{2,1} &= \begin{bmatrix} -0.099\,26 \\ 0.056\,87 \\ 0.0569 \end{bmatrix}^T & \mathbf{C}_{2,2} &= \begin{bmatrix} -0.026\,59 \\ 0.029\,36 \\ 0.0294 \end{bmatrix}^T & \mathbf{C}_{2,3} &= \begin{bmatrix} 0.008\,582 \\ 0.050\,88 \\ 0.0509 \end{bmatrix}^T & \mathbf{C}_{2,4} &= \begin{bmatrix} 0.016\,81 \\ 0.056\,44 \\ 0.0564 \end{bmatrix}^T \\
\mathbf{C}_{3,1} &= \begin{bmatrix} -0.0639 \\ 0.037\,39 \\ 0.0374 \end{bmatrix}^T & \mathbf{C}_{3,2} &= \begin{bmatrix} -0.1433 \\ 0.047\,61 \\ 0.0476 \end{bmatrix}^T & \mathbf{C}_{3,3} &= \begin{bmatrix} -0.029\,75 \\ 0.036\,95 \\ 0.0369 \end{bmatrix}^T & \mathbf{C}_{3,4} &= \begin{bmatrix} -0.049\,96 \\ 0.0817 \\ 0.0817 \end{bmatrix}^T \\
\mathbf{C}_{4,1} &= \begin{bmatrix} -0.088\,76 \\ 0.037\,58 \\ 0.0376 \end{bmatrix}^T & \mathbf{C}_{4,2} &= \begin{bmatrix} -0.106 \\ 0.008\,223 \\ 0.008\,22 \end{bmatrix}^T & \mathbf{C}_{4,3} &= \begin{bmatrix} -0.0937 \\ 0.059\,28 \\ 0.0593 \end{bmatrix}^T & \mathbf{C}_{4,4} &= \begin{bmatrix} -0.055\,26 \\ 0.043\,79 \\ 0.0438 \end{bmatrix}^T
\end{aligned}
\tag{A.4}
$$

with number of input delay time-steps, $Id_{i,j}$ given by

$$
\begin{aligned}
Id_{1,1} &= 73 & Id_{1,2} &= 70 & Id_{1,3} &= 60 & Id_{1,4} &= 20 \\
Id_{2,1} &= 70 & Id_{2,2} &= 70 & Id_{2,3} &= 45 & Id_{2,4} &= 25 \\
Id_{3,1} &= 70 & Id_{3,2} &= 70 & Id_{3,3} &= 60 & Id_{3,4} &= 50 \\
Id_{4,1} &= 63 & Id_{4,2} &= 66 & Id_{4,3} &= 65 & Id_{4,4} &= 65
\end{aligned}
\tag{A.5}
$$

Bibliography

[1] International Air Transport Association, "Global outlook for air transport - protectionism on the rise," 2025, ©International Air Transport Association, 2019. All Rights Reserved. Available on IATA Economics page.

[2] International Air Transport Association, "Hydrogen for aviation: A future decarbonization solution for air travel?" 2025, ©International Air Transport Association, 2019. All Rights Reserved. Available on IATA Economics page.

[3] H. Sugisita, H. Mori, and K. Uematsu, "A study of thermodynamic cycle and system configurations of hydrogen combustion turbines," *International Journal of Hydrogen Energy*, vol. 23(8), pp. 705–712, 1998, ISSN: 0360-3199. DOI: 10.1016/S0360-3199(97)00081-5

[4] A. C. Patrao, I. Jonsson, C. Xisto, A. Lundbladh, and T. Grönstedt, "Compact heat exchangers for hydrogen-fueled aero engine intercooling and recuperation," *Applied Thermal Engineering*, vol. 243, p. 122 538, 2024, ISSN: 1359-4311. DOI: 10.1016/j.applthermaleng.2024.122538

[5] T. Reischl, "Design and evaluation of heat exchanger concepts for hydrogen turbofan engines," *Aerotecnica Missili & Spazio*, 2025, ISSN: 2524-6968. DOI: 10.1007/s42496-025-00290-4

[6] C. T'Joen, M. D. Paepe, and F. Vanhee, "Heat exchanger behavior in non uniform flow," *Experimental Heat Transfer*, vol. 19(4), pp. 281–296, 2006, ISSN: 08916152. DOI: 10.1080/08916150600623382

[7] P. Blecich, "Experimental investigation of the effects of airflow nonuniformity on performance of a fin-and-tube heat exchanger," *International Journal of Refrigeration*, vol. 59, pp. 65–74, 2015, ISSN: 01407007. DOI: 10.1016/j.ijrefrig.2015.06.029

[8] M. M. Wojewodka, C. White, S. Shahpar, and K. Kontis, "A review of flow control techniques and optimisation in s-shaped ducts," *International Journal of Heat and Fluid Flow*, vol. 74, pp. 223–235, 2018, ISSN: 0142727X. DOI: 10.1016/j.ijheatfluidflow.2018.06.016

[9] L. Chen, K. Asai, T. Nonomura, G. Xi, and T. Liu, "A review of backward-facing step (BFS) flow mechanisms, heat transfer and control," *Thermal Science and Engineering Progress*, vol. 6, pp. 194–216, 2018, ISSN: 24519049. DOI: 10.1016/j.tsep.2018.04.004

[10] J. O'Connor, "Understanding the role of flow dynamics in thermoacoustic combustion instability," *Proceedings of the Combustion Institute*, vol. 39(4), pp. 4583–4610, 2023, ISSN: 15407489. DOI: 10.1016/j.proci.2022.07.115

[11] M. Gad-el-Hak, *Flow control : Passive, active, and reactive flow management*. Cambridge University Press, 2000, ISBN: 0521770068 (hardback).

[12] M. Gad-el Hak, "Modern developments in flow control," *Applied Mechanics Reviews*, vol. 49(7), pp. 365–379, 1996, ISSN: 0003-6900. DOI: 10.1115/1.3101931

[13] H. Choi, W.-P. Jeon, and J. Kim, "Control of flow over a bluff body," *Annual Review of Fluid Mechanics*, vol. 40, pp. 113–139, 2008, ISSN: 1545-4479. DOI: 10.1146/annurev.fluid.39.050905.110149

[14] L. Cattafesta and M. Sheplak, "Actuators for active flow control," *Annual Review of Fluid Mechanics*, vol. 43, pp. 247–272, 2011, ISSN: 1545-4479. DOI: 10.1146/annurev-fluid-122109-160634

[15] S. L. Brunton and B. R. Noack, "Closed-loop turbulence control: Progress and challenges," *Applied Mechanics Reviews*, vol. 67(5), 2015, ISSN: 0003-6900. DOI: 10.1115/1.4031175

[16] D. Sipp and P. J. Schmid, "Closed-loop control of fluid flow: A review of linear approaches and tools for the stabilization of transitional flows," *ONERA Aerospace Lab Journal*, vol. 6, 2016. DOI: 10.1115/1.4033345

[17] S. A. Gbadebo, N. A. Cumpsty, and T. P. Hynes, "Control of three-dimensional separations in axial compressors by tailored boundary layer suction," *Journal of Turbomachinery*, vol. 130(1), p. 011004, 2008, ISSN: 0889-504X. DOI: 10.1115/1.2749294

[18] G. A. Reynolds and W. S. Saric, "Experiments on the stability of the flat-plate boundary layer with suction," *AIAA Journal*, vol. 24(2), pp. 202–207, 1986, ISSN: 00011452. DOI: 10.2514/3.9246

[19] T. I. Saeed, W. R. Graham, and C. A. Hall, "Boundary-layer suction system design for laminar-flying-wing aircraft," *Journal of Aircraft*, vol. 48(4), pp. 1368–1379, 2011, ISSN: 15333868. DOI: 10.2514/1.C031283

[20] M. Gad-el Hak and D. M. Bushnell, "Separation control: Review," *Journal of Fluids Engineering*, vol. 113(1), pp. 5–30, 1991, ISSN: 0098-2202. DOI: 10.1115/1.2926497

[21] N. Gautier and J.-L. Aider, "Control of the separated flow downstream of a backward-facing step using visual feedback," *Proceedings of the Royal Society A: Mathematical, Physical and Engineering Sciences*, vol. 469(2160), p. 20 130 404, 2013, ISSN: 1364-5021. DOI: 10.1098/rspa.2013.0404

[22] R. A. Wallis, "The use of air jets for boundary layer control," Aeronautical Research Labs, Melbourne, Australia, 1952, ARL-AERO-NOTE-110, DODA-AR-005-831.

[23] J. P. Johnston and M. Nishi, "Vortex generator jets—means for flow separation control," *AIAA Journal*, vol. 28(6), pp. 989–994, 1990, ISSN: 00011452. DOI: 10.2514/3.25155

[24] Z. U. Khan and J. P. Johnston, "On vortex generating jets," *International Journal of Heat and Fluid Flow*, vol. 21(5), pp. 506–511, 2000, Turbulence and Shear Flow Phenomena 1, ISSN: 0142-727X. DOI: 10.1016/S0142-727X(00)00038-2

[25] T. N. Jukes and K. S. Choi, "On the formation of streamwise vortices by plasma vortex generators," *Journal of Fluid Mechanics*, vol. 733, pp. 370–393, 2013, ISSN: 14697645. DOI: 10.1017/jfm.2013.418

[26] B. F. Zhang, K. Liu, Y. Zhou, S. To, and J. Y. Tu, "Active drag reduction of a high-drag ahmed body based on steady blowing," *Journal of Fluid Mechanics*, vol. 856, pp. 351–396, 2018, ISSN: 14697645. DOI: 10.1017/jfm.2018.703

[27] K. R. McManus, H. H. Legner, and S. J. Davis, "Pulsed vortex generator jets for active control of flow separation," in *25th AIAA Fluid Dynamics Conference*, AIAA, 1994. DOI: 10.2514/6.1994-2218

[28] J. P. Bons, R. Sondergaard, and R. B. Rivir, "Turbine separation control using pulsed vortex generator jets," *Journal of Turbomachinery*, vol. 123(2), pp. 198–206, 2001, ISSN: 0889504X. DOI: 10.1115/1.1350410

[29] G. Raman and S. Raghu, "Cavity resonance suppression using miniature fluidic oscillators," *AIAA Journal*, vol. 42(12), pp. 2608–2612, 2004, ISSN: 00011452. DOI: 10.2514/1.521

[30] M. G. De Giorgi, C. G. De Luca, A. Ficarella, and F. Marra, "Comparison between synthetic jets and continuous jets for active flow control: Application on a naca 0015 and a compressor stator cascade," *Aerospace Science and Technology*, vol. 43, pp. 256–280, 2015, ISSN: 12709638. DOI: 10.1016/j.ast.2015.03.004

[31] F. A. Tricouros, M. Amitay, and T. V. Buren, "Comparing steady and unsteady rectangular jets issuing into a crossflow," *Journal of Fluid Mechanics*, vol. 942, A56, 2022, ISSN: 14697645. DOI: 10.1017/jfm.2022.413

[32] P Huerre and P. A. Monkewitz, "Local and global instabilities in spatially developing flows," *Annual Review of Fluid Mechanics*, vol. 22, pp. 473–537, 1990, ISSN: 1545-4479. DOI: https://doi.org/10.1146/annurev.fl.22.010190.002353

[33] C. D. Winant and F. K. Browand, "Vortex pairing: The mechanism of turbulent mixing-layer growth at moderate reynolds number," *Journal of Fluid Mechanics*, vol. 63(2), pp. 237–255, 1974, ISSN: 14697645. DOI: 10.1017/S0022112074001121

[34] A. K. Hussain and K. B. Zaman, "The free shear layer tone phenomenon and probe interference," *Journal of Fluid Mechanics*, vol. 87(2), pp. 349–383, 1978, ISSN: 14697645. DOI: 10.1017/S0022112078001652

[35] J. K. Eaton, "Turbulent flow reattachment: An experimental study of the flow and structure behind a backward-facing step," PhD thesis, Stanford University, 1980, ISBN: 9798660568862.

[36] K. B. M. Q. Zaman and A. K. M. F. Hussain, "Turbulence suppression in free shear flows by controlled excitation," *Journal of Fluid Mechanics*, vol. 103, pp. 133–159, 1981, ISSN: 14697645. DOI: 10.1017/S0022112081001274

[37] Z. D. Husain and A. K. M. F. Hussain, "Natural instability of free shear layers," *AIAA Journal*, vol. 21(11), pp. 1512–1517, 1983, ISSN: 00011452. DOI: 10.2514/3.8282

[38] C. Ho and P Huerre, "Perturbed free shear layers," *Annual Review of Fluid Mechanics*, vol. 16, pp. 365–422, 1984, ISSN: 1545-4479. DOI: 10.1146/annurev.fl.16.010184.002053

[39] M. A. Z. Hasan, "The flow over a backward-facing step under controlled perturbation: Laminar separation," *Journal of Fluid Mechanics*, vol. 238, pp. 73–96, 73 1992, ISSN: 14697645. DOI: 10.1017/S0022112092001642

[40] M. A. Z. Hasan and A. S. Khan, "On the instability characteristics of a reattaching shear layer with nonlaminar separation," *International Journal of Heat and Fluid Flow*, vol. 13(3), pp. 224–231, 1992, ISSN: 0142-727X. DOI: https://doi.org/10.1016/0142-727X(92)90035-8

[41] K. B. Chun and H. J. Sung, "Control of turbulent separated flow over a backward-facing step by local forcing," *Experiments in Fluids*, vol. 21(6), pp. 417–426, 1996, ISSN: 07234864. DOI: 10.1007/BF00189044

[42] F. Marrot, S. Pauzin, P. Gajan, F. Simon, and D. Biron, "Modification of backward-facing step flow by acoustical wave," in *4th AIAA/CEAS Aeroacoustics Conference*, AIAA, 1998, pp. 560–570. DOI: 10.2514/6.1998-2301

[43] L. P. Bernal and A. Roshko, "Strearnwise vortex structure in plane mixing layers," *Journal of Fluid Mechanics*, vol. 170, pp. 499–525, 1986, ISSN: 14697645. DOI: 10.1017/S002211208600099X

[44] S. C. Crow and F. H. Champagne, "Orderly structure in jet turbulence," *Journal of Fluid Mechanics*, vol. 48, pp. 547–591, 3 1971, ISSN: 14697645. DOI: 10.1017/S0022112071001745

[45] T. Berk, T. Medjnoun, and B. Ganapathisubramani, "Entrainment effects in periodic forcing of the flow over a backward-facing step," *Physical Review of Fluids*, vol. 2, 7 2017, ISSN: 2469990X. DOI: 10.1103/PhysRevFluids.2.074605

[46] M. Samimy, N. Webb, and M. Crawley, "Excitation of free shear-layer instabilities for high-speed flow control," *AIAA Journal*, vol. 56, pp. 1770–1791, 5 2018, ISSN: 00011452. DOI: 10.2514/1.J056610

[47] T. Duriez, J.-L. Aider, J. E. Wesfreid, and G. Artana, "Control of a backward-facing step flow through vortex pairing and phase locking," 2014. DOI: 10.48550/arXiv.1405.4234

[48] F. Marrot, P. Gajan, S. Pauzin, and F. Simon, "Experimental application of an active control loop on backward-facing step flow," *AIAA Journal*, vol. 43, pp. 1176–1186, 6 2005, ISSN: 00011452. DOI: 10.2514/1.8092

[49] H. S. Husain and F. Hussain, "Experiments on subharmonic resonance in a shear layer," *Journal of Fluid Mechanics*, vol. 304, pp. 343–372, 1995, ISSN: 14697645. DOI: 10.1017/S0022112095004459

[50] S. Evans and H. Hodson, "Separation-control mechanisms of steady and pulsed vortex-generator jets," *Journal of Propulsion and Power*, vol. 28(6), pp. 1201–1213, 2012, ISSN: 15333876. DOI: 10.2514/1.B34457

[51] J. M. Wiltse and A. Glezer, "Manipulation of free shear flows using piezoelectric actuators," *Journal of Fluid Mechanics*, vol. 249, pp. 261–285, 1993, ISSN: 14697645. DOI: 10.1017/S002211209300117X

[52] B. Vukasinovic, D. G. Lucas, and A. Glezer, "Direct manipulation of small-scale motions in a plane shear layer," in *2nd AIAA Flow Control Conference*, 2004, ISBN: 9781624100307. DOI: 10.2514/6.2004-2617

[53] C. J. Nicholls, K. Chakravarthy, B. M. Tang, B. A. Williams, and M. Bacic, "On acoustically modulated jet shear layers and the nyquist-shannon sampling theorem," *Physics of Fluids*, vol. 34, 11 2022, ISSN: 10897666. DOI: 10.1063/5.0118025

[54] K. B. Chun and H. J. Sung, "Visualization of a locally-forced separated flow over a backward-facing step," *Experiments in Fluids*, vol. 25, pp. 133–142, 1998. DOI: 10.1007/S003480050217

[55] Y. Z. Liu, W. Kang, and H. J. Sung, "Assessment of the organization of a turbulent separated and reattaching flow by measuring wall pressure fluctuations," *Experiments in Fluids*, vol. 38(4), pp. 485–493, 2005, ISSN: 07234864. DOI: 10.1007/s00348-005-0929-0

[56] S. Ghanami and M. Farhadi, "Fluidic oscillators' applications, structures and mechanisms – a review," *Journal of Transport Phenomena in Nano Micro Scales*, vol. 7(1), pp. 9–27, 2019, ISSN: 2322-3634. DOI: 10.22111/tpnms.2018.25051.1153

[57] C Nicholls, "The analysis, modelling, and acoustic control of fluidic devices," Phd thesis, University of Oxford, 2020.

[58] M. Mair, L.-W. Chen, J. Turner, M. Bacic, and P. Ireland, "Experimental and numerical analysis of a piezo driven fluidic device for active flow control," in *52nd AIAA/SAE/ASEE Joint Propulsion Conference*, 2016. DOI: 10.2514/6.2016-4860

[59] M Mair, "On dynamics of fluidic jet switching and shear layer instabilities," Phd thesis, University of Oxford, 2019.

[60] A. Glezer and M. Amitay, "Synthetic jets," *Annual Review of Fluid Mechanics*, vol. 34, pp. 503–529, 2002, ISSN: 1545-4479. DOI: 10.1146/annurev.fluid.34.090501.094913

[61] E. Moreau, "Airflow control by non-thermal plasma actuators," *Journal of Physics D: Applied Physics*, vol. 40(3), pp. 605–636, 2007, ISSN: 00223727. DOI: 10.1088/0022-3727/40/3/S01

[62] R. Dawson and J. Little, "Characterization of nanosecond pulse driven dielectric barrier discharge plasma actuators for aerodynamic flow control," *Journal of Applied Physics*, vol. 113(10), 2013, ISSN: 00218979. DOI: 10.1063/1.4794507

[63] S. H. Popkin, B. Z. Cybyk, C. H. Foster, and F. S. Alvi, "Experimental estimation of sparkjet efficiency," *AIAA Journal*, vol. 54(6), pp. 1831–1845, 2016, ISSN: 00011452. DOI: 10.2514/1.J052694

[64] L. N. Cattafesta, S. Garg, and D. Shukla, "Development of piezoelectric actuators for active flow control," *AIAA Journal*, vol. 39(8), pp. 1562–1568, 2001, ISSN: 00011452. DOI: 10.2514/2.1481

[65] G. B. Schubauer and H. K. Skramstad, "Laminar-boundary-layer oscillations and transition on a flat plate," National Advisory Committee For Aeronautics, 1948, Report number: NACA-WR-W-8.

[66] J. O'Connor, "Understanding the role of flow dynamics in thermoacoustic combustion instability," *Proceedings of the Combustion Institute*, vol. 39(4), pp. 4583–4610, 2023, ISSN: 15407489. DOI: 10.1016/j.proci.2022.07.115

[67] D. G. Crighton, "Acoustics as a branch of fluid mechanics," *Journal of Fluid Mechanics*, vol. 106, pp. 261–298, 1981, ISSN: 14697645. DOI: 10.1017/S0022112081001602

[68] D. R. Williams, M. Acharya, and J. Bernhardt, "Mechanisms of flow control with the unsteady bleed technique," *NASA. Ames Research Center, Physics of Forced Unsteady Separation*, pp. 297–307, 1992.

[69] S. Bhattacharjee, B. Scheelke, and T. R. Troutt, "Modification of vortex interactions in a reattaching separated flow," *AIAA Journal*, vol. 24(4), pp. 623–629, 1986, ISSN: 00011452. DOI: 10.2514/3.9317

[70] M. Nishioka, M. Asai, and S. Yoshida, "Control of flow separation by acoustic excitation," *AIAA Journal*, vol. 28(11), pp. 1909–1915, 1990, ISSN: 00011452. DOI: 10.2514/3.10498

[71] K. B. M. Q. Zaman and A. K. M. F. Hussain, "Vortex pairing in a circular jet under controlled excitation. part 1. general jet response," *Journal of Fluid Mechanics*, vol. 101(3), pp. 449–491, 1980, ISSN: 14697645. DOI: 10.1017/S0022112080001760

[72] M. Mair, M. Bacic, K. Chakravarthy, and B. Williams, "Jet preferred mode vs shear layer mode," *Physics of Fluids*, vol. 32(6), 2020, ISSN: 10897666. DOI: 10.1063/5.0007934

[73] B. Jubelin, "New experimental studies on jet noise amplification," in *AIAA 6th Aeroacoustics Conference*, AIAA, 1980. DOI: 10.2514/6.1980-961

[74] K. K. Ahuja and R. H. Burrin, "Control of flow separation by sound," in *AIAA/NASA 9th Aeroacoustics Conference*, AIAA, 1984. DOI: 10.2514/6.1984-2298

[75] J. Lepicovsky, K. K. Ahuja, and M. Salikuddin, "An experimental study of tone-excited heated jets," *Journal of Propulsion and Power*, vol. 2(2), pp. 149–154, 1986, ISSN: 07484658. DOI: 10.2514/3.22859

[76] R. R. Mankbadi, G. Raman, and E. J. Rice, "Effects of core turbulence on jet excitability," in *2nd Shear Flow Conference*. DOI: 10.2514/6.1989-966

[77] K. B. M. Q. Zaman, "Effect of acoustic excitation on stalled flows over an airfoil," *AIAA Journal*, vol. 30(6), pp. 1492–1499, 1992, ISSN: 00011452. DOI: 10.2514/3.11092

[78] J. K. Eaton and J. P. Johnston, "A review of research on subsonic turbulent flow reattachment," *AIAA Journal*, vol. 19, pp. 1093–1100, 9 1981, ISSN: 00011452. DOI: 10.2514/3.60048

[79] R. L. Simpson, "Turbulent boundary-layer separation," *Annual Review of Fluid Mechanics*, vol. 21, pp. 205–232, 1989, ISSN: 1545-4479. DOI: 10.1146/annurev.fl.21.010189.001225

[80] H. Coandă, "Device for deflecting a stream of elastic fluid projected into an elastic fluid," U.S. Patent 2 052 869, 1, 1936.

[81] M. V. Ötügen, "Expansion ratio effects on the separated shear layer and reattachment downstream of a backward-facing step," *Experiments in Fluids*, vol. 10(5), pp. 273–280, 1991, ISSN: 1432-1114. DOI: 10.1007/BF00202460

[82] M. V. Ötügen and G. Muckenthaler, "Study of separated shear layer in moderate reynolds number plane sudden expansion flows," *AIAA Journal*, vol. 30(7), pp. 1808–1814, 7 1992, ISSN: 00011452. DOI: 10.2514/3.11140

[83] J. H. Nie and B. F. Armaly, "Reverse flow regions in three-dimensional backward-facing step flow," *International Journal of Heat and Mass Transfer*, vol. 47(22), pp. 4713–4720, 2004, ISSN: 00179310. DOI: 10.1016/j.ijheatmasstransfer.2004.05.027

[84] P. M. Nadge and R. N. Govardhan, "High reynolds number flow over a backward-facing step: Structure of the mean separation bubble," *Experiments in Fluids*, vol. 55(1), pp. 4713–4720, 2014, ISSN: 07234864. DOI: 10.1007/s00348-013-1657-5

[85] K. Zheng, H. Setiawan, J. Philip, J. Lee, and J. P. Monty, "Flows over backward-facing steps with different spanwise widths," *Physical Review Fluids*, vol. 9(12), p. 124 601, 2024, ISSN: 2469990X. DOI: 10.1103/PhysRevFluids.9.124601

[86] V. de Brederode and P. Bradshaw, "Three-dimensional flow in nominally two-dimensional separation bubbles: Flow behind a rearward-facing step. i.," Aero report 72-19, Department of Aeronautics, Imperial College of Science and Technology, Apr. 1972.

[87] A. S. Neto, D. Grand, O. Métais, and M. Lesieur, "A numerical investigation of the coherent vortices in turbulence behind a backward-facing step," *Journal of Fluid Mechanics*, vol. 256, pp. 1–25, 1993, ISSN: 14697645. DOI: 10.1017/S0022112093002691

[88] H. Le, P. Moin, and J. Kim, "Direct numerical simulation of turbulent flow over a backward-facing step," *Journal of Fluid Mechanics*, vol. 330, pp. 349–374, 1997, ISSN: 00221120. DOI: 10.1017/S0022112096003941

[89] I Lee and H. J. Sung, "Characteristics of wall pressure fluctuations in separated flows over a backward-facing step," 2001, pp. 273–282. DOI: 10.1007/s003480000173

[90] D. Wee, T. Yi, A. Annaswamy, and A. F. Ghoniem, "Self-sustained oscillations and vortex shedding in backward-facing step flows: Simulation and linear instability analysis," *Physics of Fluids*, vol. 16(9), pp. 3361–3373, 2004, ISSN: 10706631. DOI: 10.1063/1.1773091

[91] R. Hu, L. Wang, and S. Fu, "Investigation of the coherent structures in flow behind a backward-facing step," *International Journal of Numerical Methods for Heat and Fluid Flow*, vol. 26(3-4), pp. 1050–1068, 2016, ISSN: 09615539. DOI: 10.1108/HFF-09-2015-0403

[92] T. R. Troutt, B. Scheelke, and T. R. Norman, "Organized structures in a reattaching separated flow field," *Journal of Fluid Mechanics*, vol. 143, pp. 413–427, 1984, ISSN: 14697645. DOI: 10.1017/S0022112084001415

[93] L. M. Hudy and A. Naguib, "Stochastic estimation of a separated-flow field using wall-pressure-array measurements," *Physics of Fluids*, vol. 19(2), p. 024 103, 2007, ISSN: 10706631. DOI: 10.1063/1.2472507

[94] X. Ma and A. Schröder, "Analysis of flapping motion of reattaching shear layer behind a two-dimensional backward-facing step," *Physics of Fluids*, vol. 29(11), 2017, ISSN: 10897666. DOI: 10.1063/1.4996622

[95] J. K. Eaton and J. P. Johnston, "Low frequency unsteadyness of a reattaching turbulent shear layer," in *Turbulent Shear Flows 3*, L. J. S. Bradbury, F. Durst, B. E. Launder, F. W. Schmidt, and J. H. Whitelaw, Eds., Berlin, Heidelberg: Springer Berlin Heidelberg, 1982, pp. 162–170, ISBN: 978-3-642-95410-8.

[96] D. M. Driver, H. L. Seegmiller, and J. G. Marvin, "Time-dependent behavior of a reattaching shear layer," *AIAA Journal*, vol. 25(7), pp. 914–919, 1987, ISSN: 00011452. DOI: 10.2514/3.9722

[97] A. F. Heenan and J. F. Morrison, "Passive control of pressure fluctuations generated by separated flow," *AIAA Journal*, vol. 36(6), pp. 1014–1022, 1998, ISSN: 00011452. DOI: 10.2514/2.474

[98] T. Horchler, K. V. Mani, and K. Hannemann, "Dynamic mode decomposition of backward-facing step flow simulation data," in *22nd AIAA Computational Fluid Dynamics Conference*, 2015, ISBN: 9781624103667. DOI: 10.2514/6.2015-3411

[99] V. Statnikov, I. Bolgar, S. Scharnowski, M. Meinke, C. J. Kähler, and W. Schröder, "Analysis of characteristic wake flow modes on a generic transonic backward-facing step configuration," *European Journal of Mechanics, B/Fluids*, vol. 59, pp. 124–134, 2016, ISSN: 09977546. DOI: 10.1016/j.euromechflu.2016.05.008

[100] C. Chovet, M. Lippert, L. Keirsbulck, and J. M. Foucaut, "Unsteady behavior of a backward-facing step in forced flow," *Flow, Turbulence and Combustion*, vol. 102(1), pp. 145–165, 2019, ISSN: 15731987. DOI: 10.1007/s10494-018-9944-0

[101] I. Lee, S. K. Ahn, and H. J. Sung, "Three-dimensional coherent structure in a separated and reattaching flow over a backward-facing step," *Experiments in Fluids*, vol. 36(3), pp. 373–383, 2004, ISSN: 07234864. DOI: 10.1007/s00348-003-0637-6

[102] A. Müller, A. Gyr, A. Müller, and B. M. Sumer, "Visualization of the mixing layer behind dunes," eng, in *Mechanics of Sediment Transport*, 1st ed., Taylor & Francis, 1983, pp. 41–45, ISBN: 9789061912217.

[103] P. Bradshaw and F. Y. Wong, "The reattachment and relaxation of a turbulent shear layer," *Journal of Fluid Mechanics*, vol. 52(1), pp. 113–135, 1972, ISSN: 14697645. DOI: 10.1017/S002211207200299X

[104] E. W. Adams and J. P. Johnston, "Effects of the separating shear layer on the reattachment flow structure part 2: Reattachment length and wall shear stress," *Experiments in Fluids*, vol. 6, pp. 493–499, 1988, ISSN: 1432-1114. DOI: 10.1007/BF00196511

[105] V. A. S. L. de Brederode, "Three-dimensional effects in nominally two-dimensional flows," PhD thesis, Imperial College of Science and Technology, 1975.

[106] K. Lim, S. Park, and H. Shim, "A low aspect ratio backward-facing step flow," *Experimental Thermal and Fluid Science*, vol. 3(5), pp. 508–514, 1990, ISSN: 0894-1777. DOI: 10.1016/0894-1777(90)90064-E

[107] V. Uruba, P. Jonáš, and O. Mazur, "Control of a channel-flow behind a backward-facing step by suction/blowing," *International Journal of Heat and Fluid Flow*, vol. 28(4), pp. 665–672, 2007, ISSN: 0142727X. DOI: 10.1016/j.ijheatfluidflow.2007.04.002

[108] T. Morioka and S. Honami, "A control system of backward-facing step flow by vortex generator jets," in *31st AIAA Fluid Dynamics Conference & Exhibit*, 2001. DOI: 10.2514/6.2001-3029

[109] F. Marrot, F. Simon, P. Gajan, and S. Pauzin, "Active control of a backward-facing step flow," in *6th Aeroacoustics Conference and Exhibit*, American Institute of Aeronautics and Astronautics Inc., 2000. DOI: 10.2514/6.2000-1929

[110] J. D'Adamo, R. Sosa, and G. Artana, "Active control of a backward-facing step flow with plasma actuators," *Journal of Fluids Engineering, Transactions of the ASME*, vol. 136(12), pp. 1–9, 2014, ISSN: 1528901X. DOI: 10.1115/1.4027598

[111] T. McQueen, D. Burton, J. Sheridan, and M. C. Thompson, "Active control of flow over a backward-facing step at high reynolds numbers," *International Journal of Heat and Fluid Flow*, vol. 93, p. 108 891, 2022, ISSN: 0142727X. DOI: 10.1016/j.ijheatfluidflow.2021.108891

[112] S. Yoshioka, S. Obi, and S. Masuda, "Momentum transfer in the periodically perturbed turbulent separated flow over the backward-facing step," in *Proceedings of the First International Symposium on Turbulence and Shear Flow Phenomena*, 1999. DOI: 10.1615/TSFP1.2120

[113] S. Yoshioka, S. Obi, and S. Masuda, "Organized vortex motion in periodically perturbed turbulent separated flow over a backward-facing step," *International Journal of Heat and Fluid Flow*, vol. 22(3), pp. 301–307, 2001, ISSN: 0142727X. DOI: 10.1016/S0142-727X(01)00092-3

[114] L. Henning and R. King, "Robust multivariable closed-loop control of a turbulent backward-facing step flow," *Journal of Aircraft*, vol. 44(1), pp. 201–208, 2007, ISSN: 15333868. DOI: 10.2514/1.22934

[115] N. Gautier and J.-L. Aider, "Control of the separated flow downstream of a backward-facing step using visual feedback," *Proceedings of the Royal Society A: Mathematical, Physical and Engineering Sciences*, vol. 469(2160), 2013, ISSN: 1364-5021. DOI: 10.1098/rspa.2013.0404

[116] C. Chovet, M. Lippert, L. Keirsbulck, and J. M. Foucaut, "Unsteady behavior of a backward-facing step in forced flow," *Flow, Turbulence and Combustion*, vol. 102(1), pp. 145–165, 2019, ISSN: 15731987. DOI: 10.1007/s10494-018-9944-0

[117] S. G. Pouryoussefi, M. Mirzaei, and M. Hajipour, "Experimental study of separation bubble control behind a backward-facing step using plasma actuators," *Acta Mechanica*, vol. 226(4), pp. 1153–1165, 2015, ISSN: 16196937. DOI: 10.1007/s00707-014-1245-7

[118] P. Sujar-Garrido, N. Benard, E. Moreau, and J. P. Bonnet, "Dielectric barrier discharge plasma actuator to control turbulent flow downstream of a backward-facing step," *Experiments in Fluids*, vol. 56(4), 2015, ISSN: 14321114. DOI: 10.1007/s00348-015-1939-1

[119] N. Benard, P. Sujar-Garrido, J. P. Bonnet, and E. Moreau, "Control of the coherent structure dynamics downstream of a backward-facing step by dbd plasma actuator," *International Journal of Heat and Fluid Flow*, vol. 61(A), pp. 158–173, 2016, ISSN: 0142727X. DOI: 10.1016/j.ijheatfluidflow.2016.04.009

[120] D. Gil-Prieto, P. K. Zachos, D. G. MacManus, and G. McLelland, "Unsteady characteristics of s-duct intake flow distortion," *Aerospace Science and Technology*, vol. 84, pp. 938–952, 2019, ISSN: 12709638. DOI: 10.1016/j.ast.2018.10.020

[121] T. J. Burrows, B. Vukasinovic, and A. Glezer, "Flow dynamics effected by active flow control in an offset diffuser," in *2018 Flow Control Conference*, 2018. DOI: 10.2514/6.2018-4024

[122] T. J. Burrows, B. Vukasinovic, A. Glezer, M. T. Lakebrink, and M. Mani, "Experimental and numerical investigation of active flow control of a serpentine diffuser," *AIAA Journal*, vol. 59(2), pp. 607–620, 2021, ISSN: 1533385X. DOI: 10.2514/1.J059533

[123] A. Rabe Scribben, W. Ng, and R. Burdisso, "Effectiveness of a serpentine inlet duct flow control technique at design and off-design simulated flight conditions," *Journal of Turbomachinery*, vol. 128(2), pp. 332–339, 2004, ISSN: 0889-504X. DOI: 10.1115/1.2098787

[124] A. N. Gissen, B. Vukasinovic, and A. Glezer, "Dynamics of flow control in an emulated boundary layer-ingesting offset diffuser," *Experiments in Fluids*, vol. 55(8), 2014, ISSN: 07234864. DOI: 10.1007/s00348-014-1794-5

[125] A. N. Gissen, B. Vukasinovic, M. L. McMillan, and A. Glezer, "Distortion management in a boundary layer ingestion inlet diffuser using hybrid flow control," *Journal of Propulsion and Power*, vol. 30(3), pp. 834–844, 2014, ISSN: 15333876. DOI: 10.2514/1.B34981

[126] K. Ahuja and M. Whiffen, "Tone excited jets, part ii: Flow visualization," *Journal of Sound and Vibration*, vol. 102(1), pp. 63–69, 1985, ISSN: 0022-460X. DOI: https://doi.org/10.1016/S0022-460X(85)80103-6

[127] T. C. Corke, F. Shakib, and H. M. Nagib, "Mode selection and resonant phase locking in unstable axisymmetric jets," *Journal of Fluid Mechanics*, vol. 223, pp. 253–311, 1991, ISSN: 14697645. DOI: 10.1017/S0022112091001428

[128] F. G. Collins and J. Zelenevitz, "Influence of sound upon separated flow over wings," *AIAA Journal*, vol. 13(3), pp. 408–410, 1975, ISSN: 00011452. DOI: 10.2514/3.49717

[129] K. B. M. Q. Zaman and D. J. McKinzie, "Control of laminar separation over airfoils by acoustic excitation," *AIAA Journal*, vol. 29(7), pp. 1075–1083, 1991, ISSN: 00011452. DOI: 10.2514/3.10706

[130] S. Coskun, D. J. Rajendran, V. Pachidis, and M. Bacic, "Control of flow separation over an aerofoil by external acoustic excitation at a high reynolds number," *Physics of Fluids*, vol. 36(1), 2024, ISSN: 10897666. DOI: 10.1063/5.0179439

[131] C. Nicholls and M. Bacic, "Closed-loop control of a piezo-fluidic amplifier," *AIAA Journal*, vol. 58(6), pp. 2414–2427, 2020, ISSN: 00011452. DOI: 10.2514/1.J059305

[132] C. J. Nicholls, B. M. Tang, J. Turner, and M. Bacic, "An analytical model of the dynamics of reattaching jets," *Physics of Fluids*, vol. 35(11), 2023, ISSN: 10897666. DOI: 10.1063/5.0170567

[133] K. Zhou, J. Doyle, and K. Glover, *Robust and Optimal Control* (Feher/Prentice Hall Digital and). Prentice Hall, 1996, ISBN: 9780134565675.

[134] B. Anderson and J. Moore, *Optimal Control: Linear Quadratic Methods* (Dover Books on Engineering). Dover Publications, 2007, ISBN: 9780486457666.

[135] B. D. O. Anderson and J. B. Moore, *Optimal control: linear quadratic methods* (Prentice-Hall information and system sciences series), eng. Englewood Cliffs ; Prentice-Hall, 1989, ISBN: 0136386512.

[136] R. E. Kalman, "A new approach to linear filtering and prediction problems," *Journal of Basic Engineering*, vol. 82(1), pp. 35–45, 1960, ISSN: 0021-9223. DOI: 10.1115/1.3662552

[137] J. C. Doyle, "Guaranteed margins for lqg regulators," *IEEE Transactions on Automatic Control*, vol. 23(4), pp. 756–757, 1978, ISSN: 1558-2523. DOI: 10.1109/TAC.1978.1101812

[138] J. C. Doyle and G. Stein, "Robustness with observers," *IEEE Transactions on Automatic Control*, vol. 24(4), pp. 607–611, 1979, ISSN: 1558-2523. DOI: 10.1109/TAC.1979.1102095

[139] K. Taira et al., "Modal analysis of fluid flows: An overview," *AIAA Journal*, vol. 55(12), pp. 4013–4041, 2017, ISSN: 00011452. DOI: 10.2514/1.J056060

[140] J. L. Lumley, "The structure of inhomogeneous turbulent flows," *Atmospheric Turbulence and Radio Wave Propagation*, pp. 166–178, 1967.

[141] L. Wang, "Karhunen-loeve expansions and their applications.," PhD thesis, London School of Economics and Political Science, 2008.

[142] O. T. Schmidt and T. Colonius, "Guide to spectral proper orthogonal decomposition," *AIAA Journal*, vol. 58(3), pp. 1023–1033, 2020, ISSN: 00011452. DOI: 10.2514/1.J058809

[143] L. Sirovich, "Turbulence and the dynamics of coherent structures part i: coherent structures," *Quarterly of Applied Mathematics*, vol. 45, pp. 561–571, 1987, ISSN: 1552-4485. DOI: 10.1090/qam/910462

[144] P. J. Schmid, "Dynamic mode decomposition of numerical and experimental data," *Journal of Fluid Mechanics*, vol. 656, pp. 5–28, 2010, ISSN: 14697645. DOI: 10.1017/S0022112010001217

[145] B. O. Koopman, "Hamiltonian systems and transformation in hilbert space," *Proceedings of the National Academy of Sciences*, vol. 17(5), pp. 315–318, 1931. DOI: 10.1073/pnas.17.5.315

[146] C. W. Rowley, I. Mezi, S. Bagheri, P. Schlatter, and D. S. Henningson, "Spectral analysis of nonlinear flows," *Journal of Fluid Mechanics*, vol. 641, pp. 115–127, 2009, ISSN: 00221120. DOI: 10.1017/S0022112009992059

[147] S. L. Brunton, *Notes on koopman operator theory*, 2019.

[148] J. H. Tu, C. W. Rowley, D. M. Luchtenburg, S. L. Brunton, and J. N. Kutz, "On dynamic mode decomposition: Theory and applications," *Journal of Computational Dynamics*, vol. 1(2), pp. 391–421, 2014, ISSN: 21582505. DOI: 10.3934/jcd.2014.1.391

[149] J. L. Proctor, S. L. Brunton, and J. N. Kutz, "Dynamic mode decomposition with control," *SIAM Journal on Applied Dynamical Systems*, vol. 15(1), pp. 142–161, 2016, ISSN: 15360040. DOI: 10.1137/15M1013857

[150] M. R. Jovanović, P. J. Schmid, and J. W. Nichols, "Sparsity-promoting dynamic mode decomposition," *Physics of Fluids*, vol. 26(2), 2014, ISSN: 10897666. DOI: 10.1063/1.4863670

[151] R. Becker, M. Garwon, and R. King, "Development of model-based sensors and their use for closed-loop control of separated shear flows," in *2003 European Control Conference (ECC)*, 2003, pp. 3237–3242. DOI: 10.23919/ECC.2003.7086538

[152] A. S. Morgans, J. A. Dahan, and T. Flinois, "Feedback control for reducing the pressure drag of bluff bodies terminated by a backward-facing step," in *2014 UKACC International Conference on Control (CONTROL)*, 2014, pp. 220–225. DOI: 10.1109/CONTROL.2014.6915143

[153] C. Raibaudo and F. Kerhervé, "Experimental model-based closed-loop control of a separated boundary layer at high reynolds number," *European Journal of Mechanics, B/Fluids*, vol. 91, pp. 80–93, 2022, ISSN: 09977546. DOI: 10.1016/j.euromechflu.2021.09.011

[154] E. A. Deem, L. N. Cattafesta, M. S. Hemati, H. Zhang, C. Rowley, and R. Mittal, "Adaptive separation control of a laminar boundary layer using online dynamic mode decomposition," *Journal of Fluid Mechanics*, vol. 903, 2020, ISSN: 0022-1120. DOI: 10.1017/jfm.2020.546

[155] N. Fonzi, S. L. Brunton, and U. Fasel, "Data-driven nonlinear aeroelastic models of morphing wings for control," *Proceedings of the Royal Society A: Mathematical, Physical and Engineering Sciences*, vol. 476(2239), p. 20 200 079, 2020, ISSN: 1364-5021. DOI: 10.1098/rspa.2020.0079

[156] K. B. Ariyur and M. Krstic, *Real-time optimization by extremum-seeking control*. 2003, ISBN: 9780471669784. DOI: 10.1002/0471669784

[157] M. Garwon, L. H. Darmadi, F. Urzynicok, G. Bärwolff, and R. King, "Adaptive control of separated flows," in *2003 European Control Conference (ECC)*, IEEE, 2003. DOI: 10.23919/ECC.2003.7086537

[158] R. King et al., "Adaptive flow control using slope seeking," in *14th Mediterranean Conference on Control and Automation*, IEEE, 2006. DOI: 10.1109/MED.2006.328753

[159] L. Neuhaus and W. Neise, "Active flow control to improve the aerodynamic and acoustic performance of axial turbomachines," in *1st Flow Control Conference*, AIAA, 2002. DOI: 10.2514/6.2002-2948

[160] J. E. Ffowcs Williams and B. C. Zhao, "The active control of vortex shedding," 1989, pp. 115–122. DOI: 10.1016/S0889-9746(89)90026-1

[161] K. Roussopoulos, "Feedback control of vortex shedding at low reynolds numbers," *Journal of Fluid Mechanics*, vol. 248, pp. 267–296, 1993, ISSN: 14697645. DOI: 10.1017/S0022112093000771

[162] P. M. Morse and K. U. Ingard, *Theoretical acoustics*, eng. Princeton, N.J: Princeton University Press, 1986, ISBN: 0691084254.

[163] *Fr 58_2204_2205_0*, https://www.visaton.de/sites/default/files/dd_product/FR%2058_2204_2205_0.pdf, VISATON GmbH & Co. KG, 2023.

[164] O. Sinclair, J. Turner, B. M. Tang, C. J. Nicholls, and M. Bacic, "Identification and closed-loop control of a backwards facing step by opposite side acoustic excitation," in *AIAA Science and Technology Forum and Exposition*, 2022, ISBN: 9781624106316. DOI: 10.2514/6.2022-0474

[165] A. Richards, *University of oxford advanced research computing*, 2015. DOI: 10.5281/zenodo.22558

[166] F. R. Menter, "Scale-resolving simulations in ansys cfd / 1 best practice: Scale-resolving simulations in ansys cfd," Ansys Germany Gmbh, 2021.

[167] G. N. Coleman and R. D. Sandberg, "A primer on direct numerical simulation of turbulence - methods, procedures and guidelines," University of Southampton, Project Report, 2010.

[168] D. G. Mabey, "Analysis and correlation of data on pressure fluctuations in separated flow," *Journal of Aircraft*, vol. 9(9), pp. 642–645, 1972, ISSN: 00218669. DOI: 10.2514/3.59053

[169] S. D. Hall, M. Behnia, C. A. Fletcher, and G. L. Morrison, "Investigation of the secondary corner vortex in a benchmark turbulent backward-facing step using cross-correlation particle imaging velocimetry," *Experiments in Fluids*, vol. 35(2), pp. 139–151, 2003, ISSN: 07234864. DOI: 10.1007/s00348-003-0626-9

[170] U. Ingard, "On the theory and design of acoustic resonators," eng, *The Journal of the Acoustical Society of America*, vol. 25(6), pp. 1037–1061, 1953, ISSN: 0001-4966.

[171] S. C. Morris and J. F. Foss, "Turbulent boundary layer to single-stream shear layer: The transition region," *Journal of Fluid Mechanics*, vol. 494, pp. 187 –221, 2003. DOI: 10.1017/S0022112003006049

[172] C. Barbi, D. P. Favier, C. A. Maresca, and D. P. Telionis, "Vortex shedding and lock-on of a circular cylinder in oscillatory flow," *Journal of Fluid Mechanics*, vol. 170, pp. 527–544, 1986, ISSN: 14697645. DOI: 10.1017/S0022112086001003

[173] G. Tissot, L. Cordier, N. Benard, and B. R. Noack, "Model reduction using Dynamic Mode Decomposition," *Comptes Rendus - Mecanique*, vol. 342(6-7), pp. 410–416, 2014, ISSN: 16310721. DOI: 10.1016/j.crme.2013.12.011

[174] K. Åström and R. Murray, *Feedback Systems: An Introduction for Scientists and Engineers*. Princeton University Press, 2010, ISBN: 9781400828739.

[175] M. Bacic, M. Cannon, Y. I. Lee, and B. Kouvaritakis, "General interpolation in mpc and its advantages," *IEEE Transactions on Automatic Control*, vol. 48(6), pp. 1092–1096, 2003, ISSN: 00189286. DOI: 10.1109/TAC.2003.812817

[176] F. E. Jørgensen, "How to measure turbulence with hot-wire anemometers-a practical guide," Dantec Dynamics, 2005.

[177] N. N. Mansour, F Hussain, and J. C. Buelll, "Subharmonic resonance in a mixing layer," *Center for Turbulence Research, Proceedings of the Summer Program 1988*, pp. 57–68, 1988.

[178] G. Raman and E. J. Rice, "Axisymmetric jet forced by fundamental and subharmonic tones," *AIAA Journal*, vol. 29(7), pp. 1114–1122, 1991, ISSN: 00011452. DOI: 10.2514/3.10711

[179] D. J. Leith and W. E. Leithead, "Survey of gain-scheduling analysis and design," *International Journal of Control*, vol. 73(11), pp. 1001–1025, 2000, ISSN: 00207179. DOI: 10.1080/002071700411304

[180] J. C. Doyle and G. Stein, "Robustness with observers," in *1978 IEEE Conference on Decision and Control including the 17th Symposium on Adaptive Processes*, 1978. DOI: 10.1109/CDC.1978.267883

[181] J. Maciejowski, "Asymptotic recovery for discrete-time systems," *IEEE Transactions on Automatic Control*, vol. 30(6), pp. 602–605, 1985, ISSN: 1558-2523. DOI: 10.1109/TAC.1985.1104010

[182] Z. Zhang and J. S. Freudenberg, "Discrete-time loop transfer recovery for systems with nonminimum phase zeros and time delays," *Automatica*, vol. 29(2), 351–363, 1993, ISSN: 0005-1098. DOI: 10.1016/0005-1098(93)90128-G

[183] J. S. Freudenberg and D. P. Looze, "Sensitivity reduction, nonminimum phase zeros, and design tradeoffs in single loop feedback systems," in *The 22nd IEEE Conference on Decision and Control*, 1983, pp. 625–630. DOI: 10.1109/CDC.1983.269593